Passive seismic interferometry for reflection imaging & monitoring

Passive seismic interferometry for reflection imaging & monitoring

PROEFSCHRIFT

ter verkrijging van de graad van doctor
aan de Technische Universiteit Delft,
op gezag van de Rector Magnificus Prof. ir. K.C.A.M. Luyben,
voorzitter van het College voor Promoties,
in het openbaar te verdedigen op donderdag 02 Juni 2017 om 10.00 uur

door

Carlos ALMAGRO VIDAL

Geologische Ingenieur (Technische Universiteit Madrid)
Master of Science in Toegepaste Geofysica
(Technische Universiteit Delft, ETH Zürich & RWTH Aachen)
geboren te Madrid, Spanje

Dit proefschrift is goedgekeurd door de promotor:
Prof. dr. ir. C.P.A. Wapenaar

Samenstelling promotiecommissie:

Rector Magnificus	*Voorzitter*
Prof. dr. ir. C.P.A. Wapenaar	Technische Universiteit Delft, *promotor*

Onafhankelijke leden:

Prof. Dphil. Bsc. A. Curtis	Universiteit Edinburgh
Prof. dr. ir. E.C. Slob	Technische Universiteit Delft
Prof. dr. W.A. Mulder	Technische Universiteit Delft
Dr. I. Pires de Vasconcelos	Universiteit Utrecht
Drs. A.R. Verdel	TNO Utrecht

The research for this thesis has been financially supported by Netherlands Research Centre of Integrated Solid Earth Sciences (ISES).

ISBN: 978-94-6186-817-6

Typeset with XeLaTeX.

Printed by ProefschriftMaken B.V.

A mis padres

Contents

1 Introduction

1.1 Applied passive seismics

Geophysics is the ensemble of physical theories, observations and processing methods that serve to study the Earth structure and properties. It makes use of remote-sensing techniques to complement the understanding of the subsurface, which is traditionally achieved by geological methods. These geological methods comprise measurements usually within a range of observations limited to the human senses: surface observations obtained from visual inspection, photography, cartography and rock sampling, as well as "in-depth" observations from well-logging and coring of the subsurface. Therefore, in these geological methods the observation range is limited to the location *in situ* of the observer or the observation sensor. It is precisely at this limit, beyond which the human senses cannot reach, where geophysics takes over and complements the exploration of the subsurface.

Among the many possible physical methods, geophysicists exploit the propagation of seismic waves in the subsurface in order to determine the mechanical structures of the Earth's interior. These waves feature propagation delays and wave-scattering perturbations caused by the contrasts in the mechanical properties and their distribution in the medium. Since we work with spatially-limited sensor recordings (at the surface, along a well, etc.) we require a series of processes to interpret these features and transform the recordings into 3D maps of the distribution of the elastic properties of the subsurface.

A seismic exploration survey consists of two types of elements: emitting and receiving. The control over the emitters (or seismic sources) turns the exploration procedure into an active survey, where the generation of mechanical waves can be regulated by different devices (ranging from impulsive behaviour, with *v.g.* explosives, to controlled signals with vibrating devices). On the receiving side, the perturbation of the medium (or seismic wavefield) is observed by devices that record the features caused by the mechanical waves in different physical units (*e.g.* particle velocities with geophones or pressure fields with hydrophones).

We deploy these receivers in arrays covering a surface (if not in a well). This way, the receiver arrays are sampling the wavefield at the surface of the Earth. In order to investigate the Earth's properties in depth, we make use of the time dependency of our measurements. The analysis of the arrival delay of the scattered waves observed between receivers at different locations unravels the geometrical structure and propagation velocity of the medium. Simultaneously, the analysis in amplitude of the same scattered waves determines the physical properties of the medium, including the aforementioned propagation velocity.

In passive seismics, only the receiver side is under our control, assuming the emitters to be naturally occurring events such as quakes and tremors inside the Earth, or ambient noise caused by Earth's natural sources or surface activities. Since we have no control over the sources, in applied passive seismics we aim to make the utmost use of the naturally occurring waves to extract the subsurface information and obtain an accurate result of the medium structure.

There are two main types of seismic waves exploited in applied passive seismics: surface waves and body waves. Surface waves are usually the most energetic arrivals in the ambient-noise recordings at or near the Earth's surface and therefore, the most sensitive waveforms to sources located at or close to the surface. Passive seismics often makes use of them in direct transmission measurements between receiver locations (Larose et al., 2006; Wapenaar et al., 2011a), although surface-wave scattering studies, due to medium contrasts along the acquisition array, can also be achieved. Their main application is the study of the region of the Earth closest to the surface (the near surface), and serves to estimate the mechanical parameters and their distribution at these shallower depth levels. On the other hand, body waves can propagate through the subsurface and usually are the most dominating events in passive recordings due to sources located inside the medium. This type of waves in passive seismics is in most of the cases studied as reflected waves from the subsurface (Schuster, 2001), although direct and refracted waves can also be employed (Snieder, 2004; Bharadwaj et al., 2011). The applications of passive seismics with body waves range from imaging the subsurface to deducing the mechanisms of the source that emitted the event of the passive recording. In the following, we address passive seismics exclusively as the applications that make use of body-wave reflections from passive recordings.

Passive seismics becomes an estimable alternative to active surveys in seismic studies at locations of complicated access, in exploration of remote regions or in environmentally sensitive areas. Also, its application may suppose a reduced cost of an exploration seismic survey, since it does not require active sources. Moreover, the use of passive seismics can complement active reflection surveys for a minimal additional expense. In the imaging process, the result of passive seismics for the near-to-middle depth range is usually not better in resolution than that obtained from an active survey. However, it can instead provide the low frequency information that is missing in active surveys, or even help in imaging

depth ranges that surface active sources cannot reach. Regarding its combination with active surveys, passive seismics may also become an innovative ally in analyzing the changes in the subsurface due to reservoir exploitation (oil, gas or water). However, the viability of most of these applications is directly dependent on the ambient-noise conditions at the study area. The principal limitation in the use of passive seismics is the reduced and unpredictable occurrence of telluric events or naturally occurring waves in the region of exploration. Using as analogy exposure photography and the medium luminescence, the amount of exposure to natural occurring waves defines the quality of the passive seismic imaging. Ideally, uncorrelated waves should illuminate the region of interest from all directions. Therefore, the lack of diffusivity of the propagating waves, either from a lack of sources in the area or a lack of heterogeneities which increase the scattering, show the first impeding point in the application.

Another limiting aspect regards the restricted distribution of passive sources in the medium and the uncertainty of their location. This aspect has direct implications on the way the space sampling is addressed at the acquisition surface. Incorrect orientation, limited array coverage and space sampling cause later difficulties and inaccuracies in the retrieval of the subsurface information.

Another important point concerns the resolution obtained from passive seismics, which is directly dependent on the frequency content of the propagating waves recorded. Most natural sources are generated by mechanisms yielding a considerably lower frequency band than typical active sources. Moreover, due to their sparse distribution, the generated waves travel over long distances before reaching the array, which decreases the frequency content even more due to attenuation. These considerations leave the use of passive seismics in most of the cases to achieve acceptable images of large structures, finding in lithospheric imaging one of its biggest applications.

1.2 Towards a passive seismic protocol

This thesis introduces novel processes that, combined together, may serve as a structured processing protocol for applied passive seismics. In figure 1.1 the proposed protocol is illustrated whose sections this thesis aims to describe. Green circles indicate input or required information, blue boxes represent processes and red squares stand for a family of methods related to seismic interferometry.

The protocol proposes different processes, depending on the presence of surface waves or body waves, and is also adapted to scenarios of optimal or limited subsurface illumination due to natural sources. Starting from the design of the passive acquisition geometry, these processes deal with the common passive seismic limitations and intend to improve the analysis and processing of the passive recordings towards an optimal imaging result. Some of the processes require inversion or deconvolution of the time recordings, which inherently correct for the

complex source signals of the natural sources and, therefore, obtain the best resolution from the data.

The design of these processes spin around the use of seismic interferometry (SI), the process of generating the Green's function between the receiver locations, using independent responses recorded at these same locations from different source positions. This process makes possible to retrieve active surveys by turning receivers into virtual sources (Wapenaar, 2004; Curtis et al., 2006). This virtual wave-response retrieval is theoretically founded on wavefield reciprocity theorems (Lord Rayleigh, 1894; Bojarski, 1983; Fokkema & van den Berg, 1993), accordingly adapted to the passive seismic configuration of interest. In this thesis, we adapt these theorems and processes for one-way wavefields, in order to handle the separation of different waveform conversions, and profit from the respective subsequent processing methods and imaging techniques already developed for active seismics. Additionally, the conversion of the recordings into power-flux normalized measurements (De Hoop, 1992) enables the use of source-receiver reciprocity, which is a powerful property for seismic interferometry.

The passive data consist of continuous recordings which are to be examined in detail. Therefore, in this protocol we structured the recordings into overlapping time sections (referred as quake or noise panels), whose length is designed according to the imaging depth of interest and the characteristics of the sources occurring within each time section.

This protocol is aimed for data where no control on the source location is available. Therefore, it implies a first effort in the planning of an optimal acquisition-array design. The way we place the receivers on the recording surface has implications for the space sampling, not only for vertical resolution but also for the directional one with respect to azimuth. The design aims to acquire any angle with the same resolution, while maintaining a constant receiver density at the surface. Besides the geometrical design, the inter-receiver spacing and aperture of the array are parameters chosen with regards to the desired vertical resolution and exploration depth of interest. Other implications on the array design have consequences that will be discussed later.

The next proposed process addresses the detection of passive body waves and the discrimination of surface waves in the recordings. Natural sources at the surface are the most occurring source locations in passive configurations and the surface waves originated from them are the most energetic events. The illumination diagnosis is a process that examines wave arrivals by time sections, using phase analysis at each receiver with respect to the array. At this level, illumination diagnosis is a qualitative analysis, serving as a discrimination tool to detect the dominance of surface wave or body wave events inside the respective noise panels. Needless to say, since this protocol is defined for one-way wavefields it is important to avoid surface-wave arrivals to be present during the latter step for body-waves of wavefield decomposition.

Noise panels discriminated for containing dominating surface waves are independently processed for surface wave retrieval by interferometry using either robust methods (Cross-correlation - CC) or high resolution inversion methods (Multidimensional deconvolution - MDD). The retrieved results between receivers over the acquisition surface serve for estimation of the valuable near-surface parameters at the acquisition array: Mass density (ρ), P-wave velocity (c_P) and S-wave velocity (c_S).

The noise panels selected for dominating body-wave content are proceeded for elastic wavefield separation and decomposition. Depending on the acquisition array design, this can be achieved by analytical or numerical approaches. This process requires the knowledge of the elastic near-surface parameters, which can be provided by *in situ* measurements, joint cartographic-petrological estimation or by surface-wave interferometry.

The amount of body-wave noise panels and their illumination will determine their suitability for retrieval. When the subsurface illumination angle content is sufficient, this can serve for reflection-survey retrieval by body-wave interferometry. The result is a virtual active survey serving for conventional imaging processes (common mid-point gathers, velocity semblance analysis and pre-stack depth migration, full-waveform inversion, joint-migration inversion or Marchenko imaging) in order to obtain the desired seismic image. The quality of the result will depend on the suitability of the acquisition array design to have all possible events in stationary-phase covered without knowing the source origin.

A different route for the interferometric approach is required when the natural-source distribution in the subsurface is limited, and only in case the natural-source signals present a transient behaviour. The aim in this case is the individual migration of passive-source recordings, in order to obtain information from the subsurface without depending on the retrieval of the reflection response as an intermediate result. We make use in this route of the illumination diagnosis in a quantitative sense: by analyzing the direction of the propagation and exploiting that information. The study of the illumination provided by the limited amount of natural sources, as well as the statistical analysis of this information, facilitates directional balancing during the imaging process (also applicable to methods not based on inversion in body-wave interferometry). This information serves for a passive seismic migration scheme under limited illumination conditions, based on imaging under directional constraints. The migration result consists of a partial image of the subsurface. The contribution from other passive sources can be added to the migrated result to increase the quality and coverage of the imaged reflectors and diminish spurious events due to correlation artefacts.

For a given amount of independent passive sources, the sections of the medium that are imaged by the respective passive sources define the so-called illumination-overlap region of the subsurface. This overlap in illumination serves as the basis for a stereo-tomographic estimation of the medium velocity for updating the initial

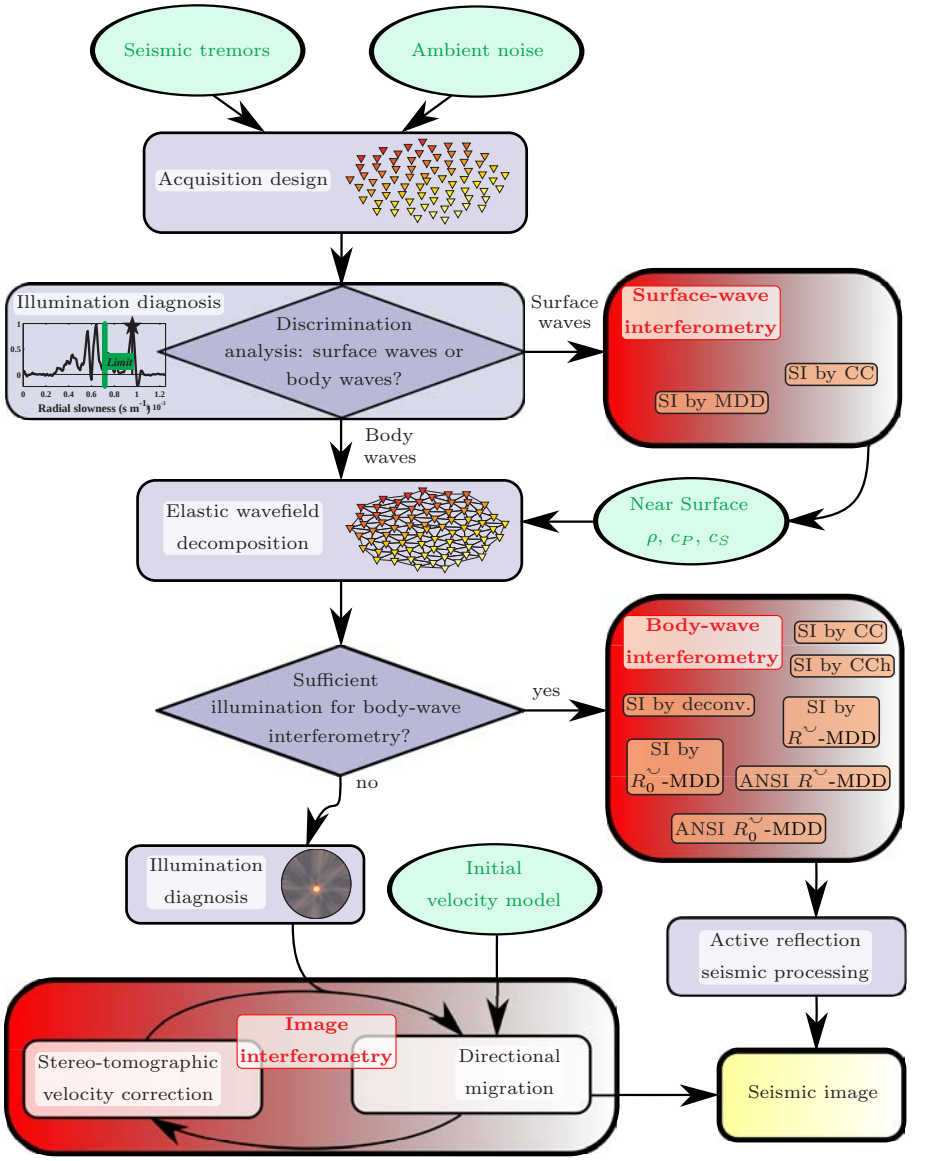

Figure 1.1: *Experimental seismic protocol for passive recordings of seismic events and ambient noise.*

velocity model employed during migration. This approach would be based on the velocity macro-model estimation by Billette & Lambaré (1998), adapted for passive seismics with the use of focusing operators (Thorbecke, 1997; Cox, 2003) with the additional aid from the information provided by midpoint interferometry (Ruigrok & Almagro Vidal, 2013).

In the sketch displayed, processes such as Notch- and band-pass filters are examples of the many essential processes, which we omitted for the sake of simplicity. Some body and surface wave interferometric methods require additional band-pass filtering and directional balancing, such as SI by CC. In case of dealing with surface and body waves, recorded simultaneously in a noise panel, velocity filters (also referred as $f-k$ filters) can be adapted to work in the space-frequency domain and therefore relax the discrimination analysis over noise panels.

This protocol is suitable for any given passive recording and is to be applied to P- and S-waves separately from the decomposition step onwards. The independent results complement one another in the structural imaging of the subsurface and help to discriminate the elastic properties of the subsurface.

Besides this one-way wavefield approach, new developments show that many of the mentioned steps can be interchanged to yield an alternative strategy towards the final seismic image. One of these new developments may include the use of wavefield separation and decomposition after retrieving the reflection response with body-wave interferometry, by using two-way wavefield SI methods instead, which would obviate the discrimination analysis and the decomposition of the passive recordings (Hartstra et al., 2017).

1.3 Thesis outline

This thesis describes some of the processing steps for the application of reflection seismic imaging to passive recordings. They consist of scientific methods and empirical engineering tools, with the intention to be the most user-independent possible. As the passive seismic protocol describes, the suitability of each of these processes depends on the subsurface illumination conditions.

Therefore this thesis is structured in two parts:

I.- The first part encompasses the passive seismic applications for the body-wave reflection-response retrieval, assuming a sufficient source distribution in the medium.

Chapter 2 describes the illumination diagnosis: first as a qualitative analysis for discrimination of surface-wave noise and, secondly, as a quantitative analysis for directional balancing in the reflection response retrieval with SI by CC.

This chapter is complemented by an annex regarding the acquisition-array design for an optimal illumination analysis.

In chapter 3, several inversion-based reflection-retrieval methods are presented. These methods originate from the reciprocity relations of the convolution and correlation type for one-way wavefields. Firstly, they are presented for transient signals (seismic tremors) and, secondly, for ambient noise recordings. The derivations from the reciprocity relations and the respective representations are described. In addition, a numerical comparison to the conventional passive seismic interferometry methods is shown.

As a continuation of the previous annex, this chapter is complemented with a one-way wavefield decomposition strategy in elastic media using particle-velocity recordings only for irregular array designs.

II.- The second part of this thesis presents the processes which deal with limited illumination scenarios, for events with transient signals. In this part it is assumed that the retrieval of the reflection response is unattainable and an alternative use of the passive body-wave recordings is proposed in order to attain seismic images: by using image interferometry.

The introduction to image interferometry is described in chapter 4. It is based on an adapted migration scheme for individual passive-source recordings. This chapter makes use of the illumination diagnosis described previously in chapter 2 but in a quantitative sense: it presents how to use this information as a directional constraint to create images directly from individual passive-source recordings. The successive adding of images from the individual passive-source recordings is called image interferometry and improves the final seismic image result.

Lastly in chapter 5, a reservoir monitoring method with passive seismics is presented. It is based on reciprocity relations between the base and monitor states, and the migration scheme introduced in the previous chapter. Despite the limited illumination provided by the passive sources, this chapter shows how individual tremors may serve for reservoir monitoring with the aid of active surveys. The new strategy makes the time-lapse analysis by means of reciprocity relations between the base active survey and the monitor passive recording.

I

Interferometry with complete illumination

2 Illumination diagnosis[§]

Seismic interferometry (SI) enables the retrieval of virtual sources at the location of receivers. In the case of passive SI, no active sources are used for the retrieval of the reflection response of the subsurface, but ambient-noise recordings only. The resulting retrieved response is determined by the illumination characteristics of the recorded ambient noise.

Characteristics like geometrical distribution and signature of the noise sources, together with the complexity of the medium and the length of the noise records, determine the quality of the retrieved virtual-shot events. To retrieve body-wave reflections, one needs to correlate body-wave noise. A source of such noise might be regional seismicity. In regions with noticeable human presence, the dominant noise sources are generally located at or close to the surface. In the latter case, the noise will be dominated by surface waves and consequently also the retrieved virtual common-source panels will contain dominant retrieved surface waves, drowning out possible retrieved reflections. In order to retrieve reflection events, suppression of the surface waves becomes the most important preprocessing goal.

Because of the reasons mentioned above, we propose a fast method to evaluate the illumination characteristics of ambient noise using the correlation results from ambient-noise records. The method is based on the analysis of the so-called source function of the retrieved virtual-shot panel, and evaluates the apparent slowness of arrivals in the correlation results that pass through the position of the virtual source and at zero time. The results of the diagnosis are used to suppress the retrieval of surface waves and therefore to improve the quality of the retrieved reflection response. We explain the approach using modelled data from transient and continuous noise sources and an example from a passive field dataset recorded at Annerveen, Northern Netherlands.

[§]This chapter has been published as a journal paper in *Geophysical Journal International*, **198** 3, 1582–1584 (Almagro Vidal et al., 2014). Note that minor changes have been introduced to make the text consistent with the other chapter of this thesis.

2

2.1 Introduction

Passive seismic reflection surveys intend to use ambient noise sources to retrieve reflection information of the subsurface. The application of seismic interferometry (SI) enables the retrieval of responses at the receiver locations as if there were a source at a chosen receiver location. Explanations and examples of how SI can be used to retrieve the subsurface response are given by Curtis et al. (2006), Wapenaar et al. (2008b), Schuster (2009) and Xu et al. (2012). This can be achieved with either correlation, convolution or deconvolution processes.

The aim of SI with passive sources, or Passive SI, is to retrieve the Green's function from ambient-noise records. Depending on the type of noise and/or preprocessing steps, surface waves could be retrieved (e.g. Shapiro & Campillo, 2004), diving body waves (e.g. Roux et al., 2005), but also body-wave reflections (e.g. Draganov et al., 2009; Poli et al., 2012a).

The quality of the retrieved response depends on the time/frequency characteristics of the recorded noise, the distribution of the noise sources, the complexity of the medium and the recording time length. Unfortunately, the preponderance in time or space of some sources with respect to others in the records limit the retrieval of the complete Green's function. When using SI by crosscorrelation, sources located near the surface would contribute predominantly to the retrieval of surface waves, whereas sources located relatively deeper would contribute mostly to the retrieval of body-wave reflections. Noise recordings in regions with relatively high local and regional seismicity would facilitate the retrieval of body-wave reflections, although in general the presence of antropogenic noise would mean predominance of sources at the surface and therefore ambient noise dominated by surface waves. When this is the case, the results retrieved by SI by crosscorrelation exhibit surface waves that drown out the possible retrieved reflections, as the latter are much weaker.

In passive seismic surveys at lithospheric scale, body waves can be identified using frequency-wavenumber spectral analysis (Nishida, 2013), and in cases of post-critical reflections, their estimated amplitude has been comparable to the amplitudes of surface waves (Zhan et al., 2010). At exploration scale, Nakata et al. (2011) showed that by equalizing or whitening the frequency spectrum during the retrieval process (that is applying crosscoherence instead of crosscorrelation), one could retrieve reflections even when the noise is dominated by surface waves. The drawback of using all the noise is that surface waves are still retrieved, which would require their removal after the retrieval. Forghani & Snieder (2010) show the balance between retrieved surface and body waves using SI by crosscorrelation, which opens the possibility of adaptive surface-wave removal by reconstruction of waveforms with isolated surface waves (van Wijk et al., 2010).

An alternative approach is to suppress the retrieval of surface waves by not using the parts of the noise dominated by surface-wave noise (Draganov et al.,

2010). The selection of noise parts dominated by body waves can be carried out using beam-forming (Draganov et al., 2013) or additionally splitting the record in frequency bands for which the body-wave noise is dominant (Ruigrok et al., 2011). However, even when reflections are retrieved, they might not be obtained correctly due to preferential illumination of the recording array with body-wave noise from certain directions. In such a case, one needs to compensate for over-illumination from dominant noise-source locations.

We propose here an efficient technique to estimate the illumination from the ambient noise. The structure of the chapter starts showing how the method is based on the properties of the virtual-source function, that is on the properties of the retrieved events that pass through the position of the virtual-shot trace at time zero. Based on the diagnosis of the illumination from the noise, we carry out the discrimination of noise sections seeking body-wave characteristics. The diagnosis also provides additional support for compensating over-illumination. In this chapter, we demonstrate its application on synthetic dataset with transient sources and simultaneous noise sources. Finally, we applied this method to ambient-noise recordings from the North of the Netherlands, and compare the retrieved response from the correlated and summed noise before and after its application.

2.2 Illumination diagnosis with transient sources

In SI by cross-correlation with transient sources, the recordings at two receivers locations $\mathbf{x}_{\mathcal{A}}$ and $\mathbf{x}_0$ make possible to retrieve the Green's function $\hat{G}_3(\mathbf{x}_{\mathcal{A}}, \mathbf{x}_0, \omega)$ between the receiver stations as if a source were located at receiver $\mathbf{x}_{\mathcal{A}}$ (Wapenaar & Fokkema, 2006). In order to achieve this, sources must act separately in time, share an equal power spectrum $\|\hat{S}(\omega)\|^2$, and be located at positions $\mathbf{x}_{\mathcal{B}}$ along an enclosing source boundary $\partial\mathbb{D}$. In the circumstance of the receivers being located at a horizontal free-surface in acoustic media, the Green's function retrieval can be attained using SI by crosscorrelation:

$$\Re\left\{\hat{R}_3^{\smile}(\mathbf{x}_{\mathcal{A}}, \mathbf{x}_0, \omega)\right\}\|\hat{S}(\omega)\|^2 \approx \oint_{\mathbf{x}_{\mathcal{B}}\in\partial\mathbb{D}} \rho(\mathbf{x}_{\mathcal{B}})c_P(\mathbf{x}_{\mathcal{B}})\left(\hat{v}_3^{obs}(\mathbf{x}_{\mathcal{A}}, \mathbf{x}_{\mathcal{B}}, \omega)\{\hat{v}_3^{obs}(\mathbf{x}_0, \mathbf{x}_{\mathcal{B}}, \omega)\}^*\right) d^2\mathbf{x}_{\mathcal{B}}, \quad (2.1)$$

where $\Re$ stands for real part, ρ and c_P are the constant mass density and velocity of the medium at the source locations in $\partial\mathbb{D}$, respectively; $\{\}^*$ denotes complex conjugation convolution and $\hat{v}_3^{obs}(\mathbf{x}_{\mathcal{A}}, \mathbf{x}_{\mathcal{B}}, \omega)$ is the observed wavefield at $\mathbf{x}_{\mathcal{A}}$ due to a transient source at $\mathbf{x}_{\mathcal{B}}$. In this configuration the observed wavefield quantity is vertical particle velocity. The product inside the integration of the right hand side represents a cross-correlation product in the time domain. The retrieved

response $\hat{R}_3^{\cup}(\mathbf{x}_{\mathcal{A}}, \mathbf{x}_0, \omega)$ is the impulsive reflection response of the medium; It is represented as a vertical particle-velocity response due to a vertical-dipole point-source and is convolved with the power spectrum of the sources ($\|\hat{S}(\omega)\|^2$) used during the retrieval.

Equation 2.1 states that to retrieve the desired Green's function, one would need to integrate the correlation results from all sources of the boundary. The correlated common-source panel $\hat{C}_{\mathbf{x}_{\mathcal{B}}}$ (or correlation function) is the correlation result from each individual boundary source $\mathbf{x}_{\mathcal{B}}$ that makes its contribution to the interferometric integration in equation 2.1. For a single transient source, it is represented at a fixed receiver position $\mathbf{x}_0$ and a variable receiver position $\mathbf{x}_{\mathcal{A}}$ as follows:

$$\hat{C}_{\mathbf{x}_{\mathcal{B}}}(\mathbf{x}_{\mathcal{A}}, \mathbf{x}_0, \omega) = \rho(\mathbf{x}_{\mathcal{B}}) c_P(\mathbf{x}_{\mathcal{B}}) \left(\hat{v}_3^{obs}(\mathbf{x}_{\mathcal{A}}, \mathbf{x}_{\mathcal{B}}, \omega) \left\{ \hat{v}_3^{obs}(\mathbf{x}_0, \mathbf{x}_{\mathcal{B}}, \omega) \right\}^* \right), \tag{2.2}$$

as if a source were located in $\mathbf{x}_0$ that emits energy within a limited range of angles to multiple receivers $\mathbf{x}_{\mathcal{A}}$.

In the time domain, the events in this panel that pass through $t = 0\ s$ and the position of the virtual source are informative of the illumination characteristics the specific source $\mathbf{x}_{\mathcal{B}}$ at the receiver locations. We call the collection of these events the virtual-source function (van der Neut, 2013).

There are several ways to study the illumination characteristics using the virtual-source function. One approach is to make use of a slant-stack transform.In our case, we evaluate this transform at correlation time $\tau = 0\ s$. Therefore, we can study the illumination contribution from $\mathbf{x}_{\mathcal{B}}$ to the virtual source at $\mathbf{x}_0$ using the simplified slant-stack transformation onto the time representation of the correlation function $C_{\mathbf{x}_{\mathcal{B}}}(\mathbf{x}_{\mathcal{A}}, \mathbf{x}_0, t)$:

$$\widetilde{C}_{\mathbf{x}_{\mathcal{B}}}(\mathbf{x}_0, \mathbf{p}) \equiv \int C_{\mathbf{x}_{\mathcal{B}}}\big(\mathbf{x}_{\mathcal{A}}, \mathbf{x}_0, \mathbf{p} \cdot (\mathbf{x}_{\mathcal{A}} - \mathbf{x}_0)\big) d^2\mathbf{x}_{\mathcal{A}}, \tag{2.3}$$

where $\widetilde{C}_{\mathbf{x}_{\mathcal{B}}}(\mathbf{x}_0, \mathbf{p})$ is the ray-parameter function at the virtual-source position $\mathbf{x}_0$ of the virtual-source function due to the transient source $\mathbf{x}_{\mathcal{B}}$. The illumination diagnosis could in principle also be implemented in the frequency-wavenumber domain, making use of slant-stacks of the virtual-source function over different velocity values. This procedure, though, would require that first the virtual-source function is isolated in the time domain by means of muting. The design of the muting window around the virtual-source function might become highly user-dependent. The reason to study the virtual-source function in the $\tau - p$ domain is that the analysis takes place right at its location, around $\tau = 0\ s$. In this way, we avoid having to isolate the virtual-source function with a time-window or to include reflections in the analysis. In addition, it has the advantage

of being faster since it does not require any additional Fourier transform. The virtual source function is analysed at every correlated common-source panel. For each slant-stack result at $t = 0\ s$, we search for the ray-parameter $\mathbf{p}^{\mathbf{x}_0}_{\mathbf{x}_\mathcal{B}}$ at the virtual-source location $\mathbf{x}_0$, for which the source function is maximum:

$$\widetilde{C}_{\mathbf{x}_\mathcal{B}}(\mathbf{x}_0, \mathbf{p}^{\mathbf{x}_0}_{\mathbf{x}_\mathcal{B}}) = \left\| \widetilde{C}_{\mathbf{x}_\mathcal{B}}(\mathbf{x}_0, \mathbf{p}) \right\|_{max}. \tag{2.4}$$

The suitability of the correlated common-source panel for reflection retrieval is now given by means of a comparison of the dominant ray-parameter in its absolute value $\|\mathbf{p}^{\mathbf{x}_0}_{\mathbf{x}_\mathcal{B}}\|$ with a predefined threshold value p_{limit} between the characteristic slowness for body waves and for surface waves. Although this discrimination test is based on the magnitude of $\mathbf{p}^{\mathbf{x}_0}_{\mathbf{x}_\mathcal{B}}$, the directional information can be employed in directional balancing. This discrimination test can be described as follows:

$$\hat{C}_{\mathbf{x}_\mathcal{B}}(\mathbf{x}_\mathcal{A}, \mathbf{x}_0, \omega) = \begin{cases} 0 & \text{if } \mathrm{BSW}_{\mathbf{x}_\mathcal{B}} \leqslant \xi \\ \rho(\mathbf{x}_\mathcal{B}) c_P(\mathbf{x}_\mathcal{B}) & \\ \left(\hat{v}_3^{obs}(\mathbf{x}_0, \mathbf{x}_\mathcal{B}, \omega) \left\{ \hat{v}_3^{obs}(\mathbf{x}_\mathcal{A}, \mathbf{x}_\mathcal{B}, \omega) \right\}^* \right) & \text{if } \mathrm{BSW}_{\mathbf{x}_\mathcal{B}} > \xi, \end{cases} \tag{2.5}$$

where ξ is an "acceptance thershold" and $\mathrm{BSW}_{\mathbf{x}_\mathcal{B}}$ is the body-wave to surface-wave ratio of passive source $\mathbf{x}_\mathcal{B}$:

$$\mathrm{BSW}_{\mathbf{x}_\mathcal{B}} = \frac{max\left(\left\| \widetilde{C}_{\mathbf{x}_\mathcal{B}}(\mathbf{x}_0, \mathbf{p}) \right\| \right)_{\|\mathbf{p}\| \leqslant p_{limit}}}{max\left(\left\| \widetilde{C}_{\mathbf{x}_\mathcal{B}}(\mathbf{x}_0, \mathbf{p}) \right\| \right)_{\|\mathbf{p}\| > p_{limit}}}, \tag{2.6}$$

Application of the discrimination test (equation 2.5), for a certain virtual-source location $\mathbf{x}_0$, takes care that a source at $\mathbf{x}_\mathcal{B}$ with ray-parameter $\|\mathbf{p}^{\mathbf{x}_0}_{\mathbf{x}_\mathcal{B}}\|$ larger than the predefined threshold value p_{limit} is not contributing to the final reflection-response retrieval. The value given to p_{limit} will depend on the elastic properties of the medium where the receiver array is located. One must first estimate expected values for body- and surface-wave velocities at the receiver location and define the threshold value with respect to these. However, it may happen that certain sources contribute in the retrieval of body and surface waves in a similar proportion. For such cases, the comparison ought to consider also the security ratio ξ of the maxima of the virtual-source function $\widetilde{C}_{\mathbf{x}_\mathcal{B}}$ inside and outside the limit interval p_{limit}. A large ξ ratio ensures only body wave contribution by the correlation panel. This allows the test to obtain a conservative character for avoiding surface-wave retrieval. For the results in this chapter, the security ratio employed was $\xi = 2$. Choosing a smaller ratio $\xi < 2$ allows including noise panels containing

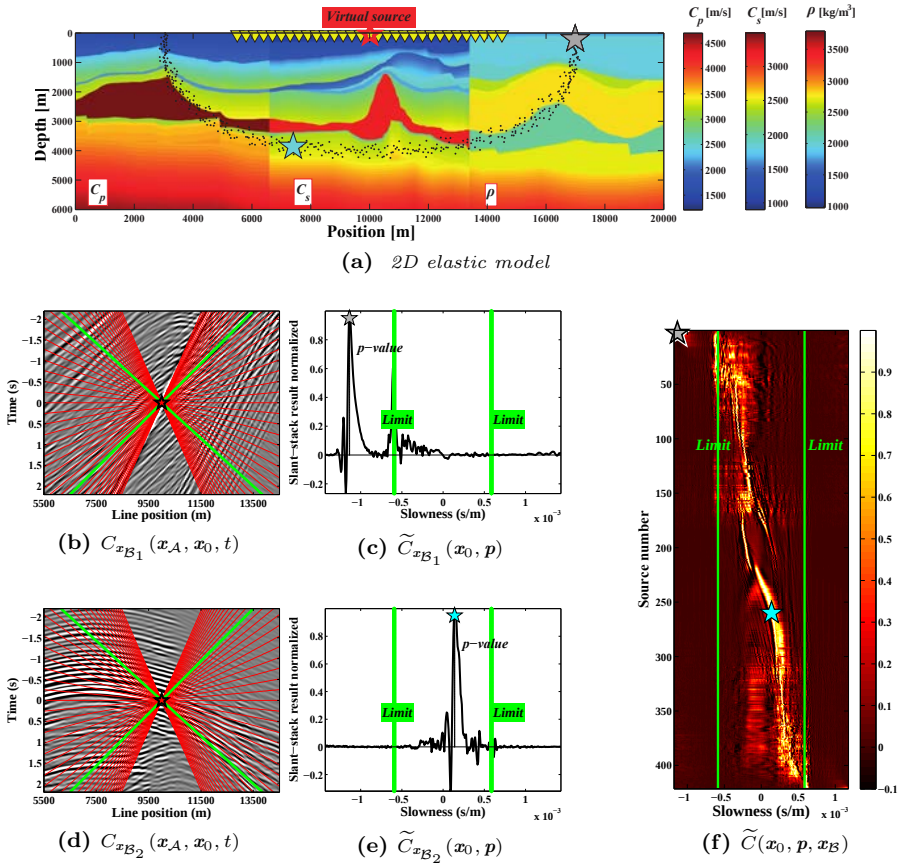

(a) *2D elastic model*

(b) $C_{x_{\mathcal{B}_1}}(x_{\mathcal{A}}, x_0, t)$ **(c)** $\widetilde{C}_{x_{\mathcal{B}_1}}(x_0, p)$

(d) $C_{x_{\mathcal{B}_2}}(x_{\mathcal{A}}, x_0, t)$ **(e)** $\widetilde{C}_{x_{\mathcal{B}_2}}(x_0, p)$ **(f)** $\widetilde{C}(x_0, p, x_{\mathcal{B}})$

Figure 2.1: *Slant-stack illumination diagnosis.* ***(a)*** *Elastic subsurface model.* 181 *receivers (yellow triangles) are placed at* 50 *m depth with* 50 *m spacing.* 421 *sources (black dots) represent the ambient-source boundary region. Two examples are shown for a shallow (gray star) and a deep source (cyan star).* ***(b)*** *Correlated common-source panel* $C_{x_{\mathcal{B}}}$ *for a virtual source at* $x_0 = 10000$ *m, resulting from the gray-star source in (a). Red lines indicate slownesses. Green lines are predefined limits between body-wave and surface-wave slownesses in the virtual-source function.* ***(c)*** *Slowness representation* $\widetilde{C}_{x_{\mathcal{B}}}$ *of the virtual-source function from (b). Green lines indicate the fore-mentioned limits between body-wave and surface-wave slownesses.* ***(d)*** *as in (b), but for the cyan-star source in (a).* ***(e)*** *as in (c), but from (d).* ***(f)*** *Illumination diagnosis, consisting of the results for the correlated common-source panels from sources in (a) (black dots), with the panel from (b) (gray star) discarded, and the panel from (d) (cyan star) included.*

surface waves. The use of such small ratio results in surface-wave retrieval in the final result.

Figure 2.1 shows an example of the application of the slowness-evaluation and discrimination procedure from equations 2.3 and 2.5: Figure 2.1b shows the correlated common-source panel, with the virtual-source function in the middle, for a virtual source located at $x_0 = 10000\ m$; the common-source panel before correlation is dominated by surface waves from a source close to the surface (see gray star in Figure 2.1a). Figure 2.1c gives the representation $\widetilde{C}_{\mathbf{x}_\mathcal{B}}(\mathbf{x}_0, \mathbf{p})$, result of the integration over different slownesses shown with red lines in Figure 2.1b. The dominant ray-parameter $\mathbf{p}^{\mathbf{x}_0}_{\mathbf{x}_\mathcal{B}}$ (p-value) is outstanding, marked with a gray star. The green lines in both 2.1b and 2.1c represent the predefined slowness limits, which serve as a threshold slowness in the correlated common-source panel. Figure 2.1d displays another correlated common-source panel for the same virtual-source location, but resulting from a relatively deep source (see cyan star in Figure 2.1a). The respective slowness-spectrum of the virtual source-function is shown in Figure 2.1e, in which the maximum ray-parameter is marked with a cyan star. The succession of such slowness distributions from correlated common-source panels for all boundary-source positions $\mathbf{x}_\mathcal{B}$ (the black dots in Figure 2.1a) produces the Illumination diagnosis in Figure 2.1f. The contributions to the reflection-response retrieval from each of the sources can be studied using the dominant ray-parameters $\mathbf{p}^{\mathbf{x}_0}_{\mathbf{x}_\mathcal{B}}$ which, after the discrimination test, are between the slowness threshold values.

As a result from the application of the discrimination test in equation 2.5, sources contributing to surface-wave retrieval are disregarded and only sources contributing to body-wave retrieval are kept. Finally, the desired retrieved response after illumination diagnosis and discrimination is obtained using

$$\Re\left\{\hat{R}_3^{\smile}(\mathbf{x}_\mathcal{A}, \mathbf{x}_0, \omega)\right\} \|\hat{S}(\omega)\|^2 \approx \sum_{\mathbf{x}_\mathcal{B}} \hat{C}_{\mathbf{x}_\mathcal{B}}(\mathbf{x}_\mathcal{A}, \mathbf{x}_0, \omega). \tag{2.7}$$

For further applications of the virtual-source function and its relation to the point-spread function, the readers are referred to van der Neut (2013).

2.2.1 Retrieval of reflections from passive transient sources

In the previous section we introduced the process of the illumination diagnosis. Here we are going to apply it on a synthetic model. Figure 2.2 presents the analysis and results of the illumination diagnosis and discrimination from transient sources used in a synthetic 2D elastic model, based on the geology of the North of the Netherlands (Duin et al., 2006). Figure 2.2a shows the P-velocity model employed (S-velocity and density models use the same subsurface distribution with non-constant values, see figure2.1a), with the location of the ambient

sources marked with black points and cyan stars, the receiver array with yellow triangles, and the location of the virtual source at $x_0 = 6000\ m$ indicated by the open red star. The sources enclose the receiver array from below, providing full illumination from the subsurface to the receiver array. The field employed in the crosscorrelation is the pressure field, and all sources employed are monopoles since the distance between the sources and the acquisition array assures that the recordings are in the far-field regime. If this were not the case, also recordings from dipole sources would have been required (Wapenaar & Fokkema, 2006). The result of integrating the contribution of each correlated common-source panel is displayed in figure 2.2c. The retrieved response is so dominated by surface waves, that reflection arrivals are hardly visible. Reflections, though, must be retrieved since the sources enclose the receivers. Figure 2.2d shows the illumination diagnosis for all correlated common-source panels. The normalization of the slant-stack results scales the amplitudes but preserves the sign. The minimum and maximum slowness values are dependent on the expected surface-wave velocity. In this modelling the surface-wave velocity is 860 $m\ s^{-1}$ (1.16 $10^{-3}\ s\ m^{-1}$). We chose values of $\pm$ 1.2 $10^{-3}\ s\ m^{-1}$ in order to ensure all expected surface waves were scanned. The rows in the diagram represent the ray-parameter distribution of the source function $\widetilde{C}_{\mathbf{x}_\mathcal{B}}(\mathbf{x}_\mathcal{A}, \mathbf{p})$ from one of the boundary sources. The black and cyan stars in the illumination diagnosis indicate dominant ray-parameter $\mathbf{p}^{\mathbf{x}_0}_{\mathbf{x}_\mathcal{B}}$ for surface-wave slowness and body-wave slowness, respectively. Panels with maximum slowness below the threshold slowness value but not fulfilling the control ratio ξ condition are also represented with black stars. Correlated common-source panels with dominant ray-parameter in cyan are kept for the following step of integration in the SI reflection-response retrieval procedure. The transient sources that lead to kept panels are indicated with the cyan stars in Figure 2.2a. The correlated common-source panels with dominant ray-parameter in black are discarded from further usage in the integration for reflection retrieval; the position of the sources giving rise to them are indicated by the black dots in figure 2.2a. Correlated panels with dispersed ray-parameter distributions around the ray-parameter limit are discarded, for the ratio of the maxima of the source function $\widetilde{C}_{\mathbf{x}_\mathcal{B}}$ inside and outside the limit interval is relatively small. This is noticeable in Figure 2.2d, for source numbers between 20 and 150. Figure 2.2e shows the result of applying equation 2.7 (the summation step in the SI retrieval process) only to the kept (the cyan) correlated common-source panels from Figure 2.2d.

The retrieved virtual common-source panel now shows clearly all the expected reflection arrivals. This can be seen by comparing it with the directly modelled panel in figure 2.2b for an active source at the position of the virtual source. The comparison also shows that our slowness evaluation and discrimination procedure has suppressed the retrieval of surface waves. Furthermore, we can see that also the direct P-wave arrivals are not retrieved. This is due to the fact that in the discrimination procedure, we chose the discrimination limit (the green line in figure 2.2d) slightly smaller than the slowness of the direct wave: $p_{limit} =$

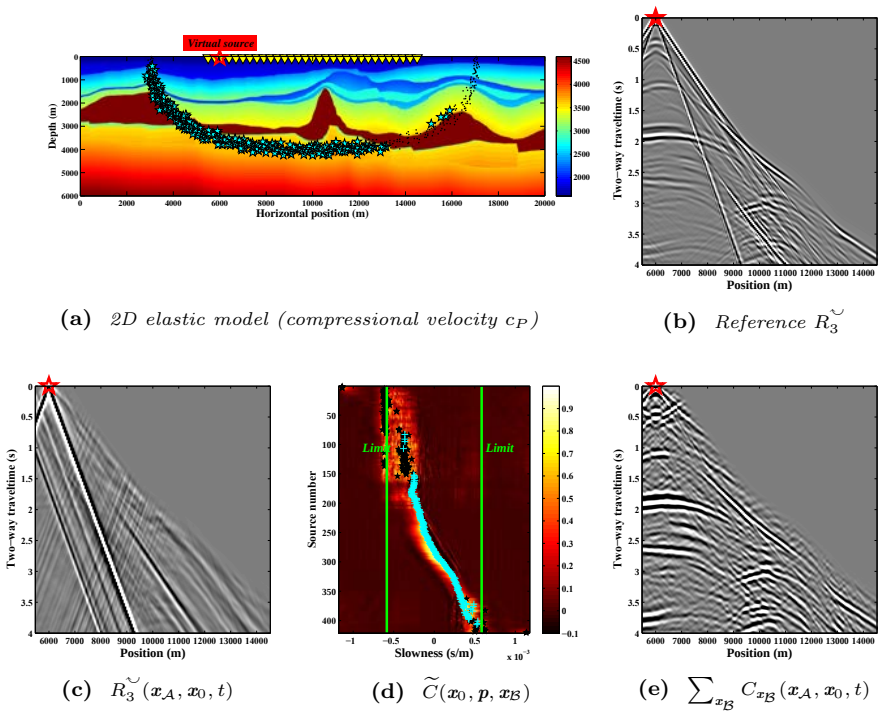

(a) *2D elastic model (compressional velocity c_P)* **(b)** *Reference* $R_3^{\smile}$

(c) $R_3^{\smile}(\boldsymbol{x}_\mathcal{A}, \boldsymbol{x}_0, t)$ **(d)** $\widetilde{C}(\boldsymbol{x}_0, \boldsymbol{p}, \boldsymbol{x}_\mathcal{B})$ **(e)** $\sum_{\boldsymbol{x}_\mathcal{B}} C_{\boldsymbol{x}_\mathcal{B}}(\boldsymbol{x}_\mathcal{A}, \boldsymbol{x}_0, t)$

Figure 2.2: *Illumination diagnosis for transient sources.* ***(a)*** *Same P-wave velocity model from Figure 2.1a, but now with the 421 subsurface sources represented differently whether they are dominated by surface wave arrivals (black dots) or by body waves (cyan stars).* ***(b)*** *Directly modelled reflection response for an active source at $x_0 = 6000\ m$ (the red open star in (a)).* ***(c)*** *Retrieved virtual common-source panel at the same location, obtained using all correlated common-source panels.* ***(d)*** *Illumination diagnosis with $\boldsymbol{p}_{\boldsymbol{x}_\mathcal{B}}^{\boldsymbol{x}_0}$ values of all correlated source panels.* ***(e)*** *As in (c), but after application of slowness evaluation and discrimination for suppression of surface-wave retrieval.*

$6\ 10^{-4}\ s\ m^{-1}$, whereas the direct-wave velocity at the virtual-source location is $6.25\ 10^{-4}\ s\ m^{-1}$.

Looking at figure 2.2a, it can also be seen that due to the complexity of the subsurface model, changing the position of the virtual source would mean changing the positions of the sources that contribute to the retrieval of reflections. For the virtual source in Figure 2.2a, the majority of the sources to the right of the steep subsurface structure do not contribute to the retrieval of reflections, even if they are relatively deep sources.

2

2.3 Illumination diagnosis for ambient-noise recordings

For SI with uncorrelated noise sources, Wapenaar & Fokkema (2006) derived a relation to retrieve the Green's function $\hat{R}_3^{\smile}(\mathbf{x}_\mathcal{A}, \mathbf{x}_0, \omega)$ at the free-surface:

$$\Re\left\{\hat{R}_3^{\smile}(\mathbf{x}_\mathcal{A}, \mathbf{x}_0, \omega)\right\} \|\hat{S}(\omega)\|^2 \approx \left\langle \hat{v}_3^{obs}(\mathbf{x}_\mathcal{A}, \omega)\left\{\hat{v}_3^{obs}(\mathbf{x}_0, \omega)\right\}^*\right\rangle, \tag{2.8}$$

where the noise sources are assumed to have the same power spectrum $\|\hat{S}(\omega)\|^2$, $\hat{v}_3^{obs}(\mathbf{x}_\mathcal{A}, \omega)$ stands for the total recorded noise at $\mathbf{x}_\mathcal{A}$ due to all the noise sources and $\langle\cdot\rangle$ denotes ensemble average. For field applications, the ensemble average is exchanged for averaging over long recording times. As the long time recordings are stored in time windows with certain length, the time averaging is exchanged for summation over all i time windows:

$$\Re\left\{\hat{R}_3^{\smile}(\mathbf{x}_\mathcal{A}, \mathbf{x}_0, \omega)\right\} \|\hat{S}(\omega)\|^2 \approx \sum_i \left(\hat{v}_3^{obs}(\mathbf{x}_\mathcal{A}, \omega)\left\{\hat{v}_3^{obs}(\mathbf{x}_0, \omega)\right\}^*\right)_i. \tag{2.9}$$

To apply the slowness evaluation and discrimination procedure to such recordings, we define the correlated noise panel $\hat{C}_i$ as:

$$\hat{C}_i(\mathbf{x}_\mathcal{A}, \mathbf{x}_0, \omega) = \left(\hat{v}_3^{obs}(\mathbf{x}_\mathcal{A}, \omega)\left\{\hat{v}_3^{obs}(\mathbf{x}_0, \omega)\right\}^*\right)_i. \tag{2.10}$$

From here on, we can apply the illumination-diagnosis procedure using equations 2.3 to 2.7 in the same way as for the transient noise sources.

In continuous ambient-noise recordings the characteristics of the virtual-source function will depend on the noise sources acting during the recording time. Evaluation of the virtual-source function for relatively short windows would diagnose the illumination characteristics of the noise sources present during that time window.

The ensemble of illumination diagnosis results over consecutive time windows produces the illumination record. This display shows the succession of the dominant illumination in time along the noise record according to the window length applied.

The choice of the time-window length before the correlation fundamentally depends on two factors: the desired deepest reflection to be retrieved and the nature of the recorded noise. The time window should be at least as long as the expected two-way traveltime down to the deepest target reflector. With such a window, the correlation process would remove the travel time of the direct arrival from the traveltime of its multiple and would retrieve the desired reflection from

the target reflector. Increasing the length of the time window would result also in the correlation of later arrivals contributing to the retrieval of the same reflection with higher signal-to-noise ratio. Concerning the nature of the noise sources, in the case of our modelled data, we are not assuming transient noise signals, so long noise panels will improve the correlation quality, enable a proper reflection retrieval from the correlated panel, and avoid the retrieval of spurious or non-physical events. Therefore, for the modelled data, both factors demand longer time windows.

With field measurements, the sources of body-wave noise would be of limited time duration and would be present at discrete time periods during the passive survey. Using longer time windows would increase the risk of more than one source of body-wave noise being captured by the window, the illumination diagnosis would produce the information only for the strongest of these sources and this would practically mean loss of useful information. Furthermore, the longer the time window, the higher the risk of capturing more surface-wave noise. The latter might drown the present body-wave noise. So, for the case of field data, the two factors state opposing demands and thus a compromise should be sought.

The diagnosed illumination characteristics are then used to decide if a correlated noise panel $\hat{C}_i(\mathbf{x}_{\mathcal{A}}, \mathbf{x}_0, \omega)$ would contribute to the retrieval of mainly body waves or of mainly surface waves, and therefore be kept or discarded, respectively, for the consecutive summation.

Nevertheless, the application of the procedure as defined for the transient sources might not be optimal for the situation with ambient-noise recordings. The results shown in the previous section assumed a regular spatial distribution of the sources in the subsurface. In practice, body-wave noise might illuminate the receiver array more frequently from some directions than from others. This would affect the retrieval process adversely by distorting the retrieved reflection response. The illumination diagnosis provides an easy remedy for such situations. Upon sorting the noise panels by their dominant ray-parameter, the subsurface illumination distribution is observed, and enables statistical estimations for illumination balancing. The frequency of occurrence of illumination from a certain direction can be used to define weights W_i for the summation of the correlated noise panels. If the panels are individually amplitude-normalized, the weights W_i are set to be inversely proportional to the occurrence frequency of the ray-parameter value $\mathbf{p}_i^{\mathbf{x}_0}$. Illumination balancing with respect to ray-parameter can also be found in Ruigrok et al. (2010). Hence, the application of the illumination diagnosis and discrimination test to the ambient-noise recordings can be defined as follows:

2

$$\hat{C}_i(\mathbf{x}_{\mathcal{A}}, \mathbf{x}_0, \omega) = \begin{cases} 0 & \text{if BSW}_i \leqslant \xi \\ W_i(\mathbf{p}_i^{\mathbf{x}_0}) \left(\hat{v}_3^{obs}(\mathbf{x}_A, \omega) \{ \hat{v}_3^{obs}(\mathbf{x}_0, \omega) \}^* \right)_i & \text{if BSW}_i > \xi, \end{cases} \tag{2.11}$$

and the respective body-wave to surface-wave ratio of the noise interval i:

$$\text{BSW}_i = \frac{max\left(\left\| \widetilde{C}_i(\mathbf{x}_0, \mathbf{p}) \right\| \right)_{\|\mathbf{p}\| \leqslant p_{limit}}}{max\left(\left\| \widetilde{C}_i(\mathbf{x}_0, \mathbf{p}) \right\| \right)_{\|\mathbf{p}\| > p_{limit}}}. \tag{2.12}$$

To minimise the possibility of not selecting body-wave noise, we allow certain time overlap between consecutive windows during our illumination diagnosis. Furthermore, this enables a smoother analysis in time of the illumination record. The choice for an optimal time-overlap between noise panels must compensate for a precise detection of surface-wave presence, without extending the computational time costs of scanning larger amount of noise panels.

2.3.1 Retrieval of reflections from synthetic ambient noise

We apply the above-described method to a synthetic continuous noise recording of 12 minutes, generated using the model and source distribution from Figure 2.2a. During the noise modelling, each ambient-noise source is activated randomly in time for 10 s. For the application of the illumination diagnosis, we divide the continuous recordings into 10 s long noise panels with 5 s overlap. Figures 2.3a, 2.3d and 2.3f show the respective results for retrieval of reflections in the form of virtual common-source panels for a virtual source at $x_0 = 6000\ m$ after application of the illumination diagnosis.

Figure 2.3a shows the retrieved virtual common-source panel after application of SI by crosscoherence as in Nakata et al. (2011), using all noise panels. Reflections show up with a whitened frequency spectrum, but under the presence of surface waves; see for comparison the directly modelled reflection response in figure 2.3c. Figure 2.3b shows the illumination record of the synthetic noise. By resorting the noise panels in Figure 2.3b according to their maximum in the slowness spectrum, we obtain the illumination diagnosis displayed in figure 2.3e. Under it, we show the histogram of $\mathbf{p}_i^{\mathbf{x}_0}$, upon which the weights (W_i) in equation 2.11 are estimated. The retrieved common-source panels using SI by crosscorrelation before and after slowness evaluation, discrimination and weighting (expression 2.11) are shown in figures 2.3d and 2.3f, respectively. In contrast to the crosscoherence result from Figure 2.3a, in Figure 2.3f the illumination diagnosis has not only succeeded to retrieve the reflections, but has successfully suppressed the surface and direct waves.

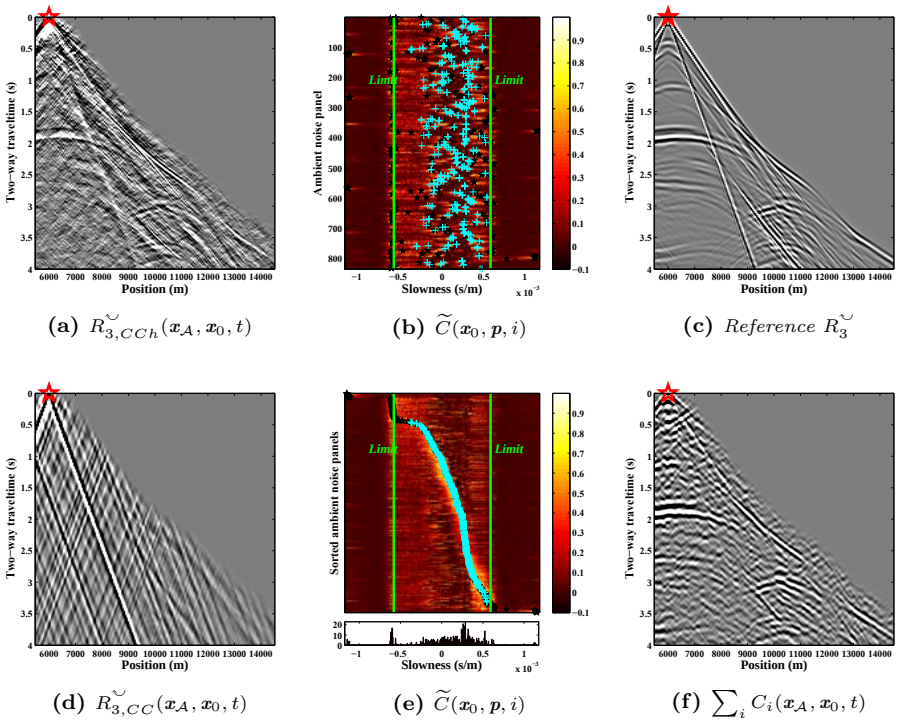

(a) $R^{\smile}_{3,CCh}(\boldsymbol{x}_{\mathcal{A}}, \boldsymbol{x}_0, t)$ **(b)** $\widetilde{C}(\boldsymbol{x}_0, \boldsymbol{p}, i)$ **(c)** *Reference* $R^{\smile}_3$

(d) $R^{\smile}_{3,CC}(\boldsymbol{x}_{\mathcal{A}}, \boldsymbol{x}_0, t)$ **(e)** $\widetilde{C}(\boldsymbol{x}_0, \boldsymbol{p}, i)$ **(f)** $\sum_i C_i(\boldsymbol{x}_{\mathcal{A}}, \boldsymbol{x}_0, t)$

Figure 2.3: *Illumination diagnosis for random noise sources in the model shown in Figure 2.2a.* ***(a)*** *Retrieved virtual common-source panel for a virtual-source position* x_0 = 6000 *m obtained using SI by crosscoherence (CCh).* ***(b)*** *Illumination record, constructed using 834 noise panels of* 10 *s length, with* 5 *s of record overlap.* ***(c)*** *Directly modelled common-source panel for an actual source at the virtual-source position.* ***(d)*** *Retrieved common-source panel with SI by cross-correlation (CC), obtained using all correlated panels.* ***(e)*** *Illumination diagnosis, with body-wave dominated panels highlightened in cyan at their characteristic ray-parameter* $\boldsymbol{p}_i^{\boldsymbol{x}_0}$*; Diagram beneath shows the histogram of* $\boldsymbol{p}_i^{\boldsymbol{x}_0}$*.* ***(f)*** *Same result as in (d) after discrimination and discard of panels with dominant surface waves, e.g. after summation only over the correlated panels with cyan stars, weighted according to the histogram in (e).*

2.3.2 Retrieval of reflections from field data

In the previous sections, we showed how the illumination diagnosis should be applied to transient or ambient-noise sources considering a line of receivers above a 2D medium. Field applications for retrieval of reflections from ambient noise using a line of receivers can lead to misleading results due to the lack of the 3D

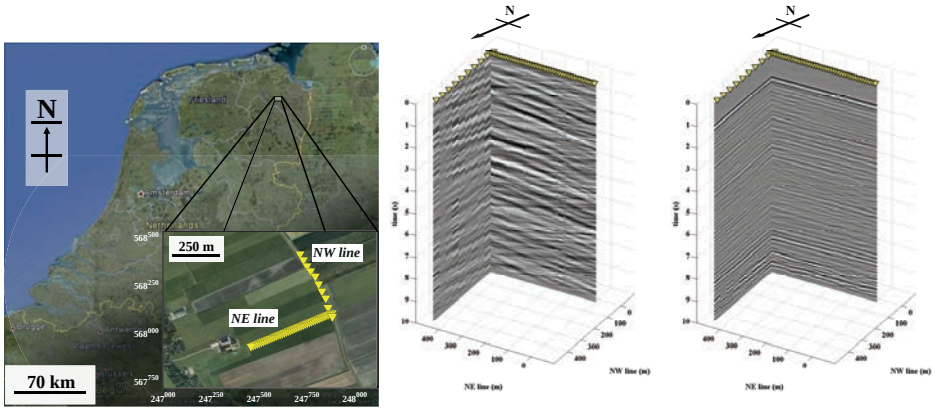

(a) *Passive seismic array location* **(b)** *Surface-wave recording* **(c)** *Body-wave recording*

Figure 2.4: ***(a)*** *Geographical location of Annerveen, Northern Netherlands, where the noise recordings are taken. Close-up: Two perpendicular receiver lines are indicated by yellow triangles. Note: Number of receivers and spacing are different in both lines: NE line has 40 receivers, while NW line has only 10; Space sampling is* 12 m *and* 48 m*, respectively.* ***(b)*** *3D display of an ambient-noise panel dominated by surface-wave noise.* ***(c)*** *3D display of an ambient-noise panel dominated by body-wave noise.*

character of the wavefield. Surface-wave noise coming at the receiver line from the crossline direction might be recorded with apparent slowness characteristic of body waves. Such arrivals will be inherited also by the SI retrieved results and be misinterpreted as retrieved reflections. To avoid such erroneous interpretations, ambient-noise recordings in the field should be carried out using areal arrays. For the application of illumination diagnosis, the minimum optimal geometry is to use crossing lines.

We apply the illumination diagnosis for retrieval of reflections to ambient noise recorded near the town of Annerveen in the North of the Netherlands. During the recording, an Earth tremor was detected by the array. We will use this event in the analysis.

For the retrieval of reflections in virtual common-source panels we work with two perpendicular lines of receivers as displayed in figure 2.4a. The first line has a NE orientation and is composed of 40 receivers equally spaced 11.75 m. The second line follows a NW orientation and has 10 receivers with 48 m spacing. Both arrays are buried at 50 m depth in the subsurface. The sampling frequency is 250 Hz. A total of 23 hours and 56 minutes of ambient noise has been processed for this work, split into 34434 noise panels of 10 s length with 7.5 s overlap between them.

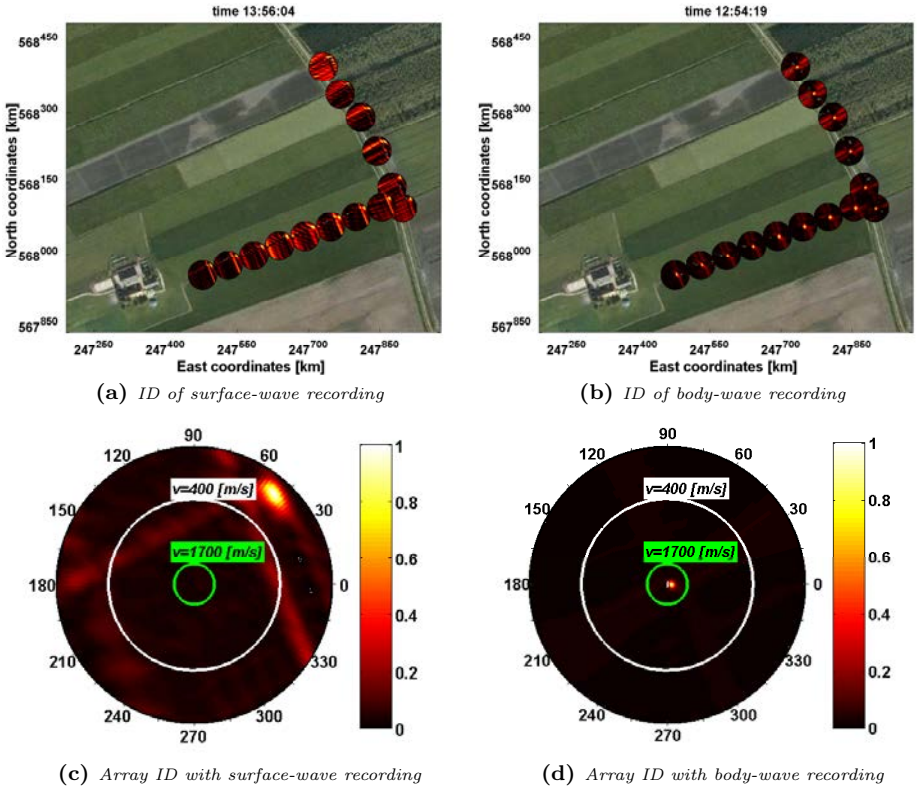

(a) *ID of surface-wave recording*

(b) *ID of body-wave recording*

(c) *Array ID with surface-wave recording*

(d) *Array ID with body-wave recording*

Figure 2.5: *Illumination diagnosis at different time sections.* ***(a)*** *Virtual-source illumination diagnosis at some of the receiver locations in Figure 2.4(a), due to surface-wave noise.* ***(b)*** *Illumination diagnosis of an Earth tremor.* ***(c)*** *Integration of the illumination diagnosis from (a).* ***(d)*** *Same as in (c), from (b).*

Figure 2.4b shows an ambient-noise panel along both lines dominated by surface waves coming from one side of the lines (road noise). We can see that along the NE line, the noise appears to be characterized by a low ray-parameter, that in a 2D setting might cause it to be interpreted as body waves; however, along the NW line, though, the arrivals are characterized by a ray-parameter typical for surface waves. Figure 2.4c is an example of another noise panel with arrivals from a deep source (Earth tremor), characterised by a low ray-parameter in both perpendicular lines.

In figure 2.5 we compare the use of the illumination diagnosis in the same area, with separate noise panels from different time sections. Figures 2.5a and 2.5b display the illumination diagnosis from some of the receiver locations ($\mathbf{x}_0$) with respect to the rest of the array, due to the ground tremor and to surface-

wave ambient noise, respectively. Figures 2.5c and 2.5d show the integration from all the individual illumination diagnosis from figures 2.5a and 2.5b, respectively. Note that the normalization of the slant-stack results here scales the amplitudes and takes the absolute value. The array required directional slowness-balancing for the illumination diagnosis not to suffer from spatial aliasing caused by the array design. Although one can identify the dominant ray-parameter $\mathbf{p}_i^{\mathbf{x}_0}$ for the Earth tremor or the ambient sources located at the surface, the results still show the spatial aliasing imprint in the perpendicular direction of the respective lines.

The illumination diagnosis is closely related to the beam-forming method (Lacoss et al., 1969), since it also analyses crosscorrelations of wavefields. However, our approach is different in the sense that we directly interpret the correlated incident field at the receiver location, as the source function of the reconstructed virtual source. For similar reasons, we apply our method in the $\tau - p$ domain at $\tau = 0\ s$ only, to restrict ourselves to the incident field only (without having to apply a time window). Moreover, the illumination diagnosis is independent between stations because one could use the source function at any virtual-source position, therefore one gets as many diagnosis results as receivers there are available.

Besides the results in Figure 2.5, due to the aliasing and differences in space sampling of the two crossing lines, NW and NE, we decided not to carry out the illumination diagnosis using both lines' receivers together, but instead using each line's independently: At each correlated noise panel, the illumination conditions are analysed by detecting the dominant $\mathbf{p}_i^{\mathbf{x}_0}$ at each of the receiver lines. The estimated surface-wave velocity at the site is 370 $m\ s^{-1}$ (2.7 $10^{-3}\ s\ m^{-1}$). Therefore, the illumination diagnosis had a minimum velocity to start scanning with of 200 $m\ s^{-1}$ (5 $10^{-3}\ s\ m^{-1}$).

In Figure 2.6, we can see that there are numerous correlated noise panels along the NE line that are dominated by arrivals with low $\mathbf{p}_i^{\mathbf{x}_0}$ values, which fall inside the limits for being characteristic of body-wave noise. But to decide in a 3D sense whether a noise panel is characterized by body- or surface-wave noise, we have to take a closer look at the illumination characteristics of the noise along the NE line (figure 2.6 middle) and compare them to the illumination characteristics of the corresponding noise panels along the NW line (figure 2.6 right). Then we can see that some of the low $\mathbf{p}_i^{\mathbf{x}_0}$ values along the NW line correspond to low $\mathbf{p}_i^{\mathbf{x}_0}$ values along the NW line (figure 2.6 middle top and right top, correspond to the Earth tremor from Figure 2.4c). On the other hand, the illumination diagnosis of both lines may inconsistently identify surface-wave noise as well when only one line exhibits low $\mathbf{p}_i^{\mathbf{x}_0}$ values (figure 2.6 middle bottom and right bottom, corresponding to road noise or farming activities). Therefore, only correlated noise panels from time windows that are dominated by low $\mathbf{p}_i^{\mathbf{x}_0}$ values on the diagrams for both the NE and NW lines are being selected for the subsequent summation of the correlated noise panels.

In figure 2.7 the illumination diagnosis is applied to 90 minutes of noise. Fig-

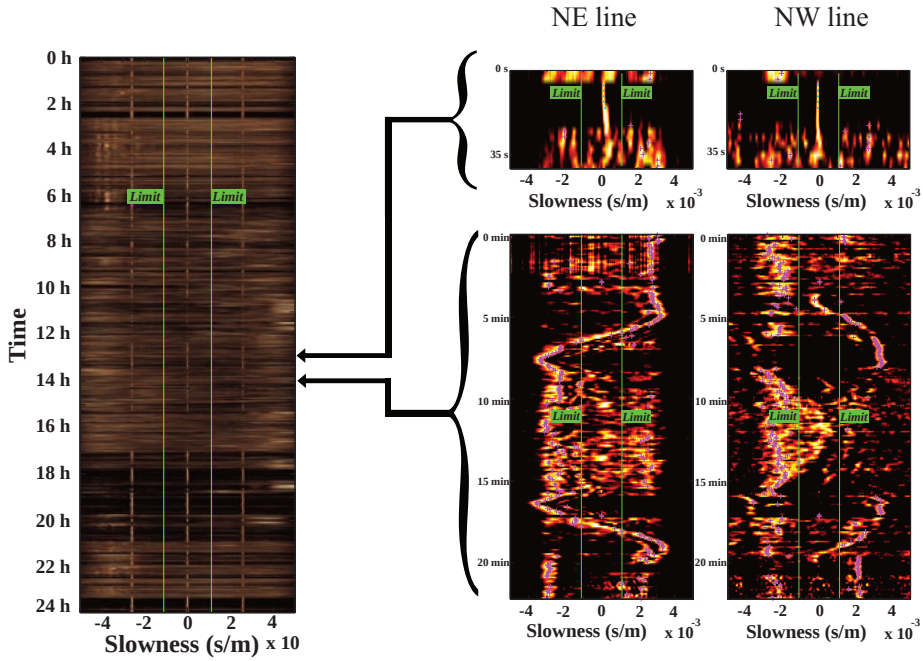

Figure 2.6: *Illumination diagnosis on nearly 24 hours of noise along line NE (left) with two different features: a weak Earth tremor (middle-top); and a surface source in motion identified by a pseudo-helix feature in the illumination records (middle-bottom). The magenta dots indicate the dominant $\boldsymbol{p}_i^{\mathbf{x}_0}$ for each of the correlated panels. The 3D nature of the noise being from body-wave or surface-wave sources can be judged when the illumination diagnosis along the NE line is complemented by the illumination diagnosis along the NW line (right).*

ures 2.7a and 2.7b show the dominating $\mathbf{p}_i^{\mathbf{x}_0}$ along the record in both NW and NE lines. For that short amount of data, very few panels were detected to be suitable for body-wave retrieval (blue stars), while the great majority was dominated by surface waves (magenta dots). The resorting of the diagnoses from the two lines are shown in Figures 2.7c and 2.7d. The weights, estimated from the ray-parameter histograms, is in this case not necessary because of the small illumination available.

Because of the difference in resolution for the analysis of the virtual-source function $\widetilde{C}_i$ along the two lines due to different amounts of receivers (NW line: 10, NE line: 40) and sampling (NW line: 48 m, NE line: 11.75 m), for this dataset an additional test is applied to the correlated panels with desired low

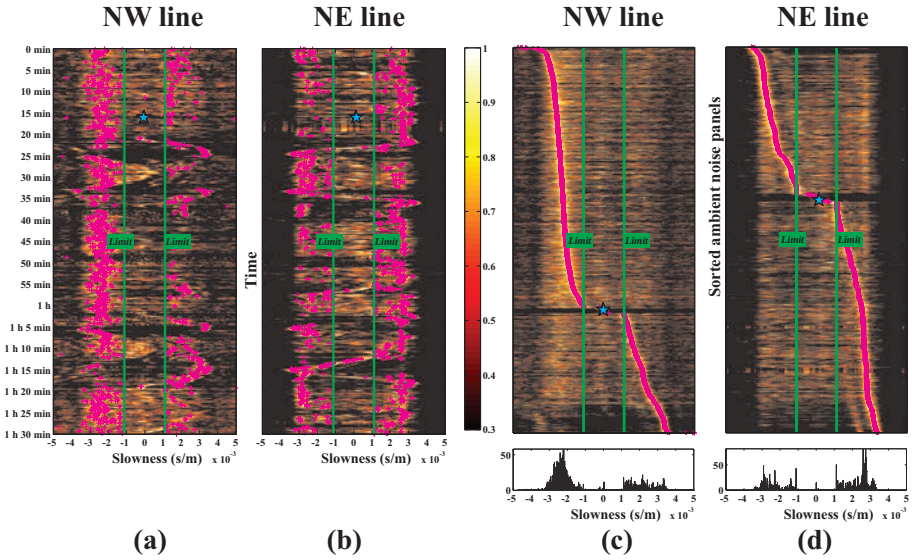

Figure 2.7: *Illumination diagnosis with 90 minutes of the total noise record from Figure 2.6.* ***(a)*** *Illumination record for the NW line at position $x_0 = 0$ m. Ray-parameter $\boldsymbol{p}_i^{x_0}$ is highlightened with a cyan star (dominating body waves) or a magenta dot (dominating surface waves),* ***(b)*** *Illumination record for the NE line at position $x_0 = 0$ m.* ***(c)*** *Illumination diagnosis for all correlated panels in (a), with the dominant ray-paramters $\boldsymbol{p}_i^{NW,x_0}$ highlightened; Diagram below shows the histogram of $\boldsymbol{p}_i^{NW,x_0}$.* ***(d)*** *Illumination diagnosis for all correlated panels in (b). Diagram below shows the histogram of $\boldsymbol{p}_i^{NE,x_0}$.*

$\mathbf{p}_i^{\mathbf{x}_0}$ values in both lines: We carried out a polarization analysis on each panel that was diagnosed to be dominated by body waves before correlation, profiting from multicomponent receivers (V_1, V_2 and V_3). Figure 2.8 shows two panels with dominant body waves (2.8a) and for comparison also dominated by surface waves (2.8b). Hodogram pairs consist of $V_1 - V_3$ and $V_2 - V_3$, in blue and red colour, respectively. These are obtained from 0.5 s sections at the same time of the respective components, every 0.9 s. Hodograms are displayed in every 6 traces of the NE line. In Figure 2.8b, surface-wave noise produce elliptical features in both hodograms. Figure 2.8a shows in its hodograms a rather more polarized behaviour, confirming body-wave particle vibration. The first section (until 6 s) corresponds to body-wave arrivals from an Earth tremor. At time 7 s appear the shear-wave arrivals.

Figures 2.9a and 2.9b display the retrieved common-source panels from cross-coherence at $x_0 = 0$ m in both lines NW and NE, respectively. The summation of all correlated noise panels is displayed in Figures 2.9c and 2.9d. Both methods

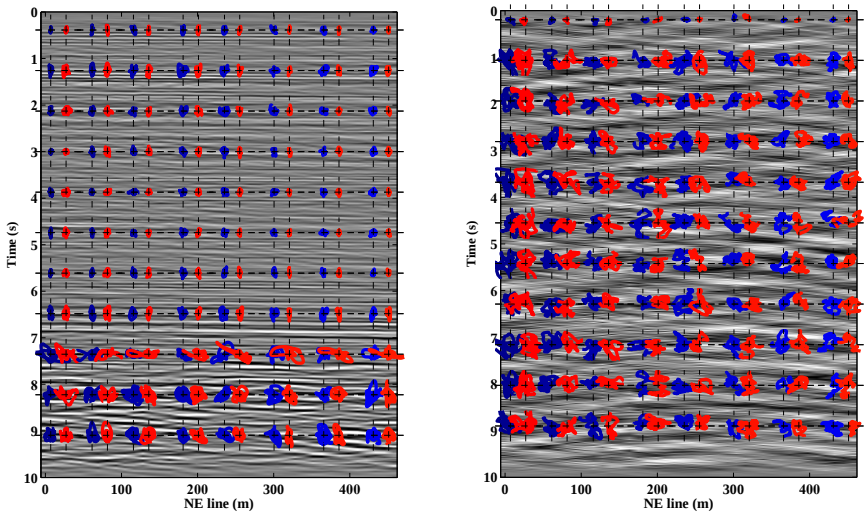

(a) *Body-wave recording* **(b)** *Surface-wave recording*

Figure 2.8: ***(a)*** *The V_3 component of a NE line ambient-noise record, dominated by body waves, with the respective hodograms every 0.8 s in every sixth trace, between components $V_1 - V_3$ (blue) and $V_2 - V_3$ (red).* ***(b)*** *as in (a), with ambient noise dominated by surface waves.*

have succeeded in retrieving arrivals, but these are surface waves, that dominate the SI results and therefore retrieved reflections are not observable. Figures 2.9e and 2.9f, present the respective results from 2.9c and 2.9d, which are using crosscorrelation, but after illumination diagnosis. Among the 34541 noise panels analysed, only 5 passed the test along both NE and NW lines. Of these positive cases, only 4 were suitable for reflection retrieval as observed at the polarization analysis, to be sure that they indeed are dominated by body-wave noise. We did this, because the NW line is sampled only by 10 geophones, which makes the illumination diagnosis, in this case, difficult. These numbers show the small amount of data available for the retrieval of reflections in the ambient noise recorded at the location of the acquisition array. This is related to the continuous anthropogenic activities, which result in continuous generation of strong surface waves, and the seismicity of the area, which is very low.

The comparison of the results from the three methods in Figure 2.9 shows that the application of illumination diagnosis has successfully suppressed the retrieval of surface waves, while the retrieval of body-wave events has been enhanced. Comparing these events with reflection arrivals recorded using an active source

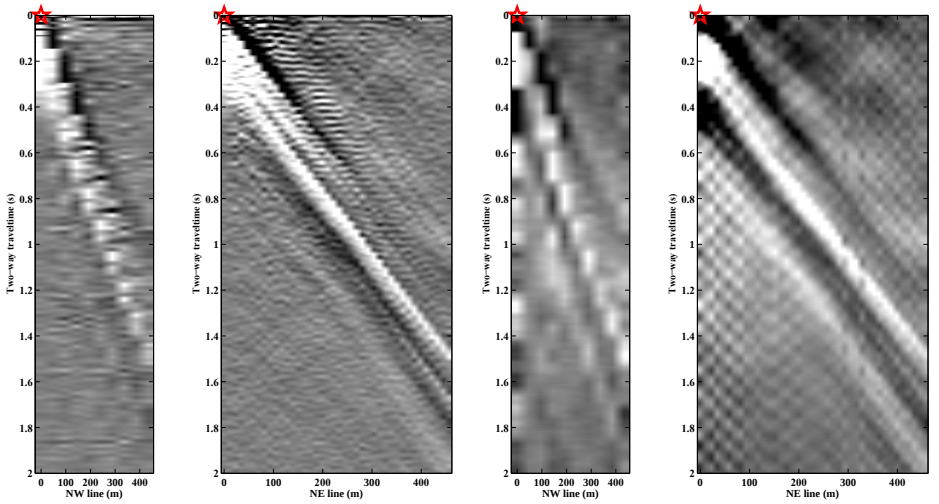

(a) $R^{\smile}_{3,NW}$ *via CCh* **(b)** $R^{\smile}_{3,NE}$ *via CCh* **(c)** $R^{\smile}_{3,NW}$ *via CC* **(d)** $R^{\smile}_{3,NE}$ *via CC*

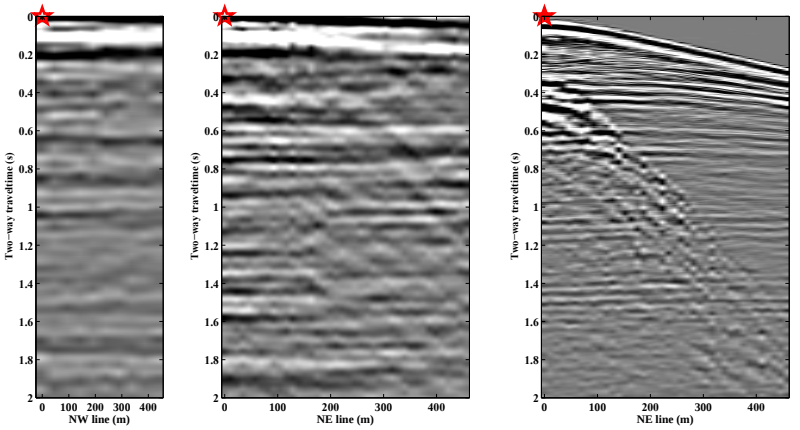

(e) $\sum_i C_i^{NW}$ **(f)** $\sum_i C_i^{NE}$ **(g)** *Active-shot gather*

Figure 2.9: *Retrieved V_3-component common-source panels for virtual source at $x_0 = 0$ m for the NE line and $x_0 = 0$ m for the NW line.* ***(a)*** *Cross-coherence result (CCh) for the NW line.* ***(b)*** *Cross-coherence result (CCh) for the NE line.* ***(c)*** *Cross-correlation result (CC) using all panels for the NW line.* ***(d)*** *Cross-correlation (CC) result using all panels for the NE line.* ***(e)*** *Same result as in (c) after discrimination and discard of panels with dominant surface waves.* ***(f)*** *Same as in (e) for the NE line.* ***(g)*** *Reference response for an active source located at the surface above the virtual-source location.*

(Figure 2.9g), we can conclude that at least some of the retrieved events are reflections. Note that the active data was shot with a source at the surface, while the virtual source in the retrieved data is at 50 m depth.

Due to the small-slowness values in the used correlated panels, together with the short aperture of the receiver array, the retrieved results exhibit predominantly nearly horizontal events. No weights were required to balance the illumination, since the dominant ray-parameters were nearly homogeneously distributed between 8 10^{-5} and 12 10^{-5} $s\ m^{-1}$ from approximately the same azimuthal direction. The move-out is not recovered due to the very limited illumination angles in the noise panels selected for retrieval. Earlier reflections are not properly estimated due to the lower-frequency content of the retrieved response. At early arrival times, there is more move-out in the reflection response, making it harder to reconstruct with limited illumination. Moreover, there is the imprint of the virtual-source function overlying the early reflections.

Note that some of the retrieved horizontal events might be non-physical. Increased illumination of the recording lines by body-wave noise could contribute, in addition to the potential retrieval of reflection hyperbolae, to the suppression of non-physical arrivals by destructive interference.

2.4 Discussion

The frequency characteristics of the retrieved body-waves would depend and be inherited from the frequency characteristics of the recorded body-wave noise. These frequency characteristics are often dominant at low frequencies (Ruigrok et al., 2011). Some studies have accomplished retrieval of reflections with frequency content comparable to that of active surveys (Draganov & Panea, 2011), even with human-induced noise (Nakata et al., 2011). Except for the case of the earthquake, however, body-wave ambient noise in the study area is more dominant at lower frequencies due to oceanic waves. The reflection response obtained from passive seismic interferometry will bear this low frequency characteristics, and might be an incentive to combine the reconstructed result with active survey results which usually lack low frequency content. By complementing passive and active results, the merging of both (virtual-) panels may produce a broader-band reflection response.

The attempt to balance the subsurface illumination could be further improved as well. In addition to the weights, other applications, such as directional balancing (Curtis & Halliday, 2010) and multidimensional deconvolution (Wapenaar et al., 2008b) could be used.

The size of the correlation windows to be used for illumination diagnosis is very important. In the above results, we used windows of 10-seconds length because of a limited amount of sources acting inside the panel in the synthetic experiment. The use of shorter time windows might improve the illumination analysis over

time by discarding less portions of the noise dominated by surface waves, but would consequently result in retrieval of reflections from shallower parts of the subsurface. This is because the window length dictates the maximum two-way travel time that could be retrieved. The optimal time windows to be used will depend on the ambient-noise source length and coincidence.

Complementary, besides avoiding the retrieval of surface waves, the proposed method also allows gathering of only the useful data for reflection retrieval, discarding unnecessary data and reducing later processing and storage costs.

2.5 Conclusions

We proposed a method to analyse the illumination characteristics of recorded ambient noise to be used for passive seismic interferometry. To apply the method, the recorded noise panels are correlated to obtain correlated panels and from them we used the events that pass through the virtual-source position at zero time. We transformed these events to the slowness domain and analysed them to classify the different noise panels as being dominated by surface-wave or body-wave noise. The illumination diagnosis from the correlated panels enables defining balancing weights in order to compensate overillumination from certain directions.

We applied the analysis to field data acquired in the North of the Netherlands. We dealt with the multiazimuth radiation recognition using two orthogonal receiver lines as acquisition setup. We showed that the retrieved results when using all recorded noise exhibit mainly surface waves. The illumination analysis of the ambient noise allowed to identify and discard parts of the recording as dominated by surface-wave noise. The illumination diagnosis detected and isolated several noise panels dominated by body-wave noise. Polarization analysis of the selected noise panels confirmed the dominant ambient noise to be due to body waves. The amount of body-wave noise panels and their respective illumination was less than desired for a complete reflection retrieval. Nevertheless, comparison of the results retrieved after illumination diagnosis with active-source seismic data confirmed that some of the retrieved events are reflection arrivals.

Annex I

Acquisition array design for optimal illumination diagnosis

In illumination diagnosis (ID) we estimate the direction of arrival of the seismic events from passive sources using the recordings at receivers deployed in an array at the acquisition surface. This process relies on the amount and geometrical distribution of the receivers at the acquisition surface. The receiver disposition of the array has consequences on the illumination diagnosis and its geometry design explains the appearance of directional aliasing artefacts. We analyze and compare different array designs on the acquisition surface for a limited amount of receivers. Among the different designs, we propose an optimal one that minimizes the artefacts due to directional aliasing without compromising seismic imaging requirements.

I.1 Introduction

In 3D land seismic acquisition the receiver array is designed in accordance with the active source array. This configuration aims to cover the range of illumination of the subsurface in an optimal way. In consistency with the source-array design, regular grids are the most popular sparse receiver-array designs employed. This design has been used in passive seismics because of several advantages: they have a simple construction and allow a satisfactory surface coverage with a regular receiver density. They also provide optimal aligning between equidistant receivers, which facilitates wavenumber processing. However, their geometric design reveals preferred angles of incidence. If the receiver amount is not sufficient, this aspect may have consequences on the passive seismic analysis: it shows that directional aliasing and the resolution on the directionality estimation of a seismic event is not optimal.

In passive seismics, the location of the sources is uncontrolled and the directionality of the seismic tremors is uncertain. In order to avoid receiver grids with preferred directions, the use of circular grid designs is very popular for a limited amount of receivers. Unlike regular grid distributions, curvilinear arrays have no privileged direction and handle with better precision the estimation of the direction of incidence of passive events. For this reason, this type of grid designs has been employed for directionality analysis of seismic events. The disadvantage of the radially staggered configuration is that it causes a transition from high to low receiver density and the equidistance condition between receivers cannot be held. Therefore, the process of imaging is compromised by the heterogeneous density of receivers at the acquisition surface.

The main goal of the acquisition design is to break the periodicity in the receiver aligning without compromising the homogeneous distribution of the receivers at the acquisition surface. In this annex we adapt the work of Martínez-Graullera et al. (2010) in ultrasonics to our passive seismic configuration. We analyze the design of different sparse acquisition arrays and study the effect of the different array geometries on the illumination analysis. Using a limited quantity of receivers, this acquisition design is to profit of the two aforementioned advantages: to randomize the receiver location in order to decrease the array imprint during the directional analysis of the seismic event, without compromising the constant receiver density for imaging purposes.

I.2 The spiral array

As an alternative to regular and circular grids, we propose the use of a new array design. The two properties we want to exploit in the array design are the constant sensitivity on the directionality of events and a constant receiver density Martínez-Graullera et al. (2010). This alternative design is inspired by the spiral patterns in phyllotaxis, which has the advantage of maximal sensitivity on directional analysis with optimal space distribution. The angular component of this configuration is related to the Golden Ratio $\varphi = \frac{1+\sqrt{5}}{2}$. In polar coordinates, the directional spread of the receivers is described by a constant divergence angle α as:

$$\theta_n = \alpha\, n. \tag{I.1}$$

In this case, the divergence angle α is defined by the golden angle $\alpha = 2\pi\varphi^{-2}$ and n is the index number of the receiver. The angle of divergence causes the periodicity in a certain direction of the receiver-index number to follow the Fibonacci series. This divergence angle has already been observed in nature in phyllotaxis patterns. In botanics, the use of the golden angle in the evolution of the arrangement between consecutive leaves has been observed as the result of optimizing their access to what they needed for growth and minimizing their interference for light harvesting and transpiration. The golden angle has also been investigated

in computed tomography applications in aims for an optimal angular sampling (Köhler, 2004; Winkelmann et al., 2007). Small variations in the divergence angle produces dramatic changes in the optimality of the design.

The second aspect we want to exploit is the constant density of elements along the surface in regards to our imaging purposes. This aspect is controlled by the radial spread of the receivers. Some of the most employed spiral patterns observed in nature are the logarithmic spirals, whose radial spread is defined as:

$$r_n = a\, e^{b\theta_n}. \tag{I.2}$$

In this case of spirals, the use of the golden angle in its radial distribution describes the golden spiral, which is featured in biological designs for its self-similarity properties (Thompson, 1942). However, we do not intend to exploit this particularity but rather to define a receiver distribution with equidistant properties. The set of spirals described in nature with a constant radial growth are the Archimedean spirals:

$$r_n = a\, n^b. \tag{I.3}$$

For the given power factor $b = 0.5$, equations I.1 and I.3 result in the form known as the Fermat spiral. This spiral describes a constant radial growth and the mean distance between neighbouring receivers is uniform (Ridley, 1982). The Fermat spiral is described by cyclotron orbits and has also been studied and implemented in heliostat field designs for thermo-solar power stations (Noone et al., 2012). Another example of this design is the configuration of florets in the head of sunflowers (Vogel, 1979). Compared to other spiral designs, the Fermat spiral shows the most homogeneous and compact distribution of its elements. This can be observed with respect to the different Archimedean spirals: a change in the exponential factor value b different of 0.5 varies the density of the receivers radially. In our array design, the location of the receivers around a reference central position following this design is presented with respect to the receiver index number as:

$$r_n = r_0\sqrt{n}, \tag{I.4}$$

where r_0 is a survey-dependent constant (Martínez-Graullera et al., 2010):

$$r_0 = \frac{L}{2\sqrt{(N-1)}}. \tag{I.5}$$

L is the desired aperture of the acquisition array and N is the total amount of receivers available. Without defining any preferred direction, the receiver arrangement in this design provides an optimal display of receivers with constant mean spacing between elements. Neither the logarithmic nor the other Archimedean

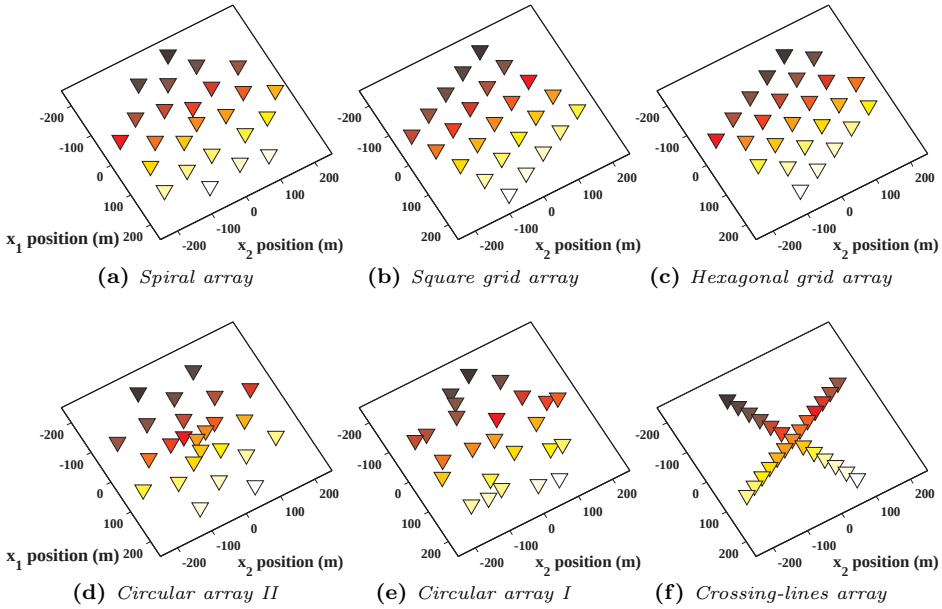

(a) *Spiral array* **(b)** *Square grid array* **(c)** *Hexagonal grid array*

(d) *Circular array II* **(e)** *Circular array I* **(f)** *Crossing-lines array*

Figure I.1: *Different receiver-array designs at the same depth level, covering the same area. The receivers are represented by triangles and every array shares the same amount of receivers, 25, and the same central receiver coordinates.* ***(a)*** *Irregular array based on the Fermat spiral.* ***(b)*** *Square grid array with* 5 x 5 *lines of* 75 *m spacing.* ***(c)*** *Hexagonal grid array with the same spacing as (b).* ***(d)*** *Circular array with concentric rings of different spacing and receiver amounts.* ***(e)*** *Circular array with growth in spiral pattern.* ***(f)*** *Receiver array organized in crossing lines with* ca. 33 *m spacing.*

spirals perform better than the Fermat spiral in arranging their receivers with a constant density. This is due to the fact that the exponential and linear radial growth functions of the two spiral patterns result in a much faster change in the receiver density than in relation I.4.

I.3 Arrays

We test 6 different acquisition designs over a horizontal acquisition surface. All the designs share the same amount of receivers (25), the same coverage area (*circa* 0.12 km^2), and a common receiver location at local coordinates $(x_1, x_2) = (0, 0)$ m. Figure I.1a shows the proposed Fermat spiral distribution (named "Spiral"). Although not supposed to, we used the geometric centre of the spiral array

to locate the central receiver; This causes small variations in the directionality analysis and sensitivity of the array design, which will be mentioned later. The square and hexagonal grids are presented in figures I.1b and I.1c, respectively.

Two circular arrays are also represented: On figure I.1d the circular array is composed of 3 concentric rings of different receiver quantity (named "Circular array II"). An irregular circular array is presented in figure I.1e, with variable ring growth and the number of ring-elements based on the Fibonacci series (named "Circular array I"). The last array used is defined by two perpendicular lines (named "Crossing lines", figure I.1f), which has been popularly employed for illumination diagnosis with imprecise results.

I.3.1 Directional aliasing

In order to analyze the suitability of the arrays for imaging, we study the minimum inter-receiver spacings and their directional occurrence. The inter-receiver spacing can be expressed by its equivalent Nyquist-wavenumber in the respective orientation between receivers. For that reason, we analyze the sensitivity that the array gives to every direction by looking at the azimuth distribution of the maximum Nyquist-wavenumber. Our goal is to detect which array design preserves the most homogeneous density of receivers without giving any preferred direction.

Given the limited amount of receivers $N = 25$, there is a total amount of $N(N-1)$ of inter-receiver relations to examine. In figure I.2 we show the directional distribution of the highest wavenumbers (Nyquist wavenumber equivalents, 12% percentile of the total) produced by each array in figure I.1. The respective display beneath shows the distribution of all the wavenumbers sampled by the array with respect to azimuth. For the spiral array, in figure I.2a, the distribution of the highest wavenumbers is concentrated in a ring of constant range $\approx 0.007\ m^{-1}$. The irregularity caused by the first pair of receivers in the spiral is visible in this result, at the wavenumber sampled pair that doubles the wavenumber range of the ring distribution, at 25° azimuth. It is caused by the central-receiver location choice as mentioned before, whose distance to the closest receiver is half with respect to the rest. Besides this detail, this array design shows that it does not contain any preferred direction and samples every direction with the same space sensitivity. The wavenumber distribution displayed below shows that these values keep the same density on the wavenumber values preserving a constant directional sampling.

The same maximum wavenumber-value range is shown for the regular grids in figures I.2b and I.2c, with the difference of having the wavenumber values repeated on the same directions. The plot below shows that the respective wavenumber distributions have 4 or 6 peaks, depending on the grid geometry, representing the preferred directions of the arrays; secondary preferred directions are also identifiable at a different wavenumber-value range than the primary ones (and so on for

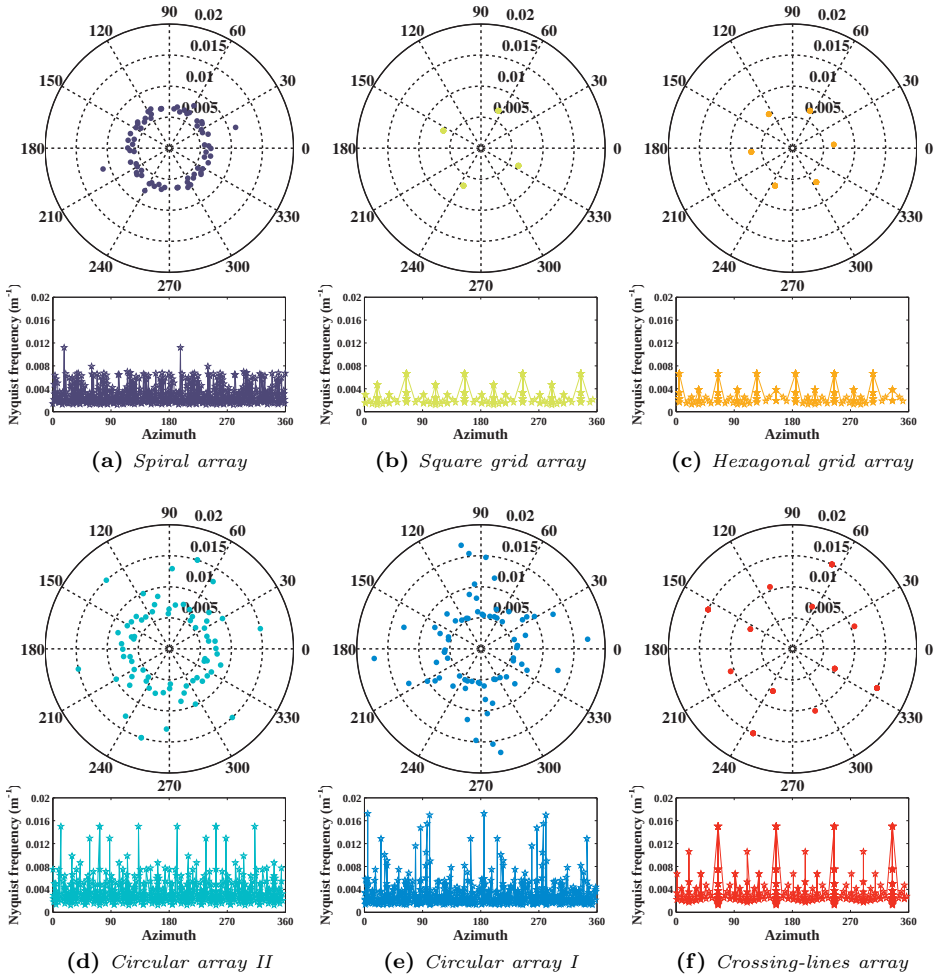

(a) *Spiral array* **(b)** *Square grid array* **(c)** *Hexagonal grid array*

(d) *Circular array II* **(e)** *Circular array I* **(f)** *Crossing-lines array*

Figure I.2: *Directional analysis based on space sampling. Top figure, polar distribution of the Nyquist-wavenumber equivalents of the respective acquisition array (top 72 out of 600 inter-receiver values). Low figure, azimuthal distribution of receiver pairs and their respective wavenumber value.* ***(a)*** *Irregular array based on the Fermat spiral.* ***(b)*** *Square grid array.* ***(c)*** *Hexagonal grid array.* ***(d)*** *Circular array with concentric rings.* ***(e)*** *Circular array with irregular radial growth.* ***(f)*** *Crossing-lines receiver array.*

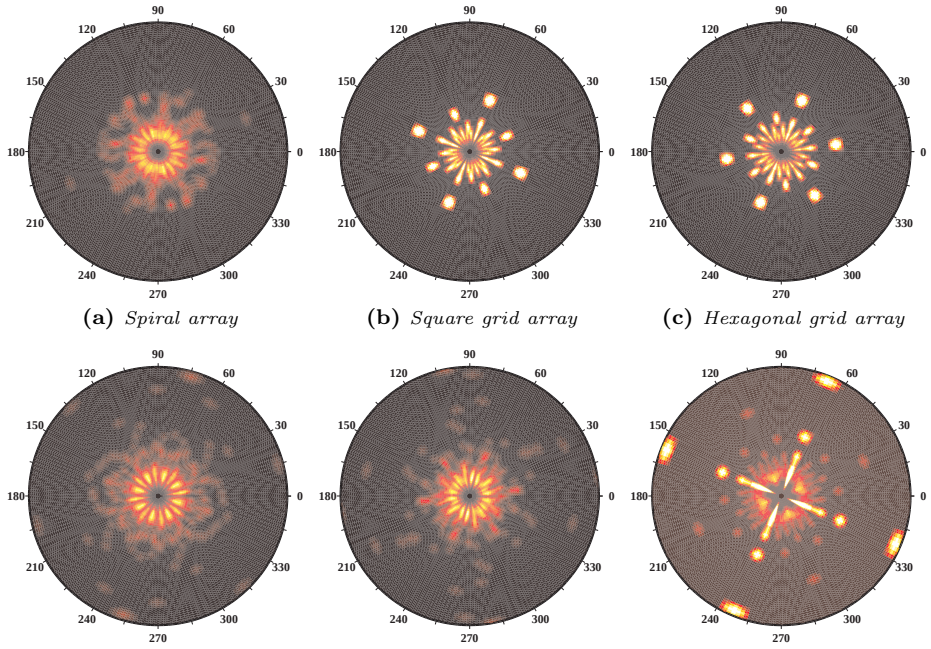

(a) *Spiral array* **(b)** *Square grid array* **(c)** *Hexagonal grid array*

(d) *Circular array II* **(e)** *Circular array I* **(f)** *Crossing-lines array*

Figure I.3: *Azimuthal distribution of the receiver pair spacings, represented by their wavenumber equivalents. All figures share the same colour axis.* ***(a)*** *Irregular array based on the Fermat spiral.* ***(b)*** *Square grid array.* ***(c)*** *Hexagonal grid array.* ***(d)*** *Circular array with concentric rings.* ***(e)*** *Circular array with irregular radial growth.* ***(f)*** *Crossing-lines receiver array.*

the tertiary preferred directions, etc).

In figures I.2d and I.2e the circular grids show no preferred direction, but the Nyquist wavenumber-equivalent range is not constant. The great variety of spacings with respect to the azimuth shows its non adequacy for imaging applications.

As for the crossing-lines array, in figure I.2f since the receiver density is located along the two lines and contains the minimum space sampling, it shows the maximum wavenumber values with respect to the other arrays, but only for the 2 preferred directions. Secondary preferred directions are the result of the combination of receiver pairs from opposite lines.

Figure I.3 depicts a statistic distribution of the receiver-pair directionality expressed in wavenumber values. These are the polar representation of the lower figures in I.2, to compare the repetition on the directional sampling between the

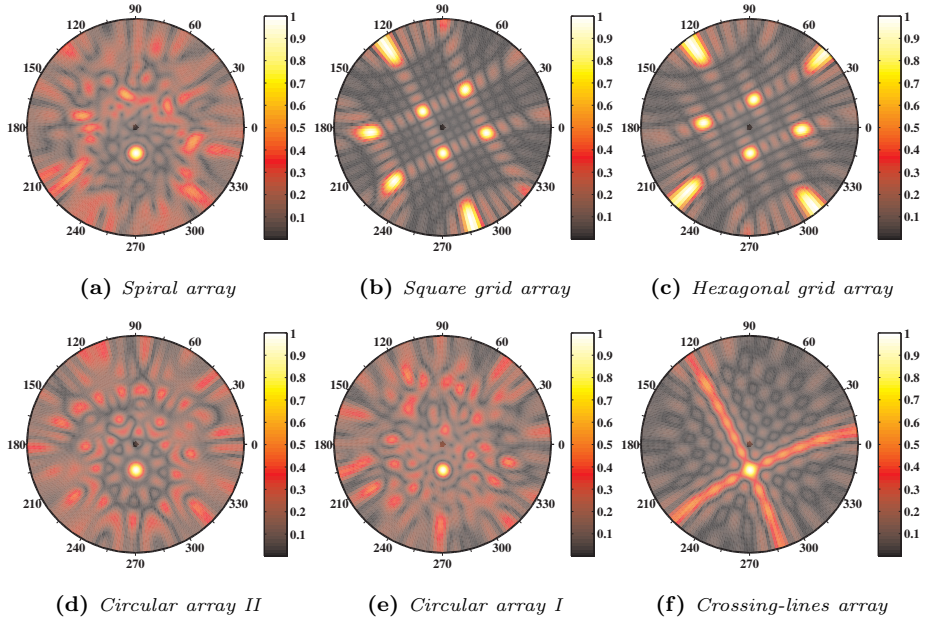

(a) *Spiral array* **(b)** *Square grid array* **(c)** *Hexagonal grid array*

(d) *Circular array II* **(e)** *Circular array I* **(f)** *Crossing-lines array*

Figure I.4: *Array factor $AF(\theta, \phi)$ of the arrays for $\omega = 215\ s^{-1}$, $c_P = 1670\ m\ s^{-1}$ in the direction $\theta_S = 90°$, $\phi_S = 21°$. θ describes the azimuthal direction (from $0°$ to $360°$). ϕ represents the nadiral angle along the radius: from vertical/normal incidence in the centre of the plot ($0°$) to horizontal/tangential incidence at the edges ($90°$). **(a)** Irregular array based on the Fermat spiral. **(b)** Square grid array. **(c)** Hexagonal grid array. **(d)** Circular array with concentric rings. **(e)** Circular array with irregular radial growth. **(f)** Crossing-lines receiver array.*

different acquisition arrays. The values have been convolved with a square function and the colour intensity is proportional to the repetition in the wavenumber sampling at any direction. The optimal result aims for a smooth constant distribution where no wavenumber value nor direction excels in the display. For the regular grid arrays, however, the intensity of their respective colour distribution in figures I.3b and I.3c shows how the sampled wavenumbers of these arrays are repeated in the preferred directions of their respective designs. The inner section of the plot shows directional lobes that explain the different sensitivity these arrays have depending on the direction of arrival. The crossing-lines array in figure I.3f shows the highest wavenumber values on the two preferred directions and an even worse directional behaviour due to the preferred directions in its geometry. As for the circular arrays, figures I.3d and I.3e, the central section shows a better homogenization on the directional sensitivity. However, these results show outlier

values with high wavenumbers at different directions, and neither of the array designs seems capable of defining a directionally-homogeneous Nyquist-wavenumber value.

The goal is an array that reads every wavenumber with the same sensitivity and does not contain outlier values beyond an omnidirectional Nyquist wavenumber value. The result in figure I.3a shows the best directional behaviour of any array since all the receiver-pair values remain within the same wavenumber interval, providing a constant maximum space sampling in every azimuthal direction (with the exception of the marginal value at 25° due to the central pair of receivers, as explained before).

Another factor employed to evaluate the efficiency of the receiver-deploy designs is the array factor. This analysis examines the directional sensitivity of the receiver geometrical distribution studying the featuring of lobes caused by the receiver arrangement with respect to the incidence of a monochromatic plane-wave to the array. The array factor AF is described as Martínez-Graullera et al. (2010):

$$AF(\theta,\phi) = \left| \sum_{n=1}^{N} e^{-i\,\frac{\omega}{c_P}\left((x_{n,1}cos(\theta)+x_{n,2}sin(\theta))sin(\phi)-\xi_n(\theta_S,\phi_S) \right)} \right|, \qquad \text{(I.6)}$$

where $\xi_n(\theta_S,\phi_S) = (x_{n,1}cos(\theta_S) + x_{n,2}sin(\theta_S))\,sin(\phi_S)$ is the phase delay corresponding to the respective n-receiver of the monochromatic plane wave incidence.

We analyze for a plane wave signal with angular frequency $\omega = 215\ s^{-1}$, assuming the velocity of the medium $c_P = 1670\ m\ s^{-1}$ and both azimuthal and nadiral directions $\theta_S = 90°$ and $\phi_S = 21°$, respectively. In figure I.4a the directionality of the signal is represented by the main lobe with high values while side lobes represent the uncertainty of the estimation on the directionality of the incident wave. The lobe-depressed zone around the main lobe represents the resolution provided by the array design at that angular frequency. This resolution zone is also featured in the circular grids with similar (figure I.4d) or worse accuracy (figure I.4e). The repetition of the inter-receiver orientation with regular grid arrays causes this analysis to show several main lobes (figures I.4b and I.4c) or undetermined long side-lobes in the case of the crossing lines (figure I.4f).

I.4 Illumination diagnosis

In the illumination diagnosis (ID) we analyze the horizontal slowness of the dominant arrival to the receiver array at every receiver location. The result is a horizontal slowness distribution with respect to azimuth of the wave energy arriving to the array at each receiver location. The precision of the method is proportional to the ratio of the signal bandwidth with respect to the acquisition aperture, the minimum inter-receiver spacing, and the receiver array geometry. The first two

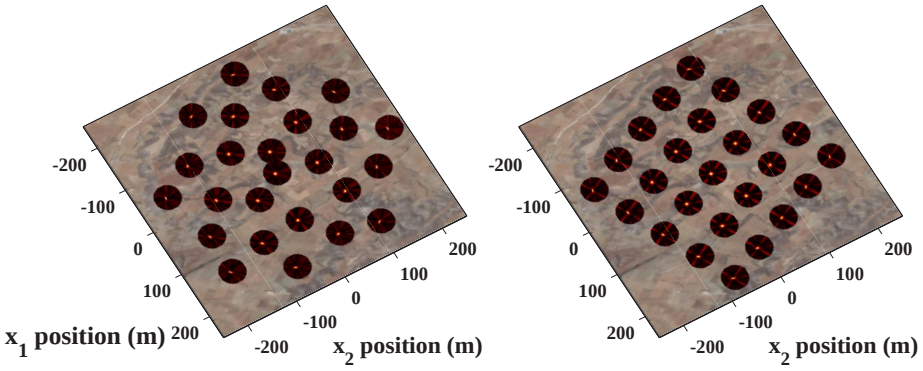

(a) *Spiral array*

(b) *Square grid array*

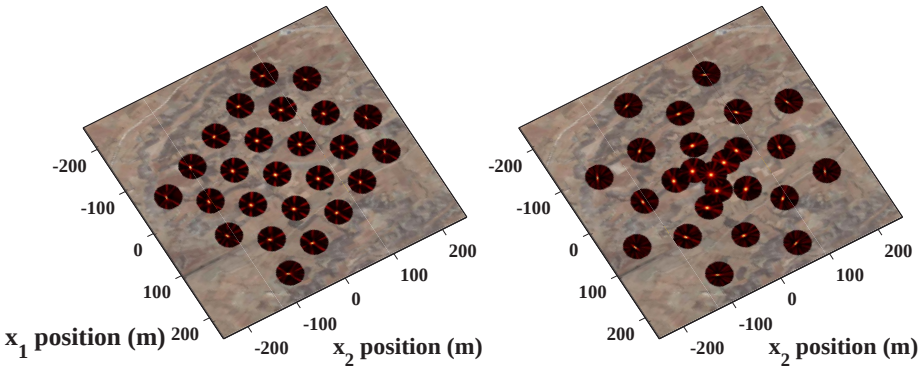

(c) *Hexagonal grid array*

(d) *Circular array II*

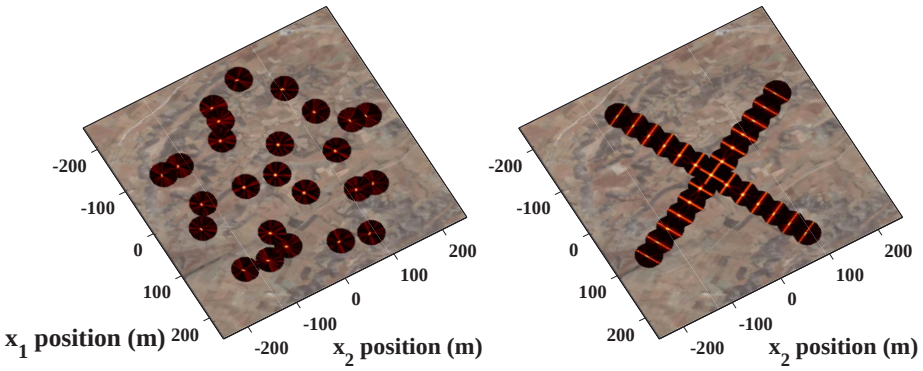

(e) *Circular array I*

(f) *Crossing-lines array*

Figure I.5: *Illumination diagnosis results displayed on the complete array, at every receiver location.* ***(a)*** *Irregular array based on the Fermat spiral.* ***(b)*** *Square grid array.* ***(c)*** *Hexagonal grid array.* ***(d)*** *Circular array with concentric rings.* ***(e)*** *Circular array with irregular radial growth.* ***(f)*** *Crossing-lines receiver array.*

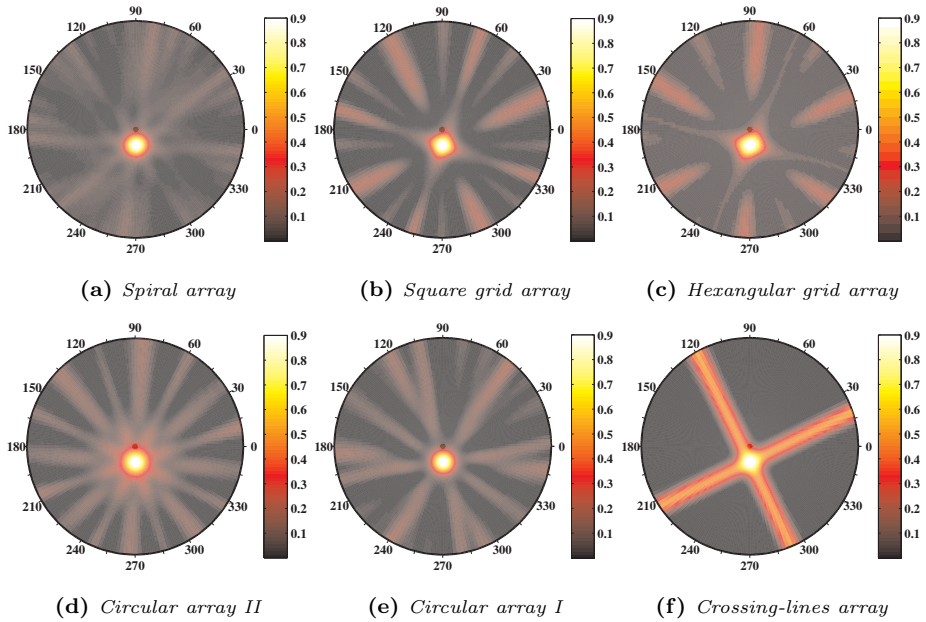

(a) *Spiral array* **(b)** *Square grid array* **(c)** *Hexangular grid array*

(d) *Circular array II* **(e)** *Circular array I* **(f)** *Crossing-lines array*

Figure I.6: *Illumination diagnosis obtained at the central receiver of the respective array, at coordinates* $(x_1, x_2) = (0, 0)$ *m, from figure I.5.* ***(a)*** *Irregular array based on the Fermat spiral.* ***(b)*** *Square grid array.* ***(c)*** *Hexagonal grid array.* ***(d)*** *Circular array with concentric rings.* ***(e)*** *Circular array with irregular radial growth.* ***(f)*** *Crossing-lines receiver array.*

factors are directly related to the source signal present in the passive recordings, while the third aspect is discussed below.

In figure I.5 we show the result of the illumination diagnosis for the arrival of a synthetic plane wave with a Gaussian-spectrum source signal and central frequency of 6 Hz. ID maximum-slowness analysis is 0.004 $s\ m^{-1}$ (minimum velocity analyzed 250 $m\ s^{-1}$). The arrival is detected with azimuthal and nadiral coordinates $\theta_S = 90°$ $\phi_S = 72°$, respectively. Since it is a plane wave, the horizontal slowness of the arrival peaks at the same value for every receiver location, but the ID resolution function varies depending on the array location of the receiver. When we make the analysis at an arbitrary receiver, depending on its location with respect to the rest of the array, the ID result features a certain array signature which gets worse the more marginal the receiver location is. Receiver triplet alignings produce radial lobes in the ID result proportional to the amount of the receivers in line, as can be seen for the regular grid arrays (figures I.5b and I.5c) and even the worst case for the crossing lines (figure I.5f). Figure I.5d

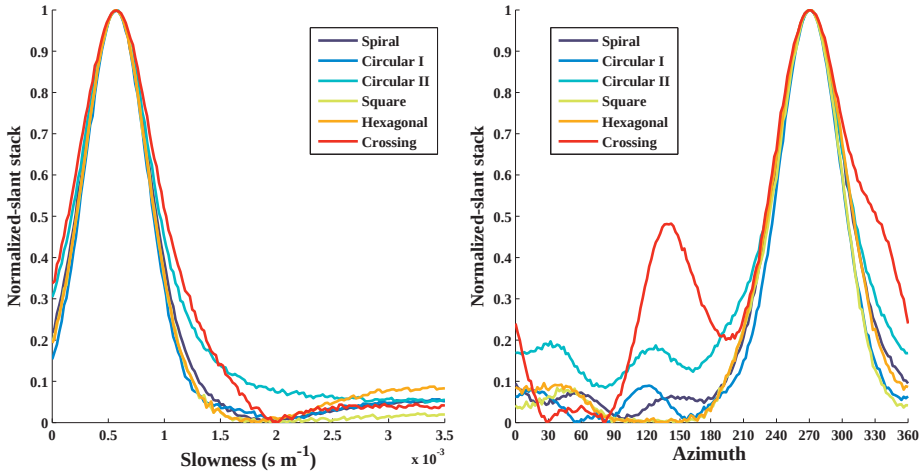

(a) *Slowness crossed section* **(b)** *Azimuth crossed section*

Figure I.7: *Comparison of the illumination diagnosis displayed in figure display I.6.* ***(a)*** *Illumination diagnosis with respect to the slowness, at the dominant-slowness' azimuth direction.* ***(b)*** *Illumination diagnosis with respect to the azimuth, at the dominant absolute-slowness value.*

shows the ID result in the regular circular array is more blurred for the central receiver locations, while for the marginal receivers the results feature tangential lobes with respect to the array location. These array-signature lobes are milder for the irregular "Circular I" and "Spiral" arrays (figures I.5e and I.5a), which profit from not containing triplet alignings of the receivers.

We also present the ID result for the central receiver location alone in figure I.6. The regular grid arrays (figures I.6b and I.6c) show the imprint of the array in radial lobes for the aliased directions of it. The worst case is presented by the crossing lines (figures I.6f). The circular grids also feature radial lobes due to casual triplet aligning of receivers (Circular array I, figure I.6e), or different distance between sensors (Circular array II, figure I.6d). The ID result in figure I.6a shows that the spiral pattern significantly outperforms the circular and regular grids in minimizing the formation of radial lobes. Displays in figure I.7 show the different array ID results at the central receiver, in the respective slowness and azimuthal sections. While the regular grids, "Spiral" and "Circular I" arrays show a similar performance, the "Circular array II" and the "Crossing lines" feature the least precision at the central receiver location.

I.5 Conclusions

Aiming for an optimal passive seismic imaging with a limited amount of receivers, we propose the use of an acquisition design based on the Fermat spiral. This design provides the best directional sensitivity, minimizing the spatial aliasing and deploys the receivers at a constant surface density. The receivers' locations are designed aiming to minimize the possible alignings between receiver triplets. Moreover, it has a simple construction since only a couple of parameters are required: Array aperture and amount of receivers. It profits of the advantages of circular arrays in the directional analysis of passive recordings, and additionally can take advantage of the quasi-constant receiver-spacing of regular grid arrays in order to perform seismic imaging. These advantages can also complement alternative analysis for body waves (Almagro Vidal et al., 2014; Gal et al., 2016) and surface waves (Maranò et al., 2012) on determining the direction of wave arrivals.

Since it shows an irregular space distribution of the receivers, the main disadvantage of this array is that the use of the wavenumber domain cannot be employed in any further processing of the data acquired with such design.

3 Implicit passive seismic interferometry for body-wave reflection retrieval[§]

Passive seismic interferometry (SI) enables the retrieval of the reflection response of the subsurface using passive seismic recordings. The current PSI methods make use of reciprocity relations with strong theoretical assumptions. Results are firmly dependent on the subsurface source distribution and the characteristics of the ambient sources and their spectra. Event driven passive SI methods allow the estimation of the reflection response with or without free-surface interaction. This estimation profits from correct amplitude retrieval even for non-uniform source distributions. This result however depends heavily on the transient behaviour of the sources' signal for it requires additionally data-sensitive time-windowing procedure.

In this chapter, we propose alternative reciprocity relations to obtain new passive SI methods. We derive new representations with one-way wavefields to retrieve the reflection response without free-surface interaction, both for passive SI with transient signals and ambient-noise SI (ANSI). These new reflection response estimations do not make any assumptions on the source characteristics and heterogeneous spectra, and deal with unequal source distribution and occurrence. These methods are also applicable to multicomponent elastic recordings, in order to obtain the different wave-mode reflection responses. Experimental results are shown on 2D synthetic scenarios: transient signals and continuous noise in an acoustic medium and continuous-noise in an elastic medium.

[§]Certain Sections of this chapter have been published as an extended abstract in the *84th annual SEG meeting, Denver, PSC*, (Almagro Vidal & Wapenaar, 2014).

3.1 Introduction

Seismic Interferometry (SI) has become a valuable method for passive seismics in exploration, regional and global geophysics. In exploration geophysics, the application of SI onto a passive acquisition array at or near the Earth's surface enables the retrieval of the subsurface information (transmission responses) using ambient recordings of different characteristics from ungoverned sources. Passive SI with surface waves makes possible the reconstruction of the surface-wave transmission response (Shapiro & Campillo, 2004; Dalen et al., 2015). The use of passive SI with body waves enables the estimation of the reflection response by using recordings of either transient natural signals (transient tremors and earthquakes) or ambient seismic noise, originated from sources in the subsurface. The retrieved reflection response may be used for subsurface imaging or may even complement active reflection seismic surveys, in case these suffer from limited-band signal, for passive SI may enhance the lower frequencies in order to improve the imaging process.

The retrieval of reflection responses, also known as Green's function retrieval (Lobkis & Weaver, 2001; Roux & Fink, 2003; Snieder et al., 2006), is achieved using operations involving wavefield reciprocity theorems to the recordings: The receiver locations are turned into virtual sources by means of correlation, convolution or deconvolutional processes, depending on which reciprocity relation is employed.

The SI relation most extensively applied in exploration geophysics makes use of crosscorrelation between receiver recordings (e.g. Claerbout, 1968; Schuster, 2009). The theory of SI by crosscorrelation is fully described by Wapenaar & Fokkema (2006). In this method, applications with ambient noise require sources to be monopoles with the same power spectrum, be mutually uncorrelated and homogeneously distributed in the subsurface for an accurate result. This approach has been applied to real datasets (Draganov et al., 2009). The frequency content of the retrieved response is band limited, depending on the power spectrum of the ambient-noise sources. The estimated response is known to suffer from spurious events due to over-illumination by clusters of sources or an irregular source distribution. The effect of these features can, however, be minimised (Curtis & Halliday, 2010; Ruigrok et al., 2011).

In order to deal with the coexistence of body and surface waves in ambient-noise recordings, passive SI also profits from SI by crosscoherence (Aki, 1957; Nakata et al., 2011). This method, conceived for ambient-noise recordings, is based on crosscorrelation but whitening the spectrum of the correlation result in order to relatively reduce in amplitude the surface-wave retrieval while enhancing the less energetic body-wave reflection response.

The employment of SI by multi-dimensional deconvolution (MDD) on passive seismics was introduced by Wapenaar et al. (2008b). This work presented acoustic results employing two-way wavefields by isolating the incident fields in

the time domain as an approximation to the required wavefield response without free-surface (reference-state transmission wavefield or reference wavefield). However, in continuous noise recordings the reference wavefield cannot be estimated nor isolated. An approximation to the deconvolution operator or point-spread function of MDD can be attained by time gating after correlation (van der Neut et al., 2010; Wapenaar et al., 2011b). This approach showed an equivalent result to crosscorrelation but with a balanced directional behaviour from the non-uniform subsurface illumination and time signal deconvolution. Using free-surface-related multiples, van Groenestijn & Verschuur (2010) employed an iterative inversion procedure to reconstruct the reflection response for the primaries only in acoustic medium.

Estimation of the reflection response without free-surface multiples has also been attempted using SI by MDD with one-way wavefields: Following time-gating procedure but applied on seismic tremors with transient signals, Nakata & Snieder (2013) used elastic one-way wavefields in a real dataset. However, the limitation of the source distribution restrained a proper estimation of reflections.

In this chapter we revise the representations of the convolution and correlation reciprocity relations, and their need of the reference wavefield as the biggest drawback. We present the two possible SI methods for passive seismics to retrieve the reflection response of the medium with transient signals, that can be obtained either by implementing the convolution representation or the correlation representation. This work also proposes an alternative procedure to work with ambient-noise to reconstruct the reflection response without free-surface multiples, avoiding the need for estimation of the point-spread function. The goal is to work with long ambient-noise data, minimising the effect of anisotropic illumination due to heterogeneities in the source distribution of the subsurface, and working independently of the ambient-source characteristics and power spectra. Results show the comparison of this method to the other SI methods with the increase of acquisition time in an acoustic medium. An extension for an elastic medium is presented making use of particle velocity components only and illumination diagnosis for preventing disturbing contributions from surface waves.

3.2 Representation of the convolution type

In this section we consider the convolutional relation that serves to estimate the reflection response inside a control domain $\mathbb{D}$, without free-surface interaction. We make use of reciprocity theorem of the convolution type, defined between a reference and a measurement state (Wapenaar et al., 2004). Both states share in common the same medium parameters in $\mathbb{D}$ and on its boundary $\partial\mathbb{D}$, but different parameters outside of it. We divide the domain boundary into an upper $\partial\mathbb{D}_0$ and an arbitrary lower boundary. The reference state defines the medium above $\partial\mathbb{D}_0$ homogeneous and locates the source outside $\mathbb{D}$ and immediately above the boundary $\partial\mathbb{D}_0$. As for the measurement state the medium includes a free-

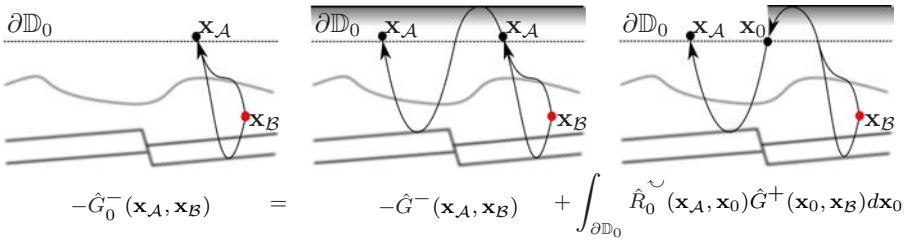

Figure 3.1: *Illustration of the reciprocity relation of the convolution type, as expressed in equation 3.1, representing the three wavefield quantities by their travel paths.*

3

surface above $\partial\mathbb{D}_0$ while the source is located outside $\mathbb{D}$ and immediately below the lower boundary. The medium is assumed heterogeneous below this boundary for both states. The aim is to estimate the reflection response of the reference state at $\partial\mathbb{D}_0$ (without free-surface interaction) analyzing the reciprocity relations between the wavefields of both reference and measurement states.

Making use of the one-way reciprocity relation of the convolution type (Wapenaar & Grimbergen, 1996) the implicit expression for the desired reflection response becomes (Appendix 3.C, equation 3.31):

$$-\hat{G}_0^-(\mathbf{x}_\mathcal{A},\mathbf{x}_\mathcal{B},\omega) = -\hat{G}^-(\mathbf{x}_\mathcal{A},\mathbf{x}_\mathcal{B},\omega) + \int_{\mathbf{x}_0\in\partial\mathbb{D}_0} \hat{R}_0^{\smile}(\mathbf{x}_\mathcal{A},\mathbf{x}_0,\omega)\hat{G}^+(\mathbf{x}_0,\mathbf{x}_\mathcal{B},\omega)d^2\mathbf{x}_0. \quad (3.1)$$

Here $\hat{G}^-(\mathbf{x}_\mathcal{A},\mathbf{x}_\mathcal{B},\omega)$ stands for the acoustic flux-normalized impulse wavefield of the measurement state, including both internal and free-surface multiples, for a source at $\mathbf{x}_\mathcal{B}$ in the subsurface and a receiver at $\mathbf{x}_\mathrm{A}$, immediately above $\partial\mathbb{D}_0$. ω represents angular frequency and superscripts refer to unidirectional receiver wavefields (minus for upgoing, and plus for downgoing). $\hat{R}_0^{\smile}$ and $\hat{G}_0^-$ are the reflection and transmission impulse responses of the reference state respectively, without free-surface interaction. The integration over $\partial\mathbb{D}_0$ represents a convolution product in the time domain of the downgoing wavefield with the reflection response without free-surface multiples over receivers at $\mathbf{x}_0$ on the upper boundary of the medium.

Expression 3.1 shows three terms or elements (see figure 3.1): The reference-state transmission field ($\hat{G}_0^-$), the total field ($\hat{G}^-$) and the surface-related multiples ($\hat{R}_0^{\smile}\hat{G}^+$). This last term holds implicitly the desired reflection response of the reference state at $\partial\mathbb{D}_0$, ($\hat{R}_0^{\smile}$). Note that this expression is the same as equation 23 from Wapenaar et al. (2004), although we have employed states with a slight difference on the source location and a modification in the definition of

the medium below the lower boundary. In both cases, though, the convolutional relation shows it is independent of the source being inside or outside the domain $\mathbb{D}$.

For practical use, equation 3.1 holds two unknowns: the reference reflection and transmission responses. The presence of the second unknown ($\hat{G}_0^-$) is due to the source being inside $\mathbb{D}$ for which we intend to obtain the reflection response.

The subtraction of the reference transmission to the total upgoing term yields the free-surface interaction ($\hat{G}^- - \hat{G}_0^-$). This interaction wavefield can be predicted or reconstructed by the convolution product of the downgoing wavefield with the reflection response of the reference state, over the upper boundary.

We can express relation 3.1 By discretizing the wavefields using the matrix notation for every frequency component (Berkhout, 1982):

$$-\hat{\mathbf{G}}_\mathbf{0}^- = -\hat{\mathbf{G}}^- + \hat{\mathbf{R}}_\mathbf{0}^{\smile}\hat{\mathbf{G}}^+. \tag{3.2}$$

For 2D and 3D media this equation is ill-posed hence the reflection response $\hat{\mathbf{R}}_\mathbf{0}^{\smile}$ requires regularized least-squares inversion:

$$\hat{\mathbf{R}}_\mathbf{0}^{\smile} = \left((\hat{\mathbf{G}}^- - \hat{\mathbf{G}}_\mathbf{0}^-)\{\hat{\mathbf{G}}^+\}^\dagger\right)\left(\hat{\mathbf{G}}^+\{\hat{\mathbf{G}}^+\}^\dagger + \epsilon^2\mathbf{I}\right)^{-1}, \tag{3.3}$$

where † represents transposition and complex conjugation, ϵ^2 is a frequency-independent stabilization parameter and $\mathbf{I}$ is the identity matrix. The matrix inversion is equivalent to the deconvolution of the free-surface interaction wavefield with the downgoing wavefield in the time domain over $\partial\mathbb{D}_0$; This procedure is denominated "**M**ulti-**D**imensional **D**econvolution" (**MDD**). The retrieval of the reflection response also includes, at least in principle, the evanescent waves away from $\partial\mathbb{D}_0$ and preserves the amplitude range in case of lossy media. The completeness of the result will depend on the availability of wavefield data illuminating from different angles boundary $\partial\mathbb{D}_0$. This is conditioned either by the source distribution in the subsurface and/or the scattering potential of the medium.

The estimation of the reference transmission response $\hat{G}_0^-$ is a tedious task (van der Neut et al., 2010). Depending on the transient characteristics of the passive source in the measurement state, an approximation to $\hat{G}_0^-$ can be held by time-gating the first arrivals from the passive recordings (Nakata et al., 2014):

$$\hat{\mathbf{R}}_\mathbf{0}^{\smile} \approx \left((\hat{\mathbf{G}}^- - \hat{\mathbf{G}}_{dir}^-)\{\hat{\mathbf{G}}^+\}^\dagger\right)\left(\hat{\mathbf{G}}^+\{\hat{\mathbf{G}}^+\}^\dagger + \epsilon^2\mathbf{I}\right)^{-1}, \tag{3.4}$$

where $\hat{\mathbf{G}}_{dir}^-$ stands for the direct field of the upgoing wavefield. The practicality of this approximation will depend on how strongly scattering the medium is, for the events left to be removed to the free-surface interaction quantity are left for

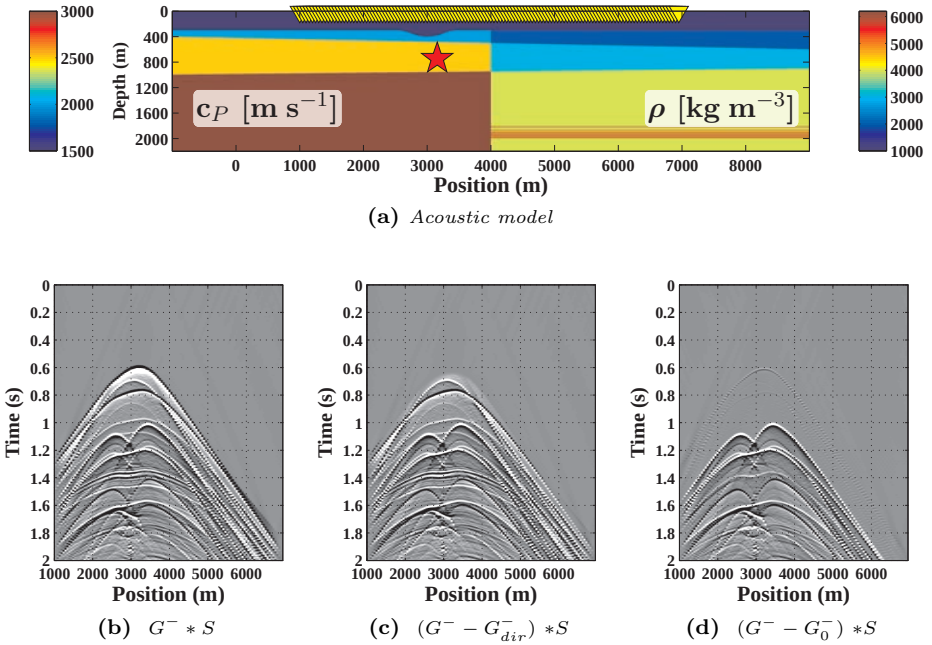

(a) *Acoustic model*

(b) $G^- * S$ **(c)** $(G^- - G^-_{dir}) * S$ **(d)** $(G^- - G^-_0) * S$

Figure 3.2: *Upgoing wavefield and the differences in approximating the free-surface interaction wavefield.* ***(a)*** *Acoustic model represented by its velocity c_P (left) and density ρ (right), with a passive source (red star) and an array of receivers at 10 m depth (yellow triangles).* ***(b)*** *Upgoing wavefield $\hat{G}$ with transient source signal $\hat{S}$.* ***(c)*** *Free-surface interaction obtained from subtracting the direct wavefield from the upgoing wavefield only, as expressed in equation 3.4 ($G^-_0 \approx G^-_{dir}$).* ***(d)****, same as in (b), using the correct reference transmission response without free surface multiples G^-_0, as required in equation 3.3. By applying the direct wave subtraction, the events present in (b) but not in (c) are left off for the inversion process to produce spurious events in the retrieved reflection response.*

the reflection response to interpret them. This means the creation of artefacts in the retrieved reflection response. Figure 3.2 shows for a passive seismic recording setting, with a transient source located inside the medium, the difference that implies the use of the direct wave approximation and the exact $\hat{G}^-_0$ term. The events removed from $\hat{G}^-$ in figure 3.2d represent the exact free-surface interaction wavefield. Should this subtraction not include all the respective events (the events that are present in figure 3.2c but not in 3.2d), it will produce an excess of events and amplitudes to be deconvolved and cause the reflection response to generate artefacts during the inversion process.

3.2.1 Results with MDD

We applied the MDD procedure of equations 3.3 and 3.4 on a 2D acoustic lossless model illustrated in figure 3.3a. This is a passive seismic configuration with transient sources inside the medium and receivers in the proximity of the free surface at the upper part. The model includes some thin layering with strong density contrast in depth, to increase the reflectivity of the medium in the subsurface. Sources are monopoles and contain a transient signal with 80 Hz maximum frequency. Receivers are located at 10 m depth and include particle velocity and pressure recordings. Wavefield decomposition is applied at the receiver level with energy-flux normalization (Wapenaar, 1998).

Results in figures 3.3b and 3.3c represent the reconstructed reflection response at the virtual source depicted with a hollow red star in figure 3.3a. These results show the differences when using MDD with the exact $\hat{G}_0^-$ term and the direct wave approximation $\hat{G}_{dir}^-$, respectively. Retrieval seems quite complete when compared to the directly modelled reflection response in figure 3.3d, due mainly to the given illumination from sources homogeneously distributed in the subsurface. A trace comparison is displayed on figure 3.3e, where waveform of the reconstructed reflection responses match the one of the reference response. However, the retrieval using the direct wave approximation shows small amplitude misfits with respect to the other two reflection responses.

As mentioned before, the incomplete estimation of the free-surface interaction wavefield leaves events, in this case the internal multiples only, that causes the inversion to produce misinterpreting artefacts in the result. Moreover, for this modelling the isolation of the direct wavefield has been sufficiently clean and easy to implement. However, in realistic scenarios where the signal of direct arrivals and multiples overlap, the time-gating procedure will be highly user-dependent and does not bring but uncertainty to the MDD method and produce more artefacts to the final result.

3.2.2 Additional passive MDD applications for one-way wavefields

MDD can ultimately be applied to retrieve the reflection response of the medium in the measurement state, this is, including its free-surface interaction (Wapenaar et al., 2008b, 2011b). In these works the representation was brought from the simplification of locating the receiver array at the free surface. Considering our configuration with receivers detached from the free-surface, and using the same notation from the previous section, the reciprocity relation of the convolution type becomes (Appendix 3.E, equation 3.42):

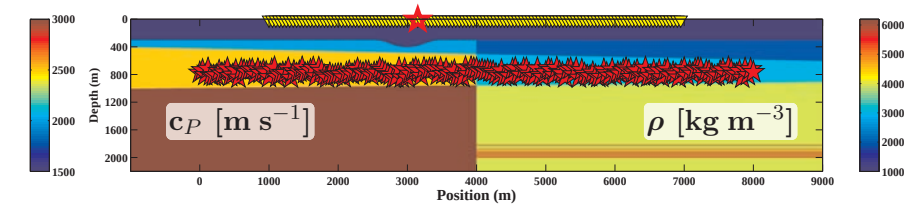

(a) *Acoustic model*

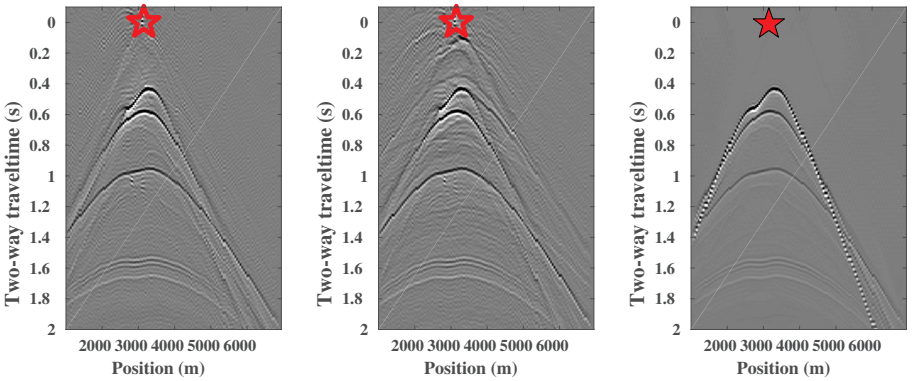

(b) $R_0^{\smile}$*-MDD with* $\hat{G}_0^-$ **(c)** $R_0^{\smile}$*-MDD with* $\hat{G}_{dir}^-$ **(d)** *Reference* $R_0^{\smile}$

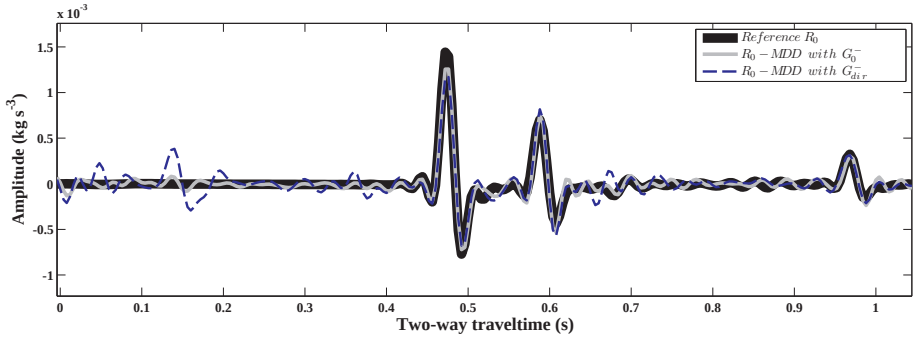

(e) *Trace comparison*

Figure 3.3: *Shot gather retrieval at* $x_0 = 3150$ *m after applying MDD with transient sources in an acoustic scenario.* ***(a)*** *Same acoustic model as in figure 3.2a, with 201 monopole sources (red stars) and 121 receivers (yellow triangles).* ***(b)*** *Retrieved reflection response* $R_0^{\smile}$ *at source location* $\boldsymbol{x}_0$ *(red hollow star in (a)), obtained using the modelled reference-state transmission response* (G_0^-)*.* ***(c)*** *Same as in (b) after using the direct wave approximation* (G_{dir}^-)*, acquired from the passive recordings.* ***(d)*** *Directly modelled reflection response.* ***(e)*** *Trace comparison of the results showed in (b), (c) and (d), at receiver location* $x_{\mathcal{A}} = 3100$ *m.*

$$\hat{G}^{-}(\mathbf{x}_{\mathcal{A}},\mathbf{x}_{\mathcal{B}},\omega)=\hat{G}_{0}^{-}(\mathbf{x}_{\mathcal{A}},\mathbf{x}_{\mathcal{B}},\omega)+\int_{\mathbf{x}_0\in\partial\mathbb{D}_0}\hat{R}^{\smile}(\mathbf{x}_{\mathcal{A}},\mathbf{x}_0,\omega)\Big\{\ldots$$
$$\ldots\int_{\mathbf{x}_0'\in\partial\mathbb{D}_0}\hat{R}^{\frown}_{\mathbb{D}',0}(\mathbf{x}_0,\mathbf{x}_0',\omega)\hat{G}_{0}^{-}(\mathbf{x}_0',\mathbf{x}_{\mathcal{B}},\omega)d^2\mathbf{x}_0'\Big\}d^2\mathbf{x}_0. \quad (3.5)$$

In equation 3.5, the reflection response $\hat{R}^{\smile}$ holds for a downgoing source wavefield and an upgoing receiver wavefield, and includes its free-surface interaction. $\hat{R}^{\frown}_{\mathbb{D}',0}$ is the reflection response of the medium above the receiver array at $\partial\mathbb{D}_0$ for an upgoing source wavefield and a downgoing receiver wavefield, as if the medium below $\partial\mathbb{D}_0$ was homogeneous.

We can represent equation 3.5 in the matrix notation and solve for the reflection response applying a regularized least-squares inversion:

$$\hat{\mathbf{R}}^{\smile}=\Big((\hat{\mathbf{G}}^{-}-\hat{\mathbf{G}}_{\mathbf{0}}^{-})\{\hat{\mathbf{R}}^{\frown}_{\mathbb{D}',\mathbf{0}}\hat{\mathbf{G}}_{\mathbf{0}}^{-}\}^{\dagger}\Big)\Big(\hat{\mathbf{R}}^{\frown}_{\mathbb{D}',\mathbf{0}}\hat{\mathbf{G}}_{\mathbf{0}}^{-}\{\hat{\mathbf{R}}^{\frown}_{\mathbb{D}',\mathbf{0}}\hat{\mathbf{G}}_{\mathbf{0}}^{-}\}^{\dagger}+\epsilon^2\mathbf{I}\Big)^{-1}. \quad (3.6)$$

This expression is a generalization to the implicit relation shown in Wapenaar et al. (2004). Under the condition of the upper boundary $\partial\mathbb{D}_0$ being at the free-surface, we obtain a similar relation to equation 3.1:

$$\hat{\mathbf{R}}^{\smile}=\Big((\hat{\mathbf{G}}_{\mathbf{0}}^{-}-\hat{\mathbf{G}}^{-})\{\hat{\mathbf{G}}_{\mathbf{0}}^{-}\}^{\dagger}\Big)\Big(\hat{\mathbf{G}}_{\mathbf{0}}^{-}\{\hat{\mathbf{G}}_{\mathbf{0}}^{-}\}^{\dagger}+\epsilon^2\mathbf{I}\Big)^{-1}. \quad (3.7)$$

However, in the case of buried acquisition arrays one is obliged to construct additionally $\hat{R}^{\frown}_{\mathbb{D}',0}$. This is possible by means of reciprocity relations and the available passive recordings (Appendix 3.D.1, equation 3.33):

$$\hat{G}^{+}(\mathbf{x}_0,\mathbf{x}_{\mathcal{B}},\omega)=\int_{\mathbf{x}_0'\in\partial\mathbb{D}_0}\hat{R}^{\frown}_{\mathbb{D}',0}(\mathbf{x}_0,\mathbf{x}_0',\omega)\hat{G}^{-}(\mathbf{x}_0',\mathbf{x}_{\mathcal{B}},\omega)d^2\mathbf{x}_0', \quad (3.8)$$

and (Appendix 3.D.2, equation 3.36):

$$\{\hat{G}^{-}(\mathbf{x}_0,\mathbf{x}_{\mathcal{B}},\omega)\}^{*}\approx\int_{\mathbf{x}_0'\in\partial\mathbb{D}_0}\hat{R}^{\frown}_{\mathbb{D}',0}(\mathbf{x}_0',\mathbf{x}_0,\omega)\{\hat{G}^{+}(\mathbf{x}_0',\mathbf{x}_{\mathcal{B}},\omega)\}^{*}d^2\mathbf{x}_0'. \quad (3.9)$$

where $\{\}^{*}$ stands for complex conjugation. One can achieve the estimation of this reflection response employing the MDD procedure, using the discretization of the wavefields and combining the respective normal equations into a regularized least-squares inversion:

$$\hat{\mathbf{R}}^{\curvearrowleft}_{\mathbb{D}',\mathbf{0}} = \left(\hat{\mathbf{G}}^{+}\{\hat{\mathbf{G}}^{-}\}^{\dagger} + \{\hat{\mathbf{G}}^{-}\}^{*}\{\hat{\mathbf{G}}^{+}\}^{t}\right)\left(\hat{\mathbf{G}}^{-}\{\hat{\mathbf{G}}^{-}\}^{\dagger} + \{\hat{\mathbf{G}}^{+}\}^{*}\{\hat{\mathbf{G}}^{+}\}^{t} + \epsilon^{2}\mathbf{I}\right)^{-1}. \quad (3.10)$$

where $\{\}^{t}$ stands for matrix transposition. When the subsurface information is not sufficient to obtain $\hat{R}^{\curvearrowleft}_{\mathbb{D}',0}$ by MDD, an adequate approximation to it in acoustic media is by means of wavefield extrapolation, assuming knowledge of the near surface is available (acoustic velocity c_P):

$$\hat{R}^{\curvearrowleft}_{\mathbb{D}',0}(\mathbf{x}_0,\mathbf{x}'_0,\omega) \approx \int_{\mathbf{x}_{\mathcal{FS}}} \hat{W}^{+}(\mathbf{x}_0,\mathbf{x}_{\mathcal{FS}},\omega) r^{-}(\mathbf{x}_{\mathcal{FS}}) \hat{W}^{-}(\mathbf{x}_{\mathcal{FS}},\mathbf{x}'_0,\omega) d^2\mathbf{x}_{\mathcal{FS}}, \quad (3.11)$$

where r^{-} is the free surface reflection coefficient and $\hat{W}^{\pm}$ corresponds to the downgoing/upgoing wavefield extrapolation operator $\tilde{W}^{\pm} = e^{-jk_3 x_{3,\mathbf{x}_0}}$. The locations $\mathbf{x}_0$ and $\mathbf{x}'_0$ belong to $\partial\mathbb{D}_0$ while $\mathbf{x}_{\mathcal{FS}}$ is situated at the free surface. $x_{3,\mathbf{x}_0}$ is the depth level difference of $\mathbf{x}_0/\mathbf{x}'_0$ with respect to the free surface and k_3 is the vertical wavenumber $\left(k_3 = \sqrt{(\frac{\omega}{c_P})^2 - k_1^2 - k_2^2}\right)$.

Since the term $\hat{G}_0^{-}$ is unknown anyway, the same approximation can be made by extracting the direct wavefields of both up- and downg-going wavefields, depending on their transient behaviour and on how strongly scattering the medium is:

$$\hat{\mathbf{R}}^{\curvearrowright} \approx \left((\hat{\mathbf{G}}^{-} - \hat{\mathbf{G}}^{-}_{dir})\{\hat{\mathbf{G}}^{+}_{dir}\}^{\dagger}\right)\left(\hat{\mathbf{G}}^{+}_{dir}\{\hat{\mathbf{G}}^{+}_{dir}\}^{\dagger} + \epsilon^{2}\mathbf{I}\right)^{-1}. \quad (3.12)$$

Results of this MDD are shown in figure 3.4 showing the same configuration and source location as in figure 3.3. Result in figure 3.4b was retrieved using wavefield extrapolators to reproduce the effect of $\hat{R}^{\curvearrowleft}_{\mathbb{D}',0}$, profiting from the medium being homogeneous along and between the receiver array and the free-surface. As for the result in figure 3.4c, the direct wave extraction was applied from the decomposed- downgoing wavefield. The reference response $\hat{R}^{\curvearrowright}$ in figure 3.4d shows both results seem quite complete. The amplitude estimation seems satisfactory accurate regarding the trace comparison in figure 3.4e.

In figure 3.5 we compare how they differ the operator elements in MDD for both equations 3.3 and 3.6, and their approximations using the direct wavefield, equations 3.4 and 3.12.

Although using the same wavefield quantities, the sensitivity to errors when using the direct wavefield approximation is not the same on both MDD applications. The $\hat{R}^{\curvearrowright}$-MDD shows a more critical difference when using the direct

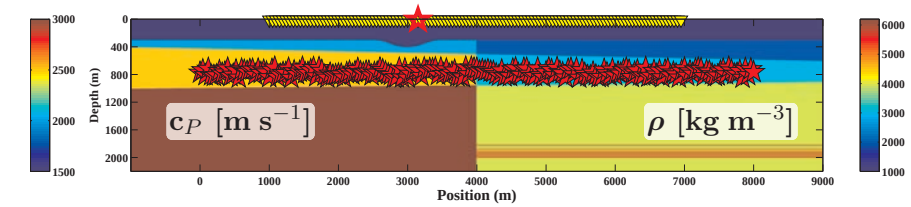

(a) *Acoustic model*

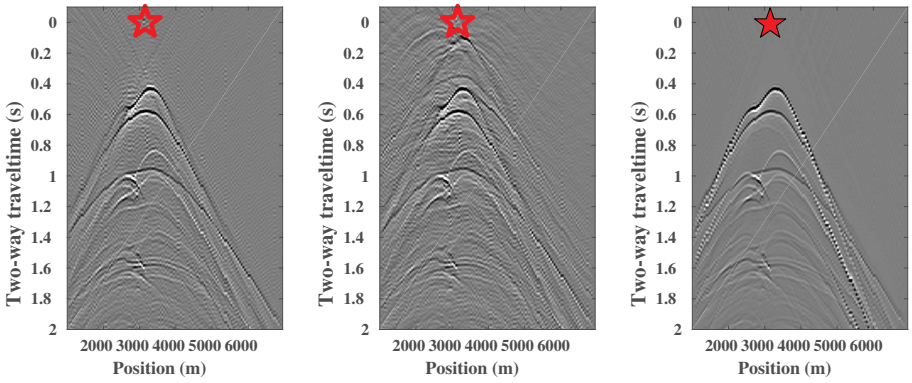

(b) $\check{R}$*-MDD with* $\hat{G}_0^-$ **(c)** $\check{R}$*-MDD with* $\hat{G}_{dir}^-$ **(d)** *Reference* $\check{R}$

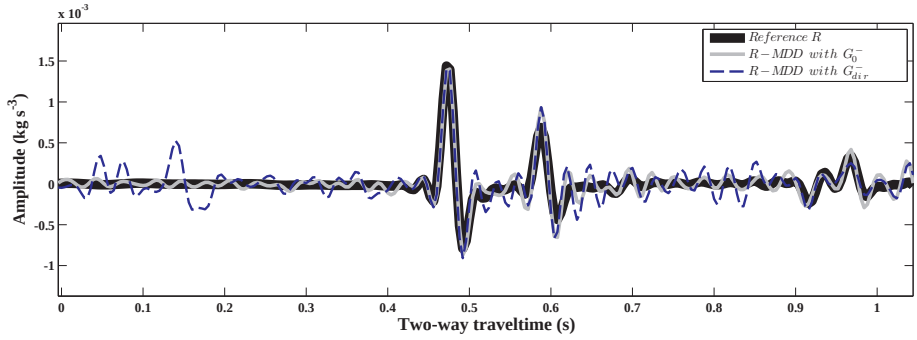

(e) *Trace comparison*

Figure 3.4: *Shot gather retrieval at* $x_0 = 3150\ m$ *after applying MDD with transient sources in an acoustic scenario.* ***(a)*** *Same acoustic model as in figure 3.2a, with 201 monopole sources (red stars) and 121 receivers (yellow triangles).* ***(b)*** *Retrieved reflection response* $\check{R}$ *at* $\boldsymbol{x}_{\mathcal{A}}$ *(red hollow star in (a)), obtained using the modelled reference-state transmission response* (G_0^-)*.* ***(c)*** *Same as in (b) after using the direct wave approximation* (G_{dir}^-)*, acquired from the passive recordings.* ***(d)*** *Directly modelled reflection response.* ***(e)*** *Trace comparison of the results showed in (b), (c) and (d), at receiver location* $x_{\mathcal{A}} = 3100\ m$*.*

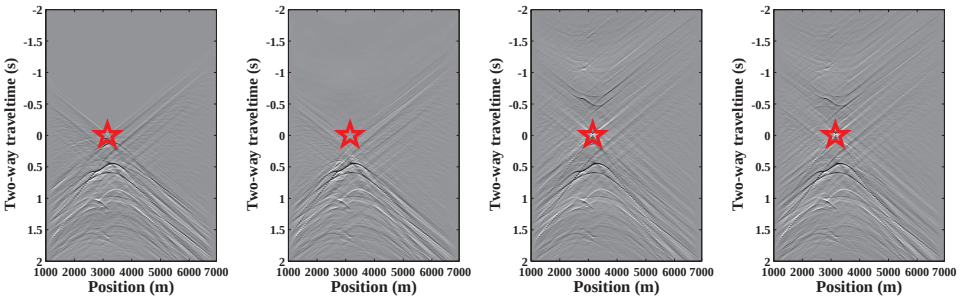

(a) $\left(\hat{\mathbf{G}}^{-} - \hat{\mathbf{G}}^{-}_{dir}\right)\left\{\hat{\mathbf{G}}^{+}_{dir}\right\}^{\dagger}$ **(b)** $\left(\hat{\mathbf{G}}^{-} - \hat{\mathbf{G}}^{-}_{\mathbf{0}}\right)\left\{\hat{\mathbf{R}}^{\frown}_{\mathbb{D}',\mathbf{0}}\hat{\mathbf{G}}^{-}_{\mathbf{0}}\right\}^{\dagger}$ **(c)** $\left(\hat{\mathbf{G}}^{-} - \hat{\mathbf{G}}^{-}_{dir}\right)\left\{\hat{\mathbf{G}}^{+}\right\}^{\dagger}$ **(d)** $\left(\hat{\mathbf{G}}^{-} - \hat{\mathbf{G}}^{-}_{\mathbf{0}}\right)\left\{\hat{\mathbf{G}}^{+}\right\}^{\dagger}$

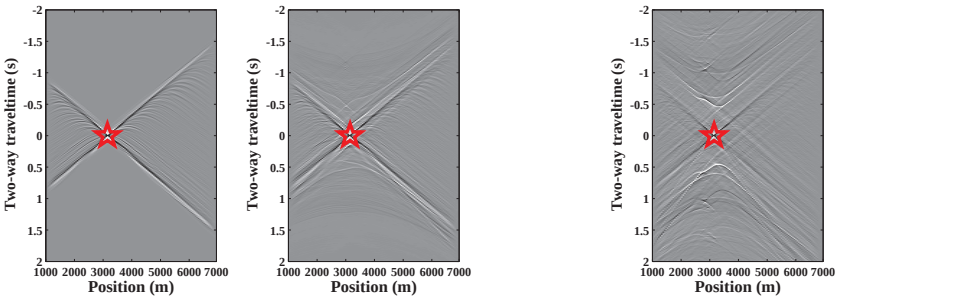

(e) $\hat{\mathbf{G}}^{+}_{dir}\left\{\hat{\mathbf{G}}^{+}_{dir}\right\}^{\dagger}$ **(f)** $\hat{\mathbf{R}}^{\frown}_{\mathbb{D}',\mathbf{0}}\hat{\mathbf{G}}^{-}_{\mathbf{0}}\left\{\hat{\mathbf{R}}^{\frown}_{\mathbb{D}',\mathbf{0}}\hat{\mathbf{G}}^{-}_{\mathbf{0}}\right\}^{\dagger}$ **(g)** $\hat{\mathbf{G}}^{+}\left\{\hat{\mathbf{G}}^{+}\right\}^{\dagger}$

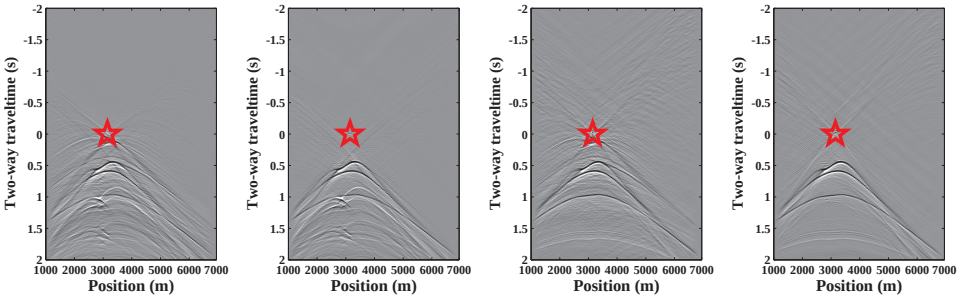

(h) $\mathbf{R}^{\smile}$*-MDD with* $\hat{\mathbf{G}}^{-}_{dir}$ **(i)** $\mathbf{R}^{\smile}$*-MDD with* $\hat{\mathbf{G}}^{-}_{\mathbf{0}}$ **(j)** $\mathbf{R}^{\smile}_{\mathbf{0}}$*-MDD with* $\hat{\mathbf{G}}^{-}_{dir}$ **(k)** $\mathbf{R}^{\smile}_{\mathbf{0}}$*-MDD with* $\hat{\mathbf{G}}^{-}_{\mathbf{0}}$

Figure 3.5: *Comparison between slices of the different functions in the MDD methods.* ***(a)*** *and* ***(b)****,* $R^{\smile}$*-MDD correlation functions with and without approximation, respectively.* ***(c)*** *and* ***(d)****, same as in (a) and (b) for* $R^{\smile}_{0}$*-MDD.* ***(e)*** *and* ***(f)****, the respective* $R^{\smile}$*-MDD point-spread functions with the direct wave approximation and the exact approach.* ***(g)****,* $R^{\smile}_{0}$*-MDD point-spread function.* ***(h)*** *and* ***(i)****,* $R^{\smile}$*-MDD result with the direct wave approximation and without, respectively.* ***(j)*** *and* ***(k)****, same as in (h) and (i) for* $R^{\smile}_{0}$*-MDD.*

wavefield approximation in the correlation function (figure 3.5a) and the point-spread function (3.5e) with respect to employing the exact reference transmission term (figures 3.5b and 3.5f). This is not the case for the $\hat{R}_0^{\cup}$-MDD, where the correlation function shows insignificant changes for their approximated (figure 3.5c) and exact expressions (figure 3.5d). Furthermore, the approximation is not required in the estimation of the point-spread function (figure 3.5g). We see in equation 3.6 the additional use of terms from the reference state which required to be approximated only increases the uncertainty in the correlation and point-spread functions. The result for $\hat{R}^{\cup}$-MDD (figure 3.5h) shows more prominent spurious events than the ones with $\hat{R}_0^{\cup}$-MDD (figure 3.5j), and deviate from their ideally retrieved reflection responses (figures 3.5i and 3.5k, respectively). $\hat{R}^{\cup}$-MDD seemed largely more sensitive to the regularization applied and its result required a stabilization one order of magnitude larger than with the result of $\hat{R}_0^{\cup}$-MDD. This is because, given the same subsurface information, when the reconstruction of the additional free-surface events are desired the inversion is less well constrained.

Both representations 3.1 and 3.5 were shown in Wapenaar et al. (2004) for arrays at the surface, and later implemented using MDD by means of the direct wavefield approximation (Wapenaar et al., 2008b; Nakata et al., 2014). However, research following the development of the $\hat{R}^{\cup}$-MDD approach initially for the point-spread function seemed easier to stabilize. Although containing fewer notches in the frequency spectrum of the point-spread function, these features seem to be more critical for stabilization with respect to the relatively larger amount of them in the $\hat{R}_0^{\cup}$-MDD point-spread function.

The result obtained from equation 3.12 does not differ much from the correlation result, including artefacts due to the cross-talk, but improves in certain aspects: The amplitude variations with respect to angle/ray-parameter produced by the heterogeneous illumination are balanced by the point-spread function in figure 3.5e (distributed in space); In this case, a directionally uniform cross-like point-spread function is due to the homogeneous source distribution in the subsurface. The power spectrum of the sources' signals, either transient or noisy, is present in the point-spread function and is responsible of the source signal deconvolution of the correlation function.

The figure in 3.5e resembles the approach that was proposed in van der Neut et al. (2010), where they applied $\hat{R}^{\cup}$-MDD with noise sources. In the situation of noise sources acting simultaneously the estimation of the direct wavefield by time gating the recordings cannot be made. They estimated instead the product $\hat{G}_0^{-}\{\hat{G}_0^{-}\}^{\dagger}$ from the correlation function, by time-gating the correlation gather around intercept time $t = 0\ s$. By doing such the autocorrelations of the internal multiples are also included in the inverse matrix and also contribute in the directional balancing during the inversion process. This is not the case with transient sources, as shown in the result in figure 3.5f. Nevertheless, in both cases (ei-

ther with transient or noise signal), when the direct wave approximation is made, MDD is not completely honoured and the point-spread function is limited to be a directional balancing filter for the irregularity in the source distribution, and the frequency spectra of the sources.

We may draw some conclusions about the different MDD processes. MDD can be applied to retrieve $\hat{R}^{\smile}$ and $\hat{R}_0^{\smile}$ using one-way wavefields from passive recordings. In both cases, the term $\hat{G}_0^{-}$ is required to be estimated, extracting the direct wavefield from the full fields for instance. In case of noise sources, an approximation can be made after correlation. The retrieval of $\hat{R}^{\smile}$ can practically only be implemented at the free-surface. Still, the direct wave approximation brings larger uncertainty to the process. $\hat{R}_0^{\smile}$-MDD does not require to have the receivers at the free surface. The inverse operator is easy to construct without any approximation needed. The uncertainties brought by the direct wave approximation are significantly smaller than for the previous case.

3.3 Ambient-noise seismic interferometry (ANSI)

In this section we present the application of $R_0^{\smile}$-MDD in 2D synthetic ambient-noise data and compare its results with other ambient-noise seismic interferometry (ANSI) methods. These methods achieve to work with ambient-seismic noise where the estimation of the reference-state transmission responses nor the direct arrivals are possible. Most of ANSI methods are based on crosscorrelation, keep no control of the irregularities related to their boundary integrals and require further processing to compensate overillumination artefacts and amplitude corrections. Yet, there are inversion-based ANSI methods that can mitigate most of these problems, but still depend on the frequency content of the signals and a stable inversion. These methods are conditioned to characteristics of the sources and their distribution in the subsurface, which make their assumptions unlikely to be met in real scenarios. Regarding mainly the sensitivity of the passive source setup, a broad range of 2D acoustic modelling experiments with SI by crosscorrelation is shown in Thorbecke & Draganov (2011). The goal in this section is to generate a more realistic ambient-noise dataset that infringes the assumptions most ANSI methods rely on, in order to compare the robustness of our new method with respect to other ambient-noise approaches.

3.3.1 Conventional ANSI methods

Conventional ANSI methods are the passive seismic interferometry methods that use body-waves ambient-noise recordings, this is, transmission responses with long source signals which disable the estimation of the direct arrival, to retrieve the reflection response of the medium with free-surface interaction. We define three conventional ANSI methods: crosscorrelation (CC), crosscoherence (CCh) and $R^{\smile}$-MDD. In our analysis, we apply these methods to reconstruct the reflection

response from the synthetic ambient-noise recordings. In the purpose of improving the results from the crosscorrelation and crosscoherence methods, these profit from reciprocity constraints (summing causal and time-reversed parts together) and illumination diagnosis (Almagro Vidal et al., 2014) in order to compensate for the uneven illumination. In order to apply crosscorrelation to the ambient-noise recordings, we adapted the method to work with noise panels together with illumination diagnosis using the equation:

$$\mathrm{CC}(\mathbf{x}_{\mathcal{A}}, \mathbf{x}_0) \rightarrow \hat{\mathbf{R}}^{\smile}_{CC} = \sum_i \mathbf{W}_i \left(\hat{\mathbf{P}}_i^{-} \left\{ \hat{\mathbf{P}}_i^{+} \right\}^{\dagger} + \left\{ \hat{\mathbf{P}}_i^{+} \right\}^{*} \left\{ \hat{\mathbf{P}}_i^{-} \right\}^{t} \right), \tag{3.13}$$

where $\hat{\mathbf{P}}_i^{\pm}$ contains the discretized version of $\hat{P}_i^{\pm}(\mathbf{x}_{\mathcal{A}}) = \left\langle \hat{G}^{\pm}(\mathbf{x}_{\mathcal{A}}, \mathbf{x}_{\mathcal{B}}^k, \omega) \hat{S}^k(\omega) \right\rangle_i$. This is the Fourier transform of the time-window recording with the ensemble of random-source transmission responses $\hat{G}^{\pm}$ with their respective noise wavelets $\hat{S}^k$ at the receiver location $\mathbf{x}_{\mathcal{A}}$. $\mathbf{x}_{\mathcal{B}}^k$ represents the locations of the k-sources acting during the noise panel i, $\mathbf{W}_i$ stands for the vector of weights at the virtual-source location $\mathbf{x}_0$ against the ray-parameter, $W_i(\mathbf{p}_i, \mathbf{x}_0)$. Illumination diagnosis takes into account the ray-parameter distribution $\mathbf{p}_i$ of each noise panel with respect to each virtual source $\mathbf{x}_0$, in order to compose noise-panel weights W_i to balance out the illumination of the final crosscorrelation result (CC). As to the crosscoherence method (CCh), we employed a similar equation:

$$\mathrm{CCh}(\mathbf{x}_{\mathcal{A}}, \mathbf{x}_0) \rightarrow \hat{\mathbf{R}}^{\smile}_{CCh} = \sum_i \mathbf{W}_i \frac{\left(\hat{\mathbf{P}}_i^{-} \left\{ \hat{\mathbf{P}}_i^{+} \right\}^{\dagger} + \left\{ \hat{\mathbf{P}}_i^{+} \right\}^{*} \left\{ \hat{\mathbf{P}}_i^{-} \right\}^{t} \right)}{\left(|\hat{\mathbf{P}}_i^{-}||\hat{\mathbf{P}}_i^{+}|^t + |\hat{\mathbf{P}}_i^{+}||\hat{\mathbf{P}}_i^{-}|^t \right)}, \tag{3.14}$$

where $|\hat{\mathbf{P}}_i^{+}|$ is the discretized version of $|\hat{P}_i^{-}(\mathbf{x}_{\mathcal{A}})|$. The only difference with respect to the crosscorrelation method is the amplitude normalization by the respective spectra of each of the receivers involved in the correlation. Through this procedure the heterogeneous frequency spectra of the signals are whitened and the noise-source signature is removed.

The inversion-based approach is the ANSI $R^{\smile}$-MDD method and is presented in van der Neut et al. (2010). In this method we run our approximations on the correlation functions and to that purpose we design the following time windows: Θ_1, selecting only the section of the point-spread function around correlation time $t = 0$ s, and Θ_0 which includes the causal events and excludes the section containing the point-spread function and the acausal events. The regularized least-squares implementation of the ANSI $R^{\smile}$-MDD method is presented as:

$$\mathrm{R}^{\smile}\text{-MDD}(\mathbf{x}_{\mathcal{A}},\mathbf{x}_0)\rightarrow\hat{\mathbf{R}}^{\smile}_{MDD}\approx \left(\hat{\mathbf{\Theta}}_{\mathbf{0}}*\left[\hat{\mathbf{P}}_i^{-}\{\hat{\mathbf{P}}_i^{+}\}^{\dagger}\right]\right)\left(\hat{\mathbf{\Theta}}_{\mathbf{1}}*\left[\hat{\mathbf{P}}_i^{+}\{\hat{\mathbf{P}}_i^{+}\}^{\dagger}\right]+\epsilon^2\mathbf{I}\right)^{-1}, \quad (3.15)$$

where $\hat{\mathbf{\Theta}}_{\mathbf{1}}*\left[...\right]$ is the convolution product in the frequency domain standing for the effect of time-gating with the corresponding time window $\mathbf{\Theta_1}$. In this method, both the correlation function and point-spread function are approximated using these time windows (Wapenaar et al., 2011b).

3.3.2 ANSI $R_0^{\smile}$-MDD

All the conventional ANSI methods retrieve the reflection response with free-surface interaction $R^{\smile}$. For SI methods retrieving the reference-state reflection response $R_0^{\smile}$ an estimation of the direct-arrival matrix can be approximated after their correlation product using the same procedure as described for $R^{\smile}$-MDD in equation 3.15. This is presented as:

$$\hat{\mathbf{P}}^{-}_{i,dir}\{\hat{\mathbf{P}}_i^{+}\}^{\dagger}\approx\alpha\,\hat{\mathbf{\Theta}}_{\mathbf{2}}*\left[\hat{\mathbf{P}}_i^{-}\{\hat{\mathbf{P}}_i^{+}\}^{\dagger}\right], \quad (3.16)$$

where $\hat{\mathbf{\Theta}}_{\mathbf{2}}*\left[...\right]$ is the corresponding operation of time-gating with the time function Θ_2, which includes the acausal events together with the section around the point-spread function. α is a scaling factor that stands for the energy difference of the reference transmission response with respect to the total field in the measurement state. Hence, we can rewrite the ANSI $R_0^{\smile}$-MDD, based on equation 3.4, as:

$$\mathrm{R}_0^{\smile}\text{-MDD}(\mathbf{x}_{\mathcal{A}},\mathbf{x}_0)\rightarrow\hat{\mathbf{R}}^{\smile}_{\mathbf{0},MDD}\approx \left(\hat{\mathbf{P}}_i^{-}\{\hat{\mathbf{P}}_i^{+}\}^{\dagger}-\alpha\,\hat{\mathbf{\Theta}}_{\mathbf{2}}*\left[\hat{\mathbf{P}}_i^{-}\{\hat{\mathbf{P}}_i^{+}\}^{\dagger}\right]\right)\left(\hat{\mathbf{P}}_i^{+}\{\hat{\mathbf{P}}_i^{+}\}^{\dagger}+\epsilon^2\mathbf{I}\right)^{-1}, \quad (3.17)$$

which preserves the construction of the point-spread function free of approximations. Unlike ANSI $R^{\smile}$-MDD, the use of an exactly reconstructed point-spread function connotes stability advantages in the retrieval process.

3.3.3 Results with acoustic ambient noise

We present the application on 2D acoustic and elastic scenarios. The retrieval of the reflection response of the medium is obtained from a horizontal passive

acquisition array located in the near surface. We modelled 52 minutes of noise on the acoustic model presented in figure 3.6a. It is an heterogeneous 2D model based on the geological setting in the North of the Netherlands (Duin et al., 2006). Recordings are acquired by 221 multicomponent (pressure and vertical particle velocity) receivers, with 50 m of space sampling and located at 10 m depth from the surface.

Regarding the ambient-noise sources, there are 421 source locations at different depths in the subsurface and effectively surrounding the acquisition array. We employed a total of 1237 sources, hence reoccurring sources in certain locations more than others. Areas of high occurrence count between 30 and 40 times, while low occurrence areas count only once. All sources are dipoles but each one displays random source orientation. All source signals are uncorrelated to any other but contain the same strength. Every source signal has a random length varying from 4 s to 19 s. Sources are blended, turning active every 2.5 s at random, according to the predefined source-location occurrence. In addition, each source signal contains an independent frequency band. The distribution of the maximum frequency in the spectra of all the 1237 sources ranges from 3 Hz to 40 Hz.

In figure 3.6a, receivers are represented by yellow triangles while sources are defined by arrows. Each arrow is situated at the source reoccurring position and its direction is the positive dipole orientation of the last source to have occurred at that location. The size of the arrow is proportional to the total occurrence of sources at that position. The infill colour represents the maximum frequency content of the last source that occurred at that location (following a continuous colour scale from light yellow -for the highest maximum frequency- to black -for the lowest-). The uneven size of the arrows together with their random orientation and different colour infill show the irregular illumination characteristics of the noise produced.

The way to proceed with the noise consists of splitting the recordings in 32 s long windows, with an overlapping margin of 27 s between consecutive windows. Each of these windows represents a noise panel. In the acoustic scenario, the definition of the noise-panel length goes according to an optimal combination of signal correlation length, proper illumination balancing and desired maximum depth of exploration. We applied power-flux normalized one-way wavefield decomposition (Wapenaar, 1998) onto the respective noise-panel recordings, vertical particle velocity and pressure. In realistic scenarios, sensors for particle velocity and pressure differ in their signal sensitivity and further processing is required. An alternative is to apply the power-flux normalized one-way wavefield decomposition used in Grobbe et al. (2013) on the recording of either one of them, geophone or hydrophone, and avoid their respective calibration.

Acoustic results are shown in figure 3.6. We tested different amounts of noise employed, to observe the evolution of the retrieved result as more data gets available. Figures 3.6c, 3.6d, 3.6e and 3.6f show the retrieval employing the same first

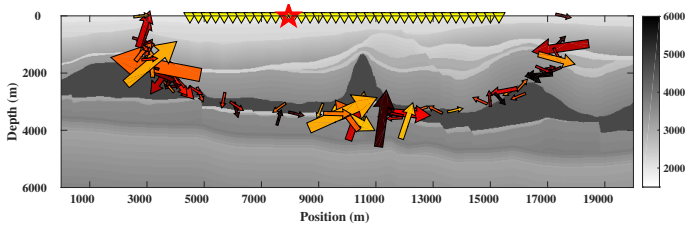

(a) *P-wave velocity model*

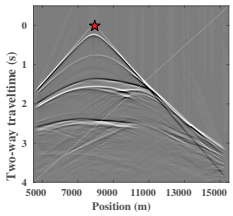

(b) *Reference* $R_0^{\smile}$

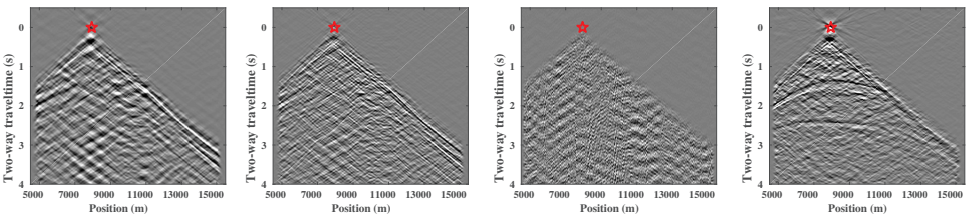

(c) *2 min CC* **(d)** *2 min CCh* **(e)** *2 min* $R^{\smile}$*-MDD* **(f)** *2 min* $R_0^{\smile}$*-MDD*

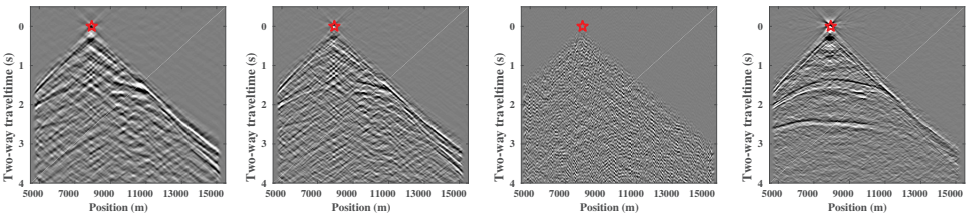

(g) *5 min CC* **(h)** *5 min CCh* **(i)** *5 min* $R^{\smile}$*-MDD* **(j)** *5 min* $R_0^{\smile}$*-MDD*

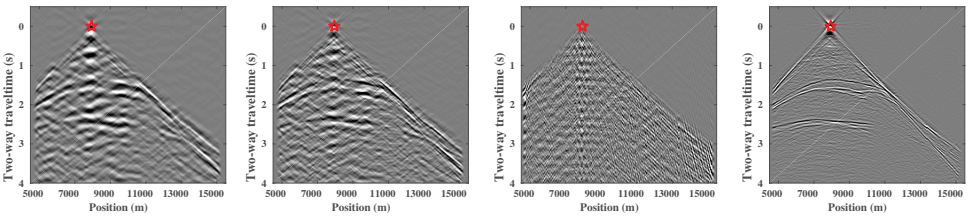

(k) *52 min CC* **(l)** *52 min CCh* **(m)** *52 min* $R^{\smile}$*-MDD* **(n)** *52 min* $R_0^{\smile}$*-MDD*

Figure 3.6: *Results of different ANSI methods with acoustic ambient noise.* ***(a)*** *P-wave velocity model, with dipole noise sources with random spectrum, random orientation and irregular occurrence.* ***(b)*** *Directly modelled reflection response for an active source at* $x_0 = 7950$ *m (the red open star in (a)).* ***(c)***, ***(d)***, ***(e)*** *and* ***(f)*** *Retrieved virtual common-source gather at the same location using 2 minutes of noise, using crosscorrelation (CC) (c), crosscoherence (CCh) (d),* $R^{\smile}$*-MDD (e) and* $R_0^{\smile}$*-MDD (f).* ***(g)***, ***(h)***, ***(i)*** *and* ***(j)*** *Same as in (c), (d), (e) and (f), after 5 mintues of noise.* ***(k)***, ***(l)***, ***(m)*** *and* ***(n)*** *Retrieved results after 52 minutes of noise.*

two minutes of noise, using ANSI by CC, CCh, $R^{\cup}$-MDD and $R_0^{\cup}$-MDD, respectively; figures 3.6g, 3.6h, 3.6i and 3.6j are the equivalent results after five minutes of noise; finally, figures 3.6k, 3.6l, 3.6m and 3.6n represent the final result after the fifty-two minutes of total noise.

On these results, we observe the inconsistency in the crosscorrelation and crosscoherence methods despite the aid of illumination diagnosis and reciprocity. These additional processes helped CC and CCh to balance out retrieved features caused by the heterogeneous source location and occurrence. If a comparison is made with the reference response in figure 3.6b, we see that despite the increasing amount of information employed the results do not converge to the desired retrieval, besides the improvement attributed to reciprocity constraints and illumination diagnosis. This is due to the dipole nature of sources and to the inefficient interferometric integration of source-signals that do not share the same frequency content. This was the intention of the synthetic dataset, which aimed to approach a realistic scenario and breaking the conditions under which CC and CCh are supposed to be applicable with ambient noise.

The results using the ANSI MDD methods show very different results. During the inversion process, the reflection result is solved at each frequency component with the available sources contributing at that specific frequency, and compensating in addition for the uneven illumination. $R^{\cup}$-MDD shows a very unstable result. This is mainly due to the operation of inverting the point-spread function approximation in equation 3.15. On the other hand, $R_0^{\cup}$-MDD manages to retrieve a better result than the previous ones. Unlike the result in figure 3.6n, the evolution in time toward the results displayed in figures 3.6k, 3.6l and 3.6m shows that the additional use of data merely brings additional information. The diversity of frequency spectra, the random orientation in the source radiation and the variety of occurrence of the different noise sources make these three last results to scarcely improve their SNR.

3.3.4 Elastic ambient-noise recordings

For the elastodynamic 2D situation we modelled the noise with exactly the same model geometry and receiver configuration as in the acoustic scenario. We employed the same amount of sources with the same source signal characteristics, frequency content variety, dipole nature, random orientation, and heterogeneous occurrence.

In this case, wavefield vectors $\hat{\mathbf{G}}^{\pm}$ are subdivided as (Wapenaar et al., 2011b):

$$\hat{\mathbf{G}}^{\pm} = \begin{pmatrix} \hat{\mathbf{\Phi}}^{\pm} \\ \hat{\mathbf{\Psi}}^{\pm} \end{pmatrix} \tag{3.18}$$

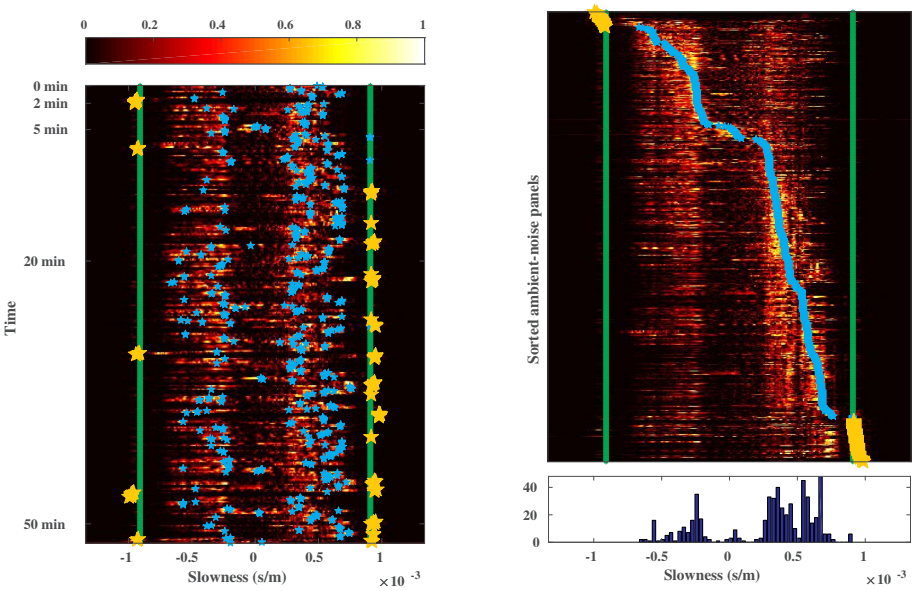

(a) *Illumination record* **(b)** *Illumination diagnosis*

Figure 3.7: *Illumination record applied on the synthetic elastic dataset, split in* 32 *s long windows, at virtual source location* $x_0 = 7950$ *m. Amplitudes are normalized. Noise panels with dominant surface waves are depicted by a yellow star at the dominant ray-parameter for that specific panel. Body-wave dominated panels are displayed with a blue star at the main ray-parameter. Noise panel discrimination is based upon definition of a slowness threshold (vertical green lines,* $p = 9\ 10^{-4} s\ m^{-1}$*) to separate surface-wave dominated panels from body-wave dominated ones.* ***(b)*** *Illumination diagram obtained from sorting the noise panels in (a). Histograms of the main ray-parameters at the body-wave dominant noise panels are used to calculate noise-panel weights* $W_i(\boldsymbol{p}_i, \boldsymbol{x}_0)$ *used in the acoustic and elastic applications of SI by CC and CCh. The dominant ray-parameter histogram is shown below the illumination diagram.*

where $\hat{\mathbf{\Phi}}$ and $\hat{\mathbf{\Psi}}$ stand for the compressional- and shear-, power flux-normalized wavefields, respectively. The term $\hat{\mathbf{R}}_{\mathbf{0}}^{\smile}$ can then be written as:

$$\hat{\mathbf{R}}_{\mathbf{0}}^{\smile} = \begin{pmatrix} \hat{\mathbf{R}}_{\mathbf{0}}^{\mathbf{\Phi},\mathbf{\Phi}\smile} & \hat{\mathbf{R}}_{\mathbf{0}}^{\mathbf{\Phi},\mathbf{\Psi}\smile} \\ \hat{\mathbf{R}}_{\mathbf{0}}^{\mathbf{\Psi},\mathbf{\Phi}\smile} & \hat{\mathbf{R}}_{\mathbf{0}}^{\mathbf{\Psi},\mathbf{\Psi}\smile} \end{pmatrix}, \tag{3.19}$$

where $\hat{R}_0^{\Psi,\Phi\smile}$, is the reflection response of the medium in $\mathbb{D}$ without free-surface

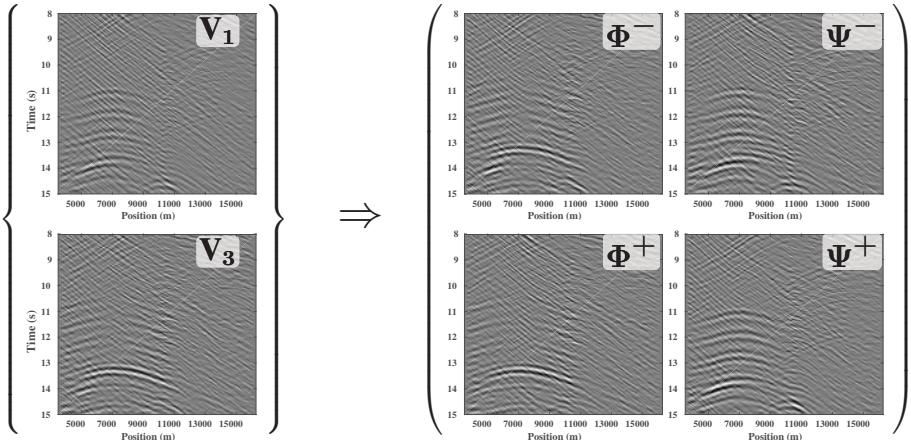

Figure 3.8: *Use of the power-flux normalized wavefield decomposition to a body-wave dominated noise panel. Particle velocity recordings (V_1 and V_3) of elastic ambient noise serve as input for the decomposed potential wavefields: Compressional down/upgoing ($\Phi^{\pm}$) and shear down/upgoing ($\Psi^{\pm}$) wavefield potentials.*

interaction in terms of a downgoing Φ-type wavefield at the source position and an upgoing Ψ-type wavefield at the receiver location. An analogous matrix structure will be used for $\hat{\mathbf{R}}^{\cup}$ for the crosscorrelation, crosscoherence and the corresponding MDD results, with their respective free-surface interaction.

The synthetic noise recordings contain the same characteristics described in the acoustic scenario. The acquisition array consist of 512 receivers with 25 m spacing. As in the acoustic scenario, the long recordings are split in several overlapping noise panels of 21 s length. Since the source locations effectively surround the acquisition array, the elastodynamic medium causes those sources located at or near the free surface to produce surface waves which will be dominating in our recordings over the other waveforms. The presence of surface waves disturbs the retrieval of reflections in $R^{\cup}$-MDD, $R_0^{\cup}$-MDD and CCh, and shrinks in amplitude the reflection response estimate in CC. To address this issue we employ the illumination diagnosis at the edges of the acquisition array over the recordings to discriminate panels for further processing: If the noise panel turns out to be dominated by body waves, it is accepted for wavefield decomposition and ANSI processing. Noise panels with surface waves are, on the other hand, discarded (see figure 3.7).

The next processing step requires wavefield separation and one-way wavefield decomposition. For the elastic scenario we used only particle-velocity recordings (V_1 and V_3) as input. This has a significant practical advantage, because it obvi-

ates the necessity of calibrating between sensors of different type and frequency sensitivity, such as between geophones and hydrophones. Since our acquisition array is located at 10 m depth, we employ the power-flux normalized decomposition scheme from Grobbe et al. (2013) in order to use the free-surface boundary condition on the stress wavefields, and achieve wavefield separation and decomposition (see figure 3.8).

Results are shown in figures 3.9, 3.10, 3.11 and 3.12. They show for each ANSI method the evolution of the reflection response estimate for each waveform response, for different amounts of noise panels (2 min, 5 min and 52 min of ambient-noise recording). Figures 3.9b, 3.10b, 3.11b and 3.12b show the approximated reference responses of the respective wave-mode in each case, although not entirely exact due to inexact finite difference modelling and Ψ-wave spatial aliasing at the receiver array. CC, CCh and the $R^{\smile}$-MDD methods show their results do not converge to an accurate reflection-response estimate despite using larger amounts of data every time and the aid of illumination diagnosis, independent of the wave-mode retrieved. On the other hand, $R_0^{\smile}$-MDD seems to obtain a satisfactory result, requiring a larger amount of data in comparison with the acoustic case, though. This is obvious in the slow evolution in figures 3.9f, 3.9j and 3.9n towards the $\hat{R}_0^{\Phi,\Phi\,\smile}$ wave-mode reflection response. The same observation is applicable to the other display series, in figures 3.10, 3.11 and 3.12.

One important drawback to keep in mind in this example is the error introduced by the decomposition approximation for the acquisition array detached from the free-surface. These uncertainties however would not exist if the acquisition array were located at the surface. In that case, only the lateral variations in the elastic parameters at the acquisition level would determine the suitability of this wavefield-decomposition scheme.

3.4 Discussion

The methods to retrieve the reflection response presented in this chapter have in common the explicit construction of the point-spread function without any approximation being considered. The result of such approach provides more stable inversion results during the reflection retrieval. The only approximations being made are in the evaluation of the correlation functions. We believe the $R_0^{\smile}$-MDD method, defined here either to work with transient signals or in ANSI applications, is not yet an established method but rather a first approach toward a more complete procedure that should take into account the limitations caused by the approximations discussed in this chapter.

Synthetic results from the different ANSI methods showed important differences between the methods in the way of handling complex noise-signal characteristics. The use of illumination diagnosis with wavefield decomposition of noise panels, utilizing only recordings of geophones in an elastic scenario, proves to be

a simple but very suitable and efficient combination in the aim to design a passive seismic protocol. By making use of the illumination diagnosis at the edges of the array, surface waves in the recordings are rejected because no further use of them has been considered in this chapter. However, they can provide very valuable information, such as the estimation of the near surface elastic parameters, very critical during the wavefield decomposition process, via surface-wave SI (Snieder et al., 2006). ANSI $R_0^{\smile}$-MDD presented an acceptable result, although we consider there is still scope to improve the reflection retrieval in such challenging ambient-noise conditions.

3.5 Conclusions

We propose new methods to retrieve the reflection response of the subsurface without free-surface multiples as an alternative to other passive SI methods. These proposed methods are based on one-way wavefield reciprocity theorems and make use of representations of the convolution and the correlation types for a surface passive-seismic configuration.

An alternative ANSI version is also presented which is conceived to work with continuous ambient-noise recordings in situations where estimates of reference-state transmission responses are not possible. In comparison with other ANSI methods, our method deals in a better manner with the heterogeneous nature of source mechanisms, the diverse frequency content of the ambient-noise signal, and it compensates for uneven illumination of the subsurface sources. In elastic media, the retrieval process involves all receiver wavefields together to solve all the wave-mode reflection responses. Also, unlike the explicit ANSI methods, our method requires a regular- or dense enough acquisition array to apply regularization.

The synthetic dataset we employed in this chapter was designed to approximate realistic scenarios with ambient-noise recordings, dealing with surface waves, complex source characteristics and an irregular source distributions. The combination of our retrieval method with illumination diagnosis and wavefield decomposition with particle velocities provides the basis for an efficient passive seismic protocol for reflection response retrieval.

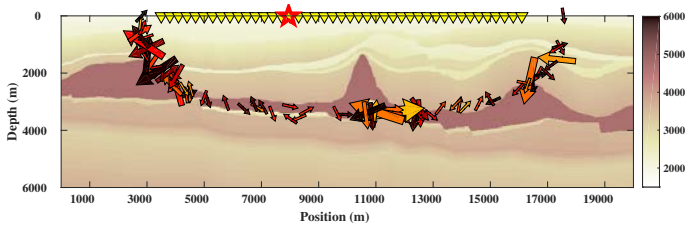

(a) *P-velocity of the elastic model*

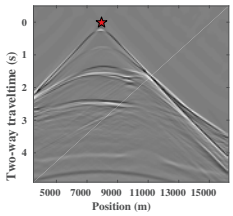

(b) *Reference* $R_0^{\smile}$

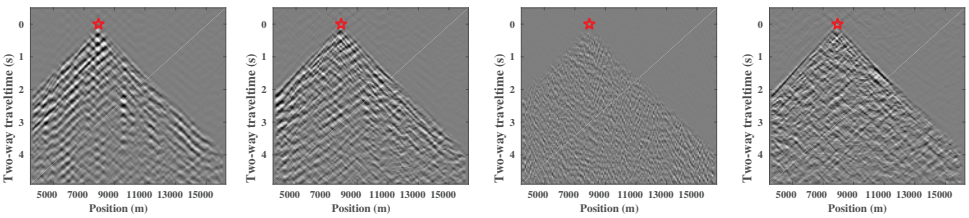

(c) *2 min CC* **(d)** *2 min CCh* **(e)** *2 min* $R^{\smile}$*-MDD* **(f)** *2 min* $R_0^{\smile}$*-MDD*

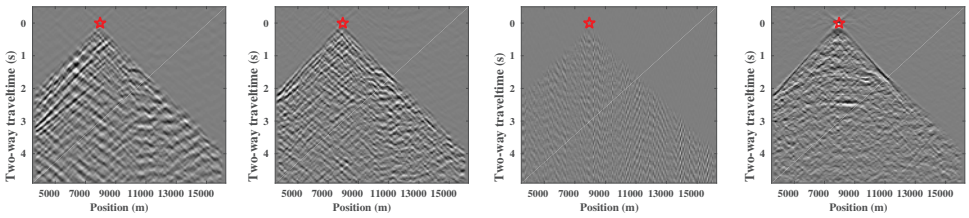

(g) *5 min CC* **(h)** *5 min CCh* **(i)** *5 min* $R^{\smile}$*-MDD* **(j)** *5 min* $R_0^{\smile}$*-MDD*

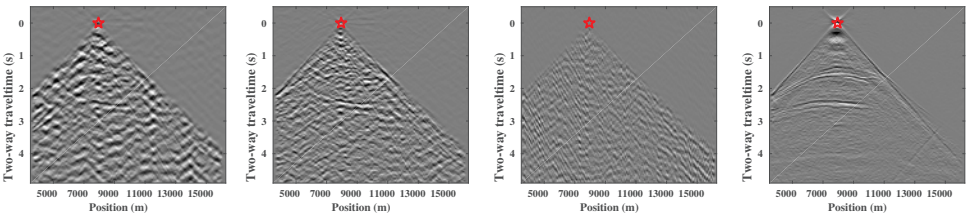

(k) *52 min CC* **(l)** *52 min CCh* **(m)** *52 min* $R^{\smile}$*-MDD* **(n)** *52 min* $R_0^{\smile}$*-MDD*

Figure 3.9: $R_0^{\overset{\Phi,\Phi}{\smile}}$ *retrieved results of different ANSI methods with different amounts of elastic ambient noise.* ***(a)*** *P-wave velocity model, with dipole noise sources with random spectrum, random orientation and irregular occurrence.* ***(b)*** *Modelled estimation of the* $R_0^{\overset{\Phi,\Phi}{\smile}}$ *reflection response for an active source at* $x_0 = 7950\ m$ *(the red open star in (a)).* ***(c)***, ***(d)***, ***(e)*** *and* ***(f)*** *Retrieved virtual common-source gather at the same location using 2 minutes of noise, using crosscorrelation (CC) (c), crosscoherence (CCh) (d),* $R_0^{\smile}$*-MDD (e) and* $R_0^{\smile}$*-MDD (f).* ***(g)***, ***(h)***, ***(i)*** *and* ***(j)*** *Same as in (c), (d), (e) and (f), after 5 mintues of noise.* ***(k)***, ***(l)***, ***(m)*** *and* ***(n)*** *Retrieved results after 52 minutes of noise.*

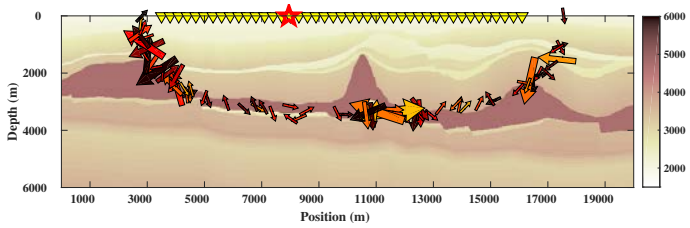

(a) *P-velocity of the elastic model*

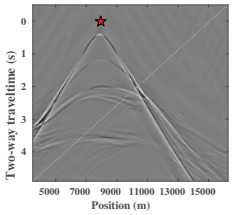

(b) *Reference* $R_0^{\smile}$

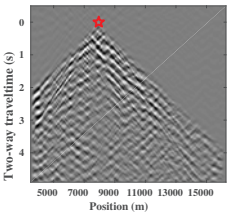

(c) *2 min CC*

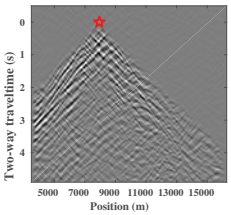

(d) *2 min CCh*

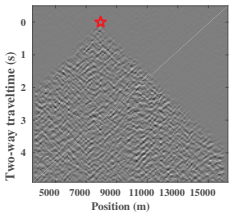

(e) *2 min* $R^{\smile}$*-MDD*

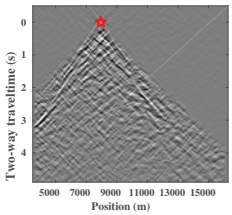

(f) *2 min* $R_0^{\smile}$*-MDD*

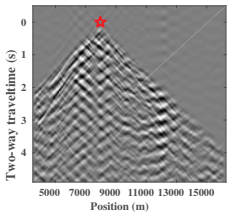

(g) *5 min CC*

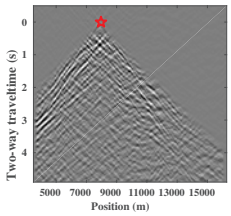

(h) *5 min CCh*

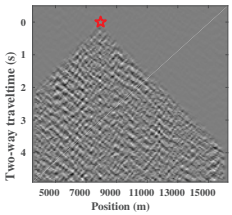

(i) *5 min* $R^{\smile}$*-MDD*

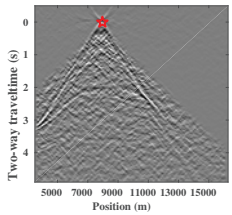

(j) *5 min* $R_0^{\smile}$*-MDD*

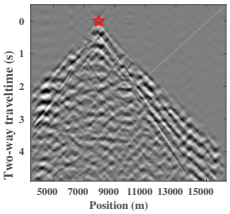

(k) *52 min CC*

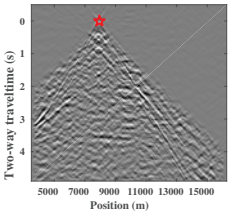

(l) *52 min CCh*

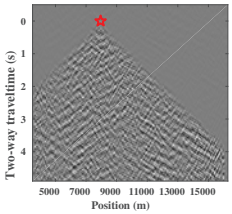

(m) *52 min* $R^{\smile}$*-MDD*

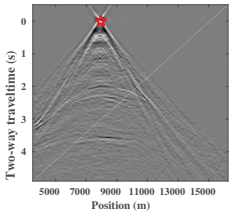

(n) *52 min* $R_0^{\smile}$*-MDD*

Figure 3.10: *Same as in 3.9 for* $R_0^{\Psi,\Psi}$.

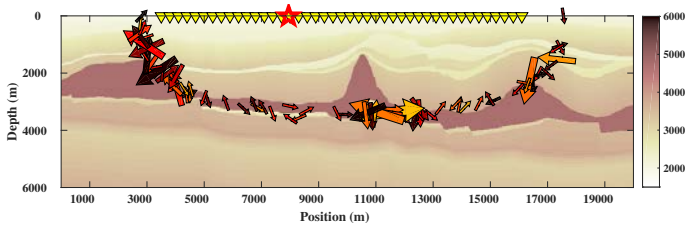

(a) *P-velocity of the elastic model*

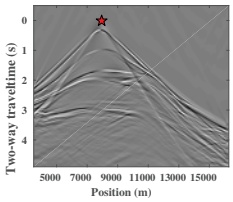

(b) *Reference* $R_0^{\smile}$

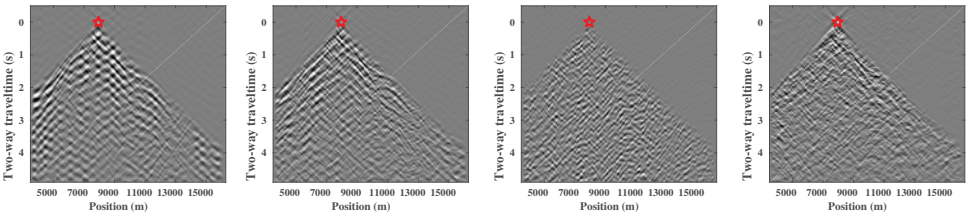

(c) *2 min CC* **(d)** *2 min CCh* **(e)** *2 min* $R^{\smile}$*-MDD* **(f)** *2 min* $R_0^{\smile}$*-MDD*

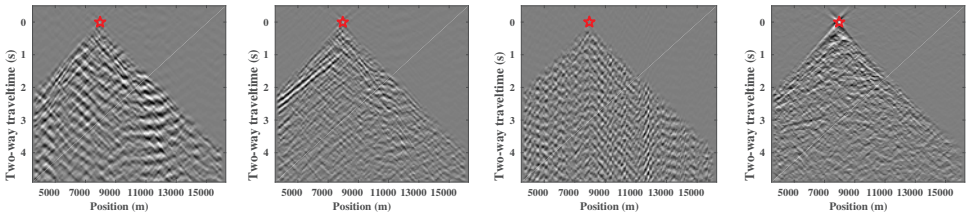

(g) *5 min CC* **(h)** *5 min CCh* **(i)** *5 min* $R^{\smile}$*-MDD* **(j)** *5 min* $R_0^{\smile}$*-MDD*

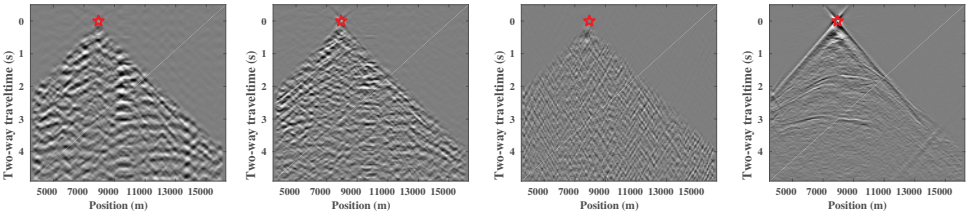

(k) *52 min CC* **(l)** *52 min CCh* **(m)** *52 min* $R^{\smile}$*-MDD* **(n)** *52 min* $R_0^{\smile}$*-MDD*

Figure 3.11: *Same as in 3.9 for* $R_0^{\Psi,\Phi\,\smile}$.

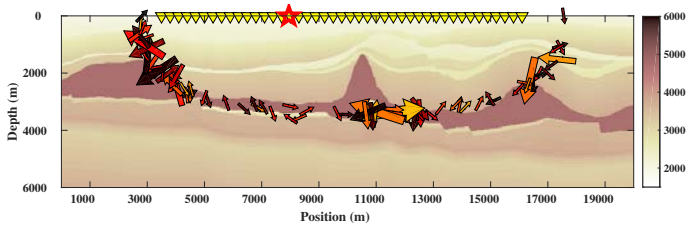

(a) *P-velocity of the elastic model*

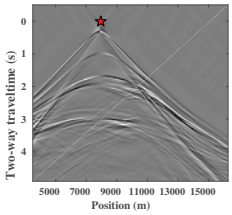

(b) *Reference* $R_0^{\smile}$

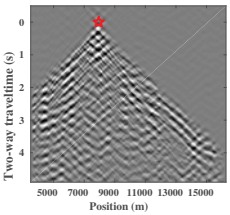

(c) *2 min CC*

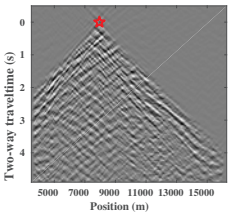

(d) *2 min CCh*

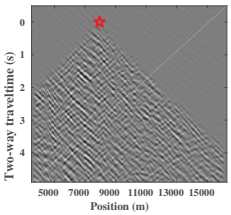

(e) *2 min* $R^{\smile}$*-MDD*

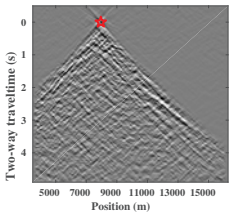

(f) *2 min* $R_0^{\smile}$*-MDD*

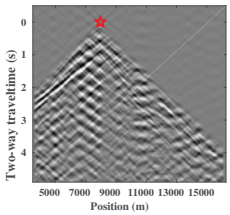

(g) *5 min CC*

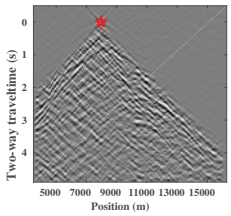

(h) *5 min CCh*

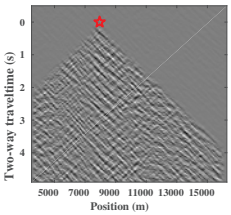

(i) *5 min* $R^{\smile}$*-MDD*

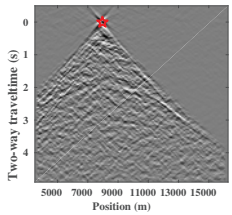

(j) *5 min* $R_0^{\smile}$*-MDD*

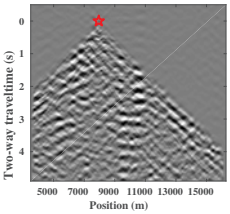

(k) *52 min CC*

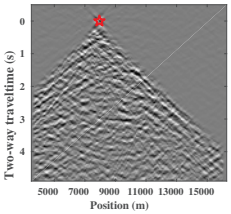

(l) *52 min CCh*

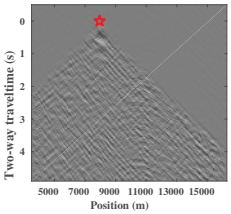

(m) *52 min* $R^{\smile}$*-MDD*

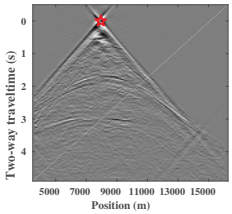

(n) *52 min* $R_0^{\smile}$*-MDD*

Figure 3.12: *Same as in 3.9 for* $R_0^{\overset{\Phi,\Psi}{\smile}}$.

3.A One-way wave equation

In the following, we will describe the wavefields that follow the unified one-way wave equation in the space-frequency domain:

$$\frac{\partial \hat{\mathbf{G}}(\mathbf{x}, \mathbf{x}_{\mathcal{A}}, \omega)}{\partial x_3} = \hat{\mathbf{B}}(\mathbf{x}, \omega)\hat{\mathbf{G}}(\mathbf{x}, \mathbf{x}_{\mathcal{A}}, \omega) + \mathbf{I}\delta(\mathbf{x} - \mathbf{x}_{\mathcal{A}}), \tag{3.20}$$

where $\hat{\mathbf{G}}$ is the one-way Green's matrix, structured as follows:

$$\hat{\mathbf{G}}(\mathbf{x}, \mathbf{x}_{\mathcal{A}}, \omega) = \begin{bmatrix} \hat{G}^{+,+} & \hat{G}^{+,-} \\ \hat{G}^{-,+} & \hat{G}^{-,-} \end{bmatrix} (\mathbf{x}, \mathbf{x}_{\mathcal{A}}, \omega). \tag{3.21}$$

Superscripts refer to receiver and source wavefields, respectively (minus for upgoing, and plus for downgoing). $\hat{\mathbf{B}}$ is the one-way operator matrix and $\mathbf{I}$ is the 2 x 2 identity matrix.

3.B Reciprocity relations

3.B.1 Convolutional reciprocity relation

The reciprocity relation of the convolution type between two states $\mathcal{A}$ and $\mathcal{B}$ is represented as follows (Wapenaar & Grimbergen, 1996):

$$\int_{\mathbb{D}} \{\hat{\mathbf{G}}^t_{\mathcal{A}}\mathbf{N}\hat{\mathbf{S}}_{\mathcal{B}} + \hat{\mathbf{S}}^t_{\mathcal{A}}\mathbf{N}\hat{\mathbf{G}}_{\mathcal{B}}\} d^3\mathbf{x} = \int_{\partial\mathbb{D}} \{\hat{\mathbf{G}}^t_{\mathcal{A}}\mathbf{N}\hat{\mathbf{G}}_{\mathcal{B}}\}\boldsymbol{n} d^2\mathbf{x} - \int_{\mathbb{D}} \{\hat{\mathbf{G}}^t_{\mathcal{A}}\mathbf{N}(\hat{\mathbf{B}}_{\mathcal{B}} - \hat{\mathbf{B}}_{\mathcal{A}})\hat{\mathbf{G}}_{\mathcal{B}}\} d^3\mathbf{x}, \tag{3.22}$$

where ^{t} means matrix transposition and $\boldsymbol{n}$ stands for the unit vector in the normal direction of $\partial\mathbb{D}$. The permutation matrix for the convolution relation $\mathbf{N}$ is constructed using null $\mathbf{0}$ and identity matrices $\mathbf{I}$ as shown:

$$\mathbf{N} = \begin{bmatrix} \mathbf{0} & \mathbf{I} \\ -\mathbf{I} & \mathbf{0} \end{bmatrix}. \tag{3.23}$$

The one-way operator matrix $\hat{\mathbf{B}}$ preserves the following symmetry relation with the permutation matrix $\mathbf{N}$:

$$-\mathbf{N}\hat{\mathbf{B}} = \hat{\mathbf{B}}^t\mathbf{N}. \tag{3.24}$$

The reciprocity relation of the convolution type in equation 3.22 shows three integration terms. The first term is the source-wavefield interaction over the domain $\mathbb{D}$. The second one is the wavefield-interaction at the domain boundary $\partial\mathbb{D}$. The third term is the medium-contrast interaction.

3.B.2 Correlational reciprocity relation

Similarly, the reciprocity relation of the correlation type between the same two states $\mathcal{A}$ and $\mathcal{B}$ is described as (Wapenaar & Grimbergen, 1996):

$$\int_{\mathbb{D}} \{\hat{\mathbf{G}}_{\mathcal{B}}^{\dagger}\mathbf{J}\hat{\mathbf{S}}_{\mathcal{A}} + \hat{\mathbf{S}}_{\mathcal{B}}^{\dagger}\mathbf{J}\hat{\mathbf{G}}_{\mathcal{A}}\} d^3\mathbf{x} = \int_{\partial\mathbb{D}} \{\hat{\mathbf{G}}_{\mathcal{B}}^{\dagger}\mathbf{J}\hat{\mathbf{G}}_{\mathcal{A}}\}\boldsymbol{n} d^2\mathbf{x} - \int_{\mathbb{D}} \{\hat{\mathbf{G}}_{\mathcal{B}}^{\dagger}\mathbf{J}(\hat{\mathbf{B}}_{\mathcal{A}} - \hat{\mathbf{B}}'_{\mathcal{B}})\hat{\mathbf{G}}_{\mathcal{A}}\} d^3\mathbf{x}. \quad (3.25)$$

In this expression † means matrix transposition and complex conjugation. The permutation matrix for the correlation expression has the following structure:

$$\mathbf{J} = \begin{bmatrix} \mathbf{I} & \mathbf{0} \\ \mathbf{0} & -\mathbf{I} \end{bmatrix}. \quad (3.26)$$

The $'$-symbol in the one-way medium operator $\hat{\mathbf{B}}$ denotes the medium operator defined in the complex conjugated medium. The medium operator $\hat{\mathbf{B}}'_{\mathcal{B}}$ is obtained from using the following symmetry property with the permutation matrix:

$$-\mathbf{J}\hat{\mathbf{B}}'_{\mathcal{B}} = \hat{\mathbf{B}}_{\mathcal{B}}^{\dagger}\mathbf{J}. \quad (3.27)$$

The same interaction terms in the convolutional relation are found in the relation of the correlation type with their respective differences.

3.C Representation relation of the convolution type for the reflection response without free-surface interaction

We employ the reciprocity theorem of the convolution type for one-way wavefields to present the Green's functions of a heterogeneous half-space medium, $\mathbb{D}$. We decompose the domain boundary $\partial\mathbb{D}$ in two: The upper boundary, $\partial\mathbb{D}_0$, is located at a constant depth level near but not immediately below the free surface. The lower boundary, $\partial\mathbb{D}_m$, is defined by the location of the sources in the subsurface, situated at an arbitrary depth level inside the medium.

For our representation we are going to make use of the two states $\mathcal{A}$ (reference state) and $\mathcal{B}$ (measurement state), each one with exactly the same observation or

	State $\mathcal{A}$	*State* $\mathcal{B}$
Wavefields	$\hat{\mathbf{G}}_{\mathcal{A}} = \hat{\mathbf{G}}_{\mathbf{0}}(\mathbf{x}, \mathbf{x}_{\mathcal{A}}, \omega)$	$\hat{\mathbf{G}}_{\mathcal{B}} = \hat{\mathbf{G}}(\mathbf{x}, \mathbf{x}_{\mathcal{B}}, \omega)$
Operators	$\hat{\mathbf{B}}_{\mathcal{A}} = \hat{\mathbf{B}}(\mathbf{x}, \omega)$	$\hat{\mathbf{B}}_{\mathcal{B}} = \hat{\mathbf{B}}(\mathbf{x}, \omega)$
Source fields	$\hat{\mathbf{S}}_{\mathcal{A}} = \mathbf{I}\delta(\mathbf{x} - \mathbf{x}_{\mathcal{A}})$	$\hat{\mathbf{S}}_{\mathcal{B}} = \mathbf{I}\delta(\mathbf{x} - \mathbf{x}_{\mathcal{B}})$
Medium above $\partial\mathbb{D}_0$	Homogeneous	Heterogeneous
Medium below $\partial\mathbb{D}_m$	Heterogeneous	Heterogeneous

Table 3.1: *Definition of the representation elements for states* $\mathcal{A}$ *and* $\mathcal{B}$ *in appendix 3.C.*

control domain $\mathbb{D}$ but with different boundary-domain characteristics and source locations. The end is to analyze the Green's function expressions without free-surface interaction (free-surface related multiples).

To this purpose, state $\mathcal{A}$ defines a homogeneous half space above the upper boundary $\partial\mathbb{D}_0$, while in state $\mathcal{B}$ the domain outside the boundary remains heterogeneous, including the free surface. Regarding the lower boundary, the medium is assumed heterogeneous below $\partial\mathbb{D}_m$ for both states. The source in state $\mathcal{A}$ is located immediately above the upper boundary, at $\mathbf{x}_{\mathcal{A}}$, while the source in state $\mathcal{B}$ is situated immediately under the lower boundary, at $\mathbf{x}_{\mathcal{B}}$.

Table 3.1 shows the representation terms for each state. $\hat{\mathbf{G}}(\mathbf{x}, \mathbf{x}_{\mathcal{B}}, \omega)$ represents the Green's function matrix in state $\mathcal{B}$ for a source located in $\mathbf{x}_{\mathcal{B}}$ and a receiver in $\mathbf{x}$, including transmission and reflection responses with internal multiples and free-surface reflections. $\hat{\mathbf{G}}_{\mathbf{0}}(\mathbf{x}, \mathbf{x}_{\mathcal{A}}, \omega)$ is the Green's function matrix for the medium in state $\mathcal{A}$, this is, without free-surface interaction. Subscript $_0$ refers to the homogenization of the medium above $\partial\mathbb{D}_0$.

The medium properties inside $\mathbb{D}$ do not change between states, therefore the one-way operator matrix $\hat{\mathbf{B}}$ will remain the same in both states $\mathcal{A}$ and $\mathcal{B}$. This means, for the following sections, the derivation of the Green's matrix representation neglects the medium-contrast interactions.

Following the configuration we proposed, we split the boundary integration into upper and lower boundaries such that $\partial\mathbb{D} = \partial\mathbb{D}_0 \cup \partial\mathbb{D}_m$. Therefore, the reciprocity relation from equation 3.22 for this representation turns into:

$$\int_{\partial\mathbb{D}_0} \{\hat{\mathbf{G}}^t_{\mathcal{A}} \mathbf{N} \hat{\mathbf{G}}_{\mathcal{B}}\} n_3 d^2\mathbf{x}_0 = -\int_{\partial\mathbb{D}_m} \{\hat{\mathbf{G}}^t_{\mathcal{A}} \mathbf{N} \hat{\mathbf{G}}_{\mathcal{B}}\} n_3 d^2\mathbf{x}_m, \tag{3.28}$$

where n_3 is the vertical component of the normal direction to the corresponding boundary. In this configuration the upper-boundary integral takes $n_3 = -1$ while the lower-boundary integral does $n_3 = +1$. We expand expression 3.28 by employing the terms that are available for our configuration. State $\mathcal{A}$ has the medium homogeneous above $\partial\mathbb{D}_0$, therefore, the Green's matrix $\hat{\mathbf{G}}_{\mathcal{A}}$ evaluated at the upper boundary contains only downgoing-source wavefields. Furthermore, since $\mathbf{x}_{\mathcal{A}}$ is defined immediately above the upper boundary, $\hat{G}_0^{+,+} = \delta(\mathbf{x}_H - \mathbf{x}_{H,\mathcal{A}})$, where subscript $_H$ refers to the horizontal coordinates only. We make use of the source-receiver reciprocity relations $\hat{G}_0^{-,+}(\mathbf{x}_0, \mathbf{x}_{\mathcal{A}}, \omega) = \hat{G}_0^{-,+}(\mathbf{x}_{\mathcal{A}}, \mathbf{x}_0, \omega)$ in the upper boundary integral, and $\hat{G}_0^{+,+}(\mathbf{x}_m, \mathbf{x}_{\mathcal{A}}, \omega) = -\hat{G}_0^{-,-}(\mathbf{x}_{\mathcal{A}}, \mathbf{x}_m, \omega)$ and $\hat{G}_0^{-,+}(\mathbf{x}_m, \mathbf{x}_{\mathcal{A}}, \omega) = \hat{G}_0^{-,+}(\mathbf{x}_{\mathcal{A}}, \mathbf{x}_m, \omega)$ in the lower boundary. Furthermore, we gather together both upgoing- and downgoing-source wavefields and sum them together to simplify the final expression into:

$$\begin{aligned}\hat{G}^{-}(\mathbf{x}_{\mathcal{A}}, \mathbf{x}_{\mathcal{B}}, \omega) - \int_{\mathbf{x}_0 \in \partial\mathbb{D}_0} \hat{G}_0^{-,+}(\mathbf{x}_{\mathcal{A}}, \mathbf{x}_0, \omega)\hat{G}^{+}(\mathbf{x}_0, \mathbf{x}_{\mathcal{B}}, \omega) d^2\mathbf{x}_0 = \\ - \int_{\mathbf{x}_m \in \partial\mathbb{D}_m} \Big\{ \hat{G}_0^{-,-}(\mathbf{x}_{\mathcal{A}}, \mathbf{x}_m, \omega)\hat{G}^{-}(\mathbf{x}_m, \mathbf{x}_{\mathcal{B}}, \omega) \\ + \hat{G}_0^{-,+}(\mathbf{x}_{\mathcal{A}}, \mathbf{x}_m, \omega)\hat{G}^{+}(\mathbf{x}_m, \mathbf{x}_{\mathcal{B}}, \omega) \Big\} d^2\mathbf{x}_m. \quad (3.29)\end{aligned}$$

Expression 3.29 is the final result we obtain from the reciprocity relation of the convolution type in our configuration. All terms with only one superscript are expressed in decomposed-receiver wavefields only. This expression shows on the left hand side the wavefield quantities we could acquire at the upper boundary with the usual passive seismic configuration at or near the free surface, $\hat{G}^{-}$ and $\hat{G}^{+}$, together with the unknown reflection response $\hat{G}_0^{-,+}$ we want to solve for. The terms on the right hand side of this equation are wavefield recordings in the subsurface which are not available in practical applications for obvious reasons. However, the same lower boundary integral at $\partial\mathbb{D}_m$ makes the definition of the reference transmission response $\hat{G}_0^{-}$ of the upper boundary from the source location $\mathbf{x}_{\mathcal{B}}$:

$$\begin{aligned}\int_{\mathbf{x}_m \in \partial\mathbb{D}_m} \Big\{ \hat{G}_0^{-,-}(\mathbf{x}_{\mathcal{A}}, \mathbf{x}_m, \omega)\hat{G}^{-}(\mathbf{x}_m, \mathbf{x}_{\mathcal{B}}, \omega) \\ + \hat{G}_0^{-,+}(\mathbf{x}_{\mathcal{A}}, \mathbf{x}_m, \omega)\hat{G}^{+}(\mathbf{x}_m, \mathbf{x}_{\mathcal{B}}, \omega) \Big\} d^2\mathbf{x}_m = -\hat{G}_0^{-}(\mathbf{x}_{\mathcal{A}}, \mathbf{x}_{\mathcal{B}}, \omega). \quad (3.30)\end{aligned}$$

The substitution of this definition yields:

$$\hat{G}^{-}(\mathbf{x}_{\mathcal{A}},\mathbf{x}_{\mathcal{B}},\omega)-\int_{\mathbf{x}_0\in\partial\mathbb{D}_0}\hat{G}_0^{-,+}(\mathbf{x}_{\mathcal{A}},\mathbf{x}_0,\omega)\hat{G}^{+}(\mathbf{x}_0,\mathbf{x}_{\mathcal{B}},\omega)d^2\mathbf{x}_0 = \hat{G}_0^{-}(\mathbf{x}_{\mathcal{A}},\mathbf{x}_{\mathcal{B}},\omega), \quad (3.31)$$

where $\hat{G}_0^{-,+}$ stands for the desired reflection response at the reference state ($\hat{R}_0^{\cup}$). This relation is the same as the one shown in Wapenaar et al. (2004), despite the representation in the last assumed the medium to be homogeneous below it.

Had we considered the source location to be inside the domain $\mathbb{D}$ and the lower boundary arbitrarily located independently of the sources in the subsurface, the reference state transmission wavefield $\hat{G}_0^{-}$ would have been present through the domain integral of the source-wavefield interaction, leaving the medium-boundary integration quantities to cancel one another. Therefore, it is shown the convolutional relation is independent of the medium boundary integral, regardless of how the boundary $\partial\mathbb{D}_m$ is defined with respect to the source location $\mathbf{x}_{\mathcal{B}}$.

3.D Representations for the reflection response of the medium above the acquisition array

In this appendix we use exactly the same reference- and measurement-state source locations as in appendix 3.C, and define a complementary control domain $\mathbb{D}'$ covering the medium between the previous upper boundary $\partial\mathbb{D}_0$ and the free surface. In this configuration, we define $\partial\mathbb{D}'_m$ as the upper boundary arbitrarily coinciding with the free surface and the lower boundary, $\partial\mathbb{D}'_0$, to have the same contour as $\partial\mathbb{D}_0$ ($\partial\mathbb{D}'_0\equiv\partial\mathbb{D}_0$). The medium below $\partial\mathbb{D}'_0$ remains homogeneous at the new complementary reference state $\mathcal{A}'$ and heterogeneous at the measurement state $\mathcal{B}$. Therefore, in this configuration the source location at the reference state $\mathbf{x}_{\mathcal{A}}$ is now considered inside $\mathbb{D}'$ while for the measurement state $\mathbf{x}_{\mathcal{B}}$ lays out of it. Table 3.2 shows the Green's function definitions applied in this section.

3.D.1 Representation relation of the convolution type

The use of the reciprocity relation of the convolution type in equation 3.22 for this configuration turns into:

$$\mathbf{N}\hat{\mathbf{G}}_{\mathcal{B}}(\mathbf{x}_{\mathcal{A}},\mathbf{x}_{\mathcal{B}},\omega)=\int_{\partial\mathbb{D}'_0}\{\hat{\mathbf{G}}^{t}_{\mathcal{A}'}\mathbf{N}\hat{\mathbf{G}}_{\mathcal{B}}\}n_3d^2\mathbf{x}_0+\int_{\partial\mathbb{D}'_m}\{\hat{\mathbf{G}}^{t}_{\mathcal{A}'}\mathbf{N}\hat{\mathbf{G}}_{\mathcal{B}}\}n_3d^2\mathbf{x}_m. \quad (3.32)$$

We have applied $n_3=-1$ on $\partial\mathbb{D}'_m$ and $n_3=+1$ on $\partial\mathbb{D}'_0$. We gather together the equations with $\hat{G}^{+,-}_{\mathcal{A}'}$ at $\partial\mathbb{D}'_0$, sum together terms with common one-way

	State $\mathcal{A}'$	*State* $\mathcal{B}$
Wavefields	$\hat{\mathbf{G}}_{\mathcal{A}'} = \hat{\mathbf{G}}_{\mathbb{D}',\mathbf{0}}(\mathbf{x}, \mathbf{x}_{\mathcal{A}}, \omega)$	$\hat{\mathbf{G}}_{\mathcal{B}} = \hat{\mathbf{G}}(\mathbf{x}, \mathbf{x}_{\mathcal{B}}, \omega)$
Source fields	$\hat{\mathbf{S}}_{\mathcal{A}'} = \mathbf{I}\delta(\mathbf{x} - \mathbf{x}_{\mathcal{A}})$	$\hat{\mathbf{S}}_{\mathcal{B}} = \mathbf{I}\delta(\mathbf{x} - \mathbf{x}_{\mathcal{B}})$
Medium above $\partial\mathbb{D}'_m$	Heterogeneous	Heterogeneous
Medium below $\partial\mathbb{D}'_0$	Homogeneous	Heterogeneous

Table 3.2: *Definition of the representation elements for states* $\mathcal{A}'$ *and* $\mathcal{B}$ *in appendix 3.D.*

source wavefield and apply the corresponding source-receiver reciprocity relations. Regarding the upper boundary integral $\partial\mathbb{D}'_m$ the wavefield interactions at this boundary cancel one another and the integral vanishes. Hence, the final result yields:

$$\hat{G}^{+}(\mathbf{x}_{\mathcal{A}}, \mathbf{x}_{\mathcal{B}}, \omega) = -\int_{\mathbf{x}_0 \in \partial\mathbb{D}'_0} \hat{G}^{+,-}_{\mathbb{D}',0}(\mathbf{x}_{\mathcal{A}}, \mathbf{x}_0, \omega)\hat{G}^{-}(\mathbf{x}_0, \mathbf{x}_{\mathcal{B}}, \omega)d^2\mathbf{x}_0. \tag{3.33}$$

This formula is the implicit representation of the convolution type for the reflection response of $\mathbb{D}'$ (above $\partial\mathbb{D}'_0/\partial\mathbb{D}_0$). $\hat{G}^{+,-}_{\mathbb{D}',0}$ stands for the desired reflection response, as $\hat{R}^{\curvearrowleft}_{\mathbb{D}',0} = -\hat{G}^{+,-}_{\mathbb{D}',0}$. For practical applications, it provides the information of the subsurface between the free surface and $\partial\mathbb{D}_0$, where the acquisition array is set.

3.D.2 Representation relation of the correlation type

The application of the reciprocity relation of the correlation type in equation 3.25 onto our configuration leaves us with:

$$\hat{\mathbf{G}}^{\dagger}_{\mathcal{B}}\mathbf{J}(\mathbf{x}_{\mathcal{A}}, \mathbf{x}_{\mathcal{B}}, \omega) = \int_{\partial\mathbb{D}'_0} \{\hat{\mathbf{G}}^{\dagger}_{\mathcal{B}}\mathbf{J}\hat{\mathbf{G}}_{\mathcal{A}'}\}n_3 d^2\mathbf{x}_0 + \int_{\partial\mathbb{D}'_m} \{\hat{\mathbf{G}}^{\dagger}_{\mathcal{B}}\mathbf{J}\hat{\mathbf{G}}_{\mathcal{A}'}\}n_3 d^2\mathbf{x}_m. \tag{3.34}$$

The set of equations with the function $\hat{G}^{+,-}_{\mathcal{A}'}$ at $\partial\mathbb{D}'_0$ put together, leaves us with the expression:

$$\begin{aligned}\big\{\hat{G}^{-}(\mathbf{x}_{\mathcal{A}},\mathbf{x}_{\mathcal{B}},\omega)\big\}^{*} = &-\int_{\mathbf{x}_0\in\partial\mathbb{D}'_0}\hat{G}^{+,-}_{\mathbb{D}',0}(\mathbf{x}_0,\mathbf{x}_{\mathcal{A}},\omega)\big\{\hat{G}^{+}(\mathbf{x}_0,\mathbf{x}_{\mathcal{B}},\omega)\big\}^{*}d^2\mathbf{x}_0\\ &+\int_{\mathbf{x}_m\in\partial\mathbb{D}'_m}\Big\{\hat{G}^{+,-}_{0}(\mathbf{x}_m,\mathbf{x}_{\mathcal{A}},\omega)\big\{\hat{G}^{+}(\mathbf{x}_m,\mathbf{x}_{\mathcal{B}},\omega)\big\}^{*}\\ &\qquad-\hat{G}^{-,-}_{0}(\mathbf{x}_m,\mathbf{x}_{\mathcal{A}},\omega)\big\{\hat{G}^{-}(\mathbf{x}_m,\mathbf{x}_{\mathcal{B}},\omega)\big\}^{*}\Big\}d^2\mathbf{x}_m. \quad (3.35)\end{aligned}$$

This formula is the implicit representation of the correlation type for the reflection response of $\mathbb{D}'$, from $\partial\mathbb{D}'_0/\partial\mathbb{D}_0$. The presence of the free surface in the control domain $\mathbb{D}'$ makes the medium strongly reflective and the lower-boundary integral contribution for this specific configuration becomes negligible:

$$\big\{\hat{G}^{-}(\mathbf{x}_{\mathcal{A}},\mathbf{x}_{\mathcal{B}},\omega)\big\}^{*} \approx -\int_{\mathbf{x}_0\in\partial\mathbb{D}'_0}\hat{G}^{+,-}_{\mathbb{D}',0}(\mathbf{x}_0,\mathbf{x}_{\mathcal{A}},\omega)\big\{\hat{G}^{+}(\mathbf{x}_0,\mathbf{x}_{\mathcal{B}},\omega)\big\}^{*}d^2\mathbf{x}_0. \quad (3.36)$$

This assumption is hold valid if $\partial\mathbb{D}'_0$ is located relatively proximate to the free surface.

3.E Representation relation of the convolution type for the reflection response with free-surface interaction

The same reciprocity relation also serves to analyze the Green's function expressions with free-surface interaction. This section describes a complementary representation where reference and measurement states interchange their respective boundary conditions at $\partial\mathbb{D}_0$. State $\mathcal{B}$ now stands for the reference state, with exactly the same source location in the subsurface as in appendix 3.C, but the medium homogeneous above the upper boundary. State $\mathcal{A}$ represents now the measurement state, having the source situated right over the upper boundary and incorporates the heterogeneities above $\partial\mathbb{D}_0$, including the free surface.

Since we consider the same boundary definitions and their respective integrals, and we also use the boundary integral orientation n_3 as in appendix 3.C, for this representation we only have to substitute the wavefield definitions in table 3.3 into equation 3.28. We make use of the corresponding source-receiver reciprocity relations, add together the Green's functions from the reference state and obtain the following expression (of two possible ones):

	State $\mathcal{A}$	*State* $\mathcal{B}$
Wavefields	$\hat{\mathbf{G}}_{\mathcal{A}} = \hat{\mathbf{G}}(\mathbf{x}, \mathbf{x}_{\mathcal{A}}, \omega)$	$\hat{\mathbf{G}}_{\mathcal{B}} = \hat{\mathbf{G}}_{\mathbf{0}}(\mathbf{x}, \mathbf{x}_{\mathcal{B}}, \omega)$
Source fields	$\hat{\mathbf{S}}_{\mathcal{A}} = \mathbf{I}\delta(\mathbf{x} - \mathbf{x}_{\mathcal{A}})$	$\hat{\mathbf{S}}_{\mathcal{B}} = \mathbf{I}\delta(\mathbf{x} - \mathbf{x}_{\mathcal{B}})$
Medium above $\partial\mathbb{D}_0$	Heterogeneous	Homogeneous
Medium below $\partial\mathbb{D}_m$	Heterogeneous	Heterogeneous

Table 3.3: *Definition of the representation elements for states $\mathcal{A}$ and $\mathcal{B}$ in appendix 3.E.*

$$\int_{\mathbf{x}_0' \in \partial\mathbb{D}_0} \hat{G}^{-,-}(\mathbf{x}_{\mathcal{A}}, \mathbf{x}_0', \omega)\hat{G}_0^{-}(\mathbf{x}_0', \mathbf{x}_{\mathcal{B}}, \omega)d^2\mathbf{x}_0' = \int_{\mathbf{x}_m \in \partial\mathbb{D}_m} \Big\{\hat{G}^{-,+}(\mathbf{x}_{\mathcal{A}}, \mathbf{x}_m, \omega)\hat{G}_0^{+}(\mathbf{x}_m, \mathbf{x}_{\mathcal{B}}, \omega) + \hat{G}^{-,-}(\mathbf{x}_{\mathcal{A}}, \mathbf{x}_m, \omega)\hat{G}_0^{-}(\mathbf{x}_m, \mathbf{x}_{\mathcal{B}}, \omega)\Big\}d^2\mathbf{x}_m, \quad (3.37)$$

Equation 3.37 shows integrals over wavefield interaction quantities along $\partial\mathbb{D}_m$ where no boundary conditions are changed between reference and measurement states. Therefore, we substitute this lower boundary integral with the wavefield definition:

$$\int_{\mathbf{x}_m \in \partial\mathbb{D}_m} \Big\{\hat{G}^{-,+}(\mathbf{x}_{\mathcal{A}}, \mathbf{x}_m, \omega)\hat{G}_0^{+}(\mathbf{x}_m, \mathbf{x}_{\mathcal{B}}, \omega) + \hat{G}^{-,-}(\mathbf{x}_{\mathcal{A}}, \mathbf{x}_m, \omega)\hat{G}_0^{-}(\mathbf{x}_m, \mathbf{x}_{\mathcal{B}}, \omega)\Big\}d^2\mathbf{x}_m = -\hat{G}^{-}(\mathbf{x}_{\mathcal{A}}, \mathbf{x}_{\mathcal{B}}, \omega). \quad (3.38)$$

The result yields:

$$\hat{G}^{-}(\mathbf{x}_{\mathcal{A}}, \mathbf{x}_{\mathcal{B}}, \omega) = -\int_{\mathbf{x}_0' \in \partial\mathbb{D}_0} \hat{G}^{-,-}(\mathbf{x}_{\mathcal{A}}, \mathbf{x}_0', \omega)\hat{G}_0^{-}(\mathbf{x}_0', \mathbf{x}_{\mathcal{B}}, \omega)d^2\mathbf{x}_0', \quad (3.39)$$

The term $\hat{G}^{-,-}$ is the reflection response from the upgoing radiating source to the upgoing radiating receiver wavefield. We see that from the reciprocity relation of the convolution type we cannot obtain a representation of the reflection response with downgoing source wavefield. However, it can be achieved combining this

expression with the representation obtained using the reciprocity relation of the convolution type on the medium above the upper boundary, $\mathbb{D}'$. For the next step, we define two complementary states, for the medium between the upper boundary and the free surface $\mathbb{D}'$, in a similar fashion as in appendix 3.D. The upper boundary in the previous configuration $\partial\mathbb{D}_0$ becomes the lower boundary of $\mathbb{D}'$ ($\partial\mathbb{D}'_0$), while the upper boundary $\partial\mathbb{D}'_m$ coincides with the free surface. In the reference state, $\mathcal{B}'$, we choose the medium to be homogeneous below $\partial\mathbb{D}'_0$ and the source to be located at $\mathbf{x}'_0$, immediately below this boundary. The measurement state $\mathcal{A}$ is exactly the same medium as in the previous configuration except now the same source location $\mathbf{x}_\mathcal{A}$, which is immediately above $\partial\mathbb{D}'_0$, is this time considered inside the control domain $\mathbb{D}'$. The result of this configuration with the corresponding reciprocity relation of the convolution type yields the identity:

$$\hat{G}^{-,-}(\mathbf{x}_\mathcal{A},\mathbf{x}'_0,\omega) = \\ -\delta(\mathbf{x}_\mathcal{A}-\mathbf{x}'_0)+\int_{\mathbf{x}_0\in\partial\mathbb{D}_0}\hat{G}^{-,+}(\mathbf{x}_\mathcal{A},\mathbf{x}_0,\omega)\hat{G}^{+,-}_{\mathbb{D}',0}(\mathbf{x}_0,\mathbf{x}'_0,\omega)d^2\mathbf{x}_0. \quad (3.40)$$

This expression can now be substituted inside equation 3.39:

$$\hat{G}^{-}(\mathbf{x}_\mathcal{A},\mathbf{x}_\mathcal{B},\omega) = \int_{\mathbf{x}'_0\in\partial\mathbb{D}_0}\Big\{\delta(\mathbf{x}_\mathcal{A}-\mathbf{x}'_0)... \\ ...-\int_{\mathbf{x}_0\in\partial\mathbb{D}_0}\hat{G}^{-,+}(\mathbf{x}_\mathcal{A},\mathbf{x}_0,\omega)\hat{G}^{+,-}_{\mathbb{D}',0}(\mathbf{x}_0,\mathbf{x}'_0,\omega)d^2\mathbf{x}_0\Big\}\hat{G}^{-}_0(\mathbf{x}'_0,\mathbf{x}_\mathcal{B},\omega)d^2\mathbf{x}'_0. \quad (3.41)$$

The implicit wavefield in the measurement state includes an upgoing-upgoing source-receiver wavefield which we have substituted by the integration product of the upper side reflection response $\hat{G}^{+,-}_{\mathbb{D}',0}$ and the reflection response of below $\hat{G}^{-,+}$. Since both integrations on the right hand side are over the same boundary $\partial\mathbb{D}_0$
$\partial\mathbb{D}'_0$ and because we are interested in simplifying for the term $\hat{G}^{-,+}$, we gather in the same integration the upper side reflection response $\hat{G}^{+,-}_{\mathbb{D}',0}$ with the reference state term $\hat{G}^{-}_0$ and exchange the integration order. Therefore the convolutional relation yields:

$$\hat{G}^{-}(\mathbf{x}_\mathcal{A},\mathbf{x}_\mathcal{B},\omega) = \hat{G}^{-}_0(\mathbf{x}_\mathcal{A},\mathbf{x}_\mathcal{B},\omega)-\int_{\mathbf{x}_0\in\partial\mathbb{D}_0}\hat{G}^{-,+}(\mathbf{x}_\mathcal{A},\mathbf{x}_0,\omega)\Big\{... \\ ...\int_{\mathbf{x}'_0\in\partial\mathbb{D}_0}\hat{G}^{+,-}_{\mathbb{D}',0}(\mathbf{x}_0,\mathbf{x}'_0,\omega)\hat{G}^{-}_0(\mathbf{x}'_0,\mathbf{x}_\mathcal{B},\omega)d^2\mathbf{x}'_0\Big\}d^2\mathbf{x}_0. \quad (3.42)$$

This formula is the implicit representation of the convolution type for the reflection response of $\mathbb{D}$ with free surface interaction. The convolution relation shows for this configuration the desired reflection response $\hat{R}^{\smile} = \hat{G}^{-,+}$ is only attainable with the help of $\hat{R}^{\curvearrowleft}_{\mathbb{D}',0} = -\hat{G}^{+,-}_{\mathbb{D}',0}$.

Annex II

One-way wavefield decomposition in laterally variant media with irregular passive seismic acquisition arrays

The acquisition design together with the near-surface parameters at the receiver locations are of extreme importance in our seismic data processing scheme. Throughout this thesis, the near-surface parameters have been assumed homogeneous along the acquisition level, which allowed wavefield decomposition to be carried-out in the wavenumber-frequency domain. 3D laterally variant media and irregular acquisition arrays disable the use of the wavenumber domain in this process. In this chapter, we show how to implement the same passive seismic processing for wavefield decomposition of passive recordings in the space-frequency domain. The decomposition is thus adapted to irregular acquisition arrays in 3D laterally variant media using a numerical approach and modal expansion of the differentiation operators.

II.1 Introduction

This annex serves as a continuation of the application of irregular acquisition arrays on 3D media for passive seismics. The wavefield decomposition in acoustic media (and separation in elastic media) requires the knowledge of the medium parameters at the acquisition surface. For passive seismic arrays, this comprises the near-surface information: mass-density and both compressional and shear velocities. For homogeneous distributions of these parameters along the acquisition depth level the decomposition can be achieved in the frequency-wavenumber domain as a linear operation. In practical applications with large arrays deployed on the Earth surface this assumption does not hold. For smooth variations of the near-surface parameters the use of local decomposition operators may still make this procedure possible, but if the parameter variations are strong the operators become unstable.

The alternative to construct the decomposition operators in laterally variant media is to have them estimated in the space-frequency domain by numerical means. In Grimbergen et al. (1998) the required operators for decomposition are estimated using a finite difference approach. However, in 3D media this procedure needs regular grids in order to estimate correctly the differentiation operators required for decomposition.

In this annex we propose the use of finite elements to estimate the differentiation operators in the space-frequency domain, which incorporates the effect of the heterogeneities of the near-surface. These differentiation operators are expressed as matrix linear operators, and by means of modal expansion the corresponding one-way wavefield-decomposition operators can be estimated.

This annex serves as an implementation of the work of Grimbergen et al. (1998) in 3D laterally variant media for wavefield decomposition applied in irregular passive acquisition arrays.

II.2 The Helmholtz operator

We describe the two-way wave equation for acoustic media with respect to a certain constant depth level x_3:

$$\frac{\partial^2 \hat{p}(\mathbf{x}_\perp, x_3, \omega)}{\partial x_3^2} = -\hat{\mathcal{H}}_2 \, \hat{p}(\mathbf{x}_\perp, x_3, \omega), \tag{II.1}$$

where $\hat{p}$ is the pressure wavefield, $\mathbf{x}_\perp = (x_1, x_2)$ are the horizontal coordinates and ω is the angular frequency. In equation II.1 we identify the Helmholtz operator $\hat{\mathcal{H}}_2$ as:

$$\hat{\mathcal{H}}_2 = \left(\frac{\omega}{c'}\right)^2 + \boldsymbol{\nabla}_\perp^2, \tag{II.2}$$

where $\boldsymbol{\nabla}_\perp = (\partial/\partial x_1, \partial/\partial x_2)$ is the transverse part of the gradient operator and c' stands for the modified velocity of the medium due to power-flux normalization. The spectral part of the Helmholtz operator in this case is defined as (Wapenaar & Grimbergen, 1996):

$$\left(\frac{\omega}{c'}\right)^2 = \left(\frac{\omega}{c}\right)^2 - \frac{3\,(\boldsymbol{\nabla}_\perp \rho) \cdot (\boldsymbol{\nabla}_\perp \rho)}{4\rho^2} + \frac{(\boldsymbol{\nabla}_\perp^2 \rho)}{2\rho}, \tag{II.3}$$

where $c = c_P(\mathbf{x}_\perp)$ and $\rho = \rho(\mathbf{x}_\perp)$ are assumed laterally variant along the same depth level x_3.

II.3 Finite Element Implementation

In our configuration we assume that the velocity and density of the medium vary in space along the acquisition array. To this supposition we add the irregular space distribution of our receiver locations due to the irregular acquisition design for passive recordings. These two conditions prevent the use of the wavenumber domain in further processing. Therefore, we aim to make a numerical estimate to the Helmholtz differentiation operator using a finite-element approach. In this approach the differentiation operator at the acquisition array is approximated with polynomial functions. Using finite elements has the advantage of handling irregular grid geometries, takes into account the heterogeneities of laterally variant media, and allows high-order approximations to the desired operator.

Let us begin defining the surface domain Ω coinciding with the boundary $\partial\mathbb{D}_0$ where we carry out our acquisition. We evaluate the wavefield $\hat{p}$ continuously in space along the domain Ω, as a function of the horizontal coordinates $\mathbf{x}_\perp$. The differentiation operator acts on $\hat{p}$ according to equation II.2:

$$\hat{\mathcal{H}}_2\langle\hat{p}\rangle = \left(\frac{\omega}{c'}\right)^2 \hat{p} + \boldsymbol{\nabla}_\perp^2 \hat{p}. \tag{II.4}$$

We define the bilinear form of the Helmholtz operator $\tilde{\mathcal{H}}_2$ over the wavefield $\hat{p}$ and an arbitrary test function $v = v(\mathbf{x}_\perp)$ which is assumed continuous and differentiable along the domain Ω. We evaluate the integration of the differentiation operator form over the acquisition domain Ω and obtain the expression:

$$\tilde{\mathcal{H}}_2\langle\hat{p}, v\rangle = \int_{\mathbf{x}_\perp\in\Omega} \left(\frac{\omega}{c'}\right)^2 \hat{p}\; v\; d^2\mathbf{x}_\perp + \int_{\mathbf{x}_\perp\in\Omega} (\boldsymbol{\nabla}_\perp^2\; \hat{p})\; v\; d^2\mathbf{x}_\perp. \tag{II.5}$$

This is the strong formulation of the differentiation operator form. We assume the test function v is differentiable and zero at the edges of the elements. Next, we apply integration by parts to the second integral term of equation II.5 in order to relocate one space derivative from $\hat{p}$ to v, hence.

$$\tilde{\mathcal{H}}_2\langle\hat{p}, v\rangle = \int_{\mathbf{x}_\perp\in\Omega} \left(\frac{\omega}{c'}\right)^2 \hat{p}\; v\; d^2\mathbf{x}_\perp - \int_{\mathbf{x}_\perp\in\Omega} (\boldsymbol{\nabla}_\perp\hat{p}) \cdot (\boldsymbol{\nabla}_\perp v)\; d^2\mathbf{x}_\perp. \tag{II.6}$$

This is the weak or variational formulation of the differentiation operator form.

In our implementation, we are dealing with a limited set of observed wavefields $\hat{p}^{obs}(\mathbf{x}_i)$ at the recording locations $\mathbf{x}_i$ at the same depth level. Without spatially continuous wavefield observations the differentiation in space is unattainable. Therefore, the Helmholtz operator and its space derivatives can be evaluated following a discretization approach with numerical methods.

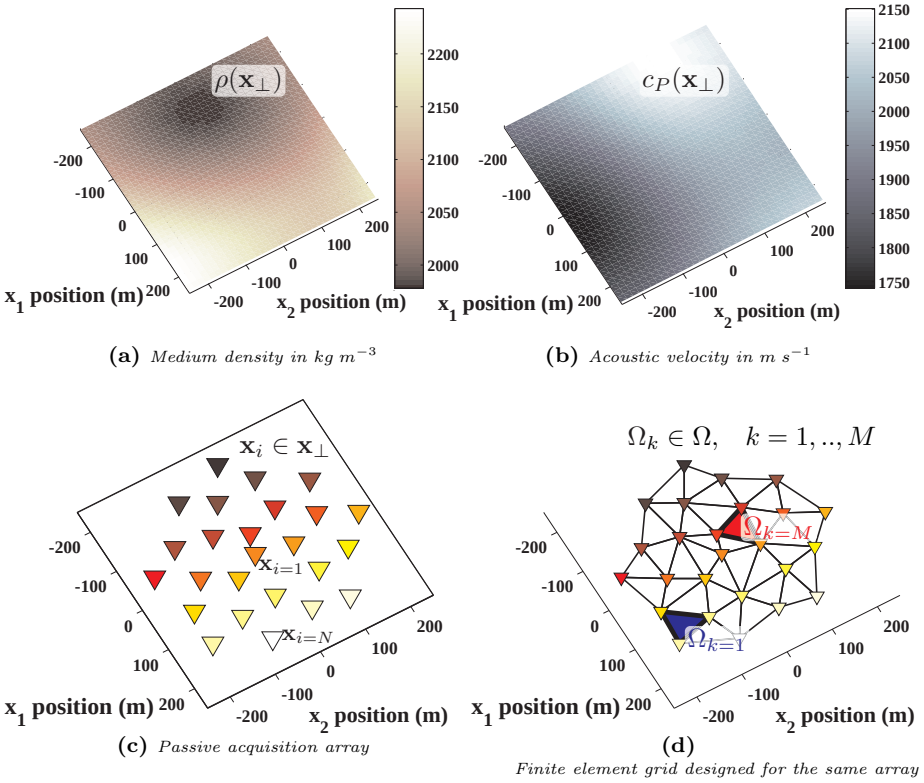

(a) *Medium density in kg m^{-3}*

(b) *Acoustic velocity in m s^{-1}*

(c) *Passive acquisition array*

(d) *Finite element grid designed for the same array*

Figure II.1: *Example of laterally variant near-surface parameters and a passive acquisition array with irregular grid design.* ***(a)*** *and* ***(b)*** *Mass-density and acoustic velocity maps at a surface of constant depth, respectively.* ***(c)*** *Passive acquisition array with 25 receivers distributed over the same depth level.* ***(d)*** *Finite element grid obtained from the given acquisition array. Elements are identified as Ω_k and the assembly of the finite elements provides the global matrix operator that approximates the Helmholtz operator. Ill-conceived elements along the edges of the array have been eliminated.*

Employing the Galerkin's discretization approach, we describe the Helmholtz equation for power-flux wavefields: we subdivide the domain Ω into M local elements Ω_k, $k = 1, ..M$, that consist of N distinct nodes at $\mathbf{x}_i$, $i = 1, ..N$. These local elements are designed using Delaunay triangulation while the receiver locations become the element nodes (or grid nodes).

We choose N-continuous basis functions $\phi_i(\mathbf{x}_\perp)$ described for every local element Ω_k. The basis function is equal to 1 at node-location $\mathbf{x}_i$ and 0 at all others, and

is only non-zero for every $\mathbf{x}_\perp$ at the elements that share the respective $i-$node. Therefore, we employ the Galerkin's discretization to relation II.6 by approximating the continuous wavefield $\hat{p}$ with a polynomial approximation, $\hat{P}$, using the piecewise basis polynomials ϕ_i at every node-location $\mathbf{x}_i$:

$$\hat{p}(\mathbf{x}_\perp, \omega) \approx \hat{P}(\mathbf{x}_\perp, \omega) = \sum_{i=1}^{N} \hat{\mathcal{P}}_i(\omega)\ \phi_i(\mathbf{x}_\perp), \tag{II.7}$$

where $\hat{\mathcal{P}}_i(\omega) = \hat{p}^{obs}(\mathbf{x}_i, \omega)$ are the actual values at the grid nodes/receivers $\mathbf{x}_i$. We use the same basis functions for the test functions $v(\mathbf{x}_\perp) = \phi_j(\mathbf{x}_\perp)$ for $j = 1, ..N$. Making the substitution using the discretization of the bilinear function, the result reads:

$$\tilde{\mathcal{H}}_2 \Big\langle \sum_{i=1}^{N} \hat{\mathcal{P}}_i(\omega)\phi_i, \phi_j \Big\rangle = \sum_{i=1}^{N} \hat{\mathcal{P}}_i(\omega) \Big(\int_{\mathbf{x}_\perp \in \Omega} \Big(\frac{\omega}{c'}\Big)^2\ \phi_i\ \phi_j\ d^2\mathbf{x}_\perp - \int_{\mathbf{x}_\perp \in \Omega} \boldsymbol{\nabla}_\perp \phi_i\ \boldsymbol{\nabla}_\perp \phi_j\ d^2\mathbf{x}_\perp \Big). \tag{II.8}$$

In the bilinear formula, we isolate the effect of the operator only for the basis functions of our elements. The result becomes:

$$\tilde{\mathcal{H}}_2 \langle \phi_i, \phi_j \rangle = \int_{\mathbf{x}_\perp \in \Omega} \Big(\frac{\omega}{c'}\Big)^2\ \phi_i\ \phi_j\ d^2\mathbf{x}_\perp - \int_{\mathbf{x}_\perp \in \Omega} \boldsymbol{\nabla}_\perp \phi_i\ \boldsymbol{\nabla}_\perp \phi_j\ d^2\mathbf{x}_\perp. \tag{II.9}$$

This definition of the differentiation operator can be expressed as a square matrix operator in a linear system:

$$\tilde{\mathcal{H}}_2 \langle \phi_i, \phi_j \rangle \rightarrow \hat{\mathbf{H}}_2 = \omega^2\ \mathbf{M}^s + \mathbf{M}^\rho - \mathbf{K}, \tag{II.10}$$

where matrix $\hat{\mathbf{H}}_2$ is a N x N matrix. The matrices employed in this case can be estimated independently of the angular frequency employed. Using the relation II.3 of the modified velocity, we have split the "Mass Matrix" into "Slowness Matrix", which is related to the time differentiation using the angular frequency, and the "Density Matrix". The Slowness Matrix is defined as:

$$\mathbf{M}^s \rightarrow M^s_{ij} = \int_{\mathbf{x}_\perp \in \Omega} \frac{1}{c^2}\ \phi_i\ \phi_j\ d^2\mathbf{x}_\perp, \tag{II.11}$$

where $c = c_P(\mathbf{x}_\perp)$. The Density Matrix is presented as:

II

$$\mathbf{M}^{\rho} \rightarrow M_{ij}^{\rho} = \int_{\mathbf{x}_{\perp} \in \Omega} \left(\frac{\left(\boldsymbol{\nabla}_{\perp}^{2} \rho\right)}{2\rho} - \frac{3\left(\boldsymbol{\nabla}_{\perp} \rho\right) \cdot \left(\boldsymbol{\nabla}_{\perp} \rho\right)}{4\rho^{2}} \right) \phi_i \, \phi_j \, d^2\mathbf{x}_{\perp}, \qquad \text{(II.12)}$$

where $\rho = \rho(\mathbf{x}_{\perp})$. These two terms introduce the discretized version of the lateral variations of the medium properties into the differentiation operator. The last matrix is the "Stiffness Matrix":

$$\mathbf{K} \rightarrow K_{ij} = \int_{\mathbf{x}_{\perp} \in \Omega} \boldsymbol{\nabla}_{\perp} \phi_i \, \boldsymbol{\nabla}_{\perp} \phi_j \, d^2\mathbf{x}_{\perp}, \qquad \text{(II.13)}$$

where $\mathbf{K}$ is positive semi-definite. This last term is the most sensitive to the array design. This turns the discretized Helmholtz differentiation operator into a symmetric matrix, similar to Grimbergen et al. (1998), but adapted also for irregular designs in acquisition arrays such as in the proposed geometry in annex 1.

This estimation of the differentiation operator allows to include all the available information about the near-surface parameters. However, the utility of this information into the differentiation operator is limited to the observation points $\mathbf{x}_i$ at the main nodes of the grid. For the specific array design proposed in annex 1, the element generation produces ill-conceived elements at the edges of the array. These elements can be removed in order to simplify the array matrix system and also because their location is marginal and contribution is not significant.

One-way wavefield differentiation operators are driven by the so-called square-root operator $\hat{\mathcal{H}}_1$. Since the Helmholtz operator matrix is positive and symmetric, we may apply the modal decomposition of $\hat{\mathbf{H}}_2$ in order to estimate the square-root operator (Grimbergen et al., 1998). This operator estimate, $\hat{\mathbf{H}}_1$, applies for the wavefields at the receiver location/nodes only.

The implementation of acoustic power-flux normalized wavefield decomposition (Wapenaar, 1998) is now possible for irregular arrays with the square-root operator estimate. The same approach can be utilized to adapt the elastic wavefield decomposition, using the corresponding formulation with power-flux normalization (Ursin, 1983; Wapenaar et al., 2008a).

II.4 Conclusions

We present an adapted scheme in the estimation of one-way wavefield decomposition operators for irregular acquisition arrays in media with laterally varying conditions. We approximate the differentiation operators with finite-elements between the receivers. This process works in the space-frequency domain. Regarding its passive seismic applications, it can be implemented to different array designs

and allows to include all available information of the near-surface parameters in laterally variant media.

II

Interferometry with incomplete illumination

4 Passive interferometric imaging with directionally constrained migration[§]

Passive seismic interferometry enables the estimation of the reflection response or Green's functions of the subsurface, using passive- receiver recordings at the surface from sources located relatively deep in the Earth. The retrieved data can be used in interferometric imaging in order to image the subsurface. Successful interferometric imaging relies upon the availability of passive records from sufficient sources in the subsurface that illuminate the receivers from all possible angles. Such a condition is difficult to meet in practical applications. Incomplete passive-source distributions result in the retrieval of inaccurate Green's functions containing artefacts that can disturb the interferometric imaging process.

We propose an alternative imaging method for passive data based on illumination diagnosis and directionally constrained migration. In this method, passive gathers from single transient sources are cross-correlated individually. The dominant radiation direction of each virtual source in each correlated gather is estimated. The correlated gathers are imaged individually using an adapted migration algorithm that takes the dominant radiation direction of the virtual source exclusively. In this way, correct partial subsurface images can be constructed from individual passive sources. These images employ only the energy in the stationary phase region (Fresnel zone) of the correlated passive source for each virtual source. The energy employed during the migration process is hence limited to useful information and the final result has a significantly reduced amount of migrated interferometric artefacts.

We also show that the summation of all individual image results together improves the subsurface image by constructive interference, while migrated crosstalk

[§]First part of this chapter has been published as an extended abstract in the *82nd SEG annual meeting, Las Vegas, SPMI E-P1.6.*, (Almagro Vidal et al., 2012).

and artefacts interfere destructively. This process, which we call Image Interferometry (II), shows the interferometric integration can rather be applied in the image domain and not in the shot gather domain in case of limited subsurface illumination, hence eliminating the need for the retrieval of the reflection response as an intermediate step.

4.1 Introduction

Seismic interferometry (SI) aims to reconstruct the impulse response between receivers, with a virtual source located at the position of one of them. To accomplish this, its application into passive seismics requires to have passive sources illuminating the receivers uniformly from the subsurface and, depending on the scattering properties of the medium, at all possible angles. The retrieval of the reflection response results from the correlation of the superposition of recordings from the passive sources at the virtual-source receiver location with respect to other receiver's. The reflection response results from constructive interference of events in stationary phase regions (Fresnel zones) between the pair of receivers, together with the suppression of the remainder of correlated events which are not in the stationary phase zone.

Examples of SI applied to passive seismics can be seen in Draganov et al. (2006) and Draganov et al. (2010). The authors applied crosscorrelation to retrieve virtual-source records which were consecutively employed into depth migration. Other uses of this conventional passive SI imaging are shown in Poli et al. (2012b), Boué et al. (2013), Nakata et al. (2015) and Olivier et al. (2015). To apply SI successfully, isotropic illumination is needed for the retrieval of the desired reflections from complete constructive interference and suppression of correlation artefacts from complete destructive interference. Incomplete illumination can result in the retrieval of spurious events that can deteriorate the interferometric image. The use of a single passive source does not result in destructive interference of correlated artefacts which are misinterpreted during the migration process. The goal is to migrate these incomplete gathers, minimizing the features produced by the migration artefacts and correlated events not at stationary phase.

The migration of correlated data from a single source in the subsurface has been referred to as interferometric imaging (II) (Schuster et al., 2004). Nowack et al. (2006) showed another example of migration from correlated data from single sources, carried out in this case by using slant-stack windows of the data and migrating the autocorrelated data by means of Gaussian beams.

The challenge of migrating data from single passive sources in the subsurface is to employ the useful information. This chapter illustrates how the data that is migrated can be limited to the events at stationary phase with the acquisition array. This is achieved in the image domain by applying directional constraints during the migration process.

4.2 Correlation function

For transient sources, Wapenaar & Fokkema (2006) introduce a relation for acoustic media to retrieve the Green's function $\hat{G}(\mathbf{x}_\mathcal{A}, \mathbf{x}_0, \omega)$ between a receiver at $\mathbf{x}_\mathcal{A}$ and a virtual source at $\mathbf{x}_0$ from recordings at these two points of a continuous distribution of passive sources (individually located at $\mathbf{x}_\mathcal{B}$). In a passive seismic configuration with an aquisition array at or near the free-surface, the retrieval stands for the reflection response of the medium from the same acquisition-array level. This relation is represented for one-way wavefields as (Appendix 4.A, equation 4.31):

$$\left(\hat{R}^{\smile}(\mathbf{x}_\mathcal{A}, \mathbf{x}_0, \omega) - \left\{\hat{R}^{\curvearrowright\!\!\smile}(\mathbf{x}_\mathcal{A}, \mathbf{x}_0, \omega)\right\}^*\right) = \int_{\mathbf{x}_\mathcal{B}\in\partial\mathbb{D}_\mathcal{B}} \Big\{\hat{G}^{-,-}(\mathbf{x}_\mathcal{A}, \mathbf{x}_\mathcal{B}, \omega)\left\{\hat{G}^{+,-}(\mathbf{x}_0, \mathbf{x}_\mathcal{B}, \omega)\right\}^* - \hat{G}^{-,+}(\mathbf{x}_\mathcal{A}, \mathbf{x}_\mathcal{B}, \omega)\left\{\hat{G}^{+,+}(\mathbf{x}_0, \mathbf{x}_\mathcal{B}, \omega)\right\}^*\Big\} d^2\mathbf{x}_\mathcal{B}, \quad (4.1)$$

where $\{\}^*$ denotes complex conjugation, ω is the angular frequency and ' $\hat{}$ ' indicates the wavefield is in the frequency domain; $\hat{G}^{-/+,-/+}(\mathbf{x}_0, \mathbf{x}_\mathcal{B}, \omega)$ are the up/downgoing-source, up/downgoing-receiver wavefield representations in the Fourier domain (minus stands for upgoing and plus for downgoing, first superscript holds for the receiver wavefield at $\mathbf{x}_0$ while the last does for the source wavefield at $\mathbf{x}_\mathcal{B}$). The result of the integration consists of the desired impulse reflection response $\hat{R}^{\smile}(\mathbf{x}_\mathcal{A}, \mathbf{x}_0, \omega)$ (this is the representation for a downgoing-source at $\mathbf{x}_0$ and upgoing-receiver wavefield at $\mathbf{x}_\mathcal{A}$: $\hat{G}^{-,+}$) and the time reversed impulse reflection response $\left\{\hat{R}^{\curvearrowright\!\!\smile}(\mathbf{x}_\mathcal{A}, \mathbf{x}_0, \omega)\right\}^*$ (which is the representation for an upgoing-source and downgoing-receiver wavefield: $\hat{G}^{+,-}$). Wavefield quantities represented here are power-flux normalized. Equation 4.1 transformed to the time domain represents a cross-correlation product between one-way source and receivers wavefields at receiver locations $\mathbf{x}_\mathcal{A}$ and $\mathbf{x}_0$.

Since source-wavefield decomposition is not possible at the receiver level without complete one-sided reflectivity data, we approximate equation 4.1 using the one-way receiver-wavefield quantities:

$$\left(\hat{R}^{\smile}(\mathbf{x}_\mathcal{A}, \mathbf{x}_0, \omega) - \left\{\hat{R}^{\curvearrowright\!\!\smile}(\mathbf{x}_\mathcal{A}, \mathbf{x}_0, \omega)\right\}^*\right) = \int_{\mathbf{x}_\mathcal{B}\in\partial\mathbb{D}_\mathcal{B}} \hat{G}^{-}(\mathbf{x}_\mathcal{A}, \mathbf{x}_\mathcal{B}, \omega)\left\{\hat{G}^{+}(\mathbf{x}_0, \mathbf{x}_\mathcal{B}, \omega)\right\}^* d^2\mathbf{x}_\mathcal{B} - 'ghost', \quad (4.2)$$

where $\hat{G}^{-/+}$ with one superscript refers to receiver-decomposed wavefields only. The second wavefield interaction quantity in the integral we are referring to it as the interferometric ghost quantity. This term stands for the crosstalk produced in right hand side of equation 4.2 by the upgoing-source wavefield correlation product with the downgoing-source wavefield, and *vice versa*. The ghost wavefield quantity vanishes if the medium is considered homogeneous below the boundary $\partial\mathbb{D}_{\mathcal{B}}$.

The crosstalk of the ghost when approximating equation 4.1 into 4.2 introduces artefacts in the reflection response retrieval. Within the correlation product in equation 4.2, the correlations that corresponds to the product of the upgoing-source with upgoing-source wavefields is invariant with respect to the source location. However the crosstalk from the interferometric ghost, caused by the correlation of opposite source-wavefields, will vary in time. In the case of constant band-limited source signals and an irregular source distribution at $\mathbf{x}_{\mathcal{B}}$ with respect to the normal of $\partial\mathbb{D}_{\mathcal{B}}$, during the integration the crosstalk introduced by the ghost quantity suffers of destructive interference and lessens its imprint. The destructive interference is optimal when the source location variations between consecutive source locations varies proportionally to half of the source-signal wavelength. Following this assumption we write the adapted one-way wavefield representation for seismic interferometry by crosscorrelation in acoustic media as:

$$\left(\hat{R}^{\smile}(\mathbf{x}_{\mathcal{A}},\mathbf{x}_0,\omega)-\left\{\hat{R}^{\curvearrowleft\!\!\smile}(\mathbf{x}_{\mathcal{A}},\mathbf{x}_0,\omega)\right\}^*\right)\,\|\hat{S}(\omega)\|^2\approx \int_{\partial\mathbb{D}_{\mathbf{x}_{\mathcal{B}}}}\hat{p}^{-}(\mathbf{x}_{\mathcal{A}},\mathbf{x}_{\mathcal{B}},\omega)\left\{\hat{p}^{+}(\mathbf{x}_0,\mathbf{x}_{\mathcal{B}},\omega)\right\}^* d^2\mathbf{x}_{\mathcal{B}}, \quad (4.3)$$

where $\hat{p}^{-/+}(\mathbf{x}_0,\mathbf{x}_B,\omega)$ are the up/down-going representation, power-flux normalized components of the observed two-way wavefield $\hat{v}_3^{obs}$ (vertical particle velocity) in the Fourier domain: $\hat{p}^{+}(\mathbf{x}_0,\mathbf{x}_{\mathcal{B}},\omega)=\hat{G}^{+}(\mathbf{x}_0,\mathbf{x}_{\mathcal{B}},\omega)\hat{S}(\omega)$. The observed wavefield is defined as the Fourier transform of the impulsive transmission response at receiver $\mathbf{x}_0$ due to a source at $\mathbf{x}_{\mathcal{B}}$, multiplied with the Fourier transform of the transient source signal $\hat{S}(\omega)$. The retrieved result is multiplied by the power spectrum of the source signals $\|\hat{S}(\omega)\|^2=\hat{S}^2(\omega)=\hat{S}(\omega)\{\hat{S}(\omega)\}^*$.

The correct estimation of the reflection response with equation 4.3 requires the cross-correlation of records from uniformly distributed passive sources with the same source signal $\hat{S}(\omega)$, that illuminate the receivers from all possible angles. In many cases, passive sources are sparsely distributed and clustered. Then we carry out the approximation by discretizing expression 4.3 making use of the correlation function:

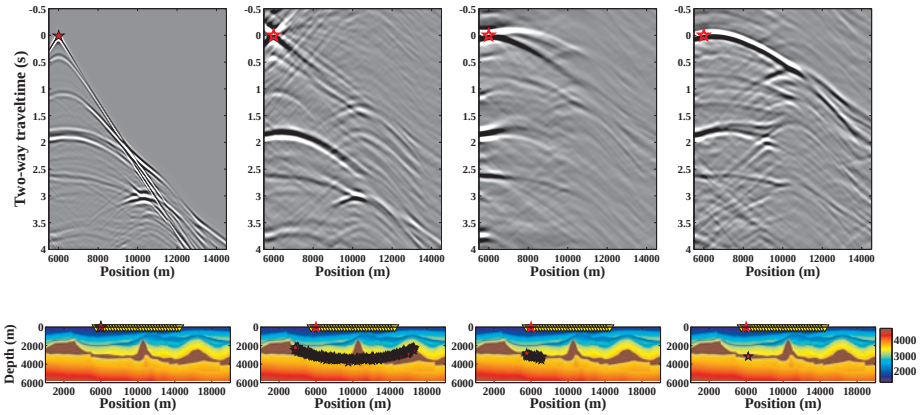

(a) *Reference* $R^{\smile}$ **(b)** $R^{\smile} \propto \sum_{x_{\mathcal{B}}} C_{x_{\mathcal{B}}}$ **(c)** $R^{\smile} \not\propto \sum_{x_{\mathcal{B}}} C_{x_{\mathcal{B}}}$ **(d)** $C_{x_{\mathcal{B}}}$

Figure 4.1: *Three different interferometric results using SI by crosscorrelation. Retrieved shot gathers are shown on top, source distribution inside the acoustic velocity model are displayed below them.* ***(a)*** *Reference reflection response* $R^{\smile}$. ***(b)*** *Scenario with equipartitioned illumination from the subsurface.* ***(c)*** *Same result from a limited clustered source distribution.* ***(d)*** *Result obtained from single source in the subsurface.*

$$\left(\hat{R}^{\smile}\left(\mathbf{x}_{\mathcal{A}},\mathbf{x}_0,\omega\right)-\left\{\hat{R}^{\curvearrowleft\smile}\left(\mathbf{x}_{\mathcal{A}},\mathbf{x}_0,\omega\right)\right\}^*\right)\|\hat{S}(\omega)\|^2 \propto \sum_{\mathbf{x}_{\mathcal{B}}}\hat{C}\left(\mathbf{x}_{\mathcal{A}},\mathbf{x}_0,\mathbf{x}_{\mathcal{B}},\omega\right), \quad (4.4)$$

where $\hat{C}\left(\mathbf{x}_0,\mathbf{x}_{\mathcal{A}},\mathbf{x}_{\mathcal{B}},\omega\right)$ defines the correlation function of a single passive source at $\mathbf{x}_{\mathcal{B}}$, described as follows:

$$\hat{C}\left(\mathbf{x}_{\mathcal{A}},\mathbf{x}_0,\mathbf{x}_{\mathcal{B}},\omega\right) \rightarrow \hat{C}_{\mathbf{x}_{\mathcal{B}}}\left(\mathbf{x}_{\mathcal{A}},\mathbf{x}_0,\omega\right) = \hat{p}^{-}\left(\mathbf{x}_{\mathcal{A}},\mathbf{x}_{\mathcal{B}},\omega\right)\left\{\hat{p}^{+}\left(\mathbf{x}_0,\mathbf{x}_{\mathcal{B}},\omega\right)\right\}^*. \quad (4.5)$$

Figure 4.1 shows three different interferometric results using SI by crosscorrelation in an acoustic medium. For this results we only consider the causal part of the left-hand side of equation 4.4, i.e., $R^{\smile}$. The case in figure 4.1b shows a complete retrieval of the reflection response due to a homogeneous source distribution in the subsurface. This result resembles the reference response in figure 4.1a. The lower figure displays the acoustic velocity model with the source distribution

surrounding the acquisition array. In this scenario, the estimation of the reflected events by constructive interference is optimal while the destructive interference of correlation artefacts and spurious events is satisfactory. The case in figure 4.1c presents the retrieved reflection result with a limited amount of sources, clustered in one region of the subsurface. The retrieved result shows the constructive interference is limited to the reflection events that can be obtained for that limited illumination range, but the destructive interference still manages to eliminate the correlation events not in stationary phase with the array. The case in figure 4.1d displays the result obtained from a single source (correlation function), where no constructive nor destructive interference can be achieved. The correlated events seem to match with the reflectors from scenario 4.1a, yet they show incorrect correlated times since they are not in stationary phase with the source-receivers geometry. In this chapter we assume the integration of individual passive recordings in equation 4.4 is not attainable. Hence, the focus lies on making use of the data in the correlation function $\hat{C}_{\mathbf{x}_\mathcal{B}}$ that is exclusively in stationary phase to migrate, and in the process avoid the rest of correlated artefacts.

4.3 Migration scheme

The reflection of the incident field into the array from a source in the subsurface brings information about the scattered field from reflectors in the subsurface.

In Figures 4.2a-c we illustrate the process of retrieving a reflection response between two receivers. The specular ray from the source (the direct arrival to the first receiver, to become virtual source at $\mathbf{x}_0$) defines the direction around which the correct retrieved reflection ray can be found in depth. For each passive source - virtual source pair, there is a unique ray-parameter that defines this specular ray. We will make use of this knowledge by using only this ray-parameter during II.

Almagro Vidal et al. (2014) (chapter 2 of this thesis) introduced a method to determine the dominant ray-parameter of a correlated gather at a specific virtual source location. The aim of the method was a qualitative analysis: to separate shot records which are dominated by surface waves from those responsible for the retrieval of body-wave reflections. The illumination diagnosis results also provides a quantitative analysis of the specular ray direction of the direct wave (Figure 4.2b). This quantification must not be applied on the correlation function but on the very similar virtual-source function Γ (also been referred as point-spread function in previous chapter):

$$\hat{\Gamma}(\mathbf{x}_\mathcal{A}, \mathbf{x}_0, \mathbf{x}_\mathcal{B}, \omega) \rightarrow \hat{\Gamma}_{\mathbf{x}_\mathcal{B}}(\mathbf{x}_\mathcal{A}, \mathbf{x}_0, \omega) = \hat{p}^+(\mathbf{x}_\mathcal{A}, \mathbf{x}_\mathcal{B}, \omega)\left\{\hat{p}^+(\mathbf{x}_0, \mathbf{x}_\mathcal{B}, \omega)\right\}^*. \quad (4.6)$$

In case of receivers in $\mathbf{x}_\mathcal{A}$ and $\mathbf{x}_0$ to be located at the free-surface, there is no

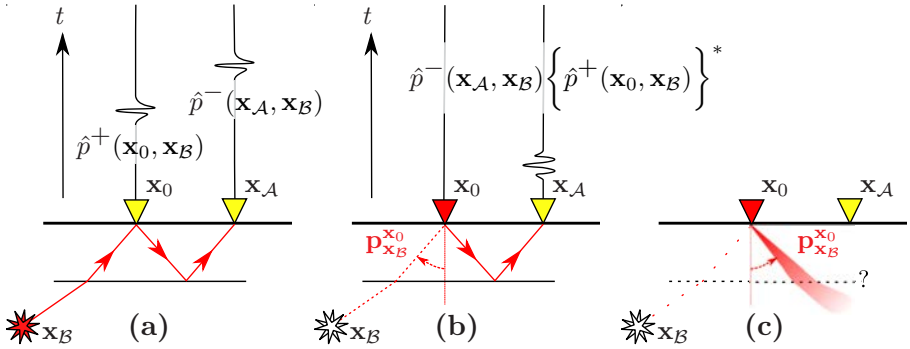

Figure 4.2: *Illustration of directionally constrained passive seismic migration from a subsurface source (red star) using two receivers (yellow triangles).* ***(a)*** *A receiver at $\boldsymbol{x}_\mathcal{A}$ records a field originating from a subsurface source ($\boldsymbol{x}_\mathcal{B}$) after being scattered by a reflector. A receiver at $\boldsymbol{x}_0$ records the direct field from the source. The source is along the specular ray passing through the receivers.* ***(b)*** *The cross-correlation of the response at $\boldsymbol{x}_\mathcal{A}$ with the one at $\boldsymbol{x}_0$ would retrieve the reflection response at $\boldsymbol{x}_\mathcal{A}$ as if a virtual source was located at receiver $\boldsymbol{x}_0$ (red triangle). The locations of the source and virtual source define a unique ray-parameter ($\boldsymbol{p}^{\boldsymbol{x}_0}_{\boldsymbol{x}_\mathcal{B}}$).* ***(c)*** *The value of this ray-parameter defines the direction in which the reflector is to be located with respect to the virtual source. Only this ray-parameter is needed (not the location of the passive source $\boldsymbol{x}_\mathcal{B}$) in order to find the desired stationary-phase region.*

difference between the virtual-source function Γ and the correlation function C except for a polarity reversal of the correlated events. As mentioned before, the dominant ray-parameter defines the specular ray with respect to the virtual-source location. We may analyze the ray-parameter distribution of the virtual-source function using a linear-slant stack:

$$\widetilde{\Gamma}_{\mathbf{x}_\mathcal{B}}(\mathbf{x}_0, \mathbf{p}) = \int \Gamma_{\mathbf{x}_\mathcal{B}}\left(\mathbf{x}_\mathcal{A}, \mathbf{x}_0, \mathbf{p} \cdot (\mathbf{x}_\mathcal{A} - \mathbf{x}_0)\right) d^2\mathbf{x}_\mathcal{A}, \tag{4.7}$$

where $\mathbf{p}$ is the ray-parameter vector and $\widetilde{\Gamma}_{\mathbf{x}_\mathcal{B}}$ is the illumination distribution of the virtual-source function in the $\tau - p$ domain at $\tau = 0$ s for each virtual source $\mathbf{x}_0$. When the distance of the passive source to the acquisition array is of the same order of magnitude of the array aperture, a linear slant-stack does not suffice and a parabolic approximation is required for better precision on the ray-parameter analysis of the virtual-source radiation. The dominant ray-parameter that defines the illumination of the record at the virtual-source location is defined by:

$$\mathbf{p}^{\mathbf{x}_0}_{\mathbf{x}_\mathcal{B}} \Rightarrow \widetilde{\Gamma}_{\mathbf{x}_\mathcal{B}}(\mathbf{x}_0, \mathbf{p}^{\mathbf{x}_0}_{\mathbf{x}_\mathcal{B}}) = \left\|\widetilde{\Gamma}_{\mathbf{x}_\mathcal{B}}(\mathbf{x}_0, \mathbf{p})\right\|_{max}. \tag{4.8}$$

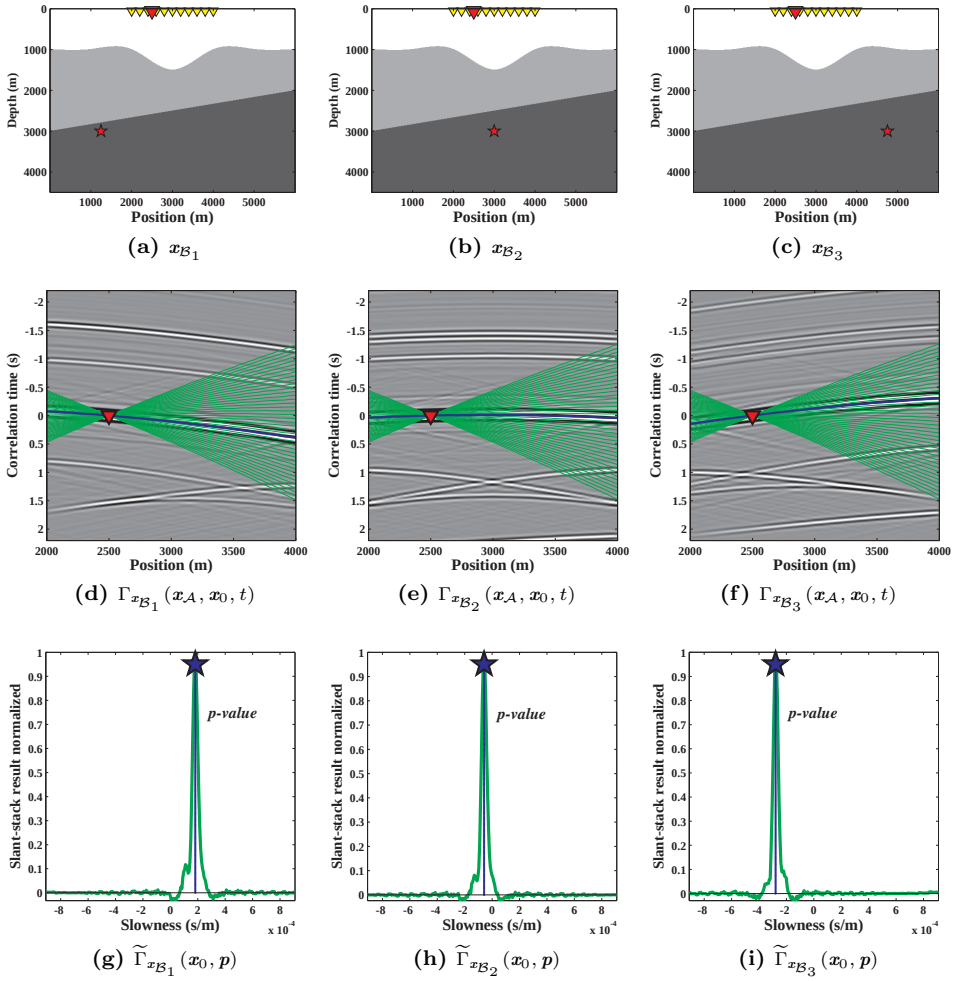

(a) $x_{\mathcal{B}_1}$ **(b)** $x_{\mathcal{B}_2}$ **(c)** $x_{\mathcal{B}_3}$

(d) $\Gamma_{x_{\mathcal{B}_1}}(\boldsymbol{x}_{\mathcal{A}}, \boldsymbol{x}_0, t)$ **(e)** $\Gamma_{x_{\mathcal{B}_2}}(\boldsymbol{x}_{\mathcal{A}}, \boldsymbol{x}_0, t)$ **(f)** $\Gamma_{x_{\mathcal{B}_3}}(\boldsymbol{x}_{\mathcal{A}}, \boldsymbol{x}_0, t)$

(g) $\widetilde{\Gamma}_{x_{\mathcal{B}_1}}(\boldsymbol{x}_0, \boldsymbol{p})$ **(h)** $\widetilde{\Gamma}_{x_{\mathcal{B}_2}}(\boldsymbol{x}_0, \boldsymbol{p})$ **(i)** $\widetilde{\Gamma}_{x_{\mathcal{B}_3}}(\boldsymbol{x}_0, \boldsymbol{p})$

Figure 4.3: *Results obtained from illumination diagnosis from three different sources in the same acoustic medium.* ***(a)***,***(b)*** *and* ***(c)*** *Passive source location (green star) and receiver array (yellow triangles) displayed inside the acoustic velocity model.* ***(d)***,***(e)*** *and* ***(f)*** *Virtual-source functions* $\Gamma_{x_{\mathcal{B}}}(\boldsymbol{x}_{\mathcal{A}}, \boldsymbol{x}_0, t)$ *at virtual source* $x_0 = 2500\ m$ *from each individual source of (a), (b) and (c). Illumination diagnosis analyzes the energy distribution in ray-parameters of the virtual source radiation (green lines), in order to locate the dominant direction of the most energetic arrivals from the passive source (blue line) into the acquisition array.* ***(g)***,***(h)*** *and* ***(i)*** *ray-parameter distribution* $\widetilde{\Gamma}_{x_{\mathcal{B}}}(\boldsymbol{x}_0, \boldsymbol{p})$ *with the dominant direction represented by* $\boldsymbol{p}_{x_{\mathcal{B}}}^{x_0}$ *(blue star).*

A display of the illumination distribution of a virtual-source function $\widetilde{\Gamma}_{\mathbf{x}_\mathcal{B}}$ is shown in figures 4.3g, 4.3h and 4.3i (with their respective dominant ray-parameter or $p-$value), corresponding to the parabolic slant-stack applied on the virtual source functions in figures 4.3d, 4.3e and 4.3f, respectively. All results correspond to the model scenario described in figures 4.3a, 4.3b and 4.3c, with the same virtual source.

Since from the cross-correlation we obtain correct reflections for this specific ray-parameter only, we require a directionally constrained migration scheme. The method we propose here is an adaptation from the work of Popov et al. (2010), where the imaging condition is defined by the correlation of a forward wavefield with the backprojection of the recorded field; in our configuration, both fields emitted from the virtual-source and receiver locations, respectively. This method uses high-frequency asymptotics of Gaussian beams to reconstruct the Green's functions with the advantage of approximating the wavefield when adding the beams in different directions together. Every individual Gaussian beam is defined by its ray-centred coordinates $s(\mathbf{x})$ and $\mathbf{n}(\mathbf{x})$ of any location $\mathbf{x}$ of the medium in the proximity of the beam (Červený et al., 1982). In Popov et al. (2010), the Green's function from location $\mathbf{x}_0$ into any point in the medium $\mathbf{x}$ is represented as the integration of individual Gaussian beams ($\hat{u}^{GB}$) over different directions (described by azimuthal and polar angles θ and ϕ). This is shown as:

$$\hat{G}(\mathbf{x},\mathbf{x}_0,\omega) = \int_0^{\pi}\int_0^{2\pi} \hat{\Xi}(\theta,\phi,\omega)\hat{u}^{GB}(s,\mathbf{n},\mathbf{x}_0,\theta,\phi,\omega)d\theta d\phi, \tag{4.9}$$

where the ray-centred coordinates s and $\mathbf{n}$ define the observation location $\mathbf{x}$ associated with the beams passing its proximity. $\hat{\Xi}$ are the initial amplitudes of the Gaussian beams (Popov, 1982). For power-flux normalized wavefields (Wapenaar, 1998), Gaussian beams $\hat{u}^{GB}$ are additionally scaled using an amplitude correction along the central-ray coordinate s: $c_P(\mathbf{x}_0)\sqrt{\frac{\rho(s)}{2j\omega q(s)}}$, where $c_P(\mathbf{x}_0)$ is the compressional velocity of the medium at the virtual-source location; $\rho(s)$ and $q(s)$ are the medium density and vertical slowness along the central-ray coordinate.

For the passive-seismic case with isotropic illumination, the full forward impulse response should be used for migration. For partial migration of the correlation function $C_{\mathbf{x}_\mathcal{B}}(\mathbf{x}_\mathcal{A},\mathbf{x}_0,\mathbf{x}_\mathcal{B},t)$ of a single source, the forward wavefield is to be limited to the dominant illumination direction only.

Using the results from the illumination diagnosis previously described, we aim to enhance the illumination obtained from the direct arrivals imposing the radiation pattern described by the virtual-source function. Making use of the medium velocity $c_P(\mathbf{x}_0)$ at the virtual source location, we convert the coordinates of the virtual-source function from ray-parameters into angular directions: $\widetilde{\Gamma}_{\mathbf{x}_\mathcal{B}}(\mathbf{x}_0,\theta,\phi) = \widetilde{\Gamma}_{\mathbf{x}_\mathcal{B}}(\mathbf{x}_0,\mathbf{p})$, using the relation $\mathbf{p}(\theta,\phi) = (\frac{cos(\theta)sin(\phi)}{c_P}, \frac{sin(\theta)sin(\phi)}{c_P})$. The approximated Green's function due to a directionally constrained virtual-

source located at $\mathbf{x}_0$ evaluated at $\mathbf{x}$ is weighted according to the radiation pattern described by the normalized ray-parameter distribution of the virtual-source function $\widetilde{\Gamma}_{\mathbf{x}_\mathcal{B}}$ (as the ones shown in figures 4.3g, 4.3h and 4.3i):

$$\hat{G}^{GB}_{\mathbf{x}_\mathcal{B}}(\mathbf{x},\mathbf{x}_0,\omega) = \int_0^{\pi}\int_0^{2\pi} \widetilde{\Gamma}_{\mathbf{x}_\mathcal{B}}(\mathbf{x}_0,\theta,\phi)\,\hat{\Xi}(\theta,\phi,\omega)\,\hat{u}^{GB}(s,\mathbf{n},\mathbf{x}_0,\theta,\phi,\omega)\,d\theta d\phi. \quad (4.10)$$

For simplicity, equation 4.10 can be simplified according to the direction to which the ray-parameter distribution $\mathbf{p}^{\mathbf{x}_0}_{\mathbf{x}_\mathcal{B}}(\theta,\phi)$ peaks maximum:

$$\hat{G}^{GB}_{\mathbf{x}_\mathcal{B}}(\mathbf{x},\mathbf{x}_0,\omega) \propto \hat{\Xi}(\mathbf{p}^{\mathbf{x}_0}_{\mathbf{x}_\mathcal{B}},\omega)\,\hat{u}^{GB}(s,\mathbf{n},\mathbf{x}_0,\mathbf{p}^{\mathbf{x}_0}_{\mathbf{x}_\mathcal{B}},\omega). \quad (4.11)$$

Therefore, $\hat{G}^{GB}_{\mathbf{x}_\mathcal{B}}(\mathbf{x},\mathbf{x}_0,\omega)$ is now constructed by a single Gaussian beam in the direction of radiation direction of the passive source $\mathbf{p}^{\mathbf{x}_0}_{\mathbf{x}_\mathcal{B}}$.

The forward or downgoing wavefield ($D^{\Downarrow}$, figure 4.4a) at the instant t_0 is generated at the virtual source position $\mathbf{x}_0$ by using the Green's function approximation of expression 4.11:

$$D^{\Downarrow}_{\mathbf{x}_\mathcal{B}}(\mathbf{x},\mathbf{x}_0,t_0) \approx \frac{1}{\pi}\Re\int_0^{\infty} \hat{G}^{GB}_{\mathbf{x}_\mathcal{B}}(\mathbf{x},\mathbf{x}_0,\omega)\,\hat{S}_{\mathbf{x}_\mathcal{B}}(\omega)\,e^{-i\omega t_0}\,d\omega, \quad (4.12)$$

where $\hat{S}_{\mathbf{x}_\mathcal{B}}(\omega)$ stands for the source signal of the passive source, directly estimated from the direct wave arrival in case of a transient signal, or indirectly from the virtual-source function $\Gamma_{\mathbf{x}_\mathcal{B}}$ at correlated time $\tau = 0\ s$.

The correlated function is transformed into its asymptotic form in terms of Gaussian beams:

$$\hat{C}^{GB}_{\mathbf{x}_\mathcal{B}}(s,\mathbf{n},\mathbf{x}_0,\theta,\phi,\omega) = \left\{\hat{\Xi}(\theta,\phi,\omega)\right\}^{*}\int_{\mathbf{x}_\mathcal{A}} \left\{\hat{u}^{GB}(s,\mathbf{n},\mathbf{x}_\mathcal{A},\theta,\phi,\omega)\right\}^{*}\hat{C}_{\mathbf{x}_\mathcal{B}}(\mathbf{x}_\mathcal{A},\mathbf{x}_0,\omega)d^2\mathbf{x}_\mathcal{A}. \quad (4.13)$$

We adapt the Kirchhoff integral to the boundary defined by the horizontal receiver array. For the backprojection of the recorded field ($U^{\Uparrow}_{\mathbf{x}_\mathcal{B}}$, figure 4.4b), we build the asymptotic form of the correlated function using the Gaussian beam approximation from expression 4.9. Therefore, the backprojected or upgoing wavefield at an instant t_0 is calculated to the imaging locations $\mathbf{x}$ summing the Gaussian beams in all directions:

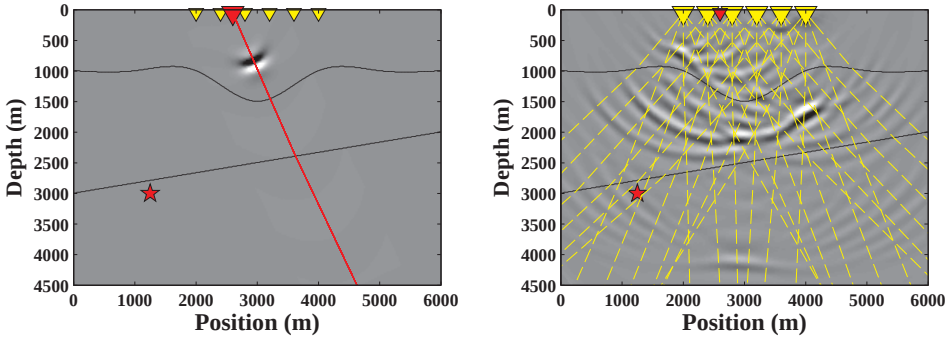

(a) $D^{\Downarrow}_{x_{\mathcal{B}_1}}(\boldsymbol{x}, \boldsymbol{x}_0)$ **(b)** $U^{\Uparrow}_{x_{\mathcal{B}_1}}(\boldsymbol{x}, \boldsymbol{x}_0)$

Figure 4.4: *Construction of the downgoing and upgoing imaging wavefields due to the passive source and model depicted in figure 4.3a, and virtual source located at* $x_0 = 2600\ m$ *(red triangle), evaluated at instant* $t_0 = 0.48\ s$. ***(a)*** *Forward field limited to a single direction (red line) from the virtual-source location* $\boldsymbol{x}_0$. ***(b)*** *Backprojection of the correlation function* $C_{x_{\mathcal{B}_1}}(\boldsymbol{x}_{\mathcal{A}}, \boldsymbol{x}_0)$*, constructed after summing Gaussian beams in a limited amount of directions in the subsurface (yellow dashed lines) from the receiver locations* $\boldsymbol{x}_{\mathcal{A}}$ *(yellow triangles).*

$$U^{\Uparrow}_{\mathbf{x}_{\mathcal{B}}}(\mathbf{x}, \mathbf{x}_0, t_0) = \frac{-2}{\pi} \int_0^{\pi} \int_0^{2\pi} \Re\left\{ \int_0^{\infty} \hat{C}^{GB}_{\mathbf{x}_{\mathcal{B}}}(s, \mathbf{n}, \mathbf{x}_0, \theta, \phi, \omega) e^{-i\omega t_0}\, d\omega \right\} d\theta d\phi. \tag{4.14}$$

The upgoing term $U^{\Uparrow}_{\mathbf{x}_{\mathcal{B}}}$ contains the power spectrum of the source signal provided by the cross-correlation product $C_{\mathbf{x}_{\mathcal{B}}}(\mathbf{x}_{\mathcal{A}}, \mathbf{x}_0, t)$.

The estimation of the backprojection of the correlation function has been described here following the Gaussian beam summation method (GBS). However, unlike the forward wavefield, the construction of the backprojected wavefield is not necessary constrained to this method of wavefield reconstruction.

The two terms $D^{\Downarrow}_{\mathbf{x}_{\mathcal{B}}}$ and $U^{\Uparrow}_{\mathbf{x}_{\mathcal{B}}}$ set the imaging condition under the zero-time-lag correlation function $I_{\mathbf{x}_{\mathcal{B}}}$:

$$I_{\mathbf{x}_{\mathcal{B}}}(\mathbf{x}, \mathbf{x}_0) = \int_{t_0=0}^{T} D^{\Downarrow}_{\mathbf{x}_{\mathcal{B}}}(\mathbf{x}, \mathbf{x}_0, t_0)\, U^{\Uparrow}_{\mathbf{x}_{\mathcal{B}}}(\mathbf{x}, \mathbf{x}_0, t_0)\, dt_0, \tag{4.15}$$

where $I_{\mathbf{x}_{\mathcal{B}}}(\mathbf{x}, \mathbf{x}_0)$ is the partial image produced by the passive source $\mathbf{x}_{\mathcal{B}}$ and illuminated by the virtual source at $\mathbf{x}_0$. The contribution of every virtual source completes the partial image:

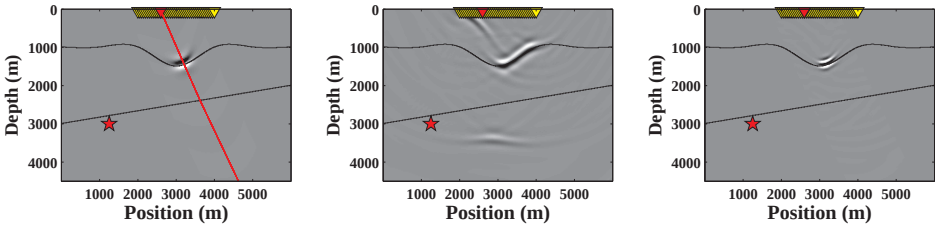

(a) $D^{\Downarrow}_{x_{\mathcal{B}_1}}(\boldsymbol{x}, \boldsymbol{x}_0)$ *at* $t_0 = 0.72$ *s.* **(b)** $U^{\Uparrow}_{x_{\mathcal{B}_1}}(\boldsymbol{x}, \boldsymbol{x}_0)$ *at* $t_0 = 0.72$ *s.* **(c)** $I_{x_{\mathcal{B}_1}}(\boldsymbol{x}, \boldsymbol{x}_0)$ *at* 0.72 *s.*

Figure 4.5: *Imaging wavefields and result at instant* $t_0 = 0.72$ *s for the model in Figure 4.3a and virtual source located at* $x_0 = 2600$ *m (red receiver):* ***(a)*** *Forward field guided on a single direction from the virtual-source location.* ***(b)*** *Backprojection of the correlation function.* ***(c)*** *Partial image result* $I_{x_{\mathcal{B}_1}}$ *by* $\boldsymbol{x}_0$ *using the correlation imaging condition between* $D^{\Downarrow}_{x_{\mathcal{B}_1}}$ *and* $U^{\Uparrow}_{x_{\mathcal{B}_1}}$ *at instant* $t_0 = 0.72$ *s.*

4

$$I_{\mathbf{x}_{\mathcal{B}}}(\mathbf{x}) = \int_{\mathbf{x}_0} I_{\mathbf{x}_{\mathcal{B}}}(\mathbf{x}, \mathbf{x}_0)\, d^2\mathbf{x}_0. \tag{4.16}$$

The result obtained in $I_{\mathbf{x}_{\mathcal{B}}}$ describes that part of the medium that can be reliably imaged for the limited ray-parameter available.

4.4 Results

We used the 2D acoustic scenarios depicted in Figures 4.3a, 4.3b and 4.3c; The three scenarios share the same acoustic model and a 41 receiver array at 50 m depth (yellow triangles, both $x_{\mathcal{A}}$ and x_0 between 2000 and 4000 m, with 50 m spacing), and a different single passive source in each one of the cases (red star).

Since virtual sources are located detached from the free surface, we employ the one-way wavefields to construct every correlation function using equation 4.5.

In figure 4.5 we show the construction of the imaging process for each correlation function. In these results no taper was applied on the array edges. To obtain the migration results we use the correlation imaging condition described in equation 4.15 (Figure 4.5c). We are interested in obtaining the image results with a similar signature as the power spectrum in the correlation function. During the construction of both wavefields, the downgoing wavefield (Figure 4.5a) and upgoing wavefield (Figure 4.5b) were multiplied in the frequency domain by a factor $\frac{-1}{i\omega}$.

Figure 4.6 shows the synthetic results for the three different source locations (passive source is represented by a red star; yellow triangles represent receivers). In order to speed up the results, only 11 out of the 41 virtual sources were employed

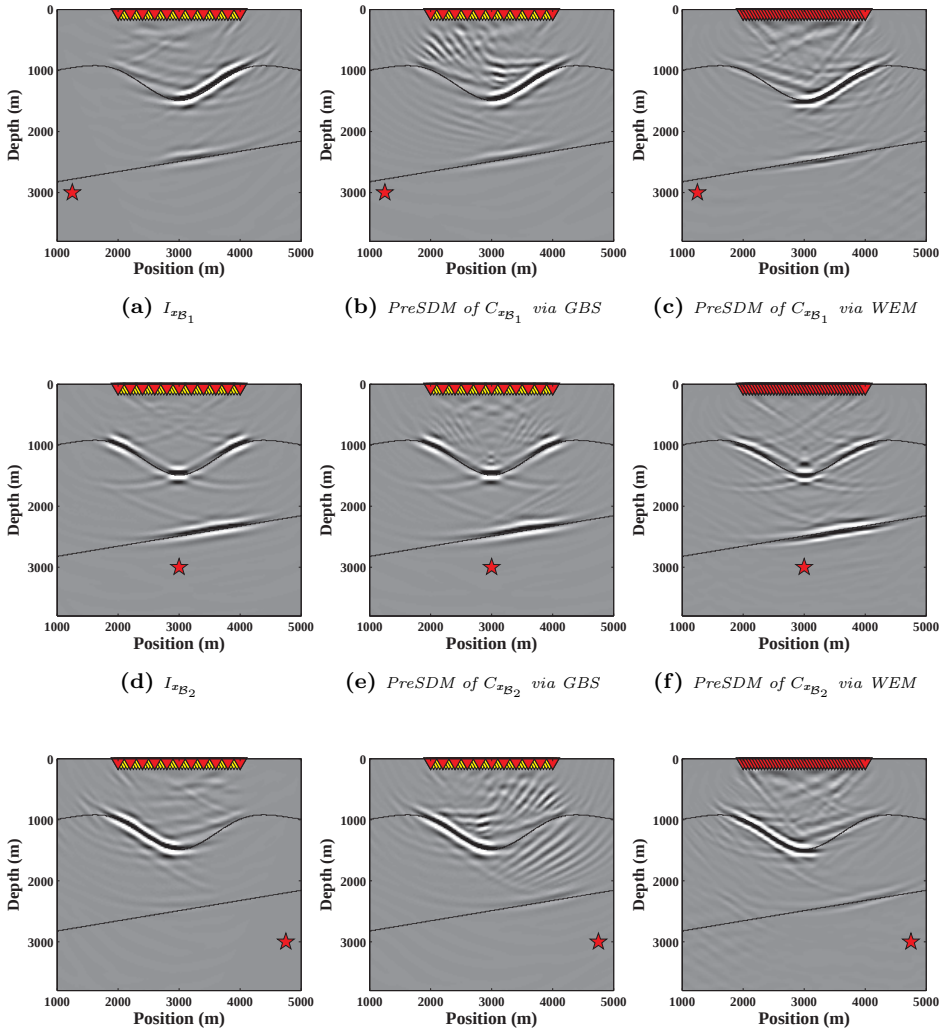

(a) $I_{x_{\mathcal{B}_1}}$ **(b)** *PreSDM of* $C_{x_{\mathcal{B}_1}}$ *via GBS* **(c)** *PreSDM of* $C_{x_{\mathcal{B}_1}}$ *via WEM*

(d) $I_{x_{\mathcal{B}_2}}$ **(e)** *PreSDM of* $C_{x_{\mathcal{B}_2}}$ *via GBS* **(f)** *PreSDM of* $C_{x_{\mathcal{B}_2}}$ *via WEM*

(g) $I_{x_{\mathcal{B}_3}}$ **(h)** *PreSDM of* $C_{x_{\mathcal{B}_3}}$ *via GBS* **(i)** *PreSDM of* $C_{x_{\mathcal{B}_3}}$ *via WEM*

Figure 4.6: ***(a)***,***(d)*** *and* ***(g)*** *Partial image results* $I_{x_{\mathcal{B}}}$ *obtained from sources* $\boldsymbol{x}_{\mathcal{B}_1}$, $\boldsymbol{x}_{\mathcal{B}_2}$ *and* $\boldsymbol{x}_{\mathcal{B}_3}$, *following scenarios in figures 4.3a, 4.3b and 4.3c.* ***(b)***,***(e)*** *and* ***(h)*** *Same as in (a), (d) and (g) using isotropic migration via Gaussian Beam summation method (GBS) on conventional passive interferometry imaging.* ***(c)***,***(f)*** *and* ***(i)*** *Same as in (b), (e) and (h) using one-way wavefield pre-stack depth migration (WEM) on conventional passive interferometry imaging.*

in the imaging process (red triangles represent the receiver locations employed as virtual sources during migration). The results are defined by the location of the subsurface sources and the receivers: reflectors that are not in stationary phase with the receiver array and the subsurface sources available are not imaged. Only sections of the reflectors in stationary phase with the array are imaged.

Figures 4.6a, 4.6d and 4.6g show the three respective partial images obtained from the subsurface sources using the directionally constrained migration scheme. These results can be compared to the respective results in figures 4.6b, 4.6e and 4.6h, which were obtained using an isotropic illumination Pre-stack depth migration scheme (GBS method) using the same receiver array and the same amount of virtual sources. In spite of using a sparse virtual source sampling, the production of migration artefacts is limited in the case of the constrained illumination method.

Isotropic migration of correlated data can reduce the imprint of the migration artefacts by destructive interference using a denser amount virtual sources. Figures 4.6c, 4.6f and 4.6i show the results produced when applying pre-stack depth migration using "wave equation migration" (WEM) to the virtual-source records retrieved for all 41 receiver positions (notice all virtual sources as red triangles).

A denser amount of virtual sources is needed to obtain sufficient destructive interference of migration artefacts. In spite of this, imaging results show migrated events from the correlated function not in stationary phase. This is observable when comparing figures 4.6d, 4.6e and 4.6f in the synform at 1400 m depth, or before the shallowest reflector in figures 4.6a, 4.6b and 4.6c, and figures 4.6g, 4.6h and 4.6i. Contrary to that, the results obtained using the directional migration scheme needed only a fourth of the virtual-source responses in order to retrieve a result with considerably less artefacts.

4.5 Field-data example

We tested the migration scheme on the recording of a transient tremor at a passive acquisition array located in Annerveen (North of the Netherlands). This array consisted at the time of the recording of 40 multicomponent receivers aligned on East-SouthEast, buried at 50 m depth and with 11.75 m spacing. Since the data are acquired in a 1D line instead of a 2D acquisition array, secondary stations away from the receiver line helped to identify the tremor's direct arrival orientation with illumination diagnosis. This analysis allowed to determine whether the tremor was in stationary phase with respect to the array orientation.

We tested different methods to construct the correlation function $C_{\mathbf{x}_B}$. The first test was applied to the recordings from the observed vertical particle velocity alone (figure 4.7a). Using matrix notation, this is represented as:

$$\hat{\mathbf{C}} = \hat{\mathbf{v}}_3^{obs}\left\{\hat{\mathbf{v}}_3^{obs}\right\}^{\dagger}. \tag{4.17}$$

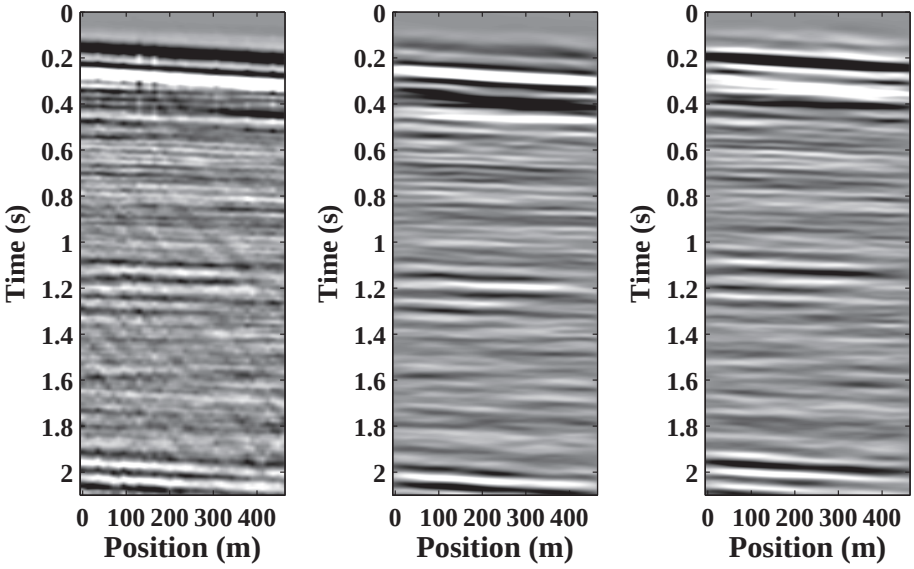

(a) $v_3^{obs}(\boldsymbol{x}_{\mathcal{A}}, \boldsymbol{x}_{\mathcal{B}}, t)$ **(b)** $p^+(\boldsymbol{x}_{\mathcal{A}}, \boldsymbol{x}_{\mathcal{B}}, t)$ **(c)** $p^-(\boldsymbol{x}_{\mathcal{A}}, \boldsymbol{x}_{\mathcal{B}}, t)$

Figure 4.7: *Field data containing a seismic tremor recorded by the Annerveen array in the Netherlands buried at 50 m depth.* ***(a)*** *Vertical particle velocity recording of the tremor including the receiver ghost from the surface.* ***(b)*** *and* ***(c)*** *Down- and upgoing wavefields of the same tremor as (a), power-flux normalized.*

The results of the two-way wavefield recordings in SI by crosscorrelation are shown in figure 4.8a. The receiver ghost of the recording made this correlation function useless for migration. Therefore, elastic one-way wavefield separation and decomposition was implemented for the array depth, using power-flux normalization (Grobbe et al., 2013). Figures 4.7b and 4.7c show the respective down- and upgoing one-way wavefields of the same tremor, power-flux normalized. The estimation of the correlation matrix using SI by crosscorrelation with one-way wavefields was taken from the matrix representation of equation 4.5:

$$\hat{\mathbf{C}} = \hat{\mathbf{p}}^- \{\hat{\mathbf{p}}^+\}^\dagger. \tag{4.18}$$

Results of SI by crosscorrelation on the one-way wavefields are shown in figure 4.8b. Given the frequency content of the data in addition to the dissipation losses of the near subsurface for the recorded multiples, the results in figure 4.8b raised doubts whether it was convenient to employ the directionally constrained

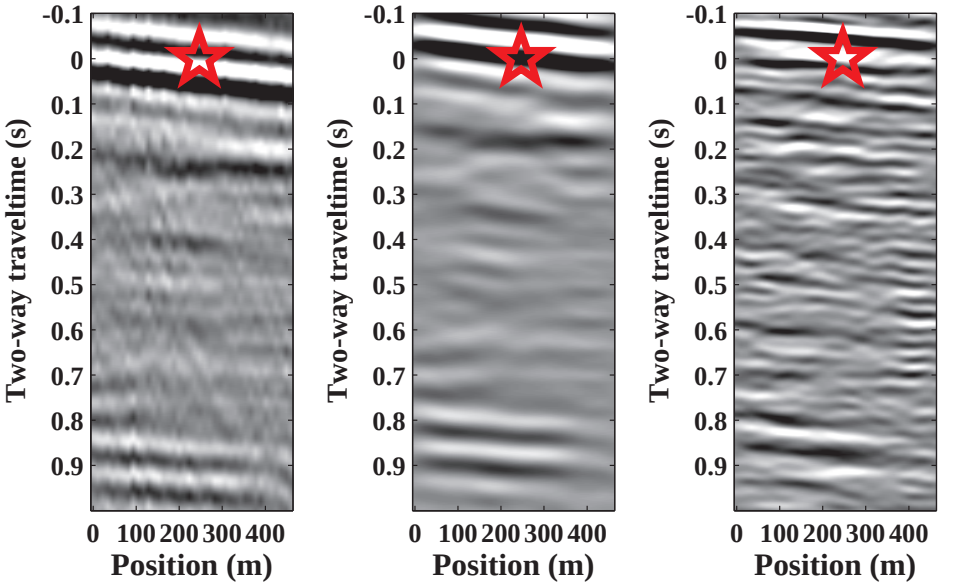

Figure 4.8: *Correlation functions of the seismic tremor in figure 4.7a, with virtual source position at $x_0 = 270$ m (red hollow star).* ***(a)*** *Correlation function using two-way wavefield cross-correlation (equation 4.17).* ***(b)*** *Correlation function using one-way wavefield cross-correlation of power-flux normalized decomposed recordings (equation 4.18).* ***(c)*** *Correlation function using MDD (equation 4.19).*

migration.

An active survey was carried out at the same location with sources at 4 m depth, with 96 receivers available at the time, including the same forty available at the time of the passive source recording. This survey served to estimate a smooth P-wave velocity model of the region. Velocity ranges from 1640 $m\ s^{-1}$ at the receiver depth level to 2500 $m\ s^{-1}$ at 1000 m depth. Given the array aperture, the imaging process is limited in depth due to the single dominant ray-parameter. Estimation of travel-times with respect to the acquisition array aperture confirmed no events later than $t = 0.4$ s from the correlation function would be imaged.

The application of an array-based source-signal deconvolution on the passive recording improved the time resolution of the correlation function. Since the array had a relative limited aperture with respect to the apparent depth of the

passive source, for the imaging process the correlation function was constructed implementing the following multidimensional deconvolution (MDD) expression (equation 3.4):

$$\hat{\mathbf{C}} = \left((\hat{\mathbf{p}}^{-} - \hat{\mathbf{p}}^{-}_{dir}) \{\hat{\mathbf{p}}^{+}\}^{\dagger} \right) \left(\hat{\mathbf{p}}^{+} \{\hat{\mathbf{p}}^{+}\}^{\dagger} + \epsilon^2 \mathbf{I} \right)^{-1}, \tag{4.19}$$

where $\hat{\mathbf{p}}^{-}_{dir}$ is an estimate of the direct arrival of the upgoing wavefield, $\mathbf{I}$ is the identity matrix and ϵ is a stabilization factor. However, the employment of the inversion approach by MDD describes an ill-conditioned problem. Assuming the medium to be laterally invariant, the inversion in expression 4.19 solves for the reflection response only for the provided ray-parameters of the data. On the other hand, the employment of MDD (figure 4.8c) removes the wavelet signature of the seismic tremor and improves the time resolution of the correlation result (figure 4.8b).

The migration result is shown in figure 4.9a for the deconvolution result. All 40 virtual-sources were employed without the use of array tapers. During the migration process an estimate of the frequency content was obtained from the correlation matrix and the following deconvolution imaging condition was applied (Popov et al., 2010):

$$I_{\mathbf{x}_{\mathcal{B}}}(\mathbf{x}, \mathbf{x}_0) = \left(\int_{t_0=0}^{T} U^{\Uparrow}_{\mathbf{x}_{\mathcal{B}}}(\mathbf{x}, \mathbf{x}_0, t_0)\, D^{\Downarrow}_{\mathbf{x}_{\mathcal{B}}}(\mathbf{x}, \mathbf{x}_0, t_0)\, dt_0 \right) \left(\int_{t_0=0}^{T} \left(D^{\Downarrow}_{\mathbf{x}_{\mathcal{B}}}(\mathbf{x}, \mathbf{x}_0, t_0) \right)^2 dt_0 \right)^{-1}. \tag{4.20}$$

Figure 4.9b shows the result of the active survey after applying PreSDM via WEM. The contrast of the depth resolution between the passive result and the active leaves little to validate the result of the first one. The spectrum gap between both surveys makes this summation a bit too harsh. The active survey lacked much of the low frequency content due to the surface-wave removal. The passive survey had a peak frequency of 12 Hz hence *a priori* the comparison of both results is not ideal nor convenient.

Even though, it could be interpreted some reflector matching at depths 240 m, 300 m, 500 m and potentially at 1000 m. Nevertheless, the low frequency content of the passive result with respect of the active leaves the interpretation to be speculative.

Some important points to remark regarding the results obtained is the small aperture of the array, given the frequency content of the passive source. Had the imaging been implemented on a larger array, the result would have imaged deeper

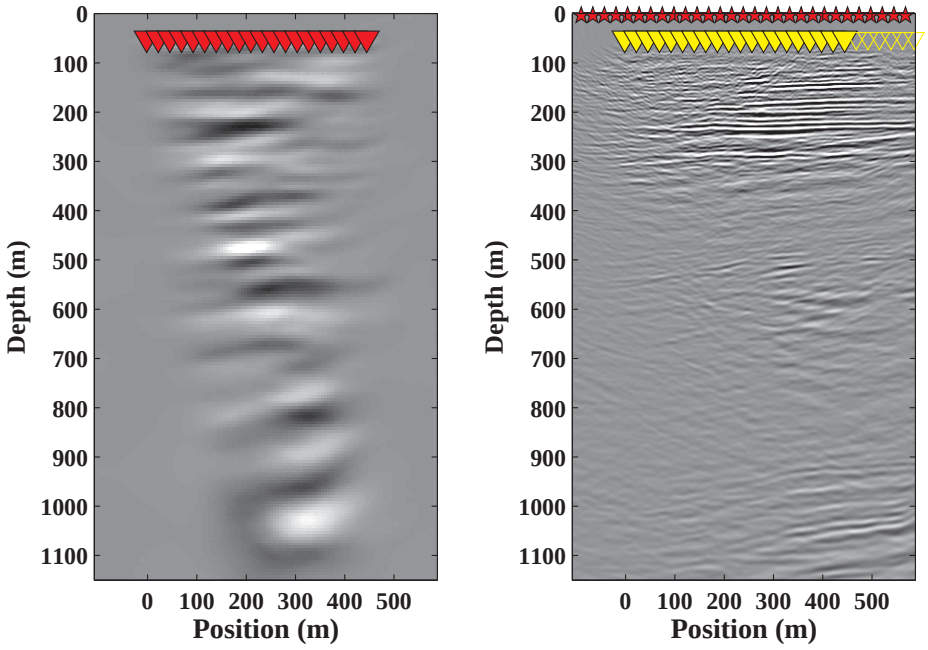

(a) *Passive survey* **(b)** *Active survey*

Figure 4.9: ***(a)*** *Partial image obtained using a deconvolution imaging condition. The data employed was obtained using MDD (figure 4.8c. Considering the length of the array and the angle of incidence of the direct arrival, horizons imaged deeper than* $x_3 \approx 800$ *m lay beyond the illumination range provided by the subsurface source.* ***(b)*** *Active survey depth image result.*

reflectors with stronger contrasts as predicted from the passive recordings in figure 4.7. The limited receiver array reduced the imaging aperture to relatively shallow depths, making the frequency content of the signal inadequate for imaging.

The second point to remark on the passive field data concerns the result of possibly inaccurate decomposition. Since the array is located at 50 m depth, the passive source employed was relatively located in the same phase plane as the receiver array. This is assumed valid for the low frequency content of the data. For the higher frequency content, however, this assumption does not hold true for the respective Fresnel zones of the receivers at higher frequencies do not coincide with the receiver array plane. This circumstance causes the decomposition to be

inaccurate and produce artefacts that as a result blur the correlation function and hence the final image result.

In order to attain good imaging results, an adequate passive seismic array needs to be employed, deployed in an optimal 2D design (regarding illumination diagnosis, wavefield- decomposition (if required) and separation, and imaging). Additionally, the array aperture must be in accordance with the low frequency content estimates of the passive recordings.

4.6 Image interferometry

Conventional seismic interferometry intends to retrieve the reflection response first, using the individual contribution of a well-sampled distribution of sources in the subsurface $\mathbf{x}_{\mathcal{B}}$ in an integral form. For two-way wavefields, with particle velocities recorded at the free surface and retrieving the dipole reflection response in the time domain $R_3^{\smile}$, it is resumed as:

$$R_3^{\smile}(\mathbf{x}_{\mathcal{A}}, \mathbf{x}_0, t) * S_{ac}(t) \propto \int_{\mathbf{x}_{\mathcal{B}}} v_3^{obs}(\mathbf{x}_{\mathcal{A}}, \mathbf{x}_{\mathcal{B}}, t) \otimes v_3^{obs}(\mathbf{x}_0, \mathbf{x}_{\mathcal{B}}, t) d^2\mathbf{x}_{\mathcal{B}}, \tag{4.21}$$

where $\otimes$ symbolises cross-correlation and $S_{ac}(t)$ is an average of the autocorrelation of the passive sources ($S_{ac}(t) = \langle S_{\mathbf{x}_{\mathcal{B}}}(t) \otimes S_{\mathbf{x}_{\mathcal{B}}}(t) \rangle$). In a second stage, the conventional seismic interferometry imaging makes use of active seismic imaging techniques, employing the contributions from well sampled receivers $\mathbf{x}_{\mathcal{A}}$ and, in this case, virtual sources $\mathbf{x}_0$ also in an integral form.

$$I(\mathbf{x}) \propto \int_{\mathbf{x}_0} \int_t D^{\Downarrow}(\mathbf{x}, \mathbf{x}_0, t) \cdot \Big(... \\ ... \int_{\mathbf{x}_{\mathcal{A}}} G(\mathbf{x}, \mathbf{x}_{\mathcal{A}}, t) \otimes R_3^{\smile}(\mathbf{x}_{\mathcal{A}}, \mathbf{x}_0, t) * S_{ac}(t) d^2\mathbf{x}_{\mathcal{A}} \Big) \, dt \, d^2\mathbf{x}_0, \tag{4.22}$$

where G stands for the Green's function of the receiver locations with respect to the medium. With this imaging procedure we propose a change in the order on which the integrals are put into effect in order to obtain the final image result. Following Schuster (2009), in this chapter we have explained the method to obtain a partial image due to a single passive source at $\mathbf{x}_{\mathcal{B}}$:

$$I_{\mathbf{x}_{\mathcal{B}}}(\mathbf{x}) \propto \int_{\mathbf{x}_0} \int_t D^{\Downarrow}(\mathbf{x}, \mathbf{x}_0, t) \cdot \Big(... \\ ... \int_{\mathbf{x}_{\mathcal{A}}} G(\mathbf{x}, \mathbf{x}_{\mathcal{A}}, t) \otimes \Big[v_3^{obs}(\mathbf{x}_{\mathcal{A}}, \mathbf{x}_{\mathcal{B}}, t) \otimes v_3^{obs}(\mathbf{x}_0, \mathbf{x}_{\mathcal{B}}, t) \Big] d^2\mathbf{x}_{\mathcal{A}} \Big) \, dt \, d^2\mathbf{x}_0, \tag{4.23}$$

where we image first and subsequently integrate over passive sources:

$$I(\mathbf{x}) = \int_{\mathbf{x}_\mathcal{B}} I_{\mathbf{x}_\mathcal{B}}(\mathbf{x}) d^2\mathbf{x}_\mathcal{B}. \tag{4.24}$$

This procedure of interchanging the integral order has previously been applied in Artman (2006), where he combined the observed wavefields v_3^{obs} with wavefield extrapolation operators to build the upgoing $U^{\Uparrow}$ and downgoing $D^{\Downarrow}$ wavefields separately first, and subsequently correlated them in the image domain in second place.

The integration of these partial images due to sources in the subsurface is due to produce an equivalent result as in expression 4.22. Directionally constrained imaging allows to produce more reliable partial images of the subsurface from individual sources in the subsurface. These partial images may complement one another to produce a complete subsurface image which is less contaminated by artefacts. The integration of partial images from sources in the subsurface can be expressed as:

$$I(\mathbf{x}) = \sum_{\mathbf{x}_\mathcal{B}} W_{\mathbf{x}_\mathcal{B}}(\mathbf{p}^{\mathbf{x}_0}_{\mathbf{x}_\mathcal{B}}, S_{\mathbf{x}_\mathcal{B}}) I_{\mathbf{x}_\mathcal{B}}(\mathbf{x}). \tag{4.25}$$

During the summation of imaging results we include the weights $W_{\mathbf{x}_\mathcal{B}}$ in order to balance the strength and contribution from events of different angles. This weighting process may additionally include frequency balancing to overcome the different frequency spectra the sources may have.

The application of this integration is the result of Image Interferometry. In this process only correlated events from primaries are being imaged by constructive interference of partial image results. The contributions from all ambient sources add up at the reflection location. In this process the reflection response is obviated. Yet, this process relies on a densely sampled array of receivers whereas it allows to have a sparsely sampled passive source array.

The imaged events identified as artefacts will not contribute to the final result since they do not coincide at the same time/depth from one partial image to another. The summation of these events in the image domain due to sources distributed homogeneously in the subsurface will cause these artefacts caused by surface multiple energy, internal multiples and correlated artefacts, to interfere destructively. With respect to coherent events for instance, surface-related multiples from the (partially-) retrieved reflection response are to be coherent from one partial image to another. In figure 4.10a we depict how to every free-surface multiple corresponds a different dominant ray-parameter at the virtual source location. However, the imaging process discriminates the imaging direction at which the surface-related multiples are expected to image reflected events and are instead imaged along the direction of primaries (see figure 4.10b). This fact

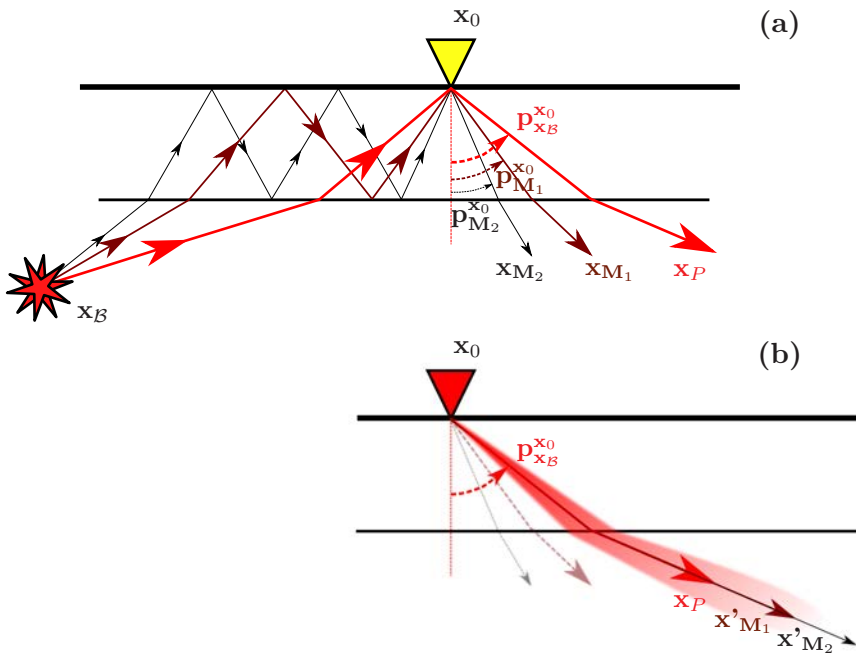

Figure 4.10: *Depiction of different order surface-related multiples and their dominant ray-parameter with respect to the virtual source $\boldsymbol{x}_0$, and the implication of directionally constrained migration.* ***(a)*** *Surface multiple scattering from the subsurface source at $\boldsymbol{x}_\mathcal{B}$ (red star) arrives to the surface receiver at $\boldsymbol{x}_0$ (yellow triangle) with different dominant ray-parameters: $\boldsymbol{p}^{\boldsymbol{x}_0}_{\boldsymbol{x}_\mathcal{B}}$, $\boldsymbol{p}^{\boldsymbol{x}_0}_{\boldsymbol{M}_1}$, $\boldsymbol{p}^{\boldsymbol{x}_0}_{\boldsymbol{M}_2}$, etc. The location of reflectors in stationary phase will be carried through by the individual rays from their respective dominant direction ($\boldsymbol{x}_P$, $\boldsymbol{x}_{M_1}$, $\boldsymbol{x}_{M_2}$).* ***(b)*** *The direction constraint in the migration process limits the migration to a single ray-parameter ($\boldsymbol{p}^{\boldsymbol{x}_0}_{\boldsymbol{x}_\mathcal{B}}$) that images the primary energy on the location. To the other multiple energy, this constraint causes them to be imaged at the wrong medium location ($\boldsymbol{x'}_{M_1}$, $\boldsymbol{x'}_{M_2}$), hence not keeping any coherence.*

causes the free-surface multiples to be imaged at different wrong locations from every virtual source $\mathbf{x}_0$ for every subsurface source $\mathbf{x}_\mathcal{B}$. Therefore, the introduction of this incoherence between free-surface multiples reduces the imprint of the free-surface multiples in the final image result. With all passive sources available, stacking the individual partial images over $\mathbf{x}_\mathcal{B}$ should give the desired total image of the subsurface. However, with scarce passive sources, already the evaluation of only one source, the partial image may give an acceptable result. The same reasoning can be applied to the interferometric ghost events due to correlation of events from heterogeneities from above and below the passive source location, and *vice versa*.

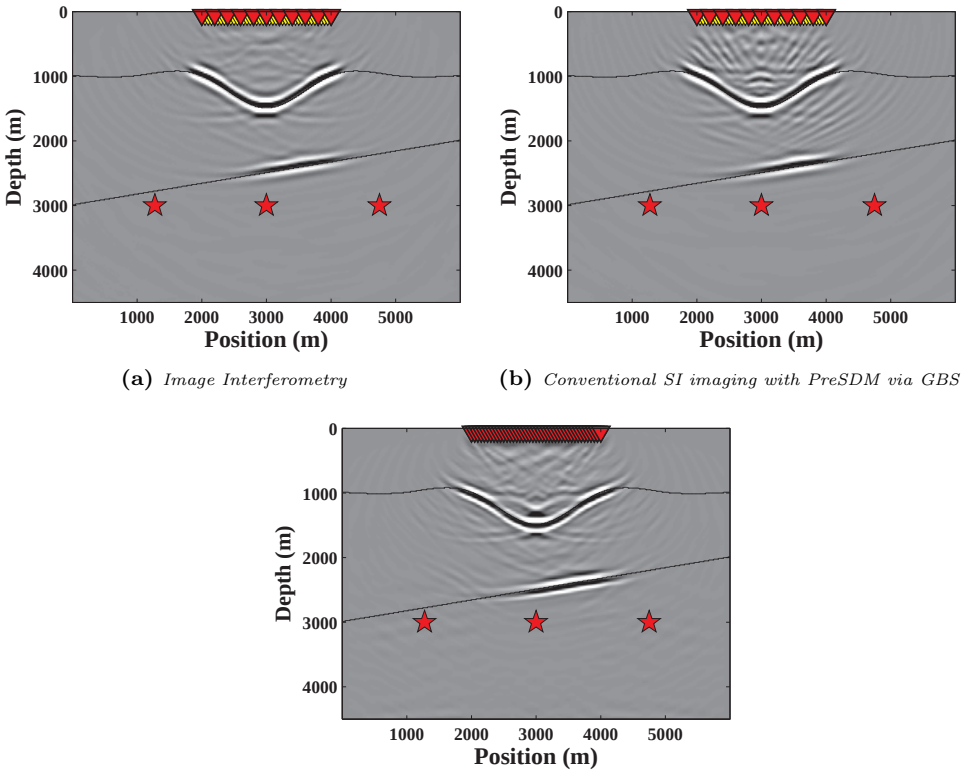

(a) *Image Interferometry*

(b) *Conventional SI imaging with PreSDM via GBS*

(c) *Conventional SI imaging with PreSDM via WEM*

Figure 4.11: *Comparison of migrated results.* ***(a)*** *Image Interferometry due to the directionally constrained migrated results of the three subsurface sources.* ***(b)*** *Prestack depth migration of conventional passive seismic interferometric imaging via Gaussian Beam summation method (GBS) with the same three subsurface sources.* ***(c)*** *Same as in (b) using one-way wavefield pre-stack depth migration (WEM).*

This process is valid if the frequency content of the data is always the same for the subsurface sources. This is an unrealistic assumption that can be obviated by working with different seismic interferometry methods or a different imaging condition.

Image results of figure 4.11 may complement one another in producing the complete image result. During the II process we carry out the integration in 4.9 by summing together the individual partial images obtained.

The integration of information provided by several sources in the subsurface improves the interferometry process. In conventional passive seismic imaging, the

integration of the different correlation functions is carried out during the virtual-shot retrieval.

Figure 4.11a is the result of stacking image results from 4.6a, 4.6d and 4.6g. The artefacts from imaging the individual sources are now largely suppressed by destructive interference from the other source images. Figure 4.11b is the conventional pre-stack migration via GBS result of all virtual shot records retrieved from cross-correlating sequentially first and adding consecutively the three subsurface sources (Following equations 4.21 and 4.22 with one-way wavefields). In this result, the same amount of virtual sources was applied as for figure 4.11a. The migration artefacts due to a sparse virtual source sampling are still visible. Figure 4.11c is the equivalent result to figure 4.11b, using WEM with all virtual sources available. The migration of events of the correlation function that are not in stationary phase leaves incorrect events, clearly visible in the centre of the synform at 1400 m depth. This is not the case in figure 4.11a where the result is expected to improve the more virtual sources are employed in the imaging process.

4.7 Discussion

In this work we show that changing the order in which the integrations are carried out in passive interferometric imaging improves the final imaging result. This change has been already tested in Schuster et al. (2004).Traditional passive seismic imaging solves the interferometric integration first in order to retrieve the reflection response, which is *a posteriori* migrated applying integrations over receivers and virtual-sources to obtain the final image result. The interferometric integration for SI by crosscorrelaton relies on the availability of sufficient subsurface illumination from different angles. Under the unlikely possibility of two passive sources occurring simultaneously in time from two different source locations in the subsurface, the methodology described in this chapter can be adapted in this case by employing equation 4.10, identifying the dominant ray-parameters of each individual passive source. The forward field would then be constructed using the respective source signal $S_{\mathbf{x}_\mathcal{B}}$ in the respective dominant angle beam, and applying a deconvolution-based imaging condition.

Since in passive seismics the occurrence of sources in the subsurface is beyond our control and may happen over long periods of time, through this migration scheme we are implicitly proposing to apply the virtual-source and receiver integrations of the migration process first, and leave the interferometric integration for the last, waiting for additional passive sources to happen eventually.

In an elastic medium, the wavefield separation would allow two independent migration results with complementary illumination, since for non-vertical incidence, P-waves and S-waves follow different ray-paths. Different velocity models can be applied using the respective P or S virtual-source function $\Gamma_{\mathbf{x}_\mathcal{B}}$ for illumination diagnosis and forward imaging wavefield, and the corresponding P or S

potential correlation function for the backprojected wavefield. This implementation should produce, for 2D media, four independent results (PP, SP, PS and SS) with coinciding imaging reflectors in stationary phase and stronger destructive interference for correlation artefacts.

This migration approach of passive sources is addressed to passive source recordings with transient signal characteristics. The transient behaviour of the source allowed us to employ a simple imaging condition based on correlation. However, for source signals with less transient signals, as expected when working with passive seismics, the image condition is to be changed for deconvolution conditions and also the possibility of employing the extended image domain.

One observation we extract from this work is the correct use of the limited information provided by the correlated function $C_{\mathbf{x}_\mathcal{B}}$. In it we identify two types of events: the ones in stationary phase and the ones which are not. The backprojection of the energy with the directional migration allows the events in stationary phase to be properly imaged, all possible thanks to the correct velocity model. However the identification inside the correlation function $C_{\mathbf{x}_\mathcal{B}}$ of the receiver pair (virtual source and receiver) and time of the correlated event that is in stationary phase remains uncertain. A future development could exploit the information brought by midpoint interferometry results. This analysis has shown positive results for laterally invariant media (Ruigrok et al., 2012). The extraction of this information allows the application of one-way time tomography between three terms: virtual source location, receiver location and reflector point location, for velocity analysis of the subsurface.

4.8 Conclusions

We presented a scheme for generating partial images from a limited number of subsurface sources when using seismic interferometry. Our scheme takes the illumination characteristics of the passive sources into account. It uses the illumination information to image only energy in stationary phase for the respective virtual source, hence limiting the migration of correlated energy that would contribute to migration artefacts. In case of limited passive-source distribution, the scheme produces better results than conventional interferometric imaging schemes.

If a smooth or background velocity model is available, the explicit reconstruction of the Green's function as an intermediate step is not necessary to image the subsurface. The contribution from one source alone can resolve reflector geometries in the subsurface, and this could be further improved with the eventual addition of images from other passive sources. This process of adding images produced by individual passive sources in the subsurface produces enhancing and complementation of the reflector image, and destructive interference of the already limited migration artefacts, cross-talk and other correlated events. By proceeding with the integration of images, we are postponing the use of the interferometric

integration to the image domain, hence obviating the explicit reconstruction of the reflection response.

	State $\mathcal{A}'$	*State* $\mathcal{A}$
Wavefields	$\hat{\mathbf{G}}(\mathbf{x}_{\mathcal{B}}, \mathbf{x}_{\mathcal{A}'}, \omega)$	$\hat{\mathbf{G}}(\mathbf{x}_{\mathcal{B}}, \mathbf{x}_{\mathcal{A}}, \omega)$
Source fields	$\mathbf{I}\delta(\mathbf{x} - \mathbf{x}_{\mathcal{A}'})$	$\mathbf{I}\delta(\mathbf{x} - \mathbf{x}_{\mathcal{A}})$

Table 4.1: *Definition of the state representation's elements.*

4.A Representation relation of the correlation type

Given two states $\mathcal{A}$ and $\mathcal{A}'$ describing a medium without changes between both states, the reciprocity relation of the correlation type between the two states is described for one-way wavefields as (Wapenaar & Grimbergen, 1996):

$$\int_{\mathbb{D}} \{\hat{\mathbf{G}}^{\dagger}_{\mathcal{A}} \mathbf{J} \hat{\mathbf{S}}_{\mathcal{A}'} + \hat{\mathbf{S}}^{\dagger}_{\mathcal{A}} \mathbf{J} \hat{\mathbf{G}}_{\mathcal{A}'}\} d^3\mathbf{x} = \int_{\partial\mathbb{D}} \{\hat{\mathbf{G}}^{\dagger}_{\mathcal{A}} \mathbf{J} \hat{\mathbf{G}}_{\mathcal{A}'}\} \boldsymbol{n} d^2\mathbf{x} \tag{4.26}$$

Permutation matrix $\mathbf{J}$ and notation in equation 4.26 are the same as in appendix 3.B. The one-way reciprocity relation will represent the Green's functions of an heterogeneous half-space medium. For our representation we define two states $\mathcal{A}$ and $\mathcal{A}'$, each with exactly the same control domain $\mathbb{D}$ and boundary definitions. The source locations for both states are defined at $\mathbf{x}_{\mathcal{A}}$ and $\mathbf{x}_{\mathcal{A}'}$ respectively, both along the same depth level and detached from the free-surface. The boundary $\partial\mathbb{D}$ consists of two parallel boundaries and is defined arbitrarily inside the subsurface and surrounding the source location of both states. One of the two boundaries coincides with the free-surface above both source locations. The medium is assumed heterogeneous inside and outside the domain boundary.

Table 4.1 shows the representation terms for each state. $\hat{\mathbf{G}}(\mathbf{x}_{\mathcal{B}}, \mathbf{x}_{\mathcal{A}}, \omega)$ represents the Green's function matrix in state state $\mathcal{A}$ for a source located in $\mathbf{x}_{\mathcal{A}}$ and a receiver in $\mathbf{x}_{\mathcal{B}}$, including transmission and reflection responses with internal multiples and free-surface reflections. $\hat{\mathbf{G}}(\mathbf{x}_{\mathcal{B}}, \mathbf{x}_{\mathcal{A}'}, \omega)$ is defined in a similar way. The source is represented by an impulse for both states.

Applying the same medium, boundary and source definitions in table 4.1 to the reciprocity relation of the correlation type in equation 4.26, its expression simplifies into:

$$\hat{\mathbf{G}}^{\dagger}_{\mathcal{A}}(\mathbf{x}_{\mathcal{A}'}, \mathbf{x}_{\mathcal{A}}, \omega)\mathbf{J} + \mathbf{J}\hat{\mathbf{G}}_{\mathcal{A}'}(\mathbf{x}_{\mathcal{A}}, \mathbf{x}_{\mathcal{A}'}, \omega) = \int_{\partial\mathbb{D}_{\mathcal{B}}} \hat{\mathbf{G}}^{\dagger}_{\mathcal{A}} \mathbf{J} \hat{\mathbf{G}}_{\mathcal{A}'} \boldsymbol{n} d^2\mathbf{x}_{\mathcal{B}}. \tag{4.27}$$

The integral along the upper boundary vanishes at the free-surface and therefore this is only evaluated over the lower boundary $\partial\mathbb{D}_{\mathcal{B}}$. At this lower boundary, the

	State $\mathcal{A}'$		*State* $\mathcal{A}$	
$\mathbf{x}_\mathcal{B} \in \partial\mathbb{D}_\mathcal{B}$	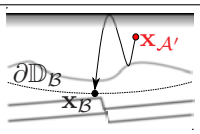	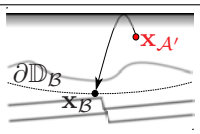	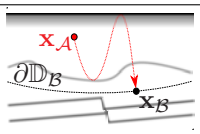	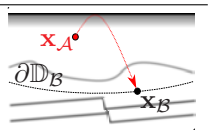
	$\hat{G}^{+,+}(\mathbf{x}_\mathcal{B}, \mathbf{x}_{\mathcal{A}'})$	$\hat{G}^{+,-}(\mathbf{x}_\mathcal{B}, \mathbf{x}_{\mathcal{A}'})$	$\{\hat{G}^{+,+}(\mathbf{x}_\mathcal{B}, \mathbf{x}_\mathcal{A})\}^*$	$\{\hat{G}^{+,-}(\mathbf{x}_\mathcal{B}, \mathbf{x}_\mathcal{A})\}^*$
	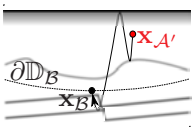	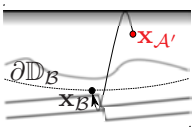	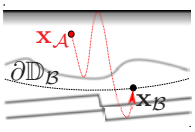	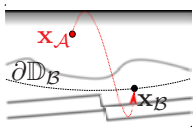
	$\hat{G}^{-,+}(\mathbf{x}_\mathcal{B}, \mathbf{x}_{\mathcal{A}'})$	$\hat{G}^{-,-}(\mathbf{x}_\mathcal{B}, \mathbf{x}_{\mathcal{A}'})$	$\{\hat{G}^{-,+}(\mathbf{x}_\mathcal{B}, \mathbf{x}_\mathcal{A})\}^*$	$\{\hat{G}^{-,-}(\mathbf{x}_\mathcal{B}, \mathbf{x}_\mathcal{A})\}^*$

Table 4.2: *Wavefields present in the acoustic one-way reciprocity theorem of the correlation type for the two states, $\mathcal{A}'$ and $\mathcal{A}$. Time-reversed wavefields are depicted in red-colour with dashed lines.*

4

outward pointing normal vector $\boldsymbol{n}$ is $(0, 0, n_3)$, with $n_3 = +1$. Taking into account the terms displayed in table 4.2, the resulting representation becomes:

$$\begin{bmatrix} \{\hat{G}^{+,+}_{\mathcal{A}}\}^* & -\{\hat{G}^{-,+}_{\mathcal{A}}\}^* \\ \{\hat{G}^{+,-}_{\mathcal{A}}\}^* & -\{\hat{G}^{-,-}_{\mathcal{A}}\}^* \end{bmatrix} (\mathbf{x}_{\mathcal{A}'}, \mathbf{x}_\mathcal{A}, \omega) + \begin{bmatrix} \hat{G}^{+,+}_{\mathcal{A}'} & \hat{G}^{+,-}_{\mathcal{A}'} \\ -\hat{G}^{-,+}_{\mathcal{A}'} & -\hat{G}^{-,-}_{\mathcal{A}'} \end{bmatrix} (\mathbf{x}_\mathcal{A}, \mathbf{x}_{\mathcal{A}'}, \omega) =$$
$$\int_{\partial\mathbb{D}_\mathcal{B}} \begin{bmatrix} \hat{G}^{+,+}_{\mathcal{A}'}\{\hat{G}^{+,+}_{\mathcal{A}}\}^* - \hat{G}^{-,+}_{\mathcal{A}'}\{\hat{G}^{-,+}_{\mathcal{A}}\}^* & \hat{G}^{+,-}_{\mathcal{A}'}\{\hat{G}^{+,+}_{\mathcal{A}}\}^* - \hat{G}^{-,-}_{\mathcal{A}'}\{\hat{G}^{-,+}_{\mathcal{A}}\}^* \\ \hat{G}^{+,+}_{\mathcal{A}'}\{\hat{G}^{+,-}_{\mathcal{A}}\}^* - \hat{G}^{-,+}_{\mathcal{A}'}\{\hat{G}^{-,-}_{\mathcal{A}}\}^* & \hat{G}^{+,-}_{\mathcal{A}'}\{\hat{G}^{+,-}_{\mathcal{A}}\}^* - \hat{G}^{-,-}_{\mathcal{A}'}\{\hat{G}^{-,-}_{\mathcal{A}}\}^* \end{bmatrix} d^2\mathbf{x}_\mathcal{B} \tag{4.28}$$

where $\{\}^*$ stands for complex conjugation. Relation 4.28 shows four equations relating the Green's function of the source locations with the interaction quantities of the wavefields from these points to the boundary surrounding them. We take the expression with the wavefield terms $\{\hat{G}^{-,+}_{\mathcal{A}}\}^*$ and $\hat{G}^{+,-}_{\mathcal{A}'}$ inside the control domain in relation 4.28 and express it as:

$$-\left\{\hat{G}^{-,+}(\mathbf{x}_{\mathcal{A}'},\mathbf{x}_{\mathcal{A}},\omega)\right\}^{*}+\hat{G}^{+,-}(\mathbf{x}_{\mathcal{A}},\mathbf{x}_{\mathcal{A}'},\omega)=\int_{\mathbf{x}_{\mathcal{B}}\in\partial\mathbb{D}_{\mathcal{B}}}\Big(\hat{G}^{+,-}(\mathbf{x}_{\mathcal{B}},\mathbf{x}_{\mathcal{A}'},\omega)\left\{\hat{G}^{+,+}(\mathbf{x}_{\mathcal{B}},\mathbf{x}_{\mathcal{A}},\omega)\right\}^{*}-\hat{G}^{-,-}(\mathbf{x}_{\mathcal{B}},\mathbf{x}_{\mathcal{A}'},\omega)\left\{\hat{G}^{-,+}(\mathbf{x}_{\mathcal{B}},\mathbf{x}_{\mathcal{A}},\omega)\right\}^{*}\Big)d^{2}\mathbf{x}_{\mathcal{B}}. \quad (4.29)$$

Now we apply the source-receiver reciprocity properties for power-flux normalized wavefields $\hat{G}^{-,+}(\mathbf{x}_{\mathcal{A}'},\mathbf{x}_{\mathcal{A}},\omega)=\hat{G}^{-,+}(\mathbf{x}_{\mathcal{A}},\mathbf{x}_{\mathcal{A}'},\omega)$, and inside the integral $\hat{G}^{+,-}(\mathbf{x}_{\mathcal{B}},\mathbf{x}_{\mathcal{A}'},\omega)=\hat{G}^{+,-}(\mathbf{x}_{\mathcal{A}'},\mathbf{x}_{\mathcal{B}},\omega)$ and $\hat{G}^{-,-}(\mathbf{x}_{\mathcal{B}},\mathbf{x}_{\mathcal{A}'},\omega)=-\hat{G}^{+,+}(\mathbf{x}_{\mathcal{A}'},\mathbf{x}_{\mathcal{B}},\omega)$ in order to turn the evaluation points in the subsurface $\mathbf{x}_{\mathcal{B}}$ into source locations:

$$\left\{\hat{G}^{-,+}(\mathbf{x}_{\mathcal{A}},\mathbf{x}_{\mathcal{A}'},\omega)\right\}^{*}-\hat{G}^{+,-}(\mathbf{x}_{\mathcal{A}},\mathbf{x}_{\mathcal{A}'},\omega)=\int_{\mathbf{x}_{\mathcal{B}}\in\partial\mathbb{D}_{\mathcal{B}}}\Big(\hat{G}^{+,-}(\mathbf{x}_{\mathcal{A}'},\mathbf{x}_{\mathcal{B}},\omega)\left\{\hat{G}^{-,-}(\mathbf{x}_{\mathcal{A}},\mathbf{x}_{\mathcal{B}},\omega)\right\}^{*}-\hat{G}^{+,+}(\mathbf{x}_{\mathcal{A}'},\mathbf{x}_{\mathcal{B}},\omega)\left\{\hat{G}^{-,+}(\mathbf{x}_{\mathcal{A}},\mathbf{x}_{\mathcal{B}},\omega)\right\}^{*}\Big)d^{2}\mathbf{x}_{\mathcal{B}}. \quad (4.30)$$

This expression shows the correlation of the Green's function due to sources at $\mathbf{x}_{\mathcal{B}}$ along $\mathbb{D}_{\mathcal{B}}$ at the two receiver locations $\mathbf{x}_{\mathcal{A}}$ and $\mathbf{x}_{\mathcal{A}'}$ allows the estimation of one-way wavefield Green's functions between the same locations. Since we are interested in the impulsive downgoing-source and upgoing-receiver reflection response defined forward in time, we express equation 4.30 by its complex conjugation, rearrange the terms in the integral and obtain:

$$\hat{G}^{-,+}(\mathbf{x}_{\mathcal{A}},\mathbf{x}_{\mathcal{A}'},\omega)-\left\{\hat{G}^{+,-}(\mathbf{x}_{\mathcal{A}},\mathbf{x}_{\mathcal{A}'},\omega)\right\}^{*}=\int_{\mathbf{x}_{\mathcal{B}}\in\partial\mathbb{D}_{\mathcal{B}}}\Big(\hat{G}^{-,-}(\mathbf{x}_{\mathcal{A}},\mathbf{x}_{\mathcal{B}},\omega)\left\{\hat{G}^{+,-}(\mathbf{x}_{\mathcal{A}'},\mathbf{x}_{\mathcal{B}},\omega)\right\}^{*}-\hat{G}^{-,+}(\mathbf{x}_{\mathcal{A}},\mathbf{x}_{\mathcal{B}},\omega)\left\{\hat{G}^{+,+}(\mathbf{x}_{\mathcal{A}'},\mathbf{x}_{\mathcal{B}},\omega)\right\}^{*}\Big)d^{2}\mathbf{x}_{\mathcal{B}}. \quad (4.31)$$

This is the final representation of SI by crosscorrelation for one-way wavefields at receivers in the subsurface. Equation 4.31 has the impulse reflection responses substituted by the expressions $\hat{G}^{-,+}=\hat{R}^{\cup}$ and $\hat{G}^{+,-}=\hat{R}^{\cap\cup}$ in equation 4.1. The source location $\mathbf{x}_{\mathcal{A}'}$ is also substituted by $\mathbf{x}_0$ for clarity's sake.

5 Reciprocity-based passive monitoring with individual sources[§]

Changes in the subsurface can be imaged by comparing seismic reflection data at two different states, one serving as the initial survey or base, and the second as the monitor survey. Conventionally, the reflection data are acquired by placing active seismic sources at the acquisition surface. Alternatively, these data can be acquired from passive sources in the subsurface, using seismic interferometry. Unfortunately, the reflection responses as retrieved by seismic interferometry inherit an imprint of the passive source distribution. Therefore, monitoring with seismic interferometry requires high passive source repeatability, which is often not achievable in practice. We propose an alternative, by using active seismic data for the base survey and a single passive source for the monitor survey. By constraining the radiation pattern of the (active) base survey according to the characteristics of the (passive) monitor survey, we succeed to extract the time-lapse response in the image domain. The proposed method is illustrated with numerically modelled data.

5.1 Introduction

With seismic interferometry (SI), a reflection response of the subsurface can be retrieved by cross-correlating the recordings at, or just below, the surface of passive seismic sources in the subsurface. One application of SI with passive seismics besides imaging of the subsurface, is monitoring the changes in the subsurface that may occur after a period of time. To this goal, the standard procedure with seismics is the application of active surveys: one serving as a base and another as monitor survey, at the two different times of study of the subsurface.

[§]Certain Sections of this chapter have been published as an extended abstract in the *83rd SEG annual meeting, Houston, PSC 2.6*, (Almagro Vidal et al., 2013).

SI provides an alternative approach for the monitor survey by making use of passive sources in order to retrieve a virtual monitor survey (Ugalde et al., 2011; Boullenger et al., 2014). This approach is referred as conventional interferometric passive monitoring.

5.1.1 Conventional interferometric passive monitoring

Figure 5.1 shows the elements for merging active (base, $R^{\smile}_{\mathcal{A}}$) and passive (monitor $R^{\smile}_{\mathcal{B}}$) surveys for monitoring, using conventional interferometric passive monitoring in acoustic media. There are different passive SI approaches to retrieve the monitor reflection response $R^{\smile}_{\mathcal{B}}$, one more convenient than the other, depending on the case. Taking the approach of SI by crosscorrelation with transient sources for example, the monitor reflection response $R^{\smile}_{\mathcal{B}}$ is obtained from the correlation of individual receivers at $\mathbf{x}_{\mathcal{A}}$ and $\mathbf{x}_0$ of passive recordings in a straightforward manner (Wapenaar & Fokkema, 2006). The passive recordings consist of transmission responses from passive sources at locations $\mathbf{x}_{\mathcal{B}}$ densely and homogeneously distributed in the subsurface and effectively illuminating the receivers. Assuming the receivers are located at the surface, the individual contribution of every passive source is quantified in the correlation function $C_{\mathcal{B}}$ for two-way wavefields:

$$\hat{C}_{\mathcal{B}}\left(\mathbf{x}_{\mathcal{A}},\mathbf{x}_0,\mathbf{x}_{\mathcal{B}},\omega\right) \rightarrow \hat{C}_{\mathcal{B},\mathbf{x}_{\mathcal{B}}}\left(\mathbf{x}_{\mathcal{A}},\mathbf{x}_0,\omega\right) = \hat{v}^{obs}_{3,\mathcal{B}}\left(\mathbf{x}_{\mathcal{A}},\mathbf{x}_{\mathcal{B}},\omega\right)\left\{\hat{v}^{obs}_{3,\mathcal{B}}\left(\mathbf{x}_0,\mathbf{x}_{\mathcal{B}},\omega\right)\right\}^{*}, \tag{5.1}$$

where ω denotes angular frequency, $\hat{v}^{obs}_{3,\mathcal{B}}$ stands for the observed vertical particle velocity in the monitor survey, character $\hat{}$ means the field is in the space-frequency domain and $\{\}^{*}$ stands for complex conjugation. For one-way wavefields the correlation function reads:

$$\hat{C}_{\mathcal{B}}\left(\mathbf{x}_{\mathcal{A}},\mathbf{x}_0,\mathbf{x}_{\mathcal{B}},\omega\right) \rightarrow \hat{C}_{\mathcal{B},\mathbf{x}_{\mathcal{B}}}\left(\mathbf{x}_{\mathcal{A}},\mathbf{x}_0,\omega\right) = \hat{p}^{-}_{\mathcal{B}}\left(\mathbf{x}_{\mathcal{A}},\mathbf{x}_{\mathcal{B}},\omega\right)\left\{\hat{p}^{+}_{\mathcal{B}}\left(\mathbf{x}_0,\mathbf{x}_{\mathcal{B}},\omega\right)\right\}^{*}, \tag{5.2}$$

where $\hat{p}^{\pm}_{\mathcal{B}}$ stands for the power flux-normalized field; minus superscript stands for upgoing-decomposed observed wavefields and plus superscript for the respective downgoing ones.

Equations 5.1 and 5.2 ignore the scaling of the medium density ρ and compressional wave velocity c_P at the source locations $\mathbf{x}_{\mathcal{B}}$, for they cannot be estimated individually.

The retrieval of the reflection response is carried out by the integration of the subsurface illumination from the passive sources. The discretization for the individual passive sources $\mathbf{x}_{\mathcal{B}}$ yields in this case:

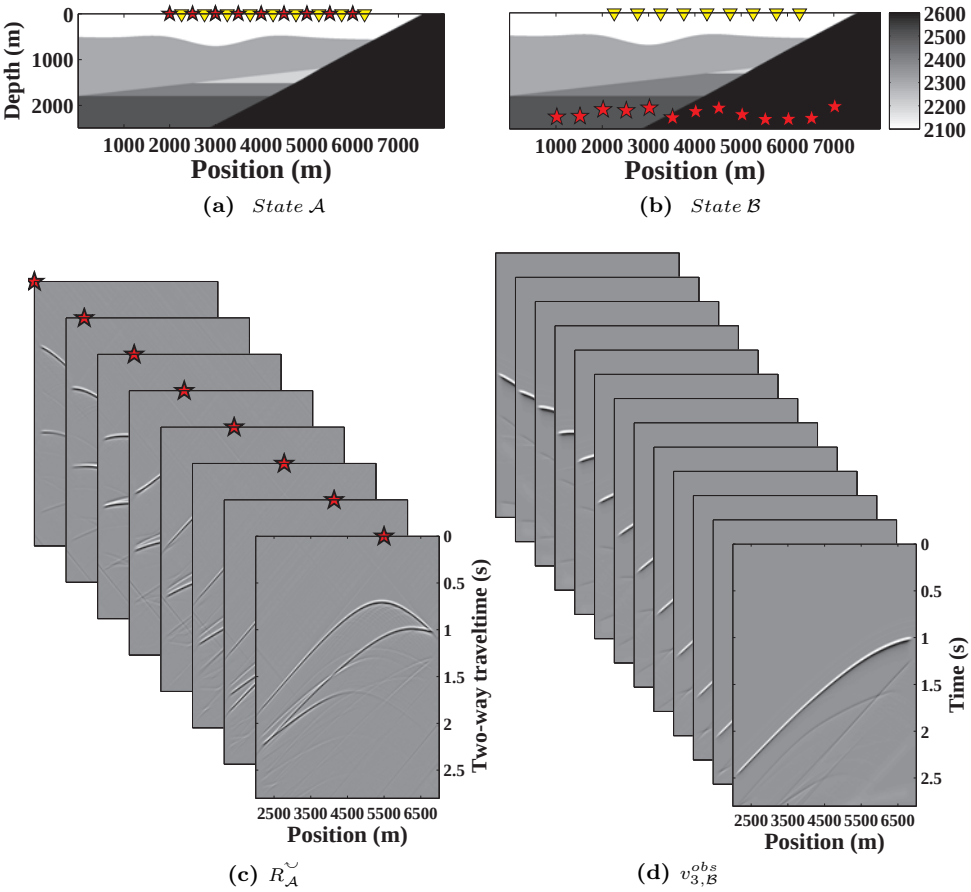

(a) *State $\mathcal{A}$* **(b)** *State $\mathcal{B}$*

(c) $R_{\mathcal{A}}^{\smile}$ **(d)** $v_{3,\mathcal{B}}^{obs}$

Figure 5.1: *Conventional interferometric passive monitoring.* **(a)** *Velocity model ($m\ s^{-1}$) representing a pinch-out reservoir with a flat-spot feature at state $\mathcal{A}$ (base survey): controlled sources (red stars) and receivers (yellow triangles) share the same distribution at the Earth's surface.* **(b)** *Same model as in* (a) *at state $\mathcal{B}$ (monitor survey), but with some local changes in the subsurface: Notice the difference at the reservoir flat-spot level at 1200 m depth. The monitoring in this state is carried out using the same receivers as in* (a)*, but with passive sources located in the subsurface (red stars).* **(c)** *Reflection response survey ($R_{\mathcal{A}}^{\smile}$) at state $\mathcal{A}$ (as displayed in* (a)*).* **(d)** *Passive source recordings $v_{3,\mathcal{B}}^{obs}$ at state $\mathcal{B}$ from every passive source $\boldsymbol{x}_{\mathcal{B}}$ illustrated in* (b)*, using the same receivers employed in* (c)*.*

$$\left(\hat{R}_{\mathcal{B}}^{\smile}\left(\mathbf{x}_{\mathcal{A}},\mathbf{x}_0,\omega\right)-\left\{\hat{R}_{\mathcal{B}}^{\frown}\left(\mathbf{x}_{\mathcal{A}},\mathbf{x}_0,\omega\right)\right\}^{*}\right)\|\hat{S}(\omega)\|^2\propto\sum_{\mathbf{x}_{\mathcal{B}}}\hat{C}_{\mathcal{B},\mathbf{x}_{\mathcal{B}}}\left(\mathbf{x}_{\mathcal{A}},\mathbf{x}_0,\omega\right), \quad (5.3)$$

where $\hat{R}_{\mathcal{B}}^{\smile}$ and $\hat{R}_{\mathcal{B}}^{\frown}$ are presented as the impulse reflection response for downgoing-source upgoing receiver, and upgoing-source downgoing-receiver wavefields respectively; $\|\hat{S}(\omega)\|^2$ is the power spectrum of the passive sources, assuming these share the same power spectrum.

Figure 5.2f shows the monitor reflection survey retrieved from homogeneously distributed passive sources. The contribution of each correlation function in equation 5.3 helps to cover all possible angles of illumination of the subsurface in order to attain the same illumination characteristics as those of the active base survey ($R_{\mathcal{A}}^{\smile}$). When this is achieved, changes in the subsurface can be identifiable in the shot gather, and even imaged using standard migration schemes for both results independently. The retrieved result still requires an additional amplitude scaling because of the medium properties at the passive source locations. In most of the cases, however, passive sources are sparsely distributed and clustered. The retrieval of the virtual reflection responses at the receiver locations using SI is conditioned by the presence of ambient sources located homogeneously around the target of study and the receiver array. If the distribution is inhomogeneous, the retrieval is not balanced and the resulting virtual reflection response is inaccurate (See Figure 5.2e).

SI by cross-correlation is based on several strong assumptions: passive sources are to be monopoles, uniformly distributed, and share the same source power spectrum. In practice, these conditions are generally not fulfilled (Draganov et al., 2009) and, as a consequence, the retrieved reflection response inherits an imprint of the passive source distribution. Removing this imprint from the recordings is a non-trivial task and requires illumination balancing for the case of SI by crosscorrelation, or solving an inverse problem for other passive SI methods (e.g. Wapenaar & van der Neut, 2010; van Groenestijn & Verschuur, 2010). However, when passive source illumination is limited to a reduced part of the subsurface, inverse SI methods become severely ill-posed and fail to achieve a good result. If passive illumination conditions are poor, for instance in cases where only a single passive source is available, this problem is unsolvable and alternative solutions are required.

5.1.2 Reciprocity-based passive monitoring with individual sources

The correlation gather of a single passive source contains correlated events induced by the presence of reflectors in the subsurface. These events are generally

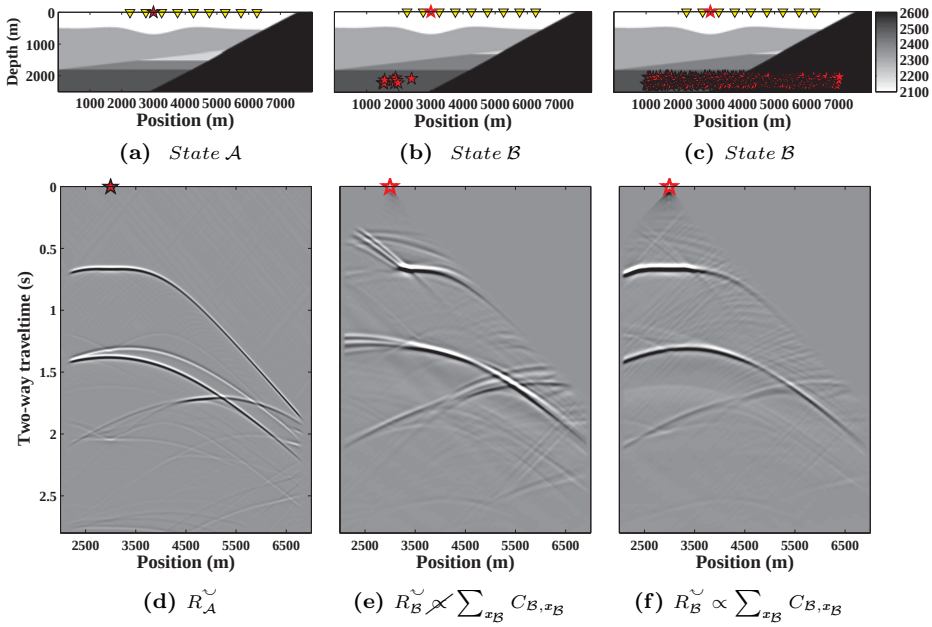

Figure 5.2: *Comparison of two different conventional interferometric monitoring results using SI by cross-correlation, with two different monitor scenarios. Model displays show acoustic velocity models ($m\ s^{-1}$).* **(a)** *Model at state $\mathcal{A}$ (base state) with source and receivers at the surface (as in figure 5.1).* **(b)** *Model at state $\mathcal{B}$ (monitor state) with passive sources clustered in depth (filled red stars) and receivers at the surface.* **(c)** *Same model during montior state $\mathcal{B}$ as in* (b)*, with a dense distribution of sources, homogeneously distributed in the subsurface.* **(d)** *Reflection response ($R^{\smile}_{\mathcal{A}}$) at state $\mathcal{A}$ in position $x_0 = 3000\ m$ (filled- red star in* (a)*).* **(e)** *Retrieved reflection response at state $\mathcal{B}$, in the same position (hollow red star in* (b)*), obtained using passive SI with the source distribution described in* (b)*.* **(f)** *Same as in* (e) *for the source distribution described in* (c)*.*

misinterpreted in time, except for those traces that cover the stationary-phase zone. In SI, destructive interference will be achieved for any other correlated trace pair, whereas constructive interference will take place within the stationary-phase zone eventually yielding the desired reflection response (Wapenaar & Fokkema, 2006). By using only the correlation gather of a single passive source, destructive interference cannot be achieved. However, the gather can still provide useful information of the subsurface, assuming that it contains traces within the desired stationary-phase zone.

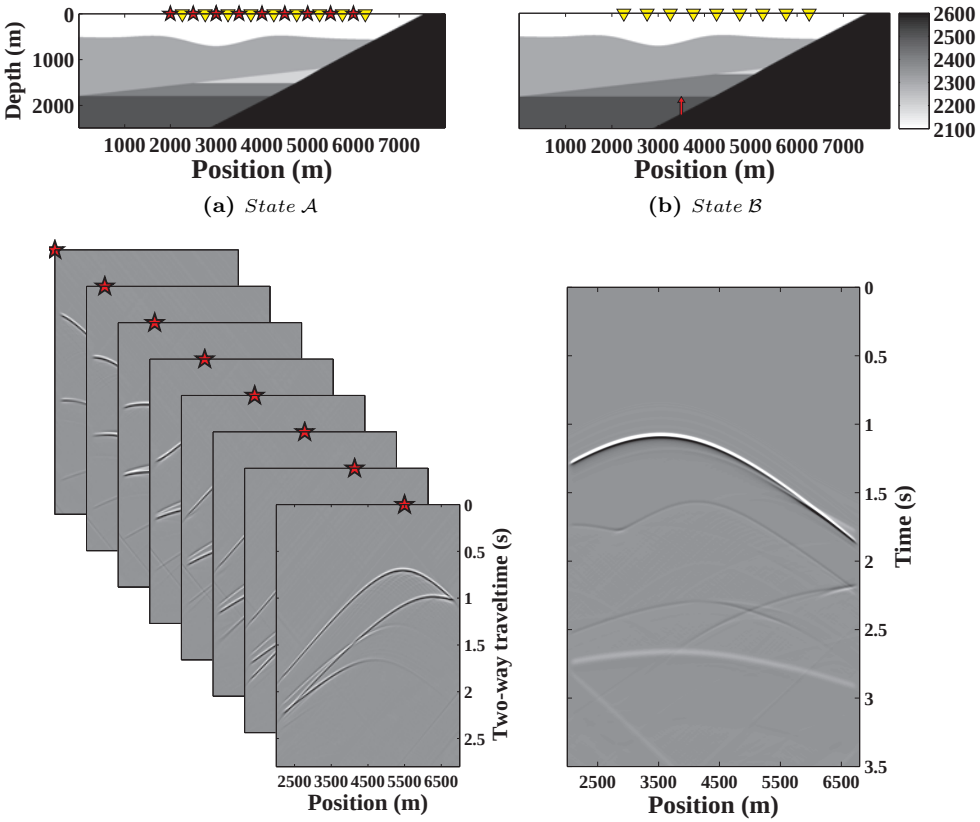

(a) *State* $\mathcal{A}$ **(b)** *State* $\mathcal{B}$

(c) $R^{\smile}_{0,\mathcal{A}}$ **(d)** $v^{obs}_{3,\mathcal{B}}$

Figure 5.3: *Set-up for one of the alternative monitoring schemes:* **(a)** *Acoustic velocity model (m* s^{-1}*) at state* $\mathcal{A}$ *(base survey): controlled sources and receivers are located at the Earth's surface.* **(b)** *Model at state* $\mathcal{B}$ *(monitor survey) with a single passive source in the subsurface (red star).* **(c)** *Reflection response survey at state* $\mathcal{A}$ *(as displayed in* (a)*), where the surface-related multiples have been removed* ($R^{\smile}_{0,\mathcal{A}}$)*.* **(d)** *Passive source recording* $v^{obs}_{3,\mathcal{B}}$ *at state* $\mathcal{B}$*, as illustrated in* (b)*.*

Almagro Vidal et al. (2012) shows an alternative method to migrate the correlation gather of a single passive source. This method is closely related to interferometric imaging (Schuster et al., 2004). However, unlike in conventional interferometric imaging, the directionality of the forward-propagated source field is constrained to avoid contributions outside the stationary-phase zone. Using this

method for time-lapse applications would require passive source locations in both the base and monitor states to coincide. This is physically unattainable. However, reciprocity relations between free-surface multiples and reflection responses from the surface may recreate, given a passive source in one of the states, the effect of the same passive source into the other state at the same location. Therefore, we propose an alternative method that requires controlled sources for the base survey and a single passive source at an arbitrary location for the monitor survey.

We present a monitoring method based on a double strategy: First to adapt the active base survey to the monitor survey by limiting the illumination characteristics, using the information from the passive source. Equalizing the illumination conditions of both base and monitor events from amplitude and phase features of the correlated events for analyzing changes in the subsurface. The process of adapting the illumination characteristics of the base survey is applied using either one of the two different relations obtained from the reciprocity relation of the convolution type with one-way wavefields. The second step is to identify among the correlated events of base and monitor surveys, the events in stationary phase. We employ an adapted migration scheme for imaging in depth the correlated events related to the monitoring target and which are in stationary phase. This migration scheme uses directional constraints based on the illumination of the passive source (Almagro Vidal et al., 2014), and is applied identically to the base and monitor surveys. Hence, the artefacts which could obscure the necessary analysis of changes in the subsurface are minimized.

We present numerical results of this method in a heterogeneous acoustic medium with structural and property changes in a reservoir between the base and monitor surveys. In figure 5.3 the available data to carry out the monitoring is presented. Figures 5.3a and 5.3b show the medium characteristics at both reference and monitor states, respectively, with coinciding receiver locations (yellow triangles) and different source locations (red stars): multiple active sources from the surface during the base survey (figure 5.3c) and a single passive source during the monitor survey (figure 5.3d).

5.2 The correlation function

In order to analyze the changes in the subsurface using passive recordings alone, we make use of correlation functions. Correlation functions are defined differently depending on the representation they are based on. The reciprocity relation of the convolution type is used to define our representations in a passive seismic configuration between states with different source location, domain boundary conditions and medium property changes. The convolutional relation was already presented in chapter 3.2 as:

$$\int_{\mathbb{D}} \{\hat{\mathbf{G}}^t_{\mathcal{A}} \mathbf{N} \hat{\mathbf{S}}_{\mathcal{B}} + \hat{\mathbf{S}}^t_{\mathcal{A}} \mathbf{N} \hat{\mathbf{G}}_{\mathcal{B}}\} d^3\mathbf{x} = \int_{\partial\mathbb{D}} \hat{\mathbf{G}}^t_{\mathcal{A}} \mathbf{N} \hat{\mathbf{G}}_{\mathcal{B}} \mathbf{n} d^2\mathbf{x} - \int_{\mathbb{D}} \{\hat{\mathbf{G}}^t_{\mathcal{A}} \mathbf{N} \Delta\hat{\mathbf{B}}_{\mathcal{B}-\mathcal{A}} \hat{\mathbf{G}}_{\mathcal{B}}\} d^3\mathbf{x}, \quad (5.4)$$

where $\Delta\hat{B}_{\mathcal{B}-\mathcal{A}}$ stands for the medium changes in the domain $\mathbb{D}$ between states. These states mean in this case, monitor state $\mathcal{B}$ and base state $\mathcal{A}$, with the purpose of monitoring the changes in the subsurface.

In this section we present, for the passive seismic configuration, two different relations of the convolution type for one-way wavefields from which the respective correlation functions are derived. However, we employ the relation of wavefields between two states without considering changes in the subsurface, but exclusively taking into account the boundary conditions and source locations. Hence, the terms "base state" and "monitor state" are not applied in this section. In appendix 5.A though, we show the resulting representations when we take into account the perturbations in the subsurface into the expression 5.4, and how they lead to the same relations describing the passive monitoring scheme in section 5.3 of this chapter.

5

5.2.1 Ballistic relation for passive seismics

As previously described in chapter 3.2, we define a reference state with an impulsive source at $\mathbf{x}_{\mathcal{B}}$ inside domain $\mathbb{D}$, and the half space above the upper boundary $\partial\mathbb{D}_0$ to be homogeneous. In the measurement state, the medium is heterogeneous above the control domain boundary $\partial\mathbb{D}_0$,.

For these state definitions, using the reciprocity relation of the convolution type in the frequency-space domain in 5.4, together with source-receiver reciprocity properties, the relation yields:

$$\hat{G}^-(\mathbf{x}_{\mathcal{A}}, \mathbf{x}_{\mathcal{B}}, \omega) = \hat{G}^-_0(\mathbf{x}_{\mathcal{A}}, \mathbf{x}_{\mathcal{B}}, \omega) - \int_{\mathbf{x}_0 \in \partial\mathbb{D}_0} \hat{R}^{\smile}(\mathbf{x}_{\mathcal{A}}, \mathbf{x}_0, \omega) \Big\{ \ldots \int_{\mathbf{x}'_0 \in \partial\mathbb{D}_0} \hat{R}^{\frown}_{\mathbb{D}',0}(\mathbf{x}_0, \mathbf{x}'_0, \omega) \hat{G}^-_0(\mathbf{x}'_0, \mathbf{x}_{\mathcal{B}}, \omega)\, d^2\mathbf{x}'_0 \Big\}\, d^2\mathbf{x}_0. \quad (5.5)$$

In this expression, $\hat{G}^-(\mathbf{x}_{\mathcal{A}}, \mathbf{x}_{\mathcal{B}}, \omega)$ is the upgoing transmission response at receiver location $\mathbf{x}_{\mathcal{A}}$, immediately above $\partial\mathbb{D}_0$ due to a passive source at $\mathbf{x}_{\mathcal{B}}$ in the subsurface including surface-related and internal multiples. For transmission responses only, both up- and downgoing-source terms are included together into $\hat{G}^-$ and

wavefield decomposition applies only at the receiver level. Subscript "$_0$" indicates the response corresponds to the domain $\mathbb{D}$ with a homogenized medium above $\partial\mathbb{D}_0$. Therefore, $\hat{G}_0^-(\mathbf{x}_\mathcal{A}, \mathbf{x}_\mathcal{B}, \omega)$ is the equivalent upgoing transmission response acquired at receiver location $\mathbf{x}_\mathcal{B}$ but without free-surface interaction. $\hat{R}^\cup(\mathbf{x}_\mathcal{A}, \mathbf{x}_0, \omega)$ is the impulsive reflection response of the domain below $\partial\mathbb{D}_0$ with free-surface interaction, recorded at receiver $\mathbf{x}_\mathcal{A}$ from a source located at $\mathbf{x}_0$ on $\partial\mathbb{D}_0$; This wavefield is a double-decomposed downgoing-source and upgoing-receiver wavefield (equivalent to $\hat{G}^{-,+}$). In a similar manner, $\hat{R}^{\curvearrowleft}_{\mathbb{D}',0}(\mathbf{x}_0, \mathbf{x}_0', \omega)$ is the impulsive reflection response of the control domain $\mathbb{D}'$ located above the upper boundary $\partial\mathbb{D}_0$ and the homogenization of the target domain $\mathbb{D}$ underneath, recorded at receiver $\mathbf{x}_0$ from a source located at $\mathbf{x}_0'$ on $\partial\mathbb{D}_0$. This wavefield is also a double-decomposed term but this time for an upgoing-source and a downgoing-receiver wavefield (this is, $\hat{G}^{+,-}_{\mathbb{D}',0}$).

In case the passive source signal is transient, we approximate the following reference-state transmission responses with the direct wave estimation from the decomposed up- and downgoing wavefields $\hat{G}^{-/+}_{dir}$:

$$\hat{G}^-_{dir}(\mathbf{x}_\mathcal{A}, \mathbf{x}_\mathcal{B}, \omega) \approx \hat{G}_0^-(\mathbf{x}_\mathcal{A}, \mathbf{x}_\mathcal{B}, \omega), \tag{5.6}$$

$$\hat{G}^+_{dir}(\mathbf{x}_0, \mathbf{x}_\mathcal{B}, \omega) \approx -\int_{\mathbf{x}_0' \in \partial\mathbb{D}_0} \hat{R}^{\curvearrowleft}_{\mathbb{D}',0}(\mathbf{x}_0, \mathbf{x}_0', \omega)\hat{G}_0^-(\mathbf{x}_0', \mathbf{x}_\mathcal{B}, \omega)\, d^2\mathbf{x}_0'. \tag{5.7}$$

Now applying these assumptions onto expression 5.5 becomes:

$$\hat{G}^-(\mathbf{x}_\mathcal{A}, \mathbf{x}_\mathcal{B}, \omega) - \hat{G}^-_{dir}(\mathbf{x}_\mathcal{A}, \mathbf{x}_\mathcal{B}, \omega) \approx \int_{\mathbf{x}_0 \in \partial\mathbb{D}_0} \hat{R}^\cup(\mathbf{x}_\mathcal{A}, \mathbf{x}_0, \omega)\hat{G}^+_{dir}(\mathbf{x}_0, \mathbf{x}_\mathcal{B}, \omega)\, d^2\mathbf{x}_0. \tag{5.8}$$

This expression becomes the same from which $R^\cup$-MDD with free surface multiples was derived in chapter 3.2. Equation 5.8 can be rewritten in the matrix-vector notation of Berkhout (1982) as

$$\hat{\boldsymbol{G}}^- - \hat{\boldsymbol{G}}^-_{dir} = \hat{\mathbf{R}}^\cup\, \hat{\boldsymbol{G}}^+_{dir}, \tag{5.9}$$

where $\hat{\boldsymbol{G}}^-$ is a column vector containing $\hat{G}^-(\mathbf{x}_\mathcal{A}, \mathbf{x}_\mathcal{B}, \omega)$ for a single passive source ($\mathbf{x}_\mathcal{B}$) and variable receiver locations ($\mathbf{x}_\mathcal{A}$). Matrix $\hat{\mathbf{R}}^\cup$ contains data from $\hat{R}^\cup(\mathbf{x}_\mathcal{A}, \mathbf{x}_0, \omega)$, where each column and row contain the data from an individual source and receiver, respectively. Now, if we apply the adjoint (indicated by †) of $\hat{\boldsymbol{G}}^+_{dir}$ to both sides of equation 5.9, we obtain:

$$(\hat{\boldsymbol{G}}^{-} - \hat{\boldsymbol{G}}^{-}_{dir})\{\hat{\boldsymbol{G}}^{+}_{dir}\}^{\dagger} = \hat{\mathbf{R}}^{\smile}\, \hat{\boldsymbol{G}}^{+}_{dir}\{\hat{\boldsymbol{G}}^{+}_{dir}\}^{\dagger}. \tag{5.10}$$

Assuming the direct field of the passive source $\hat{G}_{dir}$ can be extracted from the passive recording, the left-hand side of this expression can be computed. We refer to the result of this operation as the correlation function for the ballistic relation $C^{(1)}$:

$$\hat{\mathbf{C}}^{(1)} = (\hat{\boldsymbol{G}}^{-} - \hat{\boldsymbol{G}}^{-}_{dir})\{\hat{\boldsymbol{G}}^{+}_{dir}\}^{\dagger}. \tag{5.11}$$

Additionally, we define the source function:

$$\hat{\mathbf{\Gamma}}^{(1)} = \hat{\boldsymbol{G}}^{+}_{dir}\{\hat{\boldsymbol{G}}^{+}_{dir}\}^{\dagger}. \tag{5.12}$$

In representations based on reciprocity relations, this function has also been called point-spread function (van der Neut, 2013). We can now substitute expressions 5.11 and 5.12 into equation 5.10, leading towards:

$$\hat{\mathbf{C}}^{(1)} = \hat{\mathbf{R}}^{\smile}\, \hat{\mathbf{\Gamma}}^{(1)}. \tag{5.13}$$

This expression shows the obtained correlation function of a single passive source $C^{(1)}$ is the reflection response $R^{\smile}$ convolved with the point-spread function $\Gamma^{(1)}$ in the time domain, over the complete upper boundary $\partial\mathbb{D}_0$. Note that $\Gamma^{(1)}$ thus imposes illumination which can only be provided by the direct wavefield of the passive data.

5.2.2 Full-field relation for passive seismics

Swapping the locations of the source between the two states, provides a different representation from the same convolutional relation. If we consider the reference state with the homogeneous half space and the source located at $\mathbf{x}_{\mathcal{A}}$ immediately above $\partial\mathbb{D}_0$ and the measurement state to have the source situated at $\mathbf{x}_{\mathcal{B}}$ inside the domain $\mathbb{D}$, the representation becomes:

$$\hat{G}^{-}(\mathbf{x}_{\mathcal{A}}, \mathbf{x}_{\mathcal{B}}, \omega) - \hat{G}^{-}_{0}(\mathbf{x}_{\mathcal{A}}, \mathbf{x}_{\mathcal{B}}, \omega) = \int_{\mathbf{x}_0 \in \partial\mathbb{D}_0} \hat{R}^{\smile}_{0}(\mathbf{x}_{\mathcal{A}}, \mathbf{x}_0, \omega)\hat{G}^{+}(\mathbf{x}_0, \mathbf{x}_{\mathcal{B}}, \omega)\, d^2\mathbf{x}_0, \tag{5.14}$$

where the left hand side remains the same while the integral wavefield quantities now belong to opposite states. In this case, the same condition as for the

ballistic relation is applied: Since we cannot estimate wavefields at the reference state $\hat{G}_0^-$, we make its estimation from the direct transmission response from the measurement state, $\hat{G}_{dir}^-$. Hence, the simplification of expression 5.14 becomes:

$$\hat{G}^-(\mathbf{x}_\mathcal{A}, \mathbf{x}_\mathcal{B}, \omega) - \hat{G}_{dir}^-(\mathbf{x}_\mathcal{A}, \mathbf{x}_\mathcal{B}, \omega) \approx \int_{\mathbf{x}_0 \in \partial\mathbb{D}_0} \hat{R}_0^{\smile}(\mathbf{x}_\mathcal{A}, \mathbf{x}_0, \omega) \hat{G}^+(\mathbf{x}_0, \mathbf{x}_\mathcal{B}, \omega)\, d^2\mathbf{x}_0. \quad (5.15)$$

This expression has already been shown in chapter 3.2, for the $R_0^{\smile}$-MDD without free surface. The error due to the applied approximation corresponds to the downward-radiating source contribution and internal multiples missing in the wavefield. Equation 5.15 can have its terms rewritten in the matrix-vector notation as:

$$\hat{\boldsymbol{G}}^- - \hat{\boldsymbol{G}}_{dir}^- = \hat{\mathbf{R}}_\mathbf{0}^{\smile}\, \hat{\boldsymbol{G}}^+, \quad (5.16)$$

where the wavefield matrices and vectors follow the same structure as in equation 5.9. The normal equation from 5.16 makes use of the adjoint of $\hat{\boldsymbol{G}}^+$ as in expression 5.10 in order to obtain:

$$(\hat{\boldsymbol{G}}^- - \hat{\boldsymbol{G}}_{dir}^-)\{\hat{\boldsymbol{G}}^+\}^\dagger = \hat{\mathbf{R}}_\mathbf{0}^{\smile}\, \hat{\boldsymbol{G}}^+\{\hat{\boldsymbol{G}}^+\}^\dagger. \quad (5.17)$$

The correlation function of the full-field convolutional relation is defined in this case as:

$$\hat{\mathbf{C}}^{(2)} = (\hat{\boldsymbol{G}}^- - \hat{\boldsymbol{G}}_{dir}^-)\{\hat{\boldsymbol{G}}^+\}^\dagger, \quad (5.18)$$

and for the respective source- or point-spread function:

$$\hat{\mathbf{\Gamma}}^{(2)} = \hat{\boldsymbol{G}}^+\{\hat{\boldsymbol{G}}^+\}^\dagger. \quad (5.19)$$

This relation represents a more complicated point-spread function than the one defined in equation 5.12, but easier to construct. We can now substitute expressions 5.18 and 5.19 into equation 5.17, leading to:

$$\hat{\mathbf{C}}^{(2)} = \hat{\mathbf{R}}_\mathbf{0}^{\smile}\, \hat{\mathbf{\Gamma}}^{(2)}. \quad (5.20)$$

The product of the reflection response with the point-spread function means a convolution product in the time domain. This convolution product is an integrating operation of the complete upper boundary. According to this expression, the

obtained correlation function of a single passive source can be interpreted as the reflection response without free surface $R_0^{\cup}$, array-modulated by a complex source function $\Gamma^{(2)}$ which imposes the limiting illumination conditions. Note that $\Gamma^{(2)}$ comprises illumination information provided by the direct arrival of the passive data and the multiples scattered inside the medium.

5.3 Passive monitoring

In order to analyze the changes in the subsurface between the base and monitor states, we construct the respective state's correlation functions. Depending on the convolutional relation employed, the recording of the passive source will serve to construct the correlation function of the monitor state, and also the point-spread function to create the correlation function of the base state. For each relation, we describe the passive monitoring analysis and depict it using the numerical results obtained for a 2D acoustic medium.

5.3.1 Passive monitoring with the ballistic relation

In this section, we investigate changes in the subsurface between base state $\mathcal{A}$ and monitor state $\mathcal{B}$, represented in Figures 5.3a and 5.3b. The modelling results used an acquisition array located at 50 m depth and 5000 m of aperture. The receiver sampling is 20 m.

In state $\mathcal{A}$ we have controlled sources available at the receiver locations. In order to retrieve the reflection response $R_{\mathcal{A}}^{\cup}$ used for the base survey, double source- and receiver decomposition are applied, and the source signature is removed. Decomposition results are power-flux normalized. In state $\mathcal{B}$ we count on the passive recording $v_{3,\mathcal{B}}^{obs}$, which is decomposed into one-way wavefields and power flux-normalized, but with the source signature preserved. We employed for this passive recording a vertically oriented point-force source (vertical red arrow in figure 5.3b).

To obtain the monitor correlated gather we take the expression from equation 5.11 and carry out the time-windowed direct field simplification:

$$\hat{C}_{\mathcal{B}}^{(1)}\left(\mathbf{x}_{\mathcal{A}},\mathbf{x}_0,\omega\right) \Rightarrow \hat{\mathbf{C}}_{\mathcal{B},v_{3,\mathcal{B}}^{obs}}^{(1)} = (\hat{\boldsymbol{p}}_{\mathcal{B}}^{-} \; - \; \hat{\boldsymbol{p}}_{dir,\mathcal{B}}^{-})\{\hat{\boldsymbol{p}}_{dir,\mathcal{B}}^{+}\}^{\dagger}. \tag{5.21}$$

$\hat{\boldsymbol{p}}_{\mathcal{B}}^{-}$ symbolises the vectorial representation of the upgoing- power-flux normalized wavefield $\hat{p}_{\mathcal{B}}$, obtained out of the observed wavefield $\hat{v}_{3,\mathcal{B}}^{obs}$. In this approximation we ignore the contribution from the internal multiples of the passive source without free surface, and only the incident field (the most energetic arrival) is considered.

In order to compare the response of the base survey with the correlation function $C_{\mathcal{B},v_{3,\mathcal{B}}^{obs}}^{(1)}$, we imprint the illumination characteristics of the passive source $\hat{v}_{3,\mathcal{B}}^{obs}$

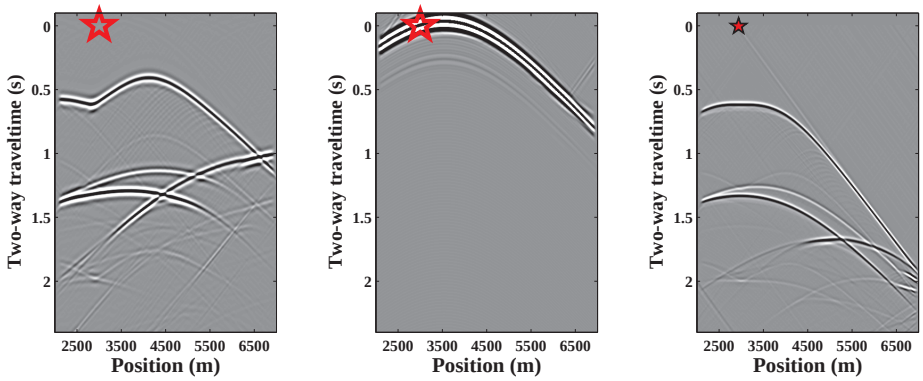

(a) $\mathbf{C}^{(1)}_{\mathcal{A},R^{\smile}_{\mathcal{A}}}$ **(b)** $\mathbf{\Gamma}^{(1)}_{\mathcal{B}}$ **(c)** $\mathbf{R}^{\smile}_{\mathcal{A}}$

Figure 5.4: (a) *Correlation function due to the ballistic relation 5.22 ($C^{(1)}_{\mathcal{A},R^{\smile}_{\mathcal{A}}}$) at virtual source $x_0 = 3000\ m$, of the reference state $\mathcal{A}$ with the illumination induced from the passive source in state $\mathcal{B}$.* **(b)** *Point-spread function $\Gamma^{(1)}_{\mathcal{B}}$ at the same location due to the passive source recording $v^{obs}_{3,\mathcal{B}}$ in state $\mathcal{B}$ (see Figures 5.3b and 5.3d).* **(c)** *Reflection response $R^{\smile}_{\mathcal{A}}$ at $x_0 = 3000\ m$ in state $\mathcal{A}$, with free-surface interaction.*

5

in state $\mathcal{A}$ using expression 5.13 into the impulsive reflection response $R^{\smile}_{\mathcal{A}}$. This operation implies a multidimensional convolution with the respective point-spread function:

$$\hat{C}^{(1)}_{\mathcal{A}}\left(\mathbf{x}_{\mathcal{A}}, \mathbf{x}_0, \omega\right) \Rightarrow \hat{\mathbf{C}}^{(1)}_{\mathcal{A},R^{\smile}_{\mathcal{A}}} = \hat{\mathbf{R}}^{\smile}_{\mathcal{A}}\, \hat{\mathbf{\Gamma}}^{(1)}_{\mathcal{B}}. \tag{5.22}$$

where the point-spread function is:

$$\hat{\mathbf{\Gamma}}^{(1)}_{\mathcal{B}} = \hat{\boldsymbol{p}}^{+}_{dir,\mathcal{B}}\{\hat{\boldsymbol{p}}^{+}_{dir,\mathcal{B}}\}^{\dagger}. \tag{5.23}$$

The point-spread function contains the same power spectrum of the passive recording, equivalent to the correlation function $\hat{C}^{(1)}_{\mathcal{B}}$. Therefore, for the time-lapse analysis, the source signal is preserved in both base and monitor correlation functions. First subscript in $\hat{C}^{(1)}_{\mathcal{A},R^{\smile}_{\mathcal{A}}}$ indicates that the correlation function belongs to the medium characteristics at state $\mathcal{A}$, while the second subscript indicates the origin of the data: reflectivity at state $\mathcal{A}$ upon which the imprint of the passive source function is applied by the point-spread function.

Following equations 5.13 and consequently 5.22, the definition of the correlation function in equation 5.21 is interpreted as a multidimensional convolution of

the desired reflection response in state $\mathcal{B}$, $R^{\smile}_{\mathcal{B}}$, with the same-state point-spread function $\Gamma^{(1)}_{\mathcal{B}}$. Therefore, the difference between the correlation functions represent the time lapse response between the respective reflection responses in states $\mathcal{A}$ and $\mathcal{B}$ according to the array- virtual-source modulation introduced by the point-spread function $\hat{\Gamma}^{(1)}_{\mathcal{B}}$:

$$\hat{\mathbf{C}}^{(1)}_{\mathcal{B},v^{obs}_{3,\mathcal{B}}} - \hat{\mathbf{C}}^{(1)}_{\mathcal{A},R^{\smile}_{\mathcal{A}}} = (\hat{\mathbf{R}}^{\smile}_{\mathcal{B}} - \hat{\mathbf{R}}^{\smile}_{\mathcal{A}})\hat{\mathbf{\Gamma}}^{(1)}_{\mathcal{B}}. \tag{5.24}$$

We limit our time-lapse observation to the angles provided by the point-spread function. $C^{(1)}_{\mathcal{A},R^{\smile}_{\mathcal{A}}}$ and $\hat{C}^{(1)}_{\mathcal{B},v^{obs}_{3,\mathcal{B}}}$ inherit the imprint of the same point-spread function $\Gamma_{\mathcal{B}}$, and therefore they can be directly compared to reveal the change of subsurface reflectivity between states $\mathcal{A}$ and $\mathcal{B}$ according the illumination angles provided by the passive source. This includes the source characteristics of the passive source in the monitor state. Hence, in our monitoring scheme we compare the correlation functions as if we were lowering the illumination characteristics of $R^{\smile}_{\mathcal{A}}$ and the hypothetical $R^{\smile}_{\mathcal{B}}$ to the limited illumination the passive source can provide, encoded in the point-spread function.

In Figure 5.4a we show the correlation function $C^{(1)}_{\mathcal{A},R^{\smile}_{\mathcal{A}}}$, obtained from the reflection response of the base survey $R^{\smile}_{\mathcal{A}}$ (Figure 5.4c) after its multi-dimensional convolution with the point-spread function $\Gamma^{(1)}_{\mathcal{B}}$ (Figure 5.4b). During this construction, the information about the subsurface is provided by the reflectivity. The point-spread function imprints the illumination characteristics over the data $R^{\smile}_{\mathcal{A}}$ and the result shows the virtually reconstructed tremor as if it had happened at state $\mathcal{A}$.

In Figure 5.5 we show the comparison of correlation functions using the ballistic relation. Figure 5.5a shows the correlation function $C^{(1)}_{\mathcal{B},v^{obs}_{3,\mathcal{B}}}$ which serves as monitor. Figure 5.5b, $C^{(1)}_{\mathcal{A},R^{\smile}_{\mathcal{A}}}$, is generated by the convolution in the time domain of $R^{\smile}_{\mathcal{A}}$ (obtained with controlled sources at the $\partial\mathbb{D}_0$) with $\Gamma^{(1)}_{\mathcal{B}}$. The difference of Figures 5.5a and 5.5b stems from the changes in the reservoir that we aim to retrieve (the differences between the model in figure 5.3a and the model in figure 5.3b).

Figure 5.5c shows the correlation function $C^{(1)}_{\mathcal{A},v^{obs}_{3,\mathcal{A}}}$, this is, the correlation function of an actual passive source at state $\mathcal{A}$ at the same location as the one in state $\mathcal{B}$ and with the same source spectrum and characteristics. Note the similarities between Figures 5.5b and 5.5c, indicating that the radiation patterns of the controlled sources in the base survey have been successfully modified to the radiation patterns that would be seen if these data were constructed from the same passive source in the subsurface.

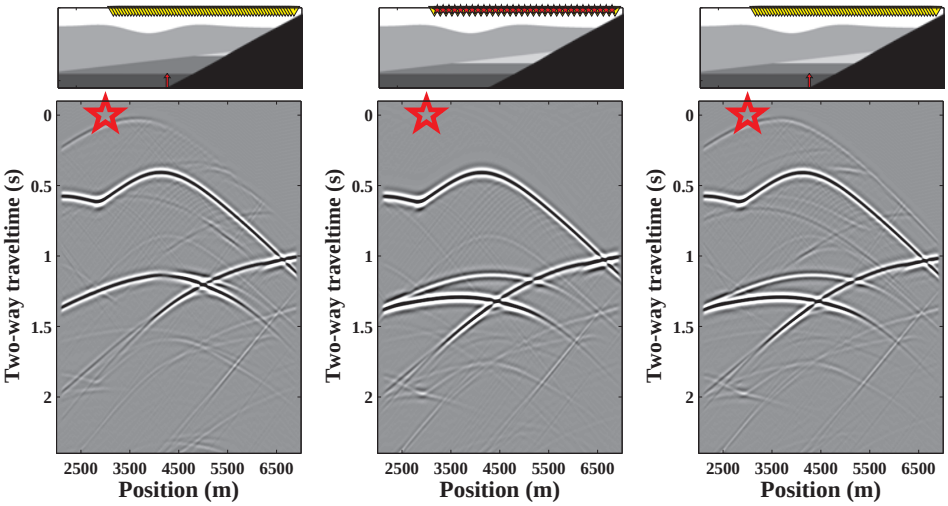

(a) $\mathbf{C}^{(1)}_{\mathcal{B},v^{obs}_{3,\mathcal{B}}}$ (b) $\mathbf{C}^{(1)}_{\mathcal{A},R^{\smile}_{\mathcal{A}}}$ (c) $\mathbf{C}^{(1)}_{\mathcal{A},v^{obs}_{3,\mathcal{A}}}$

Figure 5.5: **(a)** *Correlation function of the ballistic relation* $C^{(1)}_{\mathcal{B},v^{obs}_{3,\mathcal{B}}}$ *at virtual source* $x_0 = 3000\ m$*, of the monitor state* $\mathcal{B}$*.* **(b)** *Correlation function of the ballistic relation at the same location, virtually created with the illumination induced from the passive source at state* $\mathcal{B}$*,* $C^{(1)}_{\mathcal{A},R^{\smile}_{\mathcal{A}}}$*.* **(c)** *Correlation function of the ballistic relation* $C^{(1)}_{\mathcal{A},v^{obs}_{3,\mathcal{A}}}$ *at the same location at the base state* $\mathcal{A}$*.*

In Figure 5.6, the correlation functions match the same waveform and amplitudes. The overburden remains the same for the base and monitor states, while the reservoir top reveals the change of the reservoir properties: the interface remains in the same location while the contrast becomes negative. The corresponding reservoir-floor signal (in this case this would represent a gas-oil contact), visible in the base correlation function, it disappears in the monitor correlation function. Correlation artefacts, and amplitudes misfits of the side-reservoir signal and later signals are due to the negligence of the internal multiples in both correlation functions together with the array aperture limitation with respect to the depth of the reflector.

5.3.2 Passive monitoring with the full-field relation

Changes in the subsurface between the two states $\mathcal{A}$ and $\mathcal{B}$ can alternatively be analyzed using the full-field relation with the same tremor recording. This relation has advantages and drawbacks with respect to the ballistic relation. Correlation and source functions are easier to compute, while on the other hand the reflection response data from the base survey requires additional processing. The free-

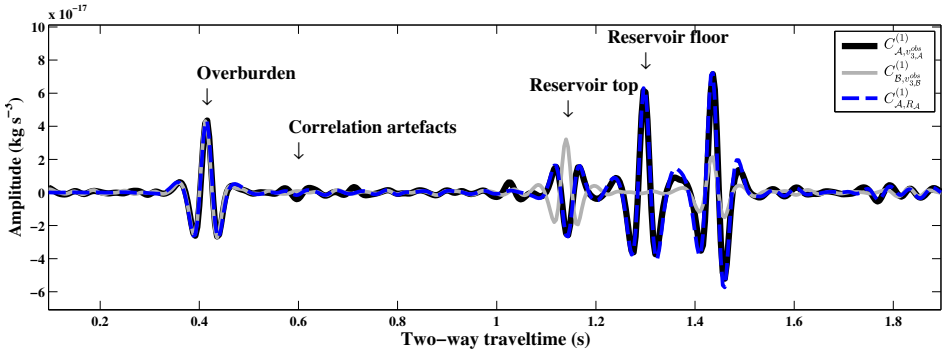

Figure 5.6: *Comparison of correlation functions for virtual source $x_0 = 3000\ m$ and receiver $x_{\mathcal{A}} = 4000\ m$ due to the ballistic relation. Monitor function ($C^{(1)}_{\mathcal{B},v^{obs}_{3,\mathcal{B}}}$, equation 5.21, gray solid line) is to be compared with respect to the base estimate function ($C^{(1)}_{\mathcal{A},R^{\cup}_{\mathcal{A}}}$, equation 5.22, blue dashed line). To corroborate the accuracy of the base estimate function, we plot the correlation function of the passive source employed at state $\mathcal{A}$ ($C^{(1)}_{\mathcal{A},v^{obs}_{3,\mathcal{A}}}$, equation 5.21 for $v^{obs}_{3,\mathcal{A}}$, black solid line).*

5

surface multiples and source wavelet should be eliminated from these data, either by surface-related multiple elimination (Verschuur et al., 1992) or by Estimation of Primaries by Sparse Inversion (van Groenestijn & Verschuur, 2009), providing us the desired impulsive reflection response $R^{\cup}_{0,\mathcal{A}}$ in state $\mathcal{A}$.

To obtain the correlation function of the monitor state, we compute equation 5.18:

$$\hat{C}^{(2)}_{\mathcal{B}}\left(\mathbf{x}_{\mathcal{A}},\mathbf{x}_0,\omega\right) \Rightarrow \hat{\mathbf{C}}^{(2)}_{\mathcal{B},v^{obs}_{3,\mathcal{B}}} = (\hat{\boldsymbol{p}}^{-}_{\mathcal{B}} - \hat{\boldsymbol{p}}^{-}_{dir,\mathcal{B}})\{\hat{\boldsymbol{p}}^{+}_{\mathcal{B}}\}^{\dagger}. \tag{5.25}$$

This expression proves to be less sensitive to the approximation of using the direct wavefield when compared to the equivalent expression from the ballistic relation in equation 5.21. As for the correlation function of the base state, this is retrieved using equation 5.19:

$$\hat{C}^{(2)}_{\mathcal{A}}\left(\mathbf{x}_{\mathcal{A}},\mathbf{x}_0,\omega\right) \Rightarrow \mathbf{C}^{(2)}_{\mathcal{A},R^{\cup}_{0,\mathcal{A}}} = \hat{\mathbf{R}}^{\cup}_{\mathbf{0},\mathcal{A}}\,\hat{\mathbf{\Gamma}}^{(2)}_{\mathcal{B}}, \tag{5.26}$$

where the respective point-spread function shows:

$$\hat{\mathbf{\Gamma}}^{(2)}_{\mathcal{B}} = \hat{\boldsymbol{p}}^{+}_{\mathcal{B}}\{\hat{\boldsymbol{p}}^{+}_{\mathcal{B}}\}^{\dagger}. \tag{5.27}$$

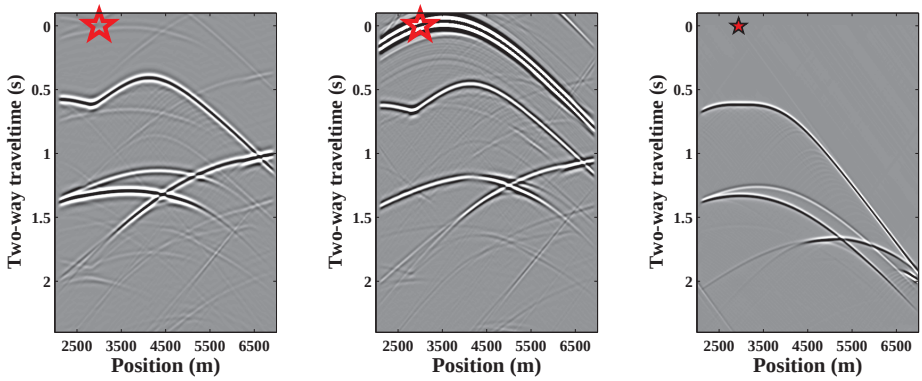

(a) $\mathbf{C}^{(2)}_{\mathcal{A},R^{\cup}_{0,\mathcal{A}}}$ (b) $\mathbf{\Gamma}^{(2)}_{\mathcal{B}}$ (c) $\mathbf{R}^{\cup}_{\mathbf{0},\mathcal{A}}$

Figure 5.7: **(a)** *Correlation function due to the full-field relation 5.26 ($C^{(2)}_{\mathcal{A},R^{\cup}_{0,\mathcal{A}}}$) at virtual source $x_0 = 3000\ m$, of the reference state $\mathcal{A}$ with the illumination induced from the passive source in state $\mathcal{B}$.* **(b)** *Point-spread function $\Gamma^{(2)}_{\mathcal{B}}$ at the same location due to the passive source recording $v^{obs}_{3,\mathcal{B}}$ in state $\mathcal{B}$ (see Figures 5.3b and 5.3d).* **(c)** *Reflection response $R^{\cup}_{0,\mathcal{A}}$ at $x_0 = 3000\ m$ at state $\mathcal{A}$, without free-surface interaction.*

Similar to the correlation function of the monitor state (equation 5.25), this base state correlation function does not run on assumptions based on reference state transmission responses nor direct wave time-windowing. Therefore, inaccuracies at the time-lapse analysis will affect exclusively the monitor correlation function for the full-field relation. The difference between the correlation functions in this case can be written as:

$$\hat{\mathbf{C}}^{(2)}_{\mathcal{B},v^{obs}_{3,\mathcal{B}}} - \hat{\mathbf{C}}^{(2)}_{\mathcal{A},R^{\cup}_{\mathcal{A}}} = (\hat{\mathbf{R}}^{\cup}_{\mathbf{0},\mathcal{B}} - \hat{\mathbf{R}}^{\cup}_{\mathbf{0},\mathcal{A}})\hat{\mathbf{\Gamma}}^{(2)}_{\mathcal{B}}. \tag{5.28}$$

Figure 5.7a shows the resulting correlation function $C^{(2)}_{\mathcal{A},R^{\cup}_{0,\mathcal{A}}}$ when carrying out the multidimensional convolution of equation 5.26 between the reflection response of the base survey $R^{\cup}_{0,\mathcal{A}}$ (Figure 5.7c) and the source function $\Gamma^{(2)}_{\mathcal{B}}$ (Figure 5.7b). Once again, the reflectivity provides the subsurface information of the resulting correlation function.

In Figure 5.8 we show the result of the correlation functions when using the full-field relation for comparison. Figure 5.8a shows the monitor correlation function $C^{(2)}_{\mathcal{B},v^{obs}_{3,\mathcal{B}}}$. Figure 5.8b, displays the correlation function $C^{(2)}_{\mathcal{A},R^{\cup}_{0,\mathcal{A}}}$ intended to serve as base, generated using $R^{\cup}_{0,\mathcal{A}}$ and $\Gamma^{(2)}_{\mathcal{B}}$. Figure 5.8c shows the correlation function

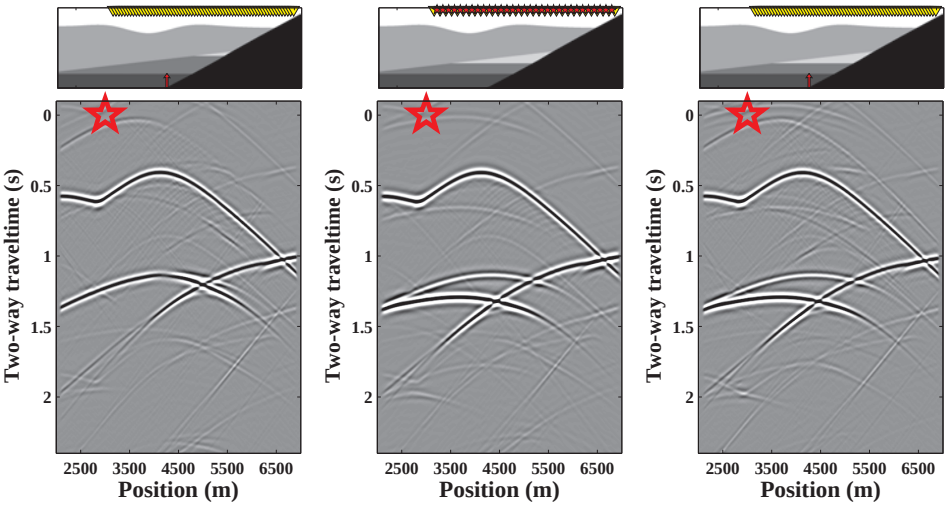

(a) $\mathbf{C}^{(2)}_{\mathcal{B},v^{obs}_{3,\mathcal{B}}}$ (b) $\mathbf{C}^{(2)}_{\mathcal{A},R^{\smile}_{0,\mathcal{A}}}$ (c) $\mathbf{C}^{(2)}_{\mathcal{A},v^{obs}_{3,\mathcal{A}}}$

Figure 5.8: (a) *Correlation function of the full-field relation* $C^{(2)}_{\mathcal{B},v^{obs}_{3,\mathcal{B}}}$ *at virtual source* $x_0 = 3000\ m$*, of the monitor state* $\mathcal{B}$*.* **(b)** *Equivalent correlation function at the same location, virtually generated with the illumination induced from the passive source at state* $\mathcal{B}$*,* $C^{(2)}_{\mathcal{A},R^{\smile}_{0,\mathcal{A}}}$*.* **(c)** *Correlation function of the full-field relation 5.25 at the base state* $\mathcal{A}$*,* $C^{(2)}_{\mathcal{A},v^{obs}_{3,\mathcal{A}}}$*.*

5

$C^{(2)}_{\mathcal{A},v^{obs}_{3,\mathcal{A}}}$, serving as reference. Once again, the features of the virtually created passive source correlation function imitates the result of the correlation function of the actual passive source at state $\mathcal{A}$ (See similarities between results in Figures 5.8b and 5.8c).

Figure 5.9 compares the results of these three correlation functions and shows the illumination imprint of the passive source is adequately generated onto the controlled sources of the base survey. The same waveform and amplitudes are retrieved in the correlation functions. Once again we identify the same signal changes in the reservoir top and bottom between the base and monitor correlation functions, while the overburden signal remains invariant. However, there is a slightly better matching of the correlation artefacts and also for the signal of the reservoir side. This confirms the full-field relation is more reliable than the ballistic one for the same given data due to its reduced sensitivity to the direct wave approximation in its formulation.

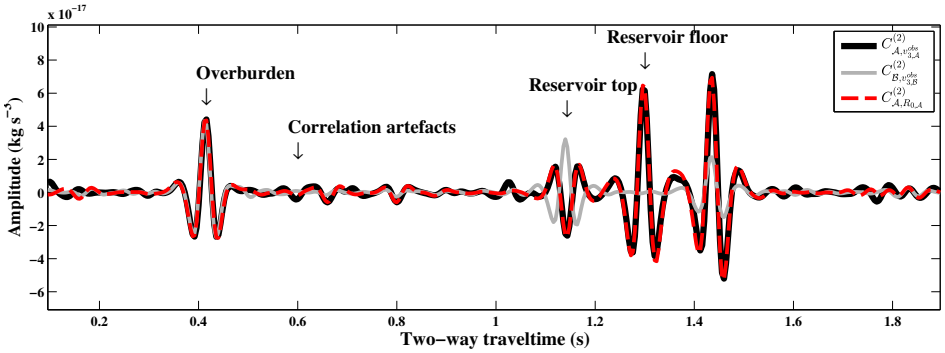

Figure 5.9: *Comparison of correlation functions for virtual source $x_0 = 3000\ m$ and receiver $x_{\mathcal{A}} = 4000\ m$ due to the full-field relation. Monitor function ($C^{(2)}_{\mathcal{B},v^{obs}_{3,\mathcal{B}}}$, equation 5.25, gray solid line) is to be compared with respect to the base estimate function ($C^{(2)}_{\mathcal{A},R^{\smile}_{0,\mathcal{A}}}$, equation 5.26, red dashed line). The display of the correlation function of the passive source employed at state $\mathcal{A}$ ($C^{(2)}_{\mathcal{A},v^{obs}_{3,\mathcal{A}}}$, equation 5.25 for $v^{obs}_{3,\mathcal{A}}$, black solid line) confirms the fidelity of the base estimate function.*

5

5.4 Directionally constrained migration of correlation functions

Imaging of correlated data from passive sources has been presented in Almagro Vidal et al. (2012), (chapter 4 of this thesis). In this method, the illumination characteristics serve as a directional constraint in the migration process, and of the primary reflections only those correlated parts that are in stationary phase are imaged. The illumination characteristics are studied using illumination analysis of either of the point-spread functions, $\Gamma^{(1)}_{\mathcal{B}}$ or $\Gamma^{(2)}_{\mathcal{B}}$, which encode the imprint of the limited illumination provided by the passive source recording $v^{obs}_{3,\mathcal{B}}$ (Almagro Vidal et al., 2014). This analysis identifies the dominant ray-parameter $\mathbf{p}^{\mathbf{x}_0}$ which defines the ray-path of the specular field for primaries only from each virtual source location $\mathbf{x}_0$ at $\partial\mathbb{D}_0$.

The forward wavefield is constructed here, for a given instant t_0, using the directional constrain $\mathbf{p}^{\mathbf{x}_0}_{v^{obs}_{3,\mathcal{B}}}$ given by $v^{obs}_{3,\mathcal{B}}$:

$$D^{\Downarrow}_{v^{obs}_{3,\mathcal{B}}}(\mathbf{x},\mathbf{x}_0,t_0) \approx \frac{1}{\pi}\Re\int_0^{\infty} \hat{G}^{GB}_{v^{obs}_{3,\mathcal{B}}}(\mathbf{x},\mathbf{x}_0,\mathbf{p}^{\mathbf{x}_0}_{v^{obs}_{3,\mathcal{B}}},\omega)\,\hat{S}_{v^{obs}_{3,\mathcal{B}}}(\omega)\,e^{i\omega t_0}\,d\omega, \tag{5.29}$$

where $\hat{G}^{GB}_{v^{obs}_{3,\mathcal{B}}}(\mathbf{x},\mathbf{x}_0,\omega)$ is a limited asymptotic approximation to the Green's func-

tion using a single Gaussian beam with initial ray-parameter $\mathbf{p}^{\mathbf{x}_0}_{v^{obs}_{3,\mathcal{B}}}$ at virtual source location $\mathbf{x}_0$ for any image point $\mathbf{x}$ in the subsurface. $\hat{S}_{v^{obs}_{3,\mathcal{B}}}(\omega)$ is the source signal of the passive recording, extracted from the direct wave arrival. $\mathbf{p}^{\mathbf{x}_0}_{v^{obs}_{3,\mathcal{B}}}$ can be estimated from either point-spread functions $\Gamma^{(1)}_{\mathcal{B}}$ or $\Gamma^{(2)}_{\mathcal{B}}$. Since they should provide a similar result for the dominant ray-parameter, the forward wavefield reconstruction in equation 5.29 remains the same regardless of the correlation function to be imaged, base or monitor, without regard also to the reciprocity relation employed in the retrieval of such correlation function.

For the following explanations, we are focusing on the full-field relation. We construct the backprojected field convolving the respective correlation function $C^{(2)}_{\mathcal{A},R^{\cup}_{0,\mathcal{A}}}$ with individual Green's function representations in Gaussian beams, $\hat{G}^{GB}$, from every receiver location $\mathbf{x}_{\mathcal{A}}$, at every image point $\mathbf{x}$:

$$\hat{C}^{(2),GB}_{\mathcal{A},R^{\cup}_{0,\mathcal{A}}}(\mathbf{x},\mathbf{x}_0,\mathbf{p},\omega) = \left\{\hat{\Xi}(\mathbf{p},\omega)\right\}^* \int_{\mathbf{x}_{\mathcal{A}}\in\partial\mathbb{D}_0} \left\{\hat{G}^{GB}(\mathbf{x},\mathbf{x}_{\mathcal{A}},\mathbf{p},\omega)\right\}^* \hat{C}^{(2)}_{\mathcal{A},R^{\cup}_{0,\mathcal{A}}}(\mathbf{x}_{\mathcal{A}},\mathbf{x}_0,\omega) d^2\mathbf{x}_{\mathcal{A}}. \quad (5.30)$$

This representation of the correlation function shows its backprojection toward the medium in a given direction (expressed in ray-parameters, $\mathbf{p}$). $\hat{\Xi}(\mathbf{p},\omega)$ stands for a scaling factor for the initial amplitudes of the Gaussian beam with respect to the ray-parameter. Using expression 5.30, we construct the backprojected field by summing the Gaussian beams homogeneously distributed in different ray-parameters. Hence, the backprojected wavefield of the base state at the instant t_0 becomes:

$$U^{\Uparrow}_{\mathcal{A},R^{\cup}_{0,\mathcal{A}}}(\mathbf{x},\mathbf{x}_0,t_0) = \frac{-2}{\pi}\int_{-\infty}^{\infty} \Re\left\{\int_0^{\infty} \hat{C}^{(2),GB}_{\mathcal{A},R^{\cup}_{0,\mathcal{A}}}(\mathbf{x},\mathbf{x}_0,\mathbf{p},\omega) e^{i\omega t_0}\, d\omega\right\} d^2\mathbf{p}. \quad (5.31)$$

As for the monitor backprojected field, we employ $C^{(2)}_{\mathcal{B},v^{obs}_{3,\mathcal{B}}}$ to construct it in the same manner:

$$\hat{C}^{(2),GB}_{\mathcal{B},v^{obs}_{3,\mathcal{B}}}(\mathbf{x},\mathbf{x}_0,\mathbf{p},\omega) = \left\{\hat{\Xi}(\mathbf{p},\omega)\right\}^* \int_{\mathbf{x}_{\mathcal{A}}\in\partial\mathbb{D}_0} \left\{\hat{G}^{GB}(\mathbf{x},\mathbf{x}_{\mathcal{A}},\mathbf{p},\omega)\right\}^* \hat{C}^{(2)}_{\mathcal{B},v^{obs}_{3,\mathcal{B}}}(\mathbf{x}_{\mathcal{A}},\mathbf{x}_0,\omega) d^2\mathbf{x}_{\mathcal{A}}, \quad (5.32)$$

and subsequently:

$$U^{\Uparrow}_{\mathcal{B},v^{obs}_{3,\mathcal{B}}}(\mathbf{x},\mathbf{x}_0,t_0)=\frac{-2}{\pi}\int_{-\infty}^{\infty}\Re\left\{\int_0^{\infty}\hat{C}^{(2),GB}_{\mathcal{B},v^{obs}_{3,\mathcal{B}}}(\mathbf{x},\mathbf{x}_0,\mathbf{p},\omega)e^{i\omega t_0}\,d\omega\right\}d^2\mathbf{p}. \quad (5.33)$$

Since all correlation functions are constructed using the same illumination characteristics, the imaging process uses the same source field $D^{\Downarrow}_{v^{obs}_{3,\mathcal{B}}}$ for each image result. The imaging condition correlates $D^{\Downarrow}_{v^{obs}_{3,\mathcal{B}}}$ with $U^{\Uparrow}_{\mathcal{A},R^{\smile}_{0,\mathcal{A}}}$:

$$I^{(2)}_{\mathcal{A},R^{\smile}_{0,\mathcal{A}}}(\mathbf{x})=\int_{\mathbf{x}_0}\int_{t_0=0}^{T}D^{\Downarrow}_{v^{obs}_{3,\mathcal{B}}}(\mathbf{x},\mathbf{x}_0,t_0)\,U^{\Uparrow}_{\mathcal{A},R^{\smile}_{0,\mathcal{A}}}(\mathbf{x},\mathbf{x}_0,t_0)\,dt_0\,d^2\mathbf{x}_0, \quad (5.34)$$

and equivalently with the monitor field $U^{\Uparrow}_{\mathcal{B},v^{obs}_{3,\mathcal{B}}}$:

$$I^{(2)}_{\mathcal{B},v^{obs}_{3,\mathcal{B}}}(\mathbf{x})=\int_{\mathbf{x}_0}\int_{t_0=0}^{T}D^{\Downarrow}_{v^{obs}_{3,\mathcal{B}}}(\mathbf{x},\mathbf{x}_0,t_0)\,U^{\Uparrow}_{\mathcal{B},v^{obs}_{3,\mathcal{B}}}(\mathbf{x},\mathbf{x}_0,t_0)\,dt_0\,d^2\mathbf{x}_0. \quad (5.35)$$

Finally, the time-lapse response caused by the changes in the subsurface is portrayed by the difference between the base and monitor depth images:

$$\Delta I_{\mathcal{B}-\mathcal{A}}\propto I^{(2)}_{\mathcal{B},v^{obs}_{3,\mathcal{B}}}-I^{(2)}_{\mathcal{A},R^{\smile}_{0,\mathcal{A}}}. \quad (5.36)$$

The same procedure can be applied using the ballistic relation, obtaining $I^{(1)}_{\mathcal{B},v^{obs}_{3,\mathcal{B}}}$ and $I^{(1)}_{\mathcal{A},R^{\smile}_{\mathcal{A}}}$, using the respective point-spread and correlation functions $\Gamma^{(1)}_{\mathcal{B}}$ and $C^{(1)}_{\mathcal{A},R^{\smile}_{\mathcal{A}}}$

In figure 5.10 we present the image results using both the ballistic and full-field relations, migrating all the correlated gathers shown in figures 5.5 and 5.8 respectively. The velocity model employed in all migration results is from the base state $\mathcal{A}$ (see Figure 5.3a). Using the ballistic convolutional relation, figure 5.10a displays image $I^{(1)}_{\mathcal{B},v^{obs}_{3,\mathcal{B}}}$: the reservoir as seen in the monitor state $\mathcal{B}$, using the recording $v^{obs}_{3,\mathcal{B}}$ caused by the passive source depicted with the red arrow indicating the point-force source orientation. Yellow triangles symbolize receiver locations and red triangles represent those receiver locations that were used as virtual sources. Only one fourth of the receiver locations were employed as virtual sources.

The result obtained by cross-convolving the base survey $R^{\smile}_{\mathcal{A}}$ with $\Gamma^{(1)}_{\mathcal{B}}$, $I^{(1)}_{\mathcal{A},R^{\smile}_{\mathcal{A}}}$ is shown in figure 5.10c. We notice the change on the reservoir contact with respect to the one in figure 5.10a, despite not having the same passive source, but using

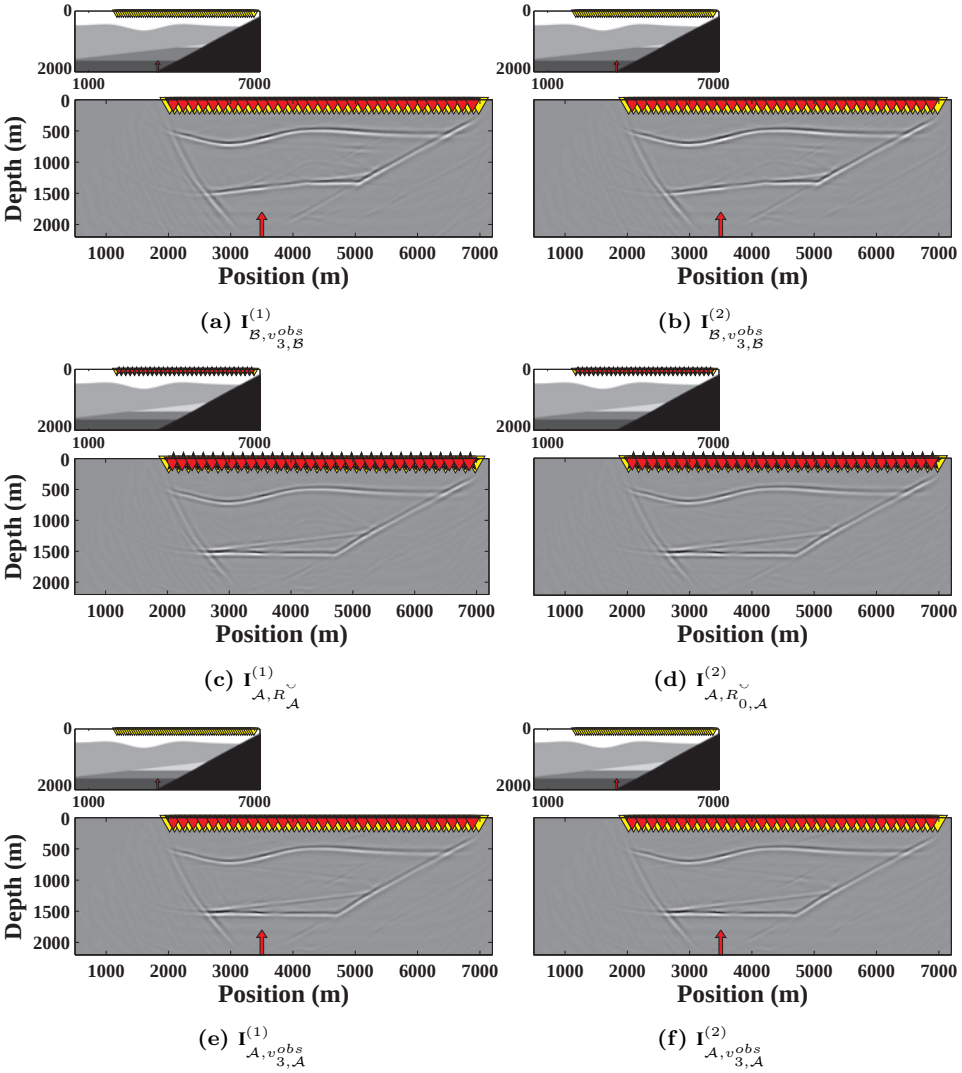

(a) $\mathbf{I}^{(1)}_{\mathcal{B},v^{obs}_{3,\mathcal{B}}}$ (b) $\mathbf{I}^{(2)}_{\mathcal{B},v^{obs}_{3,\mathcal{B}}}$

(c) $\mathbf{I}^{(1)}_{\mathcal{A},R^{\smile}_{\mathcal{A}}}$ (d) $\mathbf{I}^{(2)}_{\mathcal{A},R^{\smile}_{0,\mathcal{A}}}$

(e) $\mathbf{I}^{(1)}_{\mathcal{A},v^{obs}_{3,\mathcal{A}}}$ (f) $\mathbf{I}^{(2)}_{\mathcal{A},v^{obs}_{3,\mathcal{A}}}$

Figure 5.10: *Directionally constrained image results of the correlation functions using the ballistic $I^{(1)}$ and full-field $I^{(2)}$ convolutional relations. Yellow and red triangles represent receivers and virtual sources, respectively. Red arrow in the subsurface depicts the point force in the medium used as passive source. All figures share the same gray scale.* **(a)** *Image of the monitor state $C^{(1)}_{\mathcal{B},v^{obs}_{3,\mathcal{B}}}$, using the ballistic relation.* **(b)** *Same as in* (a) *using $C^{(2)}_{\mathcal{B},v^{obs}_{3,\mathcal{B}}}$ from the full-field relation.* **(c)** *Image of the base state $C^{(1)}_{\mathcal{A},R^{\smile}_{\mathcal{A}}}$, using the ballistic relation.* **(d)** *Same as in* (c) *using $C^{(2)}_{\mathcal{A},R^{\smile}_{0,\mathcal{A}}}$ from the full-field relation.* **(e)** *Image of the reference base state response $C^{(1)}_{\mathcal{A},v^{obs}_{3,\mathcal{A}}}$, with the same passive source as in* (a)*, using the ballistic relation.* **(f)** *Same as in* (e) *using $C^{(2)}_{\mathcal{A},v^{obs}_{3,\mathcal{A}}}$ from the full-field relation. .*

the same illumination characteristics. These changes were already visible between figures 5.5a and 5.5b. Serving as a reference, figure 5.10e shows the image result using the ballistic relation as if the same passive source were present in state $\mathcal{A}$ ($I^{(1)}_{\mathcal{A},v^{obs}_{3,\mathcal{A}}}$).

Figures 5.10b, 5.10d and 5.10f show the equivalent results using the full-field convolutional relation. We have thus successfully exposed the time-lapse response in the image domain, using a single passive source only.

The time-lapse response can alternatively be obtained from either correlation function difference (equations 5.24 or 5.28). This process spares the effort of migrating both the base and monitor states correlation functions. We apply the same imaging procedure on the correlation function difference from equation 5.28 using the full field relation, for instance, and the respective correlation functions:

$$\hat{\mathbf{C}}^{(2)}_{\mathcal{B}-\mathcal{A},R^{\cup}_{0,\mathcal{A}}} = \hat{\mathbf{C}}^{(2)}_{\mathcal{B},v^{obs}_{3,\mathcal{B}}} - \hat{\mathbf{C}}^{(2)}_{\mathcal{A},R^{\cup}_{0,\mathcal{A}}}. \tag{5.37}$$

In a similar manner, we construct the respective backprojected wavefield creating the Gaussian beam representation of the time-lapse correlation function $\hat{C}^{(2),GB}_{\mathcal{B}-\mathcal{A},R^{\cup}_{0,\mathcal{A}}}$ as in equations 5.30 and 5.32, and using the same expressions as in 5.31 and 5.33:

$$U^{\Uparrow}_{\mathcal{B}-\mathcal{A},R^{\cup}_{0,\mathcal{A}}}(\mathbf{x},\mathbf{x}_0,t_0) = \frac{-2}{\pi}\int_{-\infty}^{\infty}\Re\left\{\int_0^{\infty}\hat{C}^{(2),GB}_{\mathcal{B}-\mathcal{A},R^{\cup}_{0,\mathcal{A}}}(\mathbf{x},\mathbf{x}_0,\mathbf{p},\omega)e^{i\omega t_0}\,d\omega\right\}d^2\mathbf{p}. \tag{5.38}$$

Since the time-lapse correlation function was obtained from correlation functions with exactly the same illumination characteristics (defined by $\mathbf{p}^{\mathbf{x}_0}_{v^{obs}_{3,\mathcal{B}}}$), we employ the same forward wavefield described in equation 5.29, using the same velocity model as used before, in order to image the time-lapse response in depth:

$$\Delta I_{\mathcal{B}-\mathcal{A}} \propto I^{(2)}_{\mathcal{B}-\mathcal{A},R^{\cup}_{0,\mathcal{A}}}(\mathbf{x}) = \int_{\mathbf{x}_0}\int_{t_0=0}^{T} D^{\Downarrow}_{v^{obs}_{3,\mathcal{B}}}(\mathbf{x},\mathbf{x}_0,t_0)\,U^{\Uparrow}_{\mathcal{B}-\mathcal{A},R^{\cup}_{0,\mathcal{A}}}(\mathbf{x},\mathbf{x}_0,t_0)\,dt_0\,d^2\mathbf{x}_0. \tag{5.39}$$

Again, this procedure can implemented also to the respective ballistic-relation correlation functions.

Figure 5.11c displays the imaging result of the time-lapse response of the medium, $C^{(1)}_{\mathcal{B}-\mathcal{A},R^{\cup}_{0,\mathcal{A}}}$, displayed in figure 5.11c, for the ballistic relation. A refer-

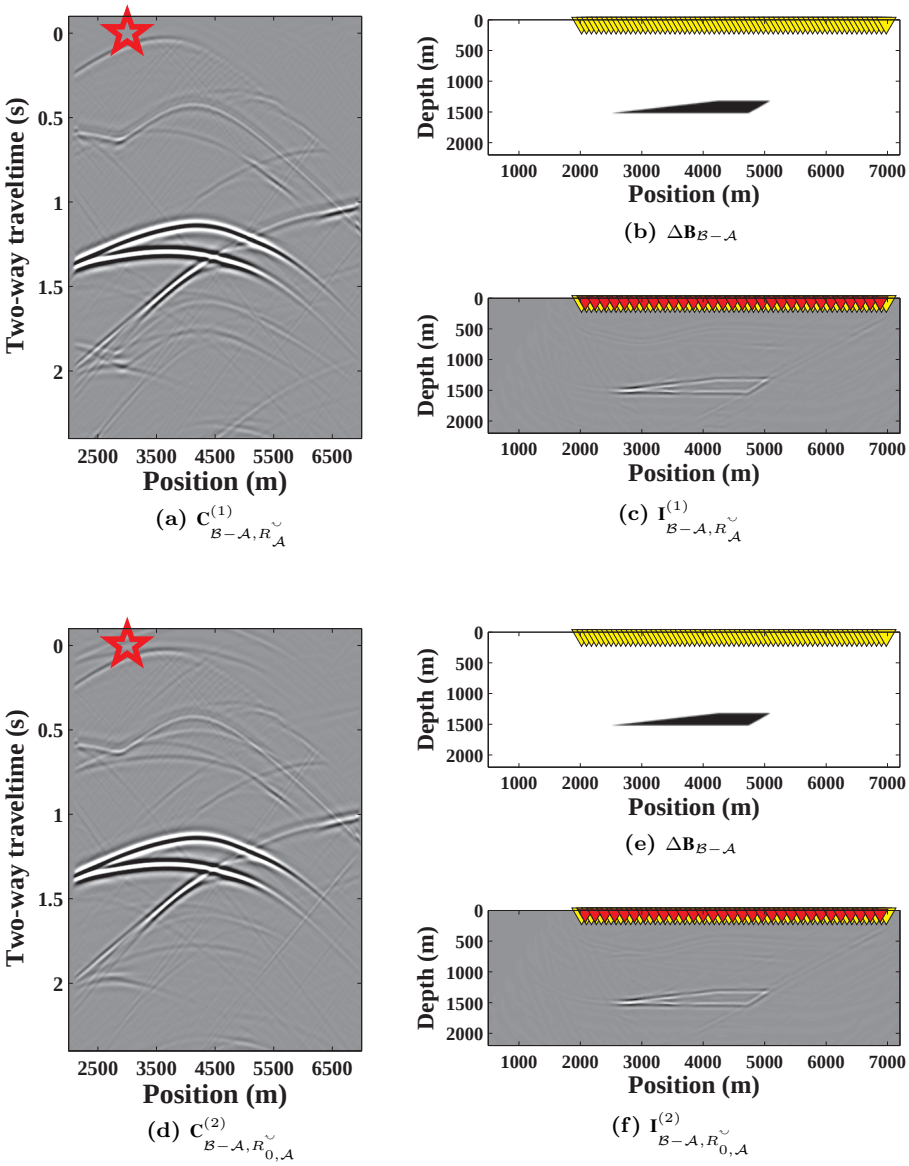

Figure 5.11: **(a)** *Correlation function difference between the monitor and base states using the ballistic relation,* $C^{(1)}_{\mathcal{B}-\mathcal{A},R^{\smile}_{\mathcal{A}}}$. *This is the difference between figures 5.5a and 5.5b.* **(b)** *Medium-property contrast between states* $\mathcal{A}$ *and* $\mathcal{B}$. **(c)** *Directionally constrained image of the correlation function difference* $C^{(1)}_{\mathcal{B}-\mathcal{A},R^{\smile}_{\mathcal{A}}}$, *using the same forward wavefield as for the results in figure 5.10.* **(d)** *Same as in (a) but using the full-field relation,* $C^{(2)}_{\mathcal{B}-\mathcal{A},R^{\smile}_{0,\mathcal{A}}}$. *This is the difference between figures 5.7a and 5.7b.* **(e)** *Medium-property contrast between states* $\mathcal{A}$ *and* $\mathcal{B}$. **(f)** *Same as in (c) but using the full-field relation.*

ence of this time-lapse is shown in figure 5.11b, where the contrast is illustrated by subtracting the velocity values only of the medium at the base and monitor states (figures 5.3a and 5.3b). Figures 5.11d and 5.11f show the equivalent results using the full-field relation. The image results obtained are at the same time equivalent to the ones obtained from the subtraction of images in figures 5.10a and 5.10c, and 5.10b and 5.10d respectively. By applying any of these procedures, the methodology accurately images the time-lapse response of the medium using a single passive source.

5.5 Discussion

One condition required for the application of this methodology is the transient behaviour of the passive source signal. This is necessary for the estimation of the direct wave as an approximation to the passive source response at the monitor state.

During the imaging process we employed mainly zero-phased correlation as imaging condition. The image resolution is then compromised by the frequency content of the passive source signal. This feature however may be overcome by employing alternative imaging conditions (deconvolution techniques, use of extended image conditions) that could remove the source signal from the migrated result.

The results shown here are adapted for an array located in depth, detached from the surface. Therefore, the derivation is shown using one-way wavefields. When the acquisition array is located at the surface, the use of two-way wavefields in this methodology is possible and also easier to implement in acoustic media for we obviate the wavefield decomposition in this case.

The extension of these techniques for an elastic medium is possible and would additionally contribute with independent image results for any waveform combination. The application of this methodology with two-way elastodynamic wavefields is not trivial since decomposition is a requirement to obtain the different waveform imaging results. This aspect remains to be investigated.

The use of reflection data for the base survey assumes this has been acquired by active sources. If sufficient illumination is provided by passive sources in the subsurface, any body-wave passive SI method by inversion may be used to retrieve the reflection responses in the base state. The advantage of these methods is that they offer the liberty to retrieve the responses either with a or without free-surface interaction. This allows the application of both ballistic and full-field monitoring methods at the same time, without requiring additional processing of the base survey. This would only hold if all sources employed in the reflection response retrieval happen during the same period of time corresponding to the base state, without changes occurring in the subsurface.

5.6 Conclusions

We have proposed a method that uses a single passive source to image the change in the reflectivity of the subsurface between two states. We employed the limited illumination from the passive source to impose the same illumination characteristics to an active reflection survey. In this process we reduce the illumination range of the active survey we employ as base survey, to the limited one provided by the passive source recording, that we intend to use as monitor survey. We use correlation functions as modified surveys of the base and monitor state with the limited illumination imprint of the monitor state. This allows their respective depth imaging using directionally constrained migration sharing the same forward wavefield and using their respective base and monitor backprojected wavefields.

The source characteristics of the passive tremor in this monitoring scheme do not affect the final result since they are additionally imprinted on the correlation functions of both states.

These methodologies allow, depending on the occurrence of seismic tremors and the adequate receiver array illumination range, the possibility of intense monitoring of the reservoir for as many time-lapses as tremors happen in the subsurface. We understand these time-lapse responses are estimated always with respect to the active survey, taking the base state as reference every time and using the respective point-spread function for each time-lapse monitoring. This would suppose the stationary receiver array to be continuously recording over time, but the information obtained would reduce the high costs of producing active monitor surveys for as much time lapse information it may provide.

5.A Passive seismic monitoring including perturbations in the reciprocity relation of the convolution type

In this chapter we have presented a monitoring method based on correlation functions. This method was described using the two different convolutional relations independently of the perturbations in the medium that happen between the base and monitor states. In this appendix we show how by taking into account the medium changes between the base and monitor states described in the section 5.2, we converge to the same formulae used for the monitoring scheme.

5.A.1 Reciprocity relation of the convolution type

The unified one-way wave equation in the space-frequency domain of the one-way Green's function $\hat{G}$ from location $\mathbf{x}_{\mathcal{A}}$ to any point $\mathbf{x}$ can be defined as:

$$\frac{\partial \hat{\mathbf{G}}(\mathbf{x}, \mathbf{x}_{\mathcal{A}}, \omega)}{\partial x_3} = \hat{\mathbf{B}}(\mathbf{x}, \omega)\hat{\mathbf{G}}(\mathbf{x}, \mathbf{x}_{\mathcal{A}}, \omega) + \hat{\mathbf{S}}(\mathbf{x}_{\mathcal{A}}, \omega), \tag{5.40}$$

where ω represents angular frequency. This equation relates the Green's function matrix $\hat{\mathbf{G}}$ with respect to the one-way operator matrix $\hat{\mathbf{B}}$ and the one-way source matrix $\hat{\mathbf{S}} = \mathbf{I}\delta(\mathbf{x} - \mathbf{x}_{\mathcal{A}})$. The Green's function matrix in this case reads:

$$\hat{\mathbf{G}}(\mathbf{x}, \mathbf{x}_{\mathcal{A}}, \omega) = \begin{bmatrix} \hat{G}^{+,+} & \hat{G}^{+,-} \\ \hat{G}^{-,+} & \hat{G}^{-,-} \end{bmatrix} (\mathbf{x}, \mathbf{x}_{\mathcal{A}}, \omega). \tag{5.41}$$

Superscripts refer to receiver and source wavefields, respectively (minus for upgoing and plus for downgoing).

The reciprocity relation of the convolution type for one-way wavefields ($\hat{\mathbf{G}}$) inside the domain $\mathbb{D}$ between two different states $\mathcal{A}$ and $\mathcal{B}$, is represented as follows (Wapenaar & Grimbergen, 1996):

$$\int_{\mathbb{D}} \{\hat{\mathbf{G}}^t_{\mathcal{A}}\mathbf{N}\hat{\mathbf{S}}_{\mathcal{B}} + \hat{\mathbf{S}}^t_{\mathcal{A}}\mathbf{N}\hat{\mathbf{G}}_{\mathcal{B}}\}d^3\mathbf{x} = \int_{\partial\mathbb{D}} \hat{\mathbf{G}}^t_{\mathcal{A}}\mathbf{N}\hat{\mathbf{G}}_{\mathcal{B}}\boldsymbol{n}d^2\mathbf{x} - \int_{\mathbb{D}} \{\hat{\mathbf{G}}^t_{\mathcal{A}}\mathbf{N}(\hat{\mathbf{B}}_{\mathcal{B}} - \hat{\mathbf{B}}_{\mathcal{A}})\hat{\mathbf{G}}_{\mathcal{B}}\}d^3\mathbf{x}, \tag{5.42}$$

where ^{t} means matrix transposition. Domain $\mathbb{D}$ is enclosed by two horizontal parallel boundaries, together denoted by $\partial\mathbb{D}$. The outward pointing normal vector to these boundaries $\boldsymbol{n}$ is $(0, 0, n_3)$, with $n_3 = -1$ on the upper boundary and $n_3 = +1$ on the lower. The permutation matrix for the convolution relation ($\mathbf{N}$) is constructed using null ($\mathbf{0}$) and identity matrices ($\mathbf{I}$) as shown:

$$\mathbf{N} = \begin{bmatrix} \mathbf{0} & \mathbf{I} \\ -\mathbf{I} & \mathbf{0} \end{bmatrix}. \tag{5.43}$$

The one-way operator matrix $\hat{\mathbf{B}}$ preserves the following symmetry relation with the permutation matrix $\mathbf{N}$:

$$-\mathbf{N}\hat{\mathbf{B}} = \hat{\mathbf{B}}^t\mathbf{N}. \tag{5.44}$$

The reciprocity relation of the convolution type in equation 5.42 shows three integration terms. The first term is the source-wavefield interaction over the domain $\mathbb{D}$. The second one is the wavefield-interaction at the domain boundary $\partial\mathbb{D}$. The third term is the medium-contrast interaction.

5.A.2 Ballistic relation for passive seismics

The convolutional relation defines the interaction of the Green's functions with the source location, the domain of study, its boundaries and the changes that might happen inside it between the two states: $\mathcal{A}$ and $\mathcal{B}$. For our seismic monitoring with passive sources we are exploiting this relation in order to identify the changes in the study or target domain $\mathbb{D}$. To this goal, we identify the state $\mathcal{A}$ as the base state, where the domain is in its original condition without any change having happened. In this state the active base survey is available, with the receiver array located at the upper boundary of the domain $\partial\mathbb{D}_0$ (not necessarily at the free surface), and sources immediately above this boundary at $\mathbf{x}_\mathcal{A}$.

The state $\mathcal{B}$ will represent the monitor state, where the domain has come across physical and structural modifications which are to be quantified with respect to the base state. In this state the monitor survey is obtained with the aid of a passive recording of a source inside the domain, at $\mathbf{x}_\mathcal{B}$, and recorded at the same receiver array at $\partial\mathbb{D}_0$ as in the base state $\mathcal{A}$. In this relation, we consider the presence of the free-surface above $\partial\mathbb{D}_0$ in the base state $\mathcal{A}$ while the monitor state $\mathcal{B}$ assumes the medium to be homogeneous above $\partial\mathbb{D}_0$. Therefore, with respect to the states described in section 5.2, the base state acts as the measurement state and the monitor plays as the reference state. The medium outside $\mathbb{D}$ and below the lower boundary, $\partial\mathbb{D}_m$, is the same for both states $\mathcal{A}$ and $\mathcal{B}$.

For these state definitions, using the reciprocity relation of the convolution type in the frequency-space domain in equation 5.42, the relation yields (for a detailed derivation, see appendix 3.E in chapter 3):

$$\hat{G}^{-}_{\mathcal{A}}(\mathbf{x}_{\mathcal{A}},\mathbf{x}_{\mathcal{B}},\omega) = -\int_{\mathbf{x}_0\in\partial\mathbb{D}_0} \hat{G}^{-,-}_{\mathcal{A}}(\mathbf{x}_{\mathcal{A}},\mathbf{x}_0,\omega)\hat{G}^{-}_{0,\mathcal{B}}(\mathbf{x}_0,\mathbf{x}_{\mathcal{B}},\omega)\, d^2\mathbf{x}_0$$
$$-\int_{\mathbf{x}_\Delta\in\mathbb{D}} \begin{bmatrix}\hat{G}^{-,+}_{\mathcal{A}}\\ \hat{G}^{-,-}_{\mathcal{A}}\end{bmatrix}^t (\mathbf{x}_{\mathcal{A}},\mathbf{x}_\Delta,\omega)\Delta\hat{\mathbf{B}}_{\mathcal{B}-\mathcal{A}}(\mathbf{x}_\Delta,\omega)\begin{bmatrix}\hat{G}^{+}_{0,\mathcal{B}}\\ \hat{G}^{-}_{0,\mathcal{B}}\end{bmatrix}(\mathbf{x}_\Delta,\mathbf{x}_{\mathcal{B}},\omega)d^3\mathbf{x}_\Delta. \quad (5.45)$$

In this expression, $\hat{G}^{-}_{\mathcal{A}}(\mathbf{x}_{\mathcal{A}},\mathbf{x}_{\mathcal{B}},\omega)$ is the upgoing transmission response at receiver location $\mathbf{x}_{\mathcal{A}}$, immediately above $\partial\mathbb{D}_0$ due to the passive source at $\mathbf{x}_{\mathcal{B}}$ in the subsurface including surface-related and internal multiples, at the base state $\mathcal{A}$. wavefields with only one superscript represent decomposition is only applied at the receiver level while both up- and downgoing-source terms are added together. Hence, $\hat{G}^{-}_{\mathcal{A}}$ is defined as $\left(\hat{G}^{-,+}_{\mathcal{A}}+\hat{G}^{-,-}_{\mathcal{A}}\right)(\mathbf{x}_{\mathcal{A}},\mathbf{x}_{\mathcal{B}},\omega)$. Subscript "$_0$" indicates the response corresponds to the domain $\mathbb{D}$ with a homogenized medium above $\partial\mathbb{D}_0$, as defined for the monitor state. Therefore, $\hat{G}^{-}_{0,\mathcal{B}}(\mathbf{x}_0,\mathbf{x}_{\mathcal{B}},\omega)$ is the equivalent upgoing transmission response acquired at receiver location $\mathbf{x}_0$ but during the monitor state $\mathcal{B}$, this is, without free-surface interaction. $\hat{G}^{-,-}_{\mathcal{A}}(\mathbf{x}_{\mathcal{A}},\mathbf{x}_0,\omega)$ is the Green's function response at receiver $\mathbf{x}_{\mathcal{A}}$ from a source located at $\mathbf{x}_0$ at $\partial\mathbb{D}_0$, due to double-decomposed upgoing-upgoing source and receiver wavefields respectively. The boundary integral only occurs along the upper boundary since the boundary conditions between the two states change along $\partial\mathbb{D}_0$. When the boundary conditions do not change the interaction quantities inside the boundary integral are the same and with opposite signs. Therefore the integral along the lower boundary $\partial\mathbb{D}_m$ cancels out. Finally, the volume integral represents the medium-contrast interaction quantities due to the perturbations in the medium properties between states $\mathcal{B}$ and $\mathcal{A}$. We express the terms inside this integral in vectorial notation for simplicity and convenience for the coming derivations. $\Delta\hat{\mathbf{B}}_{\mathcal{B}-\mathcal{A}}(\mathbf{x}_\Delta)$ is the contrast one-way wavefield operator matrix only to be evaluated at the subsurface locations where these changes occur: $\mathbf{x}_\Delta$. This is defined as:

$$\Delta\hat{\mathbf{B}}_{\mathcal{B}-\mathcal{A}}(\mathbf{x}_\Delta,\omega) = \begin{bmatrix}\hat{B}^{\swarrow}_{\mathcal{B}}-\hat{B}^{\swarrow}_{\mathcal{A}} & \hat{B}^{\curvearrowright}_{\mathcal{B}}-\hat{B}^{\curvearrowright}_{\mathcal{A}}\\ \hat{B}^{\smile}_{\mathcal{B}}-\hat{B}^{\smile}_{\mathcal{A}} & \hat{B}^{\nwarrow}_{\mathcal{B}}-\hat{B}^{\nwarrow}_{\mathcal{A}}\end{bmatrix}(\mathbf{x}_\Delta,\omega). \quad (5.46)$$

Next, we consider the relation of the upgoing-source upgoing-receiver response $\hat{G}^{-,-}_{\mathcal{A}}$ with respect to the downgoing-source upgoing-receiver reflection response $\hat{R}^{\smile}_{\mathcal{A}}$ (equivalent to $\hat{G}^{-,+}_{\mathcal{A}}$). This relation also makes use of $\hat{R}^{\curvearrowright}_{\mathbb{D}',0}$, the upgoing-source downgoing-receiver reflection response from $\partial\mathbb{D}_0$ of the medium above it, $\mathbb{D}'$, and having $\mathbb{D}$ become a homogenized halfspace below it (reference to appendix 3.D.1):

$$\hat{G}_{\mathcal{A}}^{-,-}(\mathbf{x}_{\mathcal{A}},\mathbf{x}_0,\omega) = \\ -\delta(\mathbf{x}_{H,0}-\mathbf{x}_{H,\mathcal{A}}) + \int_{\mathbf{x}_0'\in\partial\mathbb{D}_0} \hat{R}_{\mathcal{A}}^{\smile}(\mathbf{x}_{\mathcal{A}},\mathbf{x}_0',\omega)\hat{R}_{\mathbb{D}',0}^{\frown}(\mathbf{x}_0',\mathbf{x}_0,\omega)\, d^2\mathbf{x}_0', \quad (5.47)$$

and substitute it into 5.45:

$$\hat{G}_{\mathcal{A}}^{-}(\mathbf{x}_{\mathcal{A}},\mathbf{x}_{\mathcal{B}},\omega) - \hat{G}_{0,\mathcal{B}}^{-}(\mathbf{x}_{\mathcal{A}},\mathbf{x}_{\mathcal{B}},\omega) = -\int_{\mathbf{x}_0'\in\partial\mathbb{D}_0} \hat{R}_{\mathcal{A}}^{\smile}(\mathbf{x}_{\mathcal{A}},\mathbf{x}_0',\omega)\Big\{ ... \\ ... \int_{\mathbf{x}_0\in\partial\mathbb{D}_0} \hat{R}_{\mathbb{D}',0}^{\frown}(\mathbf{x}_0',\mathbf{x}_0,\omega)\hat{G}_{0,\mathcal{B}}^{-}(\mathbf{x}_0,\mathbf{x}_{\mathcal{B}},\omega)\, d^2\mathbf{x}_0 \Big\}\, d^2\mathbf{x}_0' \\ -\int_{\mathbf{x}_\Delta\in\mathbb{D}} \begin{bmatrix} \hat{G}_{\mathcal{A}}^{-,+} \\ \hat{G}_{\mathcal{A}}^{-,-} \end{bmatrix}^t (\mathbf{x}_{\mathcal{A}},\mathbf{x}_\Delta,\omega)\Delta\hat{\mathbf{B}}_{\mathcal{B}-\mathcal{A}}(\mathbf{x}_\Delta,\omega) \begin{bmatrix} \hat{G}_{0,\mathcal{B}}^{+} \\ \hat{G}_{0,\mathcal{B}}^{-} \end{bmatrix} (\mathbf{x}_\Delta,\mathbf{x}_{\mathcal{B}},\omega) d^3\mathbf{x}_\Delta. \quad (5.48)$$

On the left hand side of equation 5.48 there are wavefield terms from different states. We simplify this relation by using the reciprocity relation between wavefields in the base and monitor states both without free-surface interaction (as reference states). Both states share the same boundary conditions thus the integrals along boundaries are vanished. We define such relation as:

$$\hat{G}_{0,\mathcal{B}}^{-}(\mathbf{x}_{\mathcal{A}},\mathbf{x}_{\mathcal{B}},\omega) - \hat{G}_{0,\mathcal{A}}^{-}(\mathbf{x}_{\mathcal{A}},\mathbf{x}_{\mathcal{B}},\omega) = \\ \int_{\mathbf{x}_\Delta\in\mathbb{D}} \begin{bmatrix} \hat{G}_{0,\mathcal{A}}^{-,+} \\ \hat{G}_{0,\mathcal{A}}^{-,-} \end{bmatrix}^t (\mathbf{x}_{\mathcal{A}},\mathbf{x}_\Delta,\omega)\Delta\hat{\mathbf{B}}_{\mathcal{B}-\mathcal{A}}(\mathbf{x}_\Delta,\omega) \begin{bmatrix} \hat{G}_{0,\mathcal{B}}^{+} \\ \hat{G}_{0,\mathcal{B}}^{-} \end{bmatrix} (\mathbf{x}_\Delta,\mathbf{x}_{\mathcal{B}},\omega) d^3\mathbf{x}_\Delta. \quad (5.49)$$

The result shows the relation between the base and monitor reference transmission responses with respect to the medium-contrast interaction quantity due to the perturbations in the medium without free-surface interaction. We add this relation to expression 5.48 and change the contrast integral to the left-hand side of the equation, and the final result becomes:

$$\hat{G}_{\mathcal{A}}^{-}(\mathbf{x}_{\mathcal{A}},\mathbf{x}_{\mathcal{B}},\omega) - \hat{G}_{0,\mathcal{A}}^{-}(\mathbf{x}_{\mathcal{A}},\mathbf{x}_{\mathcal{B}},\omega) \\ + \int_{\mathbf{x}_\Delta\in\mathbb{D}} \begin{bmatrix} \left(\hat{G}_{\mathcal{A}}^{-,+} - \hat{G}_{0,\mathcal{A}}^{-,+}\right) \\ \left(\hat{G}_{\mathcal{A}}^{-,-} - \hat{G}_{0,\mathcal{A}}^{-,-}\right) \end{bmatrix}^t (\mathbf{x}_{\mathcal{A}},\mathbf{x}_\Delta,\omega)\Delta\hat{\mathbf{B}}_{\mathcal{B}-\mathcal{A}}(\mathbf{x}_\Delta,\omega) \begin{bmatrix} \hat{G}_{0,\mathcal{B}}^{+} \\ \hat{G}_{0,\mathcal{B}}^{-} \end{bmatrix} (\mathbf{x}_\Delta,\mathbf{x}_{\mathcal{B}},\omega) d^3\mathbf{x}_\Delta = \\ -\int_{\mathbf{x}_0'\in\partial\mathbb{D}_0} \hat{R}_{\mathcal{A}}^{\smile}(\mathbf{x}_{\mathcal{A}},\mathbf{x}_0',\omega)\Big\{ \int_{\mathbf{x}_0\in\partial\mathbb{D}_0} \hat{R}_{\mathbb{D}',0}^{\frown}(\mathbf{x}_0',\mathbf{x}_0,\omega)\hat{G}_{0,\mathcal{B}}^{-}(\mathbf{x}_0,\mathbf{x}_{\mathcal{B}},\omega)\, d^2\mathbf{x}_0 \Big\}\, d^2\mathbf{x}_0' \quad (5.50)$$

In this last expression, the contrast terms are reduced to the wavefield interaction quantities with the different free-surface interactions in the base state, $\left(\hat{G}^{-,+}_{\mathcal{A}} - \hat{G}^{-,+}_{0,\mathcal{A}}\right)(\mathbf{x}_{\mathcal{A}}, \mathbf{x}_{\Delta}, \omega)$ and $\left(\hat{G}^{-,-}_{\mathcal{A}} - \hat{G}^{-,-}_{0,\mathcal{A}}\right)(\mathbf{x}_{\mathcal{A}}, \mathbf{x}_{\Delta}, \omega)$. From this point on, it is unnecessary to express the free-surface interaction contrast-terms as an integral. Therefore, we summarize them into the wavefield quantity $\hat{S}^{(1)}_{\Delta\hat{B}_{\mathcal{B}-\mathcal{A}}}(\mathbf{x}_{\mathcal{A}}, \mathbf{x}_{\mathcal{B}}, \omega)$, where the superscript $^{(1)}$ indicates that this contrast interaction wavefield holds for the ballistic convolution relation. With this simplification, expression 5.50 turns into:

$$\begin{aligned}
&\hat{G}^{-}_{\mathcal{A}}(\mathbf{x}_{\mathcal{A}}, \mathbf{x}_{\mathcal{B}}, \omega) - \hat{G}^{-}_{0,\mathcal{A}}(\mathbf{x}_{\mathcal{A}}, \mathbf{x}_{\mathcal{B}}, \omega) + \hat{S}^{(1)}_{\Delta\hat{B}_{\mathcal{B}-\mathcal{A}}}(\mathbf{x}_{\mathcal{A}}, \mathbf{x}_{\mathcal{B}}, \omega) = \\
&- \int_{\mathbf{x}'_0 \in \partial\mathbb{D}_0} \hat{R}^{\smile}_{\mathcal{A}}(\mathbf{x}_{\mathcal{A}}, \mathbf{x}'_0, \omega) \left\{ \int_{\mathbf{x}_0 \in \partial\mathbb{D}_0} \hat{R}^{\frown}_{\mathbb{D}',0}(\mathbf{x}'_0, \mathbf{x}_0, \omega) \hat{G}^{-}_{0,\mathcal{B}}(\mathbf{x}_0, \mathbf{x}_{\mathcal{B}}, \omega)\, d^2\mathbf{x}_0 \right\} d^2\mathbf{x}'_0
\end{aligned} \tag{5.51}$$

Assuming the passive-source signal is transient, we approximate the following reference-state transmission responses with the direct wave estimations from the decomposed up- and downgoing wavefields $\hat{G}^{-/+}_{dir}$:

$$\hat{G}^{-}_{dir,\mathcal{A}}(\mathbf{x}_{\mathcal{A}}, \mathbf{x}_{\mathcal{B}}, \omega) \approx \hat{G}^{-}_{0,\mathcal{A}}(\mathbf{x}_{\mathcal{A}}, \mathbf{x}_{\mathcal{B}}, \omega) \tag{5.52}$$

$$\hat{G}^{+}_{dir,\mathcal{B}}(\mathbf{x}'_0, \mathbf{x}_{\mathcal{B}}, \omega) \approx - \int_{\mathbf{x}_0 \in \partial\mathbb{D}_0} \hat{R}^{\frown}_{\mathbb{D}',0}(\mathbf{x}'_0, \mathbf{x}_0, \omega) \hat{G}^{-}_{0,\mathcal{B}}(\mathbf{x}_0, \mathbf{x}_{\mathcal{B}}, \omega)\, d^2\mathbf{x}_0, \tag{5.53}$$

leaving finally the direct wave approximation:

$$\begin{aligned}
&\hat{G}^{-}_{\mathcal{A}}(\mathbf{x}_{\mathcal{A}}, \mathbf{x}_{\mathcal{B}}, \omega) - \hat{G}^{-}_{dir,\mathcal{A}}(\mathbf{x}_{\mathcal{A}}, \mathbf{x}_{\mathcal{B}}, \omega) + \hat{S}^{(1)}_{\Delta\hat{B}_{\mathcal{B}-\mathcal{A}}}(\mathbf{x}_{\mathcal{A}}, \mathbf{x}_{\mathcal{B}}, \omega) \\
&\qquad \approx \int_{\mathbf{x}'_0 \in \partial\mathbb{D}_0} \hat{R}^{\smile}_{\mathcal{A}}(\mathbf{x}_{\mathcal{A}}, \mathbf{x}'_0, \omega) \hat{G}^{+}_{dir,\mathcal{B}}(\mathbf{x}'_0, \mathbf{x}_{\mathcal{B}}, \omega)\, d^2\mathbf{x}'_0.
\end{aligned} \tag{5.54}$$

Equation 5.54 can be rewritten in the matrix-vector notation as (Berkhout, 1982):

$$\hat{\boldsymbol{G}}^{-}_{\mathcal{A}} - \hat{\boldsymbol{G}}^{-}_{dir,\mathcal{A}} + \hat{\boldsymbol{S}}^{(1)}_{\Delta\hat{B}_{\mathcal{B}-\mathcal{A}}} \approx \hat{\mathbf{R}}^{\smile}_{\mathcal{A}}\, \hat{\boldsymbol{G}}^{+}_{dir,\mathcal{B}}. \tag{5.55}$$

Applying the adjoint (indicated by †) of $\hat{\boldsymbol{G}}^{+}_{dir,\mathcal{B}}$ on both sides of equation 5.55 the relation reads:

$$\left(\hat{\boldsymbol{G}}^{-}_{\mathcal{A}} - \hat{\boldsymbol{G}}^{-}_{dir,\mathcal{A}} + \hat{\boldsymbol{S}}^{(1)}_{\Delta\hat{B}_{\mathcal{B}-\mathcal{A}}}\right) \{\hat{\boldsymbol{G}}^{+}_{dir,\mathcal{B}}\}^{\dagger} \approx \hat{\mathbf{R}}^{\smile}_{\mathcal{A}}\, \hat{\boldsymbol{G}}^{+}_{dir,\mathcal{B}} \{\hat{\boldsymbol{G}}^{+}_{dir,\mathcal{B}}\}^{\dagger}. \tag{5.56}$$

On the left hand side, we identify definition of the the correlation function for the passive source happening during the base state $\mathcal{A}$ aided by the additional wavefield quantity of the contrast terms $\hat{S}^{(1)}_{\Delta\hat{B}_{\mathcal{B}-\mathcal{A}}}$:

$$\hat{\mathbf{C}}^{(1)}_{\mathcal{A},G^{obs}_{\mathcal{A}}} \approx \left(\hat{\boldsymbol{G}}^{-}_{\mathcal{A}} \; - \; \hat{\boldsymbol{G}}^{-}_{dir,\mathcal{A}} \; + \; \hat{\boldsymbol{S}}^{(1)}_{\Delta\hat{B}_{\mathcal{B}-\mathcal{A}}}\right)\{\hat{\boldsymbol{G}}^{+}_{dir,\mathcal{B}}\}^{\dagger}. \tag{5.57}$$

This correlation function cannot be estimated using the wavefield quantities expressed since they are not available in our recording. However, the exact correlation function can instead be retrieved using the right-hand side of equation 5.56:

$$\hat{\mathbf{C}}^{(1)}_{\mathcal{A},R^{\smile}_{\mathcal{A}}} = \hat{\mathbf{R}}^{\smile}_{\mathcal{A}}\,\hat{\mathbf{\Gamma}}^{(1)}_{\mathcal{B}}, \tag{5.58}$$

where the point-spread function is approximated using the direct wave estimations:

$$\hat{\mathbf{\Gamma}}^{(1)}_{\mathcal{B}} \approx \hat{\boldsymbol{G}}^{+}_{dir,\mathcal{B}}\{\hat{\boldsymbol{G}}^{+}_{dir,\mathcal{B}}\}^{\dagger}. \tag{5.59}$$

5

These expressions define the correlation function for the base state. As for the monitor state we employ the same approximated correlation function definition in equation 5.57, but for an actual source during the monitor state:

$$\hat{\mathbf{C}}^{(1)}_{\mathcal{B},G^{obs}_{\mathcal{B}}} \approx \left(\hat{\boldsymbol{G}}^{-}_{\mathcal{B}} \; - \; \hat{\boldsymbol{G}}^{-}_{dir,\mathcal{B}}\right)\{\hat{\boldsymbol{G}}^{+}_{dir,\mathcal{B}}\}^{\dagger}. \tag{5.60}$$

The contrast wavefield quantity $\hat{S}^{(1)}_{\Delta\hat{B}_{\mathcal{B}-\mathcal{A}}}$ seen previously is not required this time because, in this correlation function, the source and wavefields are actually happening at the monitor state $\mathcal{B}$. Therefore, we obtain the same relations described previously in the chapter for the ballistic reciprocity relation (equations 5.21, 5.22 and 5.23).

5.A.3 Full-field relation for passive seismics

Swapping the description of the medium above $\partial\mathbb{D}_0$ between the two states provides a different relation from the same reciprocity theorem. For this relation we consider this half space to be homogeneous at the base state $\mathcal{A}$ and the presence of the free surface during the monitoring state $\mathcal{B}$. Hence, the base state acts as the reference state and the monitor becomes the measurement state. Using these definitions, the representation derived from equation 5.42 turns into:

$$\hat{G}^{-}_{\mathcal{B}}(\mathbf{x}_{\mathcal{A}},\mathbf{x}_{\mathcal{B}},\omega)-\hat{G}^{-}_{0,\mathcal{A}}(\mathbf{x}_{\mathcal{A}},\mathbf{x}_{\mathcal{B}},\omega)= \int_{\mathbf{x}_0\in\partial\mathbb{D}_0}\overset{\smile}{\hat{R}}_{0,\mathcal{A}}(\mathbf{x}_{\mathcal{A}},\mathbf{x}_0,\omega)\hat{G}^{+}_{\mathcal{B}}(\mathbf{x}_0,\mathbf{x}_{\mathcal{B}},\omega)\,d^2\mathbf{x}_0 + \int_{\mathbf{x}_\Delta\in\mathbb{D}}\begin{bmatrix}\hat{G}^{-,+}_{0,\mathcal{A}}\\ \hat{G}^{-,-}_{0,\mathcal{A}}\end{bmatrix}^t(\mathbf{x}_{\mathcal{A}},\mathbf{x}_\Delta,\omega)\Delta\hat{\mathbf{B}}_{\mathcal{B}-\mathcal{A}}(\mathbf{x}_\Delta,\omega)\begin{bmatrix}\hat{G}^{+}_{\mathcal{B}}\\ \hat{G}^{-}_{\mathcal{B}}\end{bmatrix}(\mathbf{x}_\Delta,\mathbf{x}_{\mathcal{B}},\omega)d^3\mathbf{x}_\Delta. \quad (5.61)$$

Equation 5.61 shows interaction quantities between wavefields of different states. Again, the lower boundary integral is absent because both states share the same boundary conditions and the interaction quantities of wavefields at this level cancel one another out.

Following a similar approach as for the ballistic relation, we define the reciprocity relation between wavefields with free-surface interaction between the base and monitor state (hence, measurement- base and monitor states). This relation reads:

$$\hat{G}^{-}_{\mathcal{B}}(\mathbf{x}_{\mathcal{A}},\mathbf{x}_{\mathcal{B}},\omega)-\hat{G}^{-}_{\mathcal{A}}(\mathbf{x}_{\mathcal{A}},\mathbf{x}_{\mathcal{B}},\omega) = \int_{\mathbf{x}_\Delta\in\mathbb{D}}\begin{bmatrix}\hat{G}^{-,+}_{\mathcal{A}}\\ \hat{G}^{-,-}_{\mathcal{A}}\end{bmatrix}^t(\mathbf{x}_{\mathcal{A}},\mathbf{x}_\Delta,\omega)\Delta\hat{\mathbf{B}}_{\mathcal{B}-\mathcal{A}}(\mathbf{x}_\Delta,\omega)\begin{bmatrix}\hat{G}^{+}_{\mathcal{B}}\\ \hat{G}^{-}_{\mathcal{B}}\end{bmatrix}(\mathbf{x}_\Delta,\mathbf{x}_{\mathcal{B}},\omega)d^3\mathbf{x}_\Delta. \quad (5.62)$$

In this relation, the boundary integrals are absent for the same reasons as in equation 5.49. The subtraction of this relation from expression 5.61 yields:

$$\hat{G}^{-}_{\mathcal{A}}(\mathbf{x}_{\mathcal{A}},\mathbf{x}_{\mathcal{B}},\omega)-\hat{G}^{-}_{0,\mathcal{A}}(\mathbf{x}_{\mathcal{A}},\mathbf{x}_{\mathcal{B}},\omega) + \int_{\mathbf{x}_\Delta\in\mathbb{D}}\begin{bmatrix}\begin{pmatrix}\hat{G}^{-,+}_{\mathcal{A}}-\hat{G}^{-,+}_{0,\mathcal{A}}\end{pmatrix}\\ \begin{pmatrix}\hat{G}^{-,-}_{\mathcal{A}}-\hat{G}^{-,-}_{0,\mathcal{A}}\end{pmatrix}\end{bmatrix}^t(\mathbf{x}_{\mathcal{A}},\mathbf{x}_\Delta,\omega)\Delta\hat{\mathbf{B}}_{\mathcal{B}-\mathcal{A}}(\mathbf{x}_\Delta,\omega)\begin{bmatrix}\hat{G}^{+}_{\mathcal{B}}\\ \hat{G}^{-}_{\mathcal{B}}\end{bmatrix}(\mathbf{x}_\Delta,\mathbf{x}_{\mathcal{B}},\omega)d^3\mathbf{x}_\Delta = \int_{\mathbf{x}_0\in\partial\mathbb{D}_0}\overset{\smile}{\hat{R}}_{0,\mathcal{A}}(\mathbf{x}_{\mathcal{A}},\mathbf{x}'_0,\omega)\hat{G}^{+}_{\mathcal{B}}(\mathbf{x}_0,\mathbf{x}_{\mathcal{B}},\omega)\,d^2\mathbf{x}_0. \quad (5.63)$$

The medium integral shows again it covers only those events related to the free-surface $\left(\hat{G}^{-,+}_{\mathcal{A}}-\hat{G}^{-,+}_{0,\mathcal{A}}\right)(\mathbf{x}_{\mathcal{A}},\mathbf{x}_\Delta,\omega)$ and $\left(\hat{G}^{-,-}_{\mathcal{A}}-\hat{G}^{-,-}_{0,\mathcal{A}}\right)(\mathbf{x}_{\mathcal{A}},\mathbf{x}_\Delta,\omega)$. For this last expression, we summarize the integral over the medium contrast interaction quantity into the wavefield quantity $\hat{S}^{(2)}_{\Delta\hat{B}_{\mathcal{B}-\mathcal{A}}}(\mathbf{x}_{\mathcal{A}},\mathbf{x}_{\mathcal{B}},\omega)$, where superscript $^{(2)}$ symbolizes that this contrast interaction wavefield accounts for the full-field convolution relation:

$$\hat{G}^{-}_{\mathcal{A}}(\mathbf{x}_{\mathcal{A}},\mathbf{x}_{\mathcal{B}},\omega) - \hat{G}^{-}_{0,\mathcal{A}}(\mathbf{x}_{\mathcal{A}},\mathbf{x}_{\mathcal{B}},\omega) + \hat{S}^{(2)}_{\Delta\hat{B}_{\mathcal{B}-\mathcal{A}}}(\mathbf{x}_{\mathcal{A}},\mathbf{x}_{\mathcal{B}},\omega) = \int_{\mathbf{x}_0\in\partial\mathbb{D}_0} \hat{R}^{\smile}_{0,\mathcal{A}}(\mathbf{x}_{\mathcal{A}},\mathbf{x}_0,\omega)\hat{G}^{+}_{\mathcal{B}}(\mathbf{x}_0,\mathbf{x}_{\mathcal{B}},\omega)\, d^2\mathbf{x}_0. \quad (5.64)$$

Assuming the passive source signal is transient, we apply the direct wave approximation of expression 5.52:

$$\hat{G}^{-}_{\mathcal{A}}(\mathbf{x}_{\mathcal{A}},\mathbf{x}_{\mathcal{B}},\omega) - \hat{G}^{-}_{dir,\mathcal{A}}(\mathbf{x}_{\mathcal{A}},\mathbf{x}_{\mathcal{B}},\omega) + \hat{S}^{(2)}_{\Delta\hat{B}_{\mathcal{B}-\mathcal{A}}}(\mathbf{x}_{\mathcal{A}},\mathbf{x}_{\mathcal{B}},\omega) \approx \int_{\mathbf{x}_0\in\partial\mathbb{D}_0} \hat{R}^{\smile}_{0,\mathcal{A}}(\mathbf{x}_{\mathcal{A}},\mathbf{x}_0,\omega)\hat{G}^{+}_{\mathcal{B}}(\mathbf{x}_0,\mathbf{x}_{\mathcal{B}},\omega)\, d^2\mathbf{x}_0. \quad (5.65)$$

We employ now the matrix-vector notation to represent equation 5.65:

$$\hat{\boldsymbol{G}}^{-}_{\mathcal{A}} - \hat{\boldsymbol{G}}^{-}_{dir,\mathcal{A}} + \hat{\boldsymbol{S}}^{(2)}_{\Delta\hat{B}_{\mathcal{B}-\mathcal{A}}} \approx \hat{\mathbf{R}}^{\smile}_{\mathbf{0},\mathcal{A}}\, \hat{\boldsymbol{G}}^{+}_{\mathcal{B}}. \quad (5.66)$$

The normal equation of expression 5.66 makes use of the adjoint of $\hat{\boldsymbol{G}}^{+}$ and yields:

$$\left(\hat{\boldsymbol{G}}^{-}_{\mathcal{A}} - \hat{\boldsymbol{G}}^{-}_{dir,\mathcal{A}} + \hat{\boldsymbol{S}}^{(2)}_{\Delta\hat{B}_{\mathcal{B}-\mathcal{A}}}\right)\{\hat{\boldsymbol{G}}^{+}_{\mathcal{B}}\}^{\dagger} \approx \hat{\mathbf{R}}^{\smile}_{\mathbf{0},\mathcal{A}}\, \hat{\boldsymbol{G}}^{+}_{\mathcal{B}}\{\hat{\boldsymbol{G}}^{+}_{\mathcal{B}}\}^{\dagger}. \quad (5.67)$$

The correlation function of the full-field relation is defined for the base state as:

$$\hat{\mathbf{C}}^{(2)}_{\mathcal{A},G^{obs}_{\mathcal{B}}} \approx \left(\hat{\boldsymbol{G}}^{-}_{\mathcal{A}} - \hat{\boldsymbol{G}}^{-}_{dir,\mathcal{A}} + \hat{\boldsymbol{S}}^{(2)}_{\Delta\hat{B}_{\mathcal{B}-\mathcal{A}}}\right)\{\hat{\boldsymbol{G}}^{+}_{\mathcal{B}}\}^{\dagger}, \quad (5.68)$$

which is again unattainable, but instead we use the right hand side of equation 5.67 to estimate it:

$$\hat{\mathbf{C}}^{(2)}_{\mathcal{A},R^{\smile}_{0,\mathcal{A}}} = \hat{\mathbf{R}}^{\smile}_{\mathbf{0},\mathcal{A}}\, \hat{\boldsymbol{\Gamma}}^{(2)}_{\mathcal{B}}. \quad (5.69)$$

And again we define the respective point-spread function in exact terms as:

$$\hat{\boldsymbol{\Gamma}}^{(2)}_{\mathcal{B}} = \hat{\boldsymbol{G}}^{+}_{\mathcal{B}}\{\hat{\boldsymbol{G}}^{+}_{\mathcal{B}}\}^{\dagger}. \quad (5.70)$$

As for the monitor state we employ the same correlation function description in expression 5.68 in state $\mathcal{B}$, approximated with the direct wave estimation:

$$\hat{\mathbf{C}}^{(2)}_{\mathcal{B},G^{obs}_{\mathcal{B}}} \approx \left(\hat{\boldsymbol{G}}^{-}_{\mathcal{B}} - \hat{\boldsymbol{G}}^{-}_{dir,\mathcal{B}}\right)\{\hat{\boldsymbol{G}}^{+}_{\mathcal{B}}\}^{\dagger}. \quad (5.71)$$

Since the passive source according to the scheme is actually happening during the monitor state, the contrast wavefield quantity $\hat{S}^{(2)}_{\Delta\hat{B}_{\mathcal{B}-\mathcal{A}}}$ is not required in the correlation function of this state. Therefore, we end up with the same full-field relation expressions shown in equations 5.25, 5.26 and 5.27.

In conclusion, the reciprocity-based monitoring scheme can be derived either from reciprocity relations independently of the changes in the subsurface, or by combining at once the changes in the medium together with the interaction quantities inside the same reciprocity relation.

6 Conclusions

This thesis has addressed some of the main difficulties encountered in passive seismic imaging. Novel applications have been described in different chapters, following the proposed applied passive seismic protocol as presented in the introduction. Some of the main conclusions of this thesis are highlighted below:

Chapter 2 proposes a method to study the illumination characteristics of recorded ambient noise: illumination diagnosis (ID). The main application of this method is in body-wave passive seismic interferometry (SI). It analyzes consecutive finite time intervals of passive recordings and detects the dominant horizontal slowness of the wave arrivals. The main characteristics of this method are:

- The identification of the direction of arrival of seismic waves is obtained by an automatic analysis of the phase information of the virtual-source function of a reference receiver with respect to the other receivers of the acquisition array. This analysis is sensitive to the array geometry and is independent for every reference receiver. Therefore, there are as many results as receivers available. It also serves as a detection tool of seismic tremors without the need for amplitude analysis.
- The direction of the arrival is expressed in azimuth and horizontal slowness. The result of ID gives a probability function of the arrival direction. The dispersion of this function around the maximum value provides information of the arrival's signal wavelength.
- In elastic media, ID provides a discrimination scheme required for retrieving body wave reflections from ambient-noise recordings. It serves as a qualitative analysis for the separation of the noise panels dominated by body waves from the ones dominated by surface waves. The respective noise panels serve for the subsequent body-wave or surface-wave interferometry applications in passive seismics.
- The continuation of illumination diagnosis over consecutive noise panels produces the illumination history of the subsurface due to the dominant arrivals

at the reference receiver. The sorting of these ID-series by their respective dominant slowness creates the illumination diagram of the reference receiver. In turn, this arrangement of the dominant slowness provides a histogram describing the dominant direction of the wave arrivals. During the retrieval of the reflection response at the reference receiver with non-inversion SI methods, this statistical information is very valuable for building a weighting function to balance the respective illumination strength of each noise-panel.

From the perspective of the array design, the ID method also provided the following conclusions:

- In 3D media, the geometrical layout of the receiver array strongly influences the appearance of directional aliasing, to which ID is very sensitive. Optimal ID results are obtained with Fermat-spiral array designs. This design is the least affected by directional aliasing because receiver-triplet alignments are minimized, while keeping a constant receiver density for imaging purposes.

Chapter 3 introduces several body-wave SI methods for passive seismics in order to retrieve the virtual reflection response of the medium. These methods are all based on the reciprocity relations with one-way wavefields and their solution for the reflection response requires inversion. They are designed for transient signals using an estimate based on the direct arrival, to approximate the transmission response of the medium without free surface: the reference-state transmission responses. In the case of noise signals the passive-source time function is long enough to cause different events to overlap, making the estimation of the direct arrival unattainable. In such a scenario, an approximation is presented for these methods. The main conclusions of these techniques may be resumed in the following points:

- The reciprocity relation of the convolution type in passive seismic configurations provides two different implicit relations of the reflection response of the medium. To solve for either of them, it is necessary to carry out a multi-dimensional deconvolution (MDD). Depending on the relation employed, one can retrieve the reflection response of the medium with free-surface interaction ($R^{\smile}$) or without it ($R_0^{\smile}$). In case of transient signals, the $R^{\smile}$-MDD makes use of the ballistic field of the recording, estimates the free-surface interaction as part of the solution and is less stable during inversion. On the other hand, the $R_0^{\smile}$-MDD employs the full field in the recording, is less sensitive to the direct wave approximation and includes the information of the free-surface interaction during the retrieval process, hence causing a more stable inversion.
- An approach to the $R_0^{\smile}$-MDD method is presented for ambient-noise seismic interferometry (ANSI). It is conceived to work with continuous ambient-noise

recordings, where estimates of the reference-state transmission responses are not possible. When compared to already existing ANSI methods (crosscorrelation, crosscoherence and $R^{\cup}$-MDD) ours deal in a better manner with the nature of source mechanisms, the heterogeneous frequency content of the ambient-noise signal, and compensates for uneven illumination of the subsurface sources.

Working in interferometry in 3D media with one-way wavefields implies a series of additional aspects to be taken into account:

- Array designs must seek optimal directional sampling in order to improve the coverage of seismic events in stationary phase. Also, the spacing between receivers and their density distribution must be constant in order to properly apply regularization during inversion.
- To meet these demands, an adapted wavefield decomposition and separation must be conveyed for this sort of irregular arrays. To implement this decomposition the differentiation operators are approximated using a finite-element approach.
- The advantage of carrying out this approach in the space-frequency domain is that it allows to include the variations of the near-surface parameters into the decomposition process.

In chapter 4 a novel method for passive seismic imaging under very limited subsurface illumination is presented. In such a condition the finite distribution of passive sources in the subsurface may not suffice in the retrieval of the reflection response. This alternative approach is a modified migration process for individual passive source recordings. The main ideas drawn by this chapter are presented as follows:

- We presented a scheme for generating partial images of the medium using seismic interferometry with a limited number of subsurface sources. Our scheme takes the illumination characteristics of the respective passive sources into account during the migration process. It uses the illumination information to image only energy in stationary phase for every virtual source, hence limiting the migration of correlated energy that would contribute to migration artefacts. In case of limited passive-source distribution, the scheme produces better results than conventional interferometric imaging schemes.
- Using the correct velocity model, the seismic image of the subsurface can be achieved without the need of an explicit estimation of the reflection response as an intermediate step. Only the correlation functions of the individual sources is needed.

- In elastic media the imaging of structures in the subsurface can be extended, utilizing the different wavefield-mode conversion images. The different wave-mode conversions do not necessarily coincide in their illumination of the subsurface, and hence do not image the same region of the medium. Therefore, the migration of every converted-wave correlation function broadens the possibilities of the subsurface interpretation since they image the same structures but with different elastic wave-mode conversions.
- When an accurate velocity model is available, each passive source images a region of the subsurface. The successive addition of individual passive source images from different locations in the medium completes the imaging result of the subsurface in a process known as image interferometry. During this addition process there is a constructive interference caused by the imaged interfaces due to primary reflections.

Chapter 5 introduces an alternative approach to analyze changes in the subsurface using passive source recordings. The method is applied to a numerical study of reservoir monitoring by combining an active survey as base survey and passive-source recordings as monitor survey. The conditions under which it is possible to retrieve a virtual seismic survey with passive sources and use it as monitor survey are unlikely to happen. Therefore, this method proposes to use the passive-source recordings individually as monitor survey. The conclusions we extract from this chapter are:

- Passive sources provide a precise and limited illumination characteristics of the subsurface. These illumination characteristics can be imprinted onto an active survey by means of the convolution reciprocity relations. By doing so, a passive-source recording can be forged using the active-survey data only. This virtually created passive source represents the transmission response of the medium as if it had happened during the same state of the active survey.
- Individual passive sources may serve to image the subsurface. This idea, together with the imprinting of the illumination characteristics, serve as basis to define a reservoir monitoring scheme using individual passive sources. The scheme uses the passive-source recording as monitor survey, and combines the illumination characteristics of the passive source to the base active survey by means of the convolution reciprocity relations. The monitoring scheme contains two variants depending on the reciprocity relation used (or active survey employed, with or without free-surface interaction), both equally valid but the one employing the full-field reciprocity relation being more consistent. In the end it is easier to imprint this limited illumination characteristics on the active survey than to retrieve an isotropic-illumination virtual survey from passive sources. The difference between the incomplete monitor survey and the created incomplete base survey is the corresponding response of the changes in

the subsurface under the illumination characteristics of the respective passive source.

- The use of a directionally constrained migration scheme allows to image the changes that occurred in the subsurface between the base survey and the monitor survey. The creation of the incomplete surveys serves to image the subsurface at the base and monitor states, employing directionally constrained migration. The changes in the subsurface can then be isolated in the image domain by subtracting the two respective image results. The image result of the subsurface changes can also be alternatively achieved, using the same migration scheme with the difference between the incomplete monitor and base surveys before migration, and employing the same illumination characteristics during the imaging process.
- The method is limited to transient signals, although it could be extended to longer source functions by changing the imaging condition.

Bibliography

Aki, K., 1957. Space and time spectra of stationary stochastic waves, with special reference to microtremors, *Bulletin of the Earthquake Research Institute*, **35**, 415–456.

Almagro Vidal, C. & Wapenaar, K., 2014. Passive seismic interferometry by multi-dimensional deconvolution-decorrelation, in *84th SEG Annual International Meeting, Denver, Colorado USA*, Society of Exploration Geophysicists.

Almagro Vidal, C., van der Neut, J., Draganov, D., Wapenaar, K., & Verdel, A., 2012. Passive interferometric imaging for limited illumination using slowness diagnosis and directionally constrained Gaussian beam migration, in *82nd SEG Annual International Meeting, Las Vegas, Nevada USA*, vol. SPMI E-P1.6, Society of Exploration Geophysicists.

Almagro Vidal, C., van der Neut, J., & Wapenaar, C., 2013. Interferometric reservoir monitoring with a single passive source, in *83rd SEG Annual International Meeting, Houston, Texas USA*, Society of Exploration Geophysicists.

Almagro Vidal, C., Draganov, D., van der Neut, J., Drijkoningen, G., & Wapenaar, K., 2014. Retrieval of reflections from ambient noise using illumination diagnosis, *Geophysical Journal International*, **198**(3), 1572–1584.

Artman, B., 2006. Imaging passive seismic data, *Geophysics*, **71**(4), SI177–SI187.

Berkhout, A., 1982. *Seismic migration. Imaging of acoustic energy by wave field extrapolation*, Elsevier.

Bharadwaj, P., Schuster, G. T., Mallinson, I., et al., 2011. Super-virtual refraction interferometry: Theory, in *81st SEG Annual International Meeting, San Antonio, Texas USA*, Society of Exploration Geophysicists.

Billette, F. & Lambaré, G., 1998. Velocity macro-model estimation from seismic reflection data by stereotomography, *Geophysical Journal International*, **135**(2), 671–690.

Bojarski, N. N., 1983. Generalized reaction principles and reciprocity theorems for the wave equations, and the relationship between the time-advanced and time-retarded fields, *The Journal of the Acoustical Society of America*, **74**(1), 281–285.

Boué, P., Poli, P., Campillo, M., Pedersen, H., Briand, X., & Roux, P., 2013. Teleseismic correlations of ambient seismic noise for deep global imaging of the Earth, *Geophysical Journal International*, **194**(2), 844–848.

Boullenger, B., Verdel, A., Paap, B., Thorbecke, J., & Draganov, D., 2014. Studying CO_2 storage with ambient-noise seismic interferometry: A combined numerical feasibility study and field-data example for Ketzin, Germany, *Geophysics*, **80**(1), Q1–Q13.

Červený, V., Popov, M. M., & Pšenčík, I., 1982. Computation of wave fields in inhomogeneous media-Gaussian beam approach, *Geophysical Journal International*, **70**(1), 109–128.

Claerbout, J. F., 1968. Synthesis of a layered medium from its acoustic transmission response, *Geophysics*, **33**(2), 264–269.

Cox, B., 2003. *Tomographic inversion of focusing operators*, Ph.D. thesis, Delft University of Technology.

Curtis, A. & Halliday, D., 2010. Directional balancing for seismic and general wavefield interferometry, *Geophysics*, **75**(1), SA1–SA14.

Curtis, A., Gerstoft, P., Sato, H., Snieder, R., & Wapenaar, K., 2006. Seismic interferometry - turning noise into signal, *The Leading Edge*, **25**(9), 1082–1092.

Dalen, K. N., Mikesell, T. D., Ruigrok, E. N., & Wapenaar, K., 2015. Retrieving surface waves from ambient seismic noise using seismic interferometry by multidimensional deconvolution, *Journal of Geophysical Research: Solid Earth*, **120**(2), 944–961.

De Hoop, M. V., 1992. *Directional decomposition of transient acoustic wave fields*, Ph.D. thesis, Delft University of Technology.

Draganov, D. & Panea, I., 2011. Seismic interferometry with ambient noise from Mizil Area, Romania, in *73rd EAGE Conference & Exhibition, Vienna, Austria*, European Association of Geoscientists & Engineers.

Draganov, D., Wapenaar, K., & Thorbecke, J., 2006. Seismic interferometry: Reconstructing the Earth's reflection response, *Geophysics*, **71**(4), SI61–SI70.

Draganov, D., Campman, X., Thorbecke, J., Verdel, A., & Wapenaar, K., 2009. Reflection images from ambient seismic noise, *Geophysics*, **74**(5), A63–A67.

Draganov, D., Campman, X., Thorbecke, J., Verdel, A., & Wapenaar, K., 2010. Event-driven seismic interferometry with ambient seismic noise, in *72nd EAGE Conference & Exhibition, Barcelona, Spain*, European Association of Geoscientists & Engineers.

Draganov, D., Campman, X., Thorbecke, J., Verdel, A., & Wapenaar, K., 2013. Seismic exploration-scale velocities and structure from ambient seismic noise (> 1 Hz), *Journal of Geophysical Research: Solid Earth*, **118**(8), 4345–4360.

Duin, E., Doornenbal, J., Rijkers, R., Verbeek, J., & Wong, T. E., 2006. Subsurface structure of the Netherlands-results of recent onshore and offshore mapping, *Netherlands Journal of Geosciences*, **85**(4), 245–276.

Fokkema, J. T. & van den Berg, P. M., 1993. *Seismic applications of acoustic reciprocity*, Elsevier.

Forghani, F. & Snieder, R., 2010. Underestimation of body waves and feasibility of surface-wave reconstruction by seismic interferometry, *The Leading Edge*, **29**(7), 790–794.

Gal, M., Reading, A., Ellingsen, S., Koper, K., Burlacu, R., & Gibbons, S., 2016. Deconvolution enhanced direction of arrival estimation using one-and three-component seismic arrays applied to ocean induced microseisms, *Geophysical Journal International*, **206**(1), 345–359.

Grimbergen, J. L., Dessing, F. J., & Wapenaar, K., 1998. Modal expansion of one-way operators in laterally varying media, *Geophysics*, **63**(3), 995–1005.

Grobbe, N., van der Neut, J. R., & Almagro Vidal, C., 2013. Flux-normalized elastodynamic wavefield decomposition using only particle velocity recordings, in *83rd SEG Annual International Meeting, Houston, Texas USA*, Society of Exploration Geophysicists.

Hartstra, I., Almagro Vidal, C., & Wapenaar, K., 2017. Full-field multidimensional deconvolution to retrieve body-wave reflections from sparse passive sources, *Geophysical Journal International*, **210**(2), 609–620.

Köhler, T., 2004. A projection access scheme for iterative reconstruction based on the golden section, in *Nuclear Science Symposium Conference Record*, vol. 6, pp. 3961–3965, IEEE.

Lacoss, R. T., Kelly, E. J., & Toksöz, M. N., 1969. Estimation of seismic noise structure using arrays, *Geophysics*, **34**(1), 21–38.

Larose, E., Margerin, L., Derode, A., van Tiggelen, B., Campillo, M., Shapiro, N., Paul, A., Stehly, L., & Tanter, M., 2006. Correlation of random wavefields: An interdisciplinary review, *Geophysics*, **71**(4), SI11–SI21.

Lobkis, O. I. & Weaver, R. L., 2001. On the emergence of the Green's function in the correlations of a diffuse field, *The Journal of the Acoustical Society of America*, **110**(6), 3011–3017.

Lord Rayleigh, 1894. *The Theory of Sound*, MacMillan, London, 1894; reprinted by Dover, New York, 1945.

Maranò, S., Reller, C., Loeliger, H.-A., & Fäh, D., 2012. Seismic waves estimation and wavefield decomposition: application to ambient vibrations, *Geophysical Journal International*, **191**(1), 175–188.

Martínez-Graullera, O., Martín, C. J., Godoy, G., & Ullate, L. G., 2010. 2D array design based on Fermat spiral for ultrasound imaging, *Ultrasonics*, **50**(2), 280–289.

Nakata, N. & Snieder, R., 2013. Body-wave interferometry using local earthquakes with multi-dimensional deconvolution and wavefield decomposition at free surface, in *83rd SEG Annual International Meeting, Houston, Texas USA*, Society of Exploration Geophysicists.

Nakata, N., Snieder, R., Tsuji, T., Larner, K., & Matsuoka, T., 2011. Shear-wave imaging from traffic noise using seismic interferometry by cross-coherence, *Geophysics*, **76**(6), SA97–SA106.

Nakata, N., Snieder, R., & Behm, M., 2014. Body-wave interferometry using regional earthquakes with multidimensional deconvolution after wavefield decomposition at free surface, *Geophysical Journal International*, **199**(2), 1125–1137.

Nakata, N., Chang, J. P., Lawrence, J. F., & Boué, P., 2015. Body wave extraction and tomography at Long Beach, California, with ambient-noise interferometry, *Journal of Geophysical Research: Solid Earth*, **120**(2), 1159–1173.

Nishida, K., 2013. Global propagation of body waves revealed by cross-correlation analysis of seismic hum, *Geophysical Research Letters*, **40**(9), 1691–1696.

Noone, C. J., Torrilhon, M., & Mitsos, A., 2012. Heliostat field optimization: A new computationally efficient model and biomimetic layout, *Solar Energy*, **86**(2), 792–803.

Nowack, R. L., Dasgupta, S., Schuster, G. T., & Sheng, J.-M., 2006. Correlation migration using Gaussian beams of scattered teleseismic body waves, *Bulletin of the Seismological Society of America*, **96**(1), 1–10.

Olivier, G., Brenguier, F., Campillo, M., Lynch, R., & Roux, P., 2015. Body-wave reconstruction from ambient seismic noise correlations in an underground mine, *Geophysics*, **80**(3), KS11–KS25.

Poli, P., Campillo, M., Pedersen, H., et al., 2012a. Body-wave imaging of Earth's mantle discontinuities from ambient seismic noise, *Science*, **338**(6110), 1063–1065.

Poli, P., Pedersen, H., & Campillo, M., 2012b. Emergence of body waves from cross-correlation of short period seismic noise, *Geophysical Journal International*, **188**(2), 549–558.

Popov, M., 1982. A new method of computation of wave fields using Gaussian beams, *Wave motion*, **4**(1), 85–97.

Popov, M. M., Semtchenok, N. M., Popov, P. M., & Verdel, A. R., 2010. Depth migration by the Gaussian beam summation method, *Geophysics*, **75**(2), S81–S93.

Ridley, J., 1982. Packing efficiency in sunflower heads, *Mathematical Biosciences*, **58**(1), 129–139.

Roux, P. & Fink, M., 2003. Green's function estimation using secondary sources in a shallow water environment, *The Journal of the Acoustical Society of America*, **113**(3), 1406–1416.

Roux, P., Sabra, K. G., Gerstoft, P., Kuperman, W., & Fehler, M. C., 2005. P-waves from cross-correlation of seismic noise, *Geophysical Research Letters*, **32**(19), L19303.

Ruigrok, E. & Almagro Vidal, C., 2013. Body-wave receiver-pair seismic interferometry, in *75th EAGE Conference & Exhibition incorporating SPE EUROPEC*, European Association of Geoscientists & Engineers.

Ruigrok, E., Campman, X., Draganov, D., & Wapenaar, K., 2010. High-resolution lithospheric imaging with seismic interferometry, *Geophysical Journal International*, **183**(1), 339–357.

Ruigrok, E., Campman, X., & Wapenaar, K., 2011. Extraction of P-wave reflections from microseisms, *Comptes Rendus Geoscience*, **343**(8), 512–525.

Ruigrok, E., Almagro Vidal, C., & Wapenaar, C., 2012. Seismic interferometry by midpoint integration, in *Neustadt Workshop on Noise and Diffuse Wavefields, Neustadt an der Weinstraße, Germany*, Deutsche Geophysikalische Gesellschaft.

Schuster, G., Yu, J., Sheng, J., & Rickett, J., 2004. Interferometric/daylight seismic imaging, *Geophysical Journal International*, **157**(2), 838–852.

Schuster, G. T., 2001. Theory of daylight/interferometric imaging-tutorial, in *63rd EAGE Conference & Exhibition, Amsterdam, The Netherlands*, European Association of Geoscientists & Engineers.

Schuster, G. T., 2009. *Seismic Interferometry*, Cambridge University Press, ISBN-13:9780521871242.

Shapiro, N. M. & Campillo, M., 2004. Emergence of broadband Rayleigh waves from correlations of the ambient seismic noise, *Geophysical Research Letters*, **31**(7), L07614.

Snieder, R., 2004. Extracting the Green's function from the correlation of coda waves: A derivation based on stationary phase, *Physical Review E*, **69**(4), 046610.

Snieder, R., Wapenaar, K., & Larner, K., 2006. Spurious multiples in seismic interferometry of primaries, *Geophysics*, **71**(4), SI111–SI124.

Thompson, D. W., 1942. *On Growth and Form*, Cambridge University Press.

Thorbecke, J. W., 1997. *Common focus point technology*, Ph.D. thesis, Delft University of Technology.

Thorbecke, J. W. & Draganov, D., 2011. Finite-difference modeling experiments for seismic interferometry, *Geophysics*, **76**(6), H1–H18.

Ugalde, A., Villaseñor, A., Gaite, B., Martí, D., Casquero, S., & Carbonell, R., 2011. Passive seismic monitoring at an experimental CO_2 geological storage site in Hontomín-Northern Spain, in *1st EAGE Sustainable Earth Sciences (SES) Conference & Exhibition*, European Association of Geoscientists & Engineers.

Ursin, B., 1983. Review of elastic and electromagnetic wave propagation in horizontally layered media, *Geophysics*, **48**(8), 1063–1081.

van der Neut, J., 2013. Downhole interferometric illumination diagnosis and balancing, *Geophysical Prospecting*, **61**(Suppl.1), 352–367.

van der Neut, J., Ruigrok, E., Draganov, D., & Wapenaar, K., 2010. Retrieving the Earth's reflection response by multi-dimensional deconvolution of ambient seismic noise, in *72nd EAGE Conference & Exhibition incorporating SPE EUROPEC*, European Association of Geoscientists & Engineers.

van Groenestijn, G. & Verschuur, D., 2009. Estimating primaries by sparse inversion and application to near-offset data reconstruction, *Geophysics*, **74**(3), A23–A28.

van Groenestijn, G. & Verschuur, D., 2010. Estimation of primaries by sparse inversion from passive seismic data, *Geophysics*, **75**(4), SA61–SA69.

van Wijk, K., Mikesell, D., Blum, T., Haney, M., Calvert, A., et al., 2010. Surface wave isolation with the interferometric Green tensor, in *80th SEG Annual International Meeting, Denver, Colorado USA*, pp. 3996–4000, Society of Exploration Geophysicists.

Verschuur, D. J., Berkhout, A., & Wapenaar, C., 1992. Adaptive surface-related multiple elimination, *Geophysics*, **57**(9), 1166–1177.

Vogel, H., 1979. A better way to construct the sunflower head, *Mathematical biosciences*, **44**(3-4), 179–189.

Wapenaar, C. & Grimbergen, J., 1996. Reciprocity theorems for one-way wavefields, *Geophysical Journal International*, **127**(1), 169–177.

Wapenaar, K., 1998. Reciprocity properties of one-way propagators, *Geophysics*, **63**(5), 1795–1798.

Wapenaar, K., 2004. Retrieving the elastodynamic Green's function of an arbitrary inhomogeneous medium by cross correlation, *Physical Review Letters*, **93**(25), 254301.

Wapenaar, K. & Fokkema, J., 2006. Green's function representations for seismic interferometry, *Geophysics*, **71**(4), SI33–SI46.

Wapenaar, K. & van der Neut, J., 2010. A representation for Green's function retrieval by multidimensional deconvolution, *The Journal of the Acoustical Society of America*, **128**(6), EL366–EL371.

Wapenaar, K., Thorbecke, J., & Draganov, D., 2004. Relations between reflection and transmission responses of three-dimensional inhomogeneous media, *Geophysical Journal International*, **156**(2), 179–194.

Wapenaar, K., Slob, E., & Snieder, R., 2008a. Seismic and electromagnetic controlled-source interferometry in dissipative media, *Geophysical Prospecting*, **56**(3), 419–434.

Wapenaar, K., van der Neut, J., & Ruigrok, E., 2008b. Passive seismic interferometry by multidimensional deconvolution, *Geophysics*, **73**(6), A51–A56.

Wapenaar, K., Ruigrok, E., van der Neut, J., & Draganov, D., 2011a. Improved surface-wave retrieval from ambient seismic noise by multi-dimensional deconvolution, *Geophysical Research Letters*, **38**(1), L01313.

Wapenaar, K., van der Neut, J., Ruigrok, E., Draganov, D., Hunziker, J., Slob, E., Thorbecke, J., & Snieder, R., 2011b. Seismic interferometry by crosscorrelation and by multidimensional deconvolution: A systematic comparison, *Geophysical Journal International*, **185**(3), 1335–1364.

Winkelmann, S., Schaeffter, T., Köhler, T., Eggers, H., & Doessel, O., 2007. An optimal radial profile order based on the golden ratio for time-resolved MRI, *IEEE Transactions on Medical Imaging*, **26**(1), 68–76.

Xu, Z., Juhlin, C., Gudmundsson, O., Zhang, F., Yang, C., Kashubin, A., & Lüth, S., 2012. Reconstruction of subsurface structure from ambient seismic noise: an example from Ketzin, Germany, *Geophysical Journal International*, **189**(2), 1085–1102.

Zhan, Z., Ni, S., Helmberger, D. V., & Clayton, R. W., 2010. Retrieval of moho-reflected shear wave arrivals from ambient seismic noise, *Geophysical Journal International*, **182**(1), 408–420.

Samenvatting

Passieve seismiek is de groep applicaties die gebruikt maakt van natuurlijk aanwezige seismische golfvelden om de mechanische eigenschappen van de Aarde in kaart te brengen. Conventionele technieken die de ondergrond in beeld brengen maken over het algemeen gebruik van reflectie seismiek, waarbij actief ruimte-golven vanaf het oppervlak de ondergrond in gestuurd worden. Passieve seismiek is onafhankelijk van het gebruik van actieve bronnen, omdat het de mogelijkheid biedt om deze zelfde soort reflecties te verkrijgen van seismische golven afkomstig van natuurlijk aanwezig omgevingsruis of aardbevingen. Dit promotie onderzoek beschrijft de ontwikkeling en toepassing van nieuwe applicaties voor passieve seismiek die trachten verbetering te brengen in het beeld van de ondergrond ten opzichte van al bestaande methoden.

De kwaliteit van het beeld dat verkregen kan worden met passieve seismiek is sterk afhankelijk van de aard van het natuurlijk aanwezige golfveld. Bij het toepassen van passieve seismische methodes is het daarom van groot belang rekening te houden met zowel de complexiteit van het medium alsook de karakteristieken van de passieve bronnen: zoals bijvoorbeeld de ruimtelijke distributie van de verschillende bronnen in de ondergrond en de kenmerken van het bronmechanisme. De registraties van seismische golfvelden ten gevolge van ondiepe bronnen zijn vaak gedomineerd door oppervlakte-golven, die het verkrijgen van de virtuele reflecties vermoeilijken wegens hun interferentie met de gewenste ruimte-golven. Met behulp van een belichtingsanalyse kan de ruimtelijke belichting van de seismografen kwantitatief in kaart gebracht worden: specifieke tijdsecties kunnen zo onderscheiden worden die gedomineerd worden door enerzijds alleen de oppervlakte-golven of anderzijds alleen de ruimte-golven. Het zo verkregen inzicht in de belichting door het natuurlijke golfveld kan vervolgens gebruikt worden om oppervlakte-golven te onderdrukken en zo de gewenste reflecties uit te lichten.

Passieve seismische interferometrie is hier gedefinieerd als een combinatie van methodes die verantwoordelijk zijn voor het transformeren van passieve seismische registraties in de gewenste reflectie respons, waarbij de ontvangers in virtuele bronnen worden omgezet. Deze zo verkregen virtuele reflectie respons is geschikt voor het toepassen van technieken die oorspronkelijk ontwikkeld zijn voor conventionele (actieve) reflectie seismiek. De passieve seismiek kent veel verschillende methodes, afhankelijk

van het type input data waarvoor de methode bestemd is (afkomstig van omgevingsruis of aardbevingen) of de wiskundige basis van de methode. Expliciet geformuleerde methodes worden over het algemeen het meest toegepast, maar dragen wel het nadeel met zich mee dat het eindresultaat gecorrigeerd dient te worden, wegens hun inherente gevoeligheid voor onregelmatigheden in de belichting van de ontvangers. Deze correctie kan onder andere in stand gebracht worden door in een aparte *processing* stap de belichting uit te balanceren, of door, in het geval dat registraties van aardbevingen gebruikt worden, een speciale filter toe te passen. Impliciet geformuleerde methodes hebben het voordeel dat deze genoemde *processing* stappen al inherent in de methode verwerkt zijn. Afhankelijk van welke reciprociteitsrelatie is gebruikt als basis, bestaan er verscheidene vormen van impliciete methoden. Van deze vertoont de methode die gekenmerkt is door een compliceerde *kernel* de grootste stabiliteit. Deze conclusie is gebaseerd op de analyse van numerieke resultaten die verkregen zijn van gesimuleerd omgevingsruis in zowel akoestische als elastische 2D modellen, waarbij gebruik is gemaakt van zeer complexe bron karakteristieken en ruis condities.

Het ontwerp van het ontvangersnetwerk speelt ook een grote rol in het verkrijgen van betrouwbare virtuele reflecties uit passieve data. Gezien er per definitie geen controle bestaat over de tijd en locatie van de passieve bronnen, is het van belang dat de ontvangers, die wel te controleren zijn, zo goed mogelijk voldoen aan bepaalde eisen. Om vouwvervorming tot een minimum te brengen en de belichtingsanalyse van de inkomende golven te verbeteren moeten de ontvangers zo geplaatst zijn dat de gevoeligheid van het ontvangersnetwerk zo constant mogelijk blijft in alle waarnemingsrichtingen. Daarnaast is een constante ruimtedichtheid van ontvangers essentieel om de verwerking van de golfregistraties tot een beeld van de ondergrond mogelijk te maken. Als aan deze twee gestelde eisen voldaan kan worden, resulteert dat automatisch ook in een toename van zones waarbinnen de golven in "interferometrische stationaire fase" verkeren, wat weer de vorming van ongewenste artefacten tegengaat. Een nadeel van het toepassen van onregelmatig geplaatste ontvangers is dat het niet meer mogelijk is in het golfnummer domein te werken en daarmee het gebruik van golfseparatie en -decompositie in het geding brengt. Dit probleem kan verholpen worden door ruimte-afgeleiden, die benodigd zijn voor golfseparatie en -decompositie, te bepalen met numerieke methoden.

In het geval dat de belichting door de passieve bronnen gelimiteerd is, wordt een alternatieve methode geïntroduceerd die ook onder deze uitdagende condities effectief een beeld van de ondergrond kan verkrijgen. Gebrekkige belichting heeft een negatieve uitwerking op het interferometrische proces en vermindert de nauwkeurigheid van het beeld dat verkregen kan worden uit de virtuele reflecties met conventionele technieken. Door het gebruik van de belichtingsanalyse is het mogelijk te bepalen vanuit welke richting het dominante golfveld vanuit de virtuele bron afkomstig is. Kennis van deze richting kan vervolgens gebruikt worden als grenswaarde voor de migratie procedure, waardoor deze alleen seismische fases die stationair zijn selecteert voor de beeldvorming. Deze alternatieve migratie methode maakt op deze manier optimaal gebruik

van elke individuele bron om zo stapsgewijs een beeld te vormen van delen van de ondergrond, zoals bepaald is door de beschikbare passieve belichting. Het voordeel van deze werkwijze is dat een volledige virtuele reflectie acquisitie niet meer benodigd is om de reflectiviteit van de ondergrond in beeld te brengen. Door de verkregen beeldsecties samen te voegen wordt de kwaliteit van het uiteindelijke beeld verbeterd door constructieve interferentie van overlappende reflectoren en destructieve interferentie van artefacten. Dit proces wordt volledig uitgevoerd in het beeld domein en wordt om die reden hier aangeduid als *Image Interferometry*. Onder natuurlijke omstandigheden zijn zeer lange meettijden benodigd om voldoende belichting vanuit alle richtingen te verkrijgen, opdat er met conventionele technieken een reflectie respons verkregen kan worden. Met *Image Interferometry* is dit niet langer nodig: het is met deze techniek mogelijk om een beeld van de ondergrond te verkrijgen zonder te moeten wachten voor optimale belichting. Deze techniek brengt veel voordelen met zich mee, ook wanneer de belichting weliswaar van alle richtingen komt, maar de bronnen te onregelmatig zijn verdeeld om betrouwbare reflecties te geven.

Deze techniek die gebruik maakt van individuele passieve bronnen inspireerde op zijn beurt de ontwikkeling van een alternatieve methode voor het monitoren van veranderingen in de ondergrond met behulp van passieve bronnen. Hiermee kunnen veranderingen in de ondergrond gedetecteerd worden die plaatsvonden tussen het moment van een actieve reflectie seismiek acquisitie en dat een natuurlijk aanwezige bron plaatsvindt in de ondergrond. Door gebruik te maken van reciprociteitsvergelijkingen van het convolutie type, kunnen twee verschillende benaderingen gedefinieerd worden voor deze nieuwe monitor methode, waarbij de actieve acquisitie als basis dient en de meting van de passieve bron als monitor. De belichtingseigenschappen van de actieve bronnen worden aangepast aan de specifieke belichting die de passieve bron kenmerkt. Deze aanpak is veel effectiever dan het wachten op passieve belichtingscondities die overeenstemmen met die van de actieve bronnen. Het is daarbij ook mogelijk de specifieke belichtingseigenschappen van de passieve meting te gebruiken om de actieve en passieve data te migreren, waardoor de veranderingen in de ondergrond ook in het beeld domein geanalyseerd kunnen worden.

Dit proefschrift beschrijft deze samenhangende procedures en bijbehorende resultaten achtereenvolgens in een apart hoofdstuk/annex. Het uiteindelijke doel van deze technieken is om tezamen met bestaande methoden een protocol te vormen voor passieve seismiek waarmee de ondergrond in kaart gebracht kan worden met passieve bronnen.

Summary

Passive seismics is the set of applications that endeavours the exploration of the Earth's mechanical properties using naturally occurring sources in the subsurface. Conventional imaging of the subsurface is achieved with the aid of reflection surveys of body waves from the surface. Passive seismics offers the possibility to retrieve these reflection surveys using recordings of ambient noise and seismic tremors, without the use of active sources. This thesis explores the use of novel applications in passive seismics with the purpose to obtain an improved subsurface image, compared to those obtained using conventional passive seismic imaging.

The quality of the image result retrieved by passive seismics is subject to the characteristics of the passive recordings employed. The main aspects to take into account are the complexity of the medium and the sources' characteristics such as signal function and mechanism, and their respective location and distribution in the subsurface. The recordings due to passive sources situated near the surface are dominated by surface waves, which interfere with the desired body-wave reflection retrieval. The analysis of the passive recording illumination allows the diagnosis and discrimination of the time-sections of the recordings suitable for body-wave processing. The results of the illumination diagnosis are used to suppress the retrieval of surface waves and, therefore, to improve the quality of the retrieved reflection response.

Passive seismic interferometry is in this case the set of processes responsible for transforming the passive seismic recordings into the desired body-wave reflection surveys where receivers were turned into virtual sources. These virtual reflection surveys enable the subsequent use of the techniques employed in conventional reflection seismic imaging. There is a wide range of methods within passive seismic interferometry: varying from the type of data it is applied to (transient-signal tremors or ambient noise), to the manner the estimation of the reflection response is carried out. Explicit methods are the most conventional approaches, yet they require corrections for their sensitivity to the passive source characteristics. These sensitivities imply directional balancing of the illumination from the subsurface and source signal shape filtering in the case of transient signals. Implicit approaches to estimate the response of the subsurface take these aspects into

consideration. There are several implicit methods depending on the reciprocity relation employed in the passive seismic configuration. The use of a complicated kernel aiming to a simpler form of the reflection response has proven to be the most stable one. This is confirmed by the numerical results obtained with ambient noise in acoustic and elastic 2D media, with complex source characteristics and noise conditions.

In the estimation of the reflection response from passive recordings, the acquisition design of the passive-seismic receiver array also plays an important role. Since there is not any control over the time and location of the sources, the distribution of the receivers along the acquisition surface is to fulfil a series of requisites. The sensitivity of the array must be omnidirectionally constant in order to minimize directional aliasing and improve the illumination analysis of the recordings. The second requisite involves the constant density of receivers along the acquisition surface for imaging purposes. In addition, these conditions are to optimize the coverage of stationary phase regions in the interferometric process and reduce artefacts in the imaging procedure. The application of irregular distributions compromises the use of the wavenumber domain for wavefield separation and decomposition. Therefore, the estimation of the operators involved in procedures concerning the space dimension are to be approximated by numerical methods.

Regarding the distribution of sources in the subsurface, an alternative imaging process is presented which responds to the conditions of limited distribution of passive sources in the subsurface. This condition restricts the interferometric process and hinders the accuracy of the imaging results with conventional reflection seismic processing. However, the result of the illumination analysis of the passive sources provides the direction from the virtual source location in which the dominating wavefields are propagating. This aspect defines a directional constraint for a migration scheme where only the events in stationary phase with the array are imaged. By using individual passive sources, the alternative migration scheme allows to obtain images of limited sections of the subsurface, according to the illumination coverage the passive sources can draw with respect to the acquisition array. The advantage of this procedure is that the complete reflection response of the subsurface is not required to produce an image of it. The addition of the different individual image contributions improves the quality of the final image result by constructive interference of commonly imaged reflectors and destructive interference of migrated artefacts. This process is called Image Interferometry, since the interferometric process is carried out in the image domain instead of the shot-gather domain. In natural conditions, conventional retrieval of the reflection response with passive seismics should average over long enough time to obtain sufficient illumination of the subsurface from all angles. With this alternative approach, the imaging of the subsurface is made possible without the need to wait for complete illumination conditions. This imaging process is advantageous, also

when there is an equipartitioned distribution of passive sources, but too sparsely located to retrieve a reliable reflection response.

The exploitation of the information from individual passive sources encouraged also an alternative for monitoring the changes in the subsurface using passive sources. This alternative is based on the changes that happened over the period of time between an active base survey and the moment a passive seismic event is recorded. Employing the reciprocity relations of the convolution type, two different approaches are defined in the new monitoring scheme, where the active survey stands for the base survey and a passive seismic event serves as monitor survey. Since the illumination characteristics of the base survey are omnidirectional due to the active sources employed, the aim is to restrict the illumination characteristics of this survey to that of the passive event. The result allows the comparison of the base and monitor surveys under the same illumination conditions. This approach is more affordable than waiting to acquire sufficient passive sources illuminating from all angles in order to retrieve the complete passive-seismic reflection survey serving as monitor. The migration of the respective surveys is possible using the directional constraints imposed by the illumination of the monitor passive event. This allows, additionally, the possibility to compare and analyze the changes between the base and monitor surveys in the image domain.

Throughout this thesis, the methods that are presented are interrelated and every chapter/annex relies on the methods described in the previous one. The final purpose is to combine these techniques with the already existing methods in order to define a passive seismic protocol to improve the acquisition and imaging of the subsurface using passive sources.